

Electron Dynamics in Double Rydberg Wavepackets

Santosh Narayanan Pisharody
Bombay, India

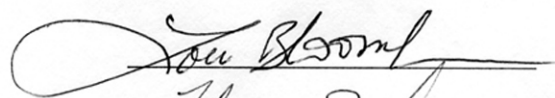
B.Tech., Indian Institute of Technology, Bombay, 1997

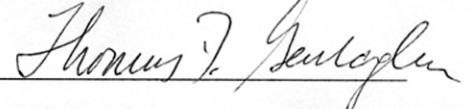
A Dissertation presented to the Graduate Faculty
of the University of Virginia in Candidacy for the
Degree of Doctor of Philosophy

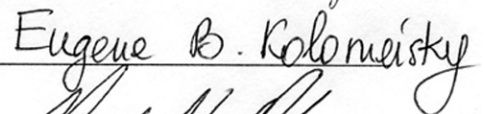
Department of Physics

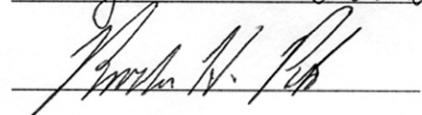
University of Virginia
May 2003











Abstract

The experiments described here represent the first time-dependent study of highly excited double Rydberg wavepackets. There are two main experiments that are described in this dissertation. The first experiment is a study of the decay of an autoionizing rydberg wavepacket in calcium. This experiment shows the decay of autoionizing wavepackets to occur in the form of stair-steps and be critically dependent on the phase of the constituent states. We have been able to control the phase of the components of the wavepackets to vary the decay rates by more than a factor of five. The second experiment is the creation of a controlled double rydberg wavepacket in barium where the two outermost electrons are excited into independently controlled wavepackets at adjustable relative delays. This study provides an experimental realization of a controlled three-body Coulomb problem. We monitor the decay products of autoionization of the double rydberg wavepacket for different initial energies of the wavepackets and as a function of the delay between exciting the wavepackets. We have been able to use an intuitive semi-classical picture to explain the features that are observed in the experiments. The two experiments that have been described here help in a better understanding of electron dynamics in two-electron atoms.

Contents

1	Introduction and Motivation	1
1.1	The Structure of the Atom	1
1.2	Spectroscopy	5
1.3	Lasers	7
1.4	Rydberg Wavepackets	11
1.4.1	Wavepackets	11
1.4.2	Rydberg States	12
1.5	One-electron atoms: Hydrogen and the Alkali atoms	14
1.6	Two-electron Atoms: Helium and the Alkaline-Earth atoms	15
1.7	Isolated Core Excitation (ICE)	17
1.8	Double Rydberg wavepackets (DRW)	18
1.8.1	Classical Three-body Coulomb Problem	18
1.8.2	Controlled double rydberg wavepackets	18
1.9	Dielectron dynamics	19
2	Experimental Setup	24
2.1	The Ti:sapphire laser	25

2.1.1	The Ti:sapphire self mode-locked oscillator	27
2.1.2	Pulse Expander	31
2.1.3	The Regenerative Amplifier	34
2.1.4	The Multipass Amplifier	37
2.1.5	Pulse Compressor	38
2.1.6	Autocorrelator	39
2.2	Optical Parametric Amplifier	43
2.3	Atom Source and the Interaction region	44
2.3.1	Vacuum System	45
2.3.2	The Interaction Region	47
2.3.3	Atom oven	47
2.4	Detection Apparatus	49
2.4.1	Microchannel Plate Assembly	49
2.4.2	Data collection software	51
2.5	State Selective Field Ionization	52
3	Autoionizing Wavepackets in Calcium	54
3.1	Introduction	54
3.2	Experimental Procedure	55
3.3	Controlling bandwidths of lasers	63
3.4	Experimental results	66
3.5	Phase-controlled wavepackets	70
3.6	Data Analysis	71

3.6.1	Semi-classical Picture	72
3.6.2	Two-channel QDT calculations	78
3.6.3	Autoionizing state decay in calcium	84
3.6.4	K-matrix MQDT calculations	85
3.7	Conclusions	95
4	Experiments in wavepacket dynamics	96
4.1	Double rydberg wavepackets in calcium	97
4.2	Autoionization suppression through wavepacket interference	102
4.3	Wavepacket creation by off-resonant ICE	106
5	Double Rydberg Wavepackets in Barium	109
5.1	Introduction	109
5.2	Excitation Scheme	113
5.3	Experimental Apparatus	117
5.4	5dnd autoionizing wavepackets	118
5.4.1	Experimental results and Analysis	119
5.4.2	R-matrix Calculations	123
5.5	Ionic Rydberg states in Ba^+	126
5.6	Double Rydberg wavepackets	132
5.7	Semi-classical Analysis	136
5.7.1	Sudden Redistribution	138
5.8	Classical simulations	143
5.8.1	Choice of initial conditions	144

5.8.2	Results	146
5.8.3	Two-electron dynamics from classical simulations	152
5.9	‘Slow’ Autoionization	156
5.10	Correspondence of classical and quantum approaches	164
5.11	Conclusions	167
6	Controlled Post Collision Interaction	168
6.1	Post-Collision Interaction	168
6.2	Experimental Realization of PCI	170
6.3	Conclusions	178
7	Conclusion and Future Prospects	179
A	Notes on creating DRWs	182
A.1	Another calibration method for N_1	182
A.2	Effects of Laser Polarization	185
B	One-electron Atoms	190
B.1	The Hydrogenic Atom	190
B.2	Non-hydrogenic Atoms	196
C	Two-Electron Atoms	199
C.1	Independent particle model	199
C.2	Multichannel Quantum Defect Theory (MQDT)	202
C.3	R-matrix formulation	205
D	Imaging Stark Spectra	208
	Bibliography	219

List of Figures

2.1	Schematic of the Ti:Sapphire Laser system	25
2.2	The Ti:Sapphire modelocker	27
2.3	Addition of longitudinal modes of a cavity	29
2.4	Pulse Expander and Pulse Compressor for Chirped Pulse Amplification	32
2.5	The Regenerative Amplifier	34
2.6	Autocorrelator for pulse width measurement	39
2.7	Optical Parametric Amplifier Schematic	42
2.8	Schematic of vacuum chamber: Top view	46
2.9	Microchannel plate Assembly	50
3.1	Detector Schematic	56
3.2	Excitation scheme in Calcium	57
3.3	State-selective field ionization (SSFI) spectra	62
3.4	Time-dependent radial probability distribution of a $4sNd$ wavepacket in calcium	64
3.5	Setup for reducing the bandwidth of the Ti:sapphire laser.	65
3.6	Survival probability of $4p_{3/2}N\ell$, $N \sim 40$ wavepackets	67

3.7	Survival probability of $4p_{3/2}N\ell$, $N \sim 35$ wavepackets	69
3.8	Radial probability distribution of the $4sNd$, $N \sim 40$ wavepacket in calcium	74
3.9	Classical Picture of Autoionization	76
3.10	Terms in two-channel QDT calculation for autoionizing state	80
3.11	Term in two-channel QDT calculation for autoionizing wavepacket	81
3.12	Data and two-channel calculations for $4p_{3/2}N\ell$ wavepacket decay	83
3.13	Data and K-matrix calculations for $4p_{3/2}N\ell$ wavepacket decay	92
3.14	Data and calculations for $4p_{3/2}40d$ state decay	93
4.1	Possible double wavepacket excitation schemes in Calcium	98
4.2	Two methods of creating coherent pulses tuned to different wavelengths	104
5.1	Excitation scheme to create ionic rydberg wavepackets in Barium by multiphoton excitation	111
5.2	Excitation scheme to create double rydberg wavepackets	115
5.3	Detector schematic for double Rydberg wavepackets in barium	117
5.4	Survival probability of $5d_{5/2}33d$ autoionizing wavepackets in barium	120
5.5	Decay of $5d_{5/2}Nd$ wavepackets for different N	124
5.6	Decay of $5d_{5/2}Nd$ wavepackets with different bandwidths	125
5.7	Gate calibration for ionic rydberg states	128
5.8	Relative signal strengths in the different gates for different ionic rydberg states	129

5.9	Relative signal strengths per gate in experimental data	134
5.10	Sudden redistribution of an $N \sim 33$ ($Z=1$) wavepacket into $Z=2$	142
5.11	Relative signal strengths per gate from classical simulation	148
5.12	Relative signal strengths per gate from classical simulation(B)	149
5.13	Final ionic state distribution	150
5.14	Radial positions of electrons in $N_1 \sim 33$, $N_2 \sim 50$ wavepacket	154
5.15	Radial positions of electrons in $N_1 \sim 33$, $N_2 \sim 70$ wavepacket	155
5.16	Final ionic state distribution from Slow Autoionization	162
6.1	Continuum wavepacket recombination	171
6.2	Gate distribution of signal from continuum wavepacket recombination	172
6.3	Total signal strength in continuum wavepacket recombination	173
6.4	Continuum wavepacket recombination - classical simulation	176
6.5	Expected signal from continuum wavepacket recombination	177
A.1	Population dependence of final ionic rydberg states on wavepacket delay	183
A.2	Population in ionic rydberg states as a measure of N_1	184
A.3	Fast electron signal when lasers are polarized horizontally	187
C.1	Two-electron system	199

List of Tables

3.1	<i>LS</i> K-matrices at energy = -0.321646 a.u. [111]	86
3.2	<i>LS</i> to <i>jj</i> transformation matrix for $J = 1$	87
3.3	<i>LS</i> to <i>jj</i> transformation matrix for $J = 3$	88
4.1	Transition probabilities in Ca II [112]	100
5.1	R-matrix for barium $J=0$ near the $5d_{5/2}^+$ limit [98]	123

Acknowledgements

The work that has led to this dissertation has been the cumulative result a process of learning for the past twenty seven years. A good bit of that time was spent with my loving family - my parents Shri. and Smt.T.P.Narayanan and sister Sandhya. Thank you all for your support and encouragement as I chose my own path of study and for pushing me hard to do better at everything I chose. I would also like to thank my teachers who, over the years of my study in school and college, have always been the best anyone could have asked for and who helped to spark my insatiable quest for knowledge.

I would like to thank all my friends and classmates at the Indian Institute of Technology in Bombay for sharing with me the best years of my adult life and letting me enjoy it all the more for your company. The four years from 1993 to 1997 will forever be etched in my mind with the memory of all the pranks and accomplishments that we shared during our time at Powai. I will also take this opportunity to once again thank all the professors at IIT Bombay that I have had the pleasure of working with for imparting the knowledge that has held me in good stead over the years.

The past few years at the University of Virginia have made a very lasting impression on me that I will carry with me for the rest of my life. Here, I have had the pleasure of finding friends among people of several nationalities and backgrounds who all share a passion for physics. I would like to thank Slava for his company at playing pool and at the movies and for teaching me to drive when I got my first car. I would like to thank Supriya for being a good friend and for being a fount of laughter in the lab. It would be hard to acknowledge everyone without a mention of Jason who introduced me to American culture by inviting me to his grandparents' house for Thanksgiving every year. Thank you Jason for being an excellent lab partner and an even better friend. Hope you have a great time designing IR vision for the ARL.

Thanks also to Matt Campbell and Tom Bensky who were very helpful in introducing me to all the aspects of the functioning of the lab when I joined the research group of Prof. Jones.

All of my work at UVa has been aided by the excellent staff of the Physics department who have been constantly helpful in clearing away any problems of paperwork and also in providing an atmosphere of cheer to the otherwise stoical department. I would like to especially thank Bobby Floyd and Chris Floyd together with the staff at the Accounting office who have helped to procure all the basic lab necessities and taking care of all the hassles of contacting the equipment suppliers. Thanks to Jim Shea from the Physics library for his endless supply of stories and philosophical discourses. Thanks to everyone in the machine shop who have provided extremely useful advice on designing parts for the detectors in some of my experiments. Thank you also to Suzie, Tammie, Teresa, Pam, Dawn and Brenda for making the departmental office such a welcoming place. Thanks to Bryan and Shawn for being extremely helpful in answering all of my questions on programming and operating systems.

I would also like to thank Prof. Tom Gallagher and his entire research group for providing me the opportunity to be involved with their research on rydberg atoms and for offering a closer view of several interesting experiments.

A big credit for the work presented here must go to Prof. Bob Jones who provided me the opportunity to work in his lab for the past five years. Thank you Bob for being a good experimentalist and a great teacher. If I could think of anyone who can teach by example or even just by their presence, it would have to be you as I have often found myself answering my own doubts while standing at your door. Thank you for all your patience and confidence in me even at times when I was more inclined to believe that I was on a wrong track in an experiment but eventually wound up on a better path. Thank you Prof. Jones because this dissertation would not have been possible without your constant guidance and counsel throughout the course of my research.

Thanks to AFOSR, DOE, NSF and the Packard Foundation for providing the funding for the research presented here.

Santosh Narayanan Pisharody

Chapter 1

Introduction and Motivation

1.1 The Structure of the Atom

One of the fundamental foundations of science as we know it today has been the drive to study and understand the universe from the macroscopic structure of the universe as studied in astronomy and astrophysics to the smallest constituents of matter as studied under high energy physics.

Some of the earliest recorded references to the study of the structure of matter is found in the work of Greek philosophers around 420 BC. The Greeks taught that every body is divisible without limit, that gold is composed of “little seeds of gold” or wood is made of “little seeds of wood” and so on. This and similar views had been the prevalent view of the nature of matter in most of the world until the Renaissance period in Europe in the 16th and 17th centuries.

In 1704, Newton published “*Optics*” in which he presented his corpuscular the-

ory of matter. In the corpuscular theory, all elements were composed of different arrangements of atoms which in turn consisted of small, hard, billiard-like particles. He explained chemistry in terms of chemical affinities of the participating substances. This was one of the earliest attempts to describe atoms as being the fundamental particles that dictate the properties of different materials.

In 1803, John Dalton proposed his *Atomic Theory* and presented it in the *New System of Chemical Philosophy* (1808-1827). The theory stated that (1) all matter was composed of small indivisible particles termed atoms, (2) atoms of a given element possess unique characteristics and weight, and (3) three types of atoms exist: simple (elements), compound (simple molecules), and complex (complex molecules). He was the first to identify different elements as composed of different kinds of atoms and the concept of atoms of different elements combining in integral ratios to form molecules. It would take almost a century before another discovery would increase our understanding of the structure of atoms or explain the difference between atoms of different elements.

Scientific progress over the 19th century led to the discovery of new properties of matter and the model of the atom underwent several changes. Different elements were found to emit light in distinct series of unique wavelengths. This led to the ability to uniquely identify the components of complex molecules and to the discovery of new elements. The discovery of the electron by J.J.Thomson [1] in 1897 was a major turning point for the study of atomic structure. Until the discovery of the electron, the atom was considered the smallest indivisible constituent of matter. The

discovery of the electron and the alpha particle in the last decade of the nineteenth century sparked a revolution in the study of atomic structure. Thomson's "plum-pudding" model of the atom [2] was able to explain some of the properties of gases and emission of radiation by atoms but it could not give a quantitative explanation for experimentally observed optical spectra like that of the Balmer series [3].

The alpha-scattering experiments of Geiger and Marsden [4] led to the Rutherford model of the atom [5]. This model predicted a heavy positively charged nucleus which consisted of most of the mass of the atom surrounded by a lot of empty space in which the electrons could exist. However, this did not explain the distribution of electrons around the nucleus. A possible explanation for the distribution of electrons in the atom came with the Bohr theory of the hydrogen atom [6]. The basic postulates of his theory are: (1) An electron in an atom can only move in certain circular orbits around the nucleus without radiating. These are called discrete stationary states of the atom. (2) Only those stationary states are allowed for which the orbital angular momentum of the electron is an integral multiple of $h/2\pi$ where h is the Planck's constant. (3) An electron can jump from a high-energy state to a low-energy state by the release of a photon with an energy corresponding to the energy difference between the two states.

Bohr's theory was able to account for the optical spectra of hydrogen with one electron orbiting a positively charged nucleus. The energy levels in hydrogen-like atoms as predicted by Bohr's theory are expressed as

$$E_n = -\frac{1}{2n^2} \frac{m_e Z^2 e^4}{\hbar^2} \frac{1}{(4\pi\epsilon_0)^2} \quad (1.1)$$

where n is called the principal quantum number, m_e is the mass of the electron, Z is the charge on the nucleus, e is the charge of the electron, ϵ_0 is the dielectric constant of vacuum and, $\hbar = h/2\pi$. In the rest of this dissertation, the atomic system of units will be used ($e = 1, \hbar = 1, m_e = 1$ and $\frac{1}{4\pi\epsilon_0} = 1$) so that this expression reduces to

$$E_n = -\frac{Z^2}{2n^2} \quad (1.2)$$

Our understanding of atomic structure was increased over the years by the improvements made to Bohr's model of the atom. Sommerfeld extended the model to include elliptic orbits and also relativistic corrections which led to explanations for the fine splitting of the energy levels and quantization of angular momentum at each energy. The Wilson-Sommerfeld quantization rules [7] also led to space quantization to distinguish between different orientations of the electronic orbits in space with respect to some fixed axis. The magnetic quantum number was introduced which explained the spectra of hydrogen in the presence of a magnetic field.

In spite of the successes of the Bohr-Sommerfeld model of the atom in explaining the spectra of hydrogen, they were based on several assumptions of quantization which were not fully explained. Moreover, the model did not explain the spectra of more complex atoms than hydrogen. The giant leap forward in understanding atoms came with de Broglie's quantum hypothesis [8] in 1924 and the subsequent development of quantum mechanics by Schrödinger [9] and matrix mechanics by Heisenberg [10]. The solution to Schrödinger's wave equation automatically leads to the quantization conditions proposed by the Bohr-Sommerfeld model and could be further extended to more complex systems. The solution to the Schrödinger equation for hydrogen is

presented in Appendix B.

The discovery of the neutron by Chadwick [11] in 1932 led to the currently accepted neutron-proton model of the nucleus. Modern atomic physics since the 1930s has led to refinements in the model of the atom to explain discoveries of new features in the energy level spectra of complex atoms but the essential model of the atom as a positively charged nucleus surrounded by negatively charged electron clouds has remained the same over the latter part of the past century.

1.2 Spectroscopy

The study of atoms has progressed alongside the study of light and optics. Once again, Newton played an important role in the early development of the theories of light. The term “spectrum” was coined by Newton to describe the distribution of light of different colors when sunlight was passed through a glass prism [12, 13]. “Spectrum” has now come to refer to any distribution but in the context of atomic physics, it refers to the distribution of energy states of an atom or molecule. The study of the energy levels in an an atomic (or molecular) system is termed “spectroscopy”.

Regular and reproducible bright and dark bands in the light seen through a prism when looking at different sources like the sun or stars or flames from different compounds were the early indicators of the presence of different kinds of atoms in molecules. The development of the diffraction grating by Fraunhofer was crucial to the extension of spectroscopy to explain the different colors on the basis of their

wavelengths rather than just prism angles as was the case preceding it. Spectroscopy was the most important method for identifying different elements present in compounds and the distribution of colors in the spectra formed the basis for explaining the structure of the atom by various theories.

Early methods of spectroscopy involved burning elements or compounds in flames and looking at the light from the flame through a prism or a diffraction grating to study the distribution of colors in the spectrum. The observation of absorption spectra and the realization that the absorption and emission spectra are identical led to the theories of black-body radiation and eventually the quantum hypothesis by Max Planck. Spectroscopy has been and still remains the method of studying atoms and molecules but the techniques of spectroscopy have undergone several improvements over the years.

The flames used in early experiments were later replaced by electric discharge tubes. White-light generators were developed to study absorption spectra. The quality and design of diffraction gratings have improved over the years and led to increased spectral resolution allowing the identification of several previously unobserved lines in the spectra. Even today, the study of any new state of an element or compound is performed by the use of spectroscopy to identify the energy levels of the system. The biggest change in the methods of spectroscopy came with the development of the laser and the maser.

1.3 Lasers

Most of the early experimental work in atomic physics concentrated on optical spectroscopic studies of various elements under different conditions. Many elements were studied by looking at their emission and absorption spectra in gas-discharge tubes. These studies using incoherent light sources with broad bandwidths limited the number of states that can be directly accessed through photo-excitation. The invention of the maser and eventually the laser in the 1950s and 1960s made it possible to excite individual states in atoms with increased precision and this led to a significant improvement in the ability to study atomic systems spectroscopically. Modern atomic physics is then the study of the interaction of atoms with laser radiation (or any coherent EM radiation) under different environmental conditions (i.e. presence of electric or magnetic fields which can affect the properties of the atom).

Lasers owe their origins to the work of Einstein and Bose who developed the theory of photon statistics (Bose-Einstein statistics). The work of Einstein on black-body radiation combined with the photon statistics developed by S.N.Bose suggested the concept of stimulated emission of radiation from excited atoms being coherent and unidirectional [14]. While Bose-Einstein condensation (BEC) in atoms has only been observed recently [15], the original observation of the BEC effect was in photons with the development of the maser in 1954 [16]. The concept of the laser is similar to that of the maser but extended to visible electromagnetic radiation.

The early lasers were only able to operate at specific wavelengths without any tunability. The development of the earliest lasers was a matter of choosing the right

lasing medium and design and after the development of the first ruby laser by Maiman [17], several different lasers operating with different lasing media were developed in rapid succession [18]. Some of the important developments of lasers for spectroscopic studies include the invention of the dye lasers [19,20] which enabled lasers to be tuned over a range of wavelengths and the development of high-power Nd-based lasers [21]. Pulsed lasers have been in use since the early 1960s to create short pulses of coherent radiation with high peak powers [22]. The development of the Ti:sapphire laser in the late 1980s was the single biggest contributor to the creation of ultrashort laser pulses with pulse widths of less than a picosecond allowing peak powers of over $10^{14}W$ [22]. The Kerr-lens effect in Ti:sapphire crystals allows us to use these crystals to create laser pulses with durations of less than 0.1ps [22,23]. Different methods were used to generate sub-picosecond duration pulses with dye lasers before the advent of the Ti:sapphire laser. However, they were generally less stable in terms of their ability to maintain the power output levels in comparison to the solid-state Ti:sapphire laser.

Lasers can emit light over a small and finite wavelength in a coherent manner which is determined by the lasing medium as well as the quality and geometry of the optical elements in the laser. The tunability of a laser is determined by the emission levels/bands in the laser medium while the pump for the laser is determined by its absorption levels/bands. The choice of a laser for an experiment in atomic physics is determined by the requirements of the experiment: range of energy levels to be excited determines the required tunability range of the laser; the line-widths of the states to be excited would determine the bandwidth of the laser to be used; the

excitation probability of the states would determine the power output required from the laser. In the case of experiments to study temporal dynamics in an atom, the pulse width of the laser also becomes a determining factor in the choice of the laser.

The aim of atomic physics has always been to understand the structure and dynamics of an atom. However, experiments in atomic physics are always limited by the technical capabilities of the era. Until the development of lasers, for example, it would have been impractical to be able to excite individual states in an atom that could only be accessed by multiphoton excitation. With the development of tunable lasers, it became possible to access excited states of atoms that were inaccessible with any other form of excitation and gave rise to coherent spectroscopy. Emission and absorption spectroscopy of atoms before the development of tunable lasers was a passive experimental method - the atoms emitted or absorbed different frequencies in the spectrum but there was no control over specific excitation schemes. The use of tunable dye lasers to study the spectra of atoms can also be considered a passive method in the sense that even though one can access several states in the atom and get a detailed information about the energy level structure, the states that are excited are stationary states which do not provide any direct information about the atom dynamics.

An electron in the ground state of hydrogen moves at high velocities ($c/137 = 1$ a.u. $= 2.19 \times 10^6 m/s$). It completes a revolution around the nuclear core in 0.15 femtoseconds (1 femtosecond= 10^{-15} s). This is much shorter than the shortest laser pulses that have so far been produced regularly in labs around the world although

we are fast approaching this limit in creating shorter pulses [24]. However, when we put the atom in an excited state, the classical period of revolution of the electron around the nucleus (Kepler period), increases with the principal quantum number of the excited state as $2\pi n^3$. So, for an excited state with $n = 30$, the Kepler period becomes 4.1 picoseconds. We can create laser pulses of much shorter duration than a picosecond with tunable Ti:sapphire lasers and optical parametric amplifiers (OPAs). This makes it possible to study such highly excited states with short laser pulses that can be used to probe their dynamics.

The concept of producing ultrashort pulses in lasers is based on the ability to excite multiple wavelengths of laser radiation in a coherent manner. According to Fourier theory, time and frequency are conjugates of each other. A short pulse in time therefore corresponds to a pulse with a broad frequency spectrum. However, a broad frequency spectrum does not always lead to a short pulse unless the phases of all the frequency components are matched precisely.

The laser pulses that we typically generate in our lab have pulse widths of 120-150 fs. This is comparable to the Kepler period of an $n = 10$ state in a hydrogenic atom. So these laser pulses can be used to probe dynamics of states that are excited with higher energies than $n = 10$. For reasonable resolution of the dynamics in the atoms, we typically excite atoms to states higher than $n = 30$. The detailed working of the Ti:sapphire laser is explained in chapter 2 along with the laser setup.

1.4 Rydberg Wavepackets

1.4.1 Wavepackets

If we have an isolated system that is completely described by a set of basis states, $\phi_i(\vec{r})$ ($i = 1, \dots, n$), with energies, E_i , a general state of the system can be expressed as

$$\Psi(\vec{r}, t) = \sum_{i=1}^n C_i \phi_i(\vec{r}) e^{iE_i t + \rho_i} \quad (1.3)$$

where C_i are the real amplitudes of each eigenstate in the wavefunction and ρ_i are constant phases associated with each eigenstate.

The spatial probability distribution of the wavefunction can then be expressed as

$$\begin{aligned} P(\vec{r}, t) &= |\Psi(\vec{r}, t)|^2 \\ &= \Psi^*(\vec{r}, t) \cdot \Psi(\vec{r}, t) \\ &= \sum_{i=1}^n \sum_{j=1}^n C_i^* C_j \phi_i^*(\vec{r}) \phi_j(\vec{r}) e^{i(\rho_j - \rho_i)} e^{i(E_j - E_i)t} \end{aligned} \quad (1.4)$$

The spatial probability distribution has a well-defined and constant spatial structure at all times if all the states with a non-negligible contribution to the wavefunction have the same energy so that the time-dependent term vanishes. Such a superposition of degenerate states with a constant spatial probability distribution is termed as a stationary state.

If the states that make up the wavefunction have different energies, the relative phase between any two components of the wavefunction varies with a period that is inversely proportional to the energy difference between the components ($\tau_{ij} \propto \frac{1}{\Delta E_{ij}}$

where $\Delta E_{ij} = |E_i - E_j|$). Such a coherent superposition of non-degenerate eigenstates of a system with a time-dependent spatial probability distribution is termed a ‘wavepacket.’ In an atomic system, coherent excitation of two or more non-degenerate states produces an electronic wavepacket.

1.4.2 Rydberg States

A “rydberg atom” is the term used to refer to atoms in excited states where at least one electron is in a state with high principal quantum number ($n > 10$) [25]. It is also common usage to term the excited state as a “rydberg state”. A coherent excitation of more than one rydberg state is called a rydberg wavepacket. There are some uniquely appealing characteristics of these states which endear them to researchers in atomic physics-

- 1) Rydberg states are accessible for excitation using lasers in the visible spectrum within one or two photon energy levels for most atoms. Visible laser systems have the advantages of being easier to operate as well as to align accurately in an experimental setup.

- 2) Rydberg states have large orbital radii. Excited states of atoms other than hydrogen are affected by the screening effect of other electrons and the structure of the nucleus. At distances far from the atomic core, effects of screening by other electrons can be treated as a perturbation to the core potential. This allows us to treat rydberg atoms similar to a Coulomb problem for most calculations.

- 3) Rydberg states have a relatively high density of states enabling coherent exci-

tation of multiple states using pulsed lasers with relatively low bandwidths. The high density of states also increases the time-periods of the dynamic processes in atoms excited to rydberg states making them more accessible to time-dependent probing with short pulsed lasers. The development of sub-picosecond lasers over the past two decades have enabled us to study time-dependent dynamics in atoms excited into rydberg states.

A coherent excitation of multiple rydberg states with different principal quantum numbers but the same orbital angular momentum quantum number produces what is known as a radial wavepacket. The dynamic evolution of such a wavepacket can be modelled classically as an electron moving in the field of the positively charged core. A radial rydberg wavepacket can be visualized as a shell of negative charge that oscillates radially about the positively charged atomic core [26]. The principal period of oscillation of the negatively charged shell is equivalent to the Kepler period of an electron orbiting a positively charged core with the energy equivalent to the central energy of the wavepacket. In the rest of this dissertation, the term “Kepler period” would be used to refer to the period of oscillation of the radial wavepackets as well as the orbital period of an electron orbiting the atomic core in a classical model of the atom.

1.5 One-electron atoms: Hydrogen and the Alkali atoms

When we study atomic physics, we like to start from the simplest atomic system and then proceed to more and more complicated systems. The simplest atom that can be studied is hydrogen with one electron orbiting a proton. The energy levels of the hydrogen atom (if we neglect effects of spin and relativistic corrections) are found by directly solving the Schrödinger equation as (see appendix B)

$$E_n = -\frac{1}{2n^2} \quad (1.5)$$

In the case of alkali elements with one valence electron outside a core formed by the nucleus and one or more closed shells of electrons, the outermost electron experiences a net charge of $+1$ at distances far from the nucleus due to the screening effect of the closed shells of electrons. The electron can then be treated as being in a Coulomb potential far from the core but experiences a modification of the potential close to the core due to the presence of the inner electrons. The effect of the core on the energy levels can be treated as a perturbation to the Coulomb potential. This modification presents itself in the form of shifts in the energy levels in comparison to the energy levels of hydrogen in the form

$$E_n = -\frac{1}{2(n - \delta)^2} \quad (1.6)$$

where δ is called the quantum defect for the series. The value $\pi\delta$ is also interpreted as the phase shift of the wavefunctions for the alkali atoms from the case of hydrogen

at radial distances outside the core. δ is dependent on the interaction between the core and the rydberg states. In a classical picture, the point of closest approach of the rydberg electron to the core is decided by the angular momentum of the rydberg electron. The quantum defect is found to be a function of the orbital angular momentum of the rydberg series and a slowly-varying function of the principal quantum number [27]. δ removes the degeneracy of angular momentum states unlike the case of hydrogen [25].

A radial rydberg wavepacket in hydrogen or in alkali atoms can be modelled classically as an electron in a Coulomb potential with an energy corresponding to the central energy of the wavepacket, E_n . This model works well for short times up to a few Kepler periods before wavepacket dispersion and quantum interference phenomena make it hard to localize the wavepacket [26].

1.6 Two-electron Atoms: Helium and the Alkaline-Earth atoms

The simplest case of a two electron atom is helium. With two protons and two neutrons forming the nuclear core, one electron orbiting the nucleus represents a hydrogenic helium ion. The addition of another electron to form the helium atom significantly increases the complexity of the problem of finding the energy levels of the system. The Schrödinger equation can no longer be solved to get an analytical expression for the energy levels for a two-electron atom. Converging to each energy

level of the helium ion, the two electrons in the helium atom can occupy an infinite series of energy levels. Each of these series of states with energies converging to an energy level of the ion is termed as a ‘channel’ or a ‘configuration’ and there are an infinite number of possible configurations. We can also consider alkaline earth elements in a manner similar to helium with the modification of the core to include the inner filled shells of electrons along with the nucleus.

The two-electron system can exist in a superposition of several possible configurations in which both the electrons can be bound or one of the electrons gains sufficient energy to escape the atom leaving behind the other electron tightly bound to the ion. A configuration in which both electrons are bound is termed as a *bound* or *closed* channel while a configuration with one of the electrons free is termed as a *continuum* or *open* channel. As long as one of the electrons in the doubly excited atom remains bound close to the core and the other electron is in an excited rydberg state with a greater radial extent than the core, the system can be analyzed using multi-channel quantum defect theory (MQDT) [27, 28] (see Appendix C). Autoionization processes in two-electron atoms have been extensively analyzed using these methods [29, 30, 31].

At energies where both electrons are excited into states of comparable radial extent such that one electron can no longer be considered as being farther from the core than the other for most of the time, the MQDT analysis is no longer valid. When the number of channels to be considered in an interaction between two electrons becomes large, MQDT analysis starts to get very difficult. In such cases, we have to rely on developing semi-classical models to understand spectral structure and electron

dynamics [32].

1.7 Isolated Core Excitation (ICE)

One of the most important developments for the experimental study of doubly excited states in two-electron atoms has been the use of isolated core excitation(ICE). The basic idea of ICE in a two-electron atom is that one electron is initially excited into a rydberg state while the other electron remains close to the core in the ground or a low energy excited state of the positive ion. A second laser tuned over the resonance levels of the positive ion can then excite the inner electron from the ground state (or low-energy excited state) of the ion into an excited state while the first electron is far from the core. This excitation of the inner electron while the outer electron is far from the core and remains a spectator without itself absorbing any energy is termed as isolated core excitation [25, 29, 33, 34, 35, 36].

Direct excitation of a two-electron atom from the ground state to an energy level corresponding to double rydberg states does not allow independent control of the energies of the two electrons. The use of ICE makes it possible to excite the two electrons in a dielectronic atom in an independent and sequential manner which is a necessary requirement to create controlled double rydberg wavepackets as described in the following sections [37].

1.8 Double Rydberg wavepackets (DRW)

1.8.1 Classical Three-body Coulomb Problem

A set of three charged particles moving in their combined fields forms a classical three body Coulomb problem. Such a system has no unique analytical solution for the motion of the particles. One way to study such a system theoretically is by using numerical methods of calculating the instantaneous motion of the particles. Experimental verification of such calculations is limited by the fact that it is practically impossible to create a completely isolated system of three charges to study their dynamic evolution.

1.8.2 Controlled double rydberg wavepackets

A two-electron radial wavepacket in which the energies and relative radial positions of the wavepackets can be chosen by adjusting laser wavelengths can therefore serve as a controlled three-body Coulomb system. The two electrons can be excited individually by making use of isolated core excitation (ICE) techniques [37, 38, 39]. The initial positions of the three particles in this system would be controlled by adjusting the time delay between exciting the two wavepackets. In a doubly excited two electron system, one of the electrons gains enough energy to become free while the other electron becomes more tightly bound in an excited state of the ion through a process of autoionization. We can detect either the emitted electron or probe the resultant excited ion to study the interaction process.

1.9 Dielectron dynamics

People have studied two electron atoms spectroscopically for over a century. The development of the Bohr-Sommerfeld model of the atom which was able to explain several of the spectral lines observed in hydrogen was unable to account for the spectra in two-electron atoms like helium. The inability of the early atomic models to explain spectra of helium is sometimes credited as being one of the driving forces behind the development of quantum mechanics [40]. A nice review of theoretical and experimental work on two-electron atoms has been given by Tanner et.al in the Reviews of Modern Physics [40].

The early theoretical study of two-electron atoms, mainly helium, was driven in two main directions - one path was to devise methods for expressing the hamiltonian of the doubly excited states of helium in suitable coordinates to try and quantize the energy levels of the atom to match them with experimental spectra. The works of Unsöld [41] using first order perturbation theory, Slater [42] using molecular models, Kellner [43] and Hylleraas [44] using variational methods, Ho using complex coordinate rotation [45] and Pekeris [46] and Bürgers [47] using perimetric coordinates to calculate the ground state in helium are just some of the examples of work along this path. Another path that was followed was to use semi-classical methods to look for stable orbits in the combined motion of the two electrons and comparing the energies of these stable orbital configurations to experimental helium spectra [6, 48, 49, 50, 51, 52, 53, 54]. Classical mechanics has also been applied to study the motion of two-electron atoms to determine stable orbital configurations [55, 56].

Mathematical methods for finding solutions to the three-body Coulomb problem in two dimensions have also been explored to provide insights into finding possible solutions to the problem in three dimensions [57].

Several experiments in helium have followed the early experiments by Madden and Codling [58] to look at electron correlations between the two electrons [59,60]. Such experiments on doubly excited states in helium require very high energies that are available in synchrotron sources which also limits the resolution of the energy levels that can be observed. The use of lasers and resonant multi-step laser excitation to access double rydberg states in alkaline-earth elements opened up new possibilities of generating doubly excited states with different angular momenta in a controlled manner [40,61]. Two-electron alkaline-earth atoms have been studied extensively to understand the dependence of electron-electron correlation on the principal quantum number of the excited states [62,63], angular momentum and energy of the excited states [64,65,66], relative electron positions [67], and core polarization effects of inner electrons [69]. In all of these studies, lasers are used to measure the excitation spectrum into the double rydberg states and the results are interpreted based on different, yet complementary models of the two-electron atom. The results of spectroscopy of doubly excited states are used to get an idea about the dynamics in two electron atoms that give rise to these spectral lines [70,71,72,73] and are also interpreted in the MQDT model [74,75]. In these experiments in the frequency domain, the energy levels that are excited are limited to cases where the radial extent of one rydberg state (r_1) is about four times the radial extent of the inner electron (r_2) in the excited

state. As r_2 approaches r_1 at higher excitation energies, the excitation spectrum appears continuous thereby making it difficult to use the excitation spectrum at higher energies to determine electron dynamics [65].

As an example of the method of using excitation spectra to infer the dynamics of electrons in an atom, Appendix D presents an experiment that uses the excitation spectrum of sodium in the presence of an electric field to determine symmetries in the fourier space by appropriate scaling of the coordinates and interpret the symmetries as corresponding to different kinds of orbits of the electron in the atom in the presence of an electric field. However, although these kinds of studies of the excitation spectrum can be used to predict the motion of electrons in a particular field under very specific circumstances, it does not give us any direct information on the dynamics that actually occur in the atom in the presence of the field.

Some recent experiments have been able to directly study time-dependent features in doubly excited states [76, 77, 78, 79] but these have been limited to states with one electron in a low-lying excited state. The advantage of studying a system in a time-dependent manner is that in addition to providing information about the dynamics of the system, it allows us real-time control over a dynamic property of the system. Instead of studying the energy levels of a system to understand the dynamical properties of a system, a direct study of the dynamics with short pulse lasers can give us a more intuitive feel for the processes that occur in the two-electron system. This method is useful when the dynamics are slow in comparison to the duration of the laser pulses.

Our aim in the experiments described in this dissertation is to excite both the electrons in the valence shell in barium into excited states and to see if we can learn anything about the dynamic processes that take place in the doubly excited atom by studying the variation in its dissociation pathways.

While the theoretical studies of dynamics in two-electron atoms consider only the case of helium as a three-body Coulomb problem, the presence of the core in alkaline earth atoms makes the potential experienced by the electrons in orbits that penetrate the core in these atoms to be non-Coulombic. To overcome this problem, we excite both the electrons in our barium atoms into highly excited rydberg states with radial extents far from the core so that for all theoretical considerations, the two electrons can be assumed to be in the Coulombic potential of the core.

Since the doubly excited atom can be classically equated to a three-body Coulomb problem whose solution depends on its initial conditions, we would like to have good control over initial positions and velocities of the two electrons. In a manner akin to the methodology used by theorists, we would like to choose the initial position and velocities of the excited wavepackets [40]. We make use of our knowledge of rydberg wavepacket dynamics to place one of the electrons at a position in space with a velocity of our choice at some instant in time. We can then excite the second electron at that instant by the use of ICE to place this second electron close to the core and moving radially outwards with a velocity that is chosen by the energy of the ICE. We monitor the products of the interaction in the form of rydberg states of the ion that remain after autoionization. We have measured the variations in the

distribution of the ionic rydberg states as a function of the initial conditions and can explain many of the observed features with a classical model of the two-electron atom as a three-body Coulomb problem. We find that for doubly excited atoms with a given energy, there is a critical radius from the core within which the interaction between the electrons needs to occur in order to produce autoionization. When the electrons interact outside this critical radius, the energy exchange occurs without autoionization and leads to relatively long-lived states that decay at a slower rate.

The importance of studying two-electron atoms arises from their similarity to more complicated atomic systems and molecules. The two-electron atom is the simplest many-body problem in physics and a study of electron dynamics this system is relevant for the understanding of the dynamics of electrons and atoms in more complicated atoms or molecules.

Chapter 2

Experimental Setup

The experimental setup consists of a Ti:sapphire laser system which is used to create the sub-picosecond laser pulses needed for all the experiments described here. Two Optical Parametric Amplifiers (OPAs) are used to produce tunable short pulses at desired wavelengths using the fundamental output of the Ti:sapphire laser as the inputs. The interaction region for the experiments is located in a sealed vacuum chamber kept at pressures of less than 10^{-6} torr. Microchannel plates are used to detect ions and electrons extracted from the interaction region. The various parts of the experimental setup are described in the following sections in this chapter. The entire setup is mounted on optical tables with tuned damping provided by compressed air in the legs supporting the tables. The temperature on the tables is kept constant by the use of a temperature controller fitted with an air exchanger over the table. The region over the optical tables is enclosed in slit plastic sheets to prevent dust particles from the rest of the room from settling on the optics.

2.1 The Ti:sapphire laser

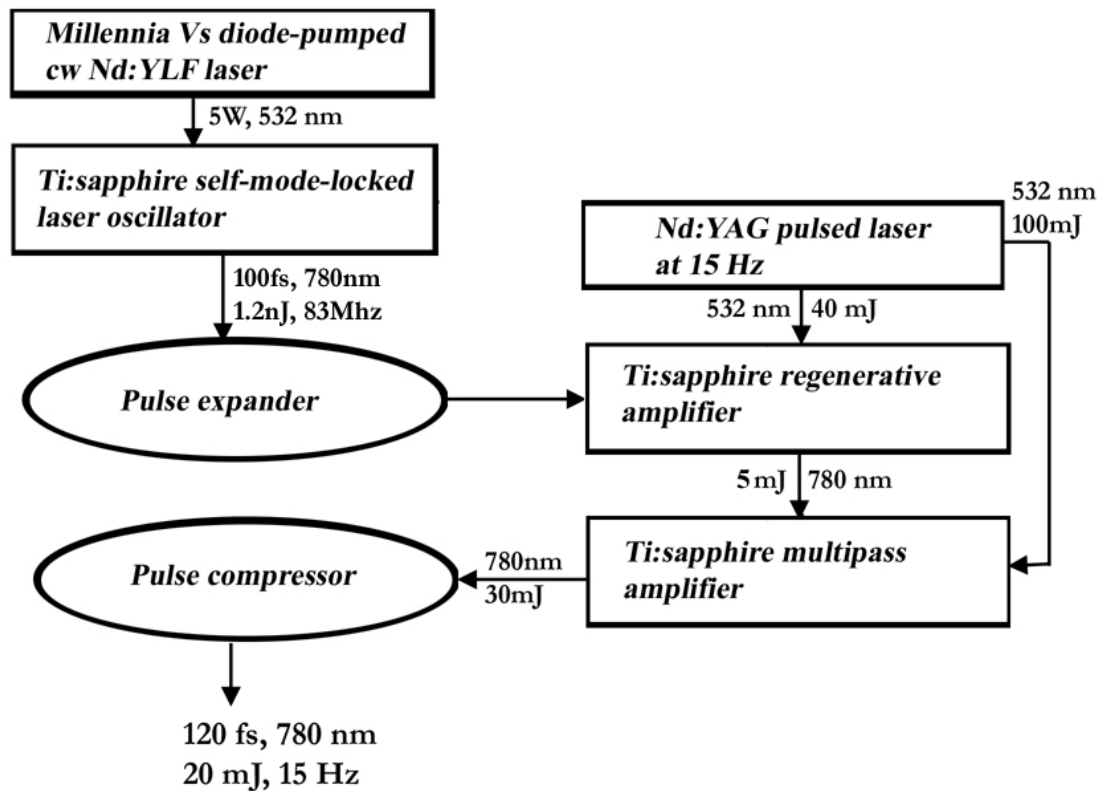


Figure 2.1: Schematic of the Ti:Sapphire Laser system

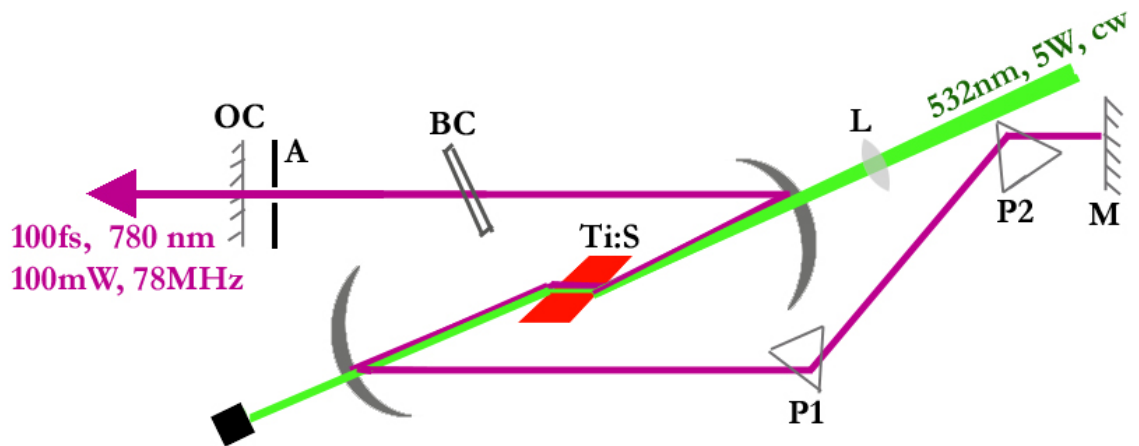
Fig 2.1 shows a schematic of the Ti:sapphire laser system used in the laboratory. The seed light for the Ti:sapphire laser used in the laboratory is produced by a tunable self-mode-locked Ti:sapphire oscillator (see Fig 2.2) pumped by the 5W cw output of a Spectra Physics Millennia Vs laser at 532 nm. The output of the mode-locked Ti:sapphire laser is a series of 100 fs pulses with a tunable central wavelength of ~ 780 nm at a repetition rate of 83 MHz. The pulse train has an average power

output of 100 mW corresponding to about 1.2 nJ of energy per pulse. The central wavelength of the pulses can be tuned using a single birefringent crystal plate in the oscillator. The pulse train is sent into a pulse expander where the different frequency components of each pulse are delayed with respect to each other as a linear function of the frequency to increase the temporal pulsewidth before sending it into the amplifier stages [23]. This is done to prevent non-linear intensity-dependent distortions in the pulse during amplification as well as to avoid damaging the optical elements in the amplifier stages.

Individual pulses are chosen from the pulse train (after pulse expansion) as the seed light for a Ti:sapphire regenerative amplifier pumped by 40 mJ of the 532 nm pulsed laser output of a Nd:YAG laser at 15 Hz. The output of the regenerative amplifier is a pulse with 5 mJ. This pulse is further amplified through a Ti:sapphire multi-pass amplifier pumped by 100 mJ of the 532 nm pulse from the Nd:YAG laser. The output of the multi-pass amplifier is a pulse with about 30 mJ of energy. This pulse is compressed in a pulse compressor which consists of a grating arranged in a manner such as to exactly reverse the expansion process undergone by the pulse in the pulse expander before amplification. The final output of the Ti:sapphire laser system after the pulse compression is a 120 fs pulse with 20 mJ of energy at a central wavelength of ~ 780 nm. These pulses are generated at a repetition rate of 15 Hz corresponding to the repetition rate of the Nd:YAG laser. In the experiments with barium that are described in this dissertation, the bandwidth of the pulse is reduced in the compressor to obtain longer pulses with durations of about 250 fs at a central

wavelength of ~ 770 nm.

2.1.1 The Ti:sapphire self mode-locked oscillator



- OC** : Output Coupler
- BC** : Birefringent Crystal for wavelength tuning
- L** : Focussing Lens for pump beam
- M** : Oscillator end mirror
- P1,P2** : GVD compensating prism pair
- Ti:S** : 2.5cm long Ti:Sapphire crystal
- A** : Aperture

Figure 2.2: The Ti:Sapphire modelocker
The schematic of the Kerr-lens modelocked Ti:sapphire laser oscillator

Fig 2.2 shows the setup of the Ti:sapphire self-modelocked oscillator. The oscillator is pumped by a 532 nm Spectra Physics Millennia Vs diode-pumped $Nd : YVO_4$ solid state laser operating at 5W. It has been noted that the oscillator has a more stable operation at higher power and so the pump laser has been made to run at

5.15W for some of the later experiments. The pump laser as well as the Ti:sapphire crystal in the oscillator are maintained at a temperature of 65 F by water cooling with a Lytron Kodiak RC006 chiller unit.

A Spectra Physics 3900S Ti:sapphire laser designed originally to run in the cw mode was modified by Prof. Jones to run in self-mode-locked oscillation by changing the length of the cavity and introducing a prism pair to compensate for linear group velocity dispersion(GVD) introduced by the optical elements in the cavity.

With a broad gain bandwidth of about 10^{14} Hz [22], the Ti:sapphire laser cavity can sustain standing waves over a wide range of wavelengths. It is possible to simultaneously excite several longitudinal modes (say N) of the cavity separated in frequency by $c/2L$ where c is the speed of light in the cavity and L is the length of the cavity. When all the longitudinal modes are excited in phase, i.e., all the modes have the same phase in space and time at some instant, the modes add up coherently to produce a series of pulses of width $2L/cN$ separated in time by $2L/c$ with peak intensity proportional to N^2 . Ti:sapphire crystals exhibit the Kerr-lens effect [23] which is a non-linear intensity-dependent variation in the refractive index of the medium. The Kerr-lens effect is a self focussing effect because in the case of a pulse with a Gaussian beam profile, the center of the beam with a higher intensity experiences a higher refractive index than the edge of the beam in the same manner as a lens. This effectively changes the beam propagation characteristics of the pulse in the laser cavity depending on its intensity profile. An aperture placed next to the output coupler is used to preferentially introduce higher losses in the cw modes

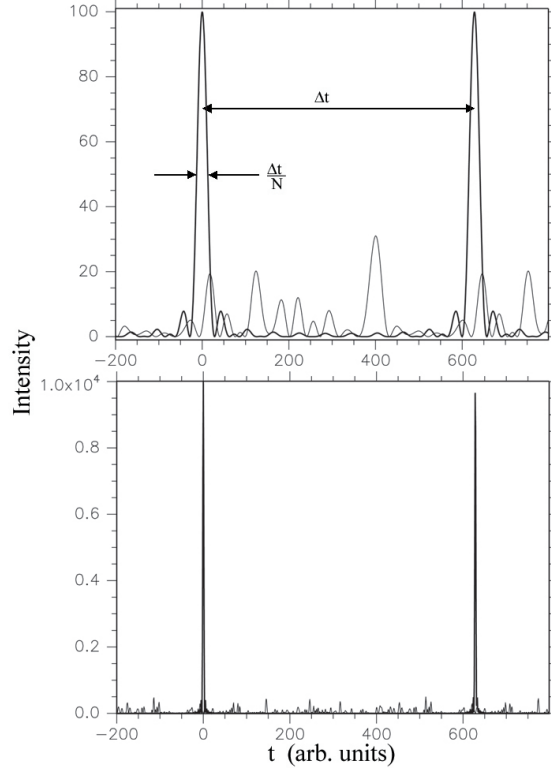


Figure 2.3: Addition of longitudinal modes of a cavity

The upper graph shows the square of the sum of 10 cosine waves while the lower graph shows the square of the sum of 100 cosine waves. The cosine waves have a constant difference in frequency, $\Delta\nu$. The thicker curves in both graphs show the case where the cosine waves have the same phase at 0 while the thinner curves have a random phase in all the waves. In the lower graph, all the thin curves are very small and show up as tiny blips at the bottom of the graph. It is clear that in the case with all the waves in phase, the intensity which is proportional to the square of the sum of the amplitudes in the waves has a significantly greater peak value than in the case with random phases of the waves. The effect increases as N^2 with the number of waves being added together. The time between the peaks Δt is determined by the frequency difference between successive waves as $\Delta t = 1/\Delta\nu$. The width of the pulse produced by phase-matching of the waves is proportional to $\Delta t/N$.

in comparison to the mode-locked pulses. By choosing the focussing characteristics of the pump pulse inside the Ti:sapphire crystal, the efficiency of pumping the cw modes is reduced significantly compared to a mode-locked pulse which experiences self-focussing and is preferentially amplified over the cw mode. In principle, the large number of longitudinal modes allowed by the broad gain bandwidth allows for the creation of pulses that are a few femtoseconds in duration. The self-phase modulation which also occurs along with the self-focussing, enhances the effect by increasing the effective bandwidth of the pulse, thereby allowing shorter pulses [22]. The prism pair is necessary to compensate for the linear GVD by the active lasing medium as well as by the curved optics [23].

The Ti:sapphire oscillator used in the lab has a length of $\sim 1.8\text{m}$. This supports longitudinal modes in the cavity separated in frequency by 83 MHz. Over the range of its gain bandwidth, the cavity can sustain over 10^6 longitudinal modes which corresponds to a transform-limited pulse duration of < 7 fs. A birefringent crystal placed in the cavity is used to preferentially sustain longitudinal modes over a smaller range of wavelengths and is used to tune the central wavelength of the output pulses. This automatically limits the shortest duration of the pulse that can be generated in the cavity. In the Ti:sapphire laser oscillator we use in the lab, we can obtain laser pulses of about 100 fs duration polarized horizontally. The output power of the mode-locked Ti:sapphire oscillator is about 100mW which corresponds to an energy per pulse of 1.2 nJ. A 100 fs pulse has a length in space of 0.03 mm. It is therefore useful to think of a femtosecond pulse as passing from optic to optic and arriving at

different optics at different times.

In the absence of any mode-locked pulses in the cavity, several cw modes of the laser can be simultaneously sustained in the cavity but the high losses (due to the design of the cavity) which exceed the gain per pass for each cw mode prevent the lasing of the cavity in any one cw mode. The oscillator requires a pulse to begin with to start the mode-locked operation since the cavity is designed to operate with a pulse and not a cw mode. In practice, this is done by tapping on the output coupler which is placed on a translation stage to introduce a spike in the background noise of the modes operating in the cavity. The noise spike is better matched to the cavity than the cw modes and gets amplified in each pass through the cavity leading to mode-locked operation of the cavity [80]. A glass slide placed at the output of the modelocked oscillator sends a part of the light into a fast photodiode which is used to trigger a Spectra Physics SM-1 sync module. The sync module is used to provide the trigger for the pulsed Nd:YAG laser used in the amplifier stages with a trigger so that all the components of the laser system are synchronized with the pulsed output of the mode-locker to within a nanosecond.

2.1.2 Pulse Expander

The energy per pulse (1.2 nJ) in the output of the mode-locked oscillator is very small for the purposes of our experiments. We use multiple amplifier stages to increase the pulse energy. However, amplification of the short pulses directly would increase the peak power in the pulses beyond the damage threshold of the optics used in the

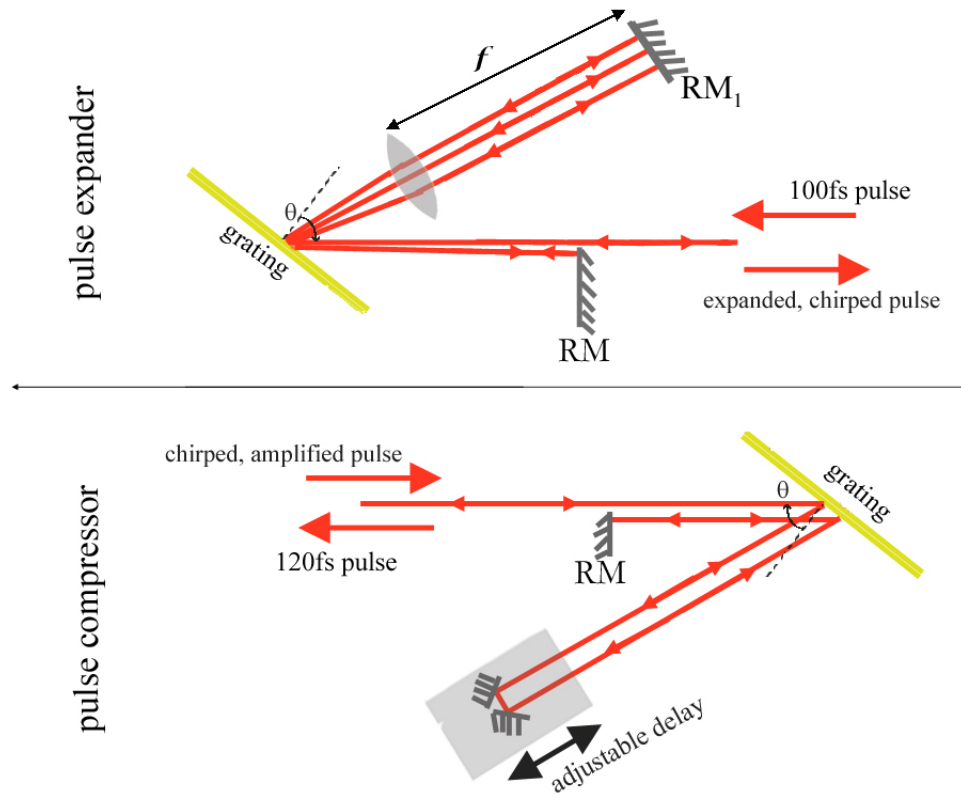


Figure 2.4: Pulse Expander and Pulse Compressor for Chirped Pulse Amplification

The schematic of the pulse expander and pulse compressor. The expander and compressor are aligned such that the compressor exactly compensates for the expansion in the pulse introduced by the expander. The delay in the arm of the compressor is adjusted to maximize the compression of the pulse. The mirrors RM in the expander and compressor are retroreflecting in the horizontal direction but introduce a small deviation in the vertical direction to enable the incoming and outgoing pulses to be separated. The angle of incidence θ is $\sim 54^\circ$ in both the compressor and the expander. The gratings introduce a linear frequency-dependent delay between the components of the pulse. The geometry of the expander and compressor are chosen to introduce and remove exactly the same amount of chirp from the pulse respectively. [23]

amplifier. Since the amplification is performed using Ti:sapphire crystals, increased intensities can also introduce non-linear effects like self-focussing and self-phase modulation which can alter the beam profile as well as the temporal intensity profile of the pulse. To avoid damage to the optics and to retain pulse shape characteristics during amplification, we use the method of chirped pulse amplification [23] to introduce a wavelength-dependent phase delay in the pulse thereby reducing the peak intensity in the pulses before sending it to the amplifiers.

A schematic of the pulse expander is shown in Fig 2.4. The 100 fs output of the mode-locked oscillator is incident at an angle of $\sim 54^\circ$ with respect to the normal of the grating. The components of the pulse at different wavelengths are diffracted at different angles by the grating. The spread in angles of the divergent beams is mapped onto a line on a retroreflecting mirror (RM_1) by the use of a spherical achromatic convex lens placed a focal length away from the mirror. The retroreflecting components of the beam retrace their path with a small vertical offset and are incident normally on another retroreflecting mirror, RM , and the process continues once again. Overall, the pulse is incident on the grating four times and on each pass, the grating introduces a linear relative delay between the frequency components (also known as *linear frequency chirp*). The vertically displaced output of the pulse expander is about 2000 times longer than the incident 100 fs pulse, i.e. about 200ps long [81]. The amount of frequency chirp is determined by the geometry of the expander. The use of the lens together with a grating increases the effective frequency chirp significantly in comparison to a design without a lens [23].

2.1.3 The Regenerative Amplifier

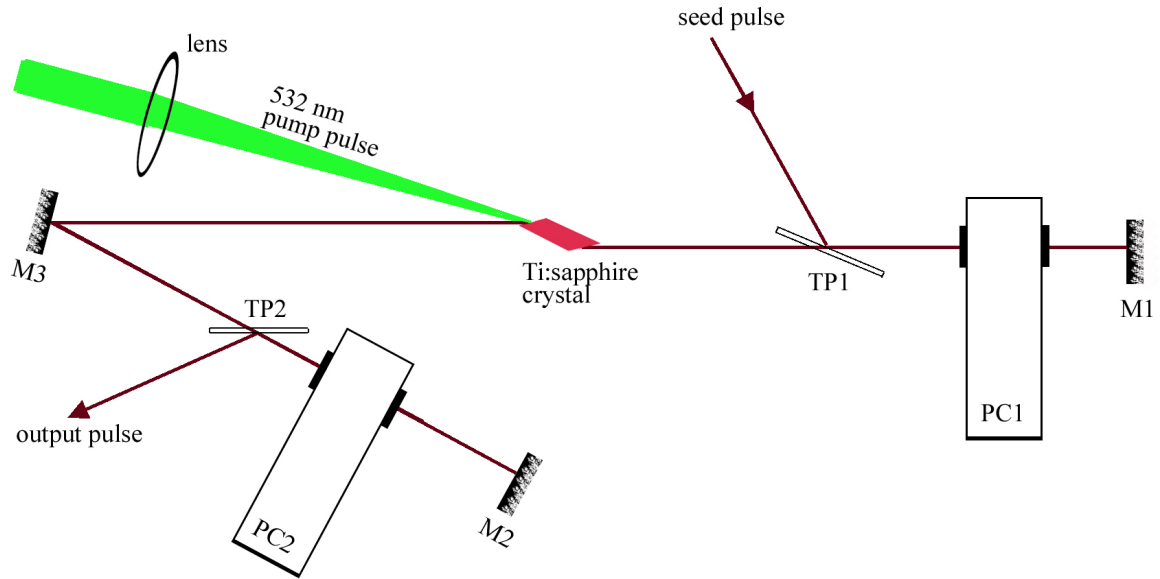


Figure 2.5: The Regenerative Amplifier

A schematic of the Ti:sapphire regenerative amplifier cavity. The laser cavity is formed between mirrors M1 and M2. Thin-film polarizers TP1 and TP2 are used to introduce the seed light into the cavity and to extract the amplified light from the cavity respectively. Pockels cells PC1 and PC2 are used to adjust the time spent by the pulses in the cavity. The 532 nm pump pulse is from a Nd:YAG laser. The cavity has a length of ~ 1.6 m.

Fig 2.5 shows the schematic of the regenerative amplifier cavity which we will also refer to as the “regen”. We use Pockels cells to pick a pulse coming from the pulse expander to be used as the seed pulse in the regen. Pockels cells work by rotating the polarization of light passing through the cell by an angle proportional to the voltage applied along the Pockels cell. We apply a voltage along the Pockels cells sufficient to rotate the polarization of the light by 45° . The voltages applied on the Pockels cells at specific times are used to control the number of round-trips of the pulse in the

cavity. The thin film polarizers TP1 and TP2 are placed at their polarization angles to the incident pulses in the cavity and reflect only the S-polarized light while allowing P-polarized pulses to pass through. In the regen cavity, S-polarized corresponds to vertically polarized light while P-polarized light has horizontal polarization. The input seed light is vertically polarized. A 200 ps pulse with a spatial extent (length) of about 6 cm can still be viewed as going from optic to optic at fixed times.

When PC1 is ‘ON’, i.e., there is a voltage applied on it, a vertically polarized seed pulse reflected off TP1 and sent through PC1 gets its polarization rotated by 45° on its way from TP1 to M1 and again on its way from M1 to TP1 so that it is horizontally polarized when it arrives at TP1 after reflection from M1. The horizontally polarized pulse passes through TP1 to the Ti:sapphire crystal and continues on to TP2. The pulse passes through TP2 also and arrives at PC2 horizontally polarized. If PC2 is ‘ON’, the pulse having passed through PC2 and returning through PC2 after reflection from M2 will be vertically polarized and will be reflected by TP2 out of the cavity. However, if PC2 is ‘OFF’, the horizontally polarized amplified pulse retains its polarization and passes through TP2 to retrace its path through the cavity until it gets to PC1. If PC1 is still ‘ON’, the pulse is vertically polarized when it passes through PC1 to M1 and returns through PC1 to TP1. The vertically polarized pulse is then switched out of the cavity. If PC1 is ‘OFF’, the vertically polarized seed pulses pass through without change of polarization and get switched out following a path in-TP1-PC1-M1-PC1-TP1-out. Thus, keeping PC1 ‘ON’ or ‘OFF’ at all times would mean all the pulses entering the regen get sent back out along the input path of the

seed light. Keeping PC2 ‘ON’ is equivalent to switching the pulse out of the cavity.

A Pockels cell placed in series with polarization filters on either side that are aligned to reject vertically polarized light acts as a gatekeeper to prevent amplified pulses from the regen from going back towards the mode-locked oscillator. The horizontally polarized pulses returning from the regen pass through this Pockels cell (say PC) before passing through to the filter. The voltage on PC is adjusted to produce a polarization rotation by 90° . When PC is ‘ON’, the horizontally polarized pulses entering PC are rotated to vertical polarization and blocked by the polarized filter. When PC is ‘OFF’, the horizontally polarized pulses pass through the filter. Meanwhile, the horizontally polarized pulses from the oscillator that pass through PC and the polarizers are rotated to vertical polarization by mirrors before going to the regen cavity.

For most of the time, PC and PC2 are kept ‘OFF’ while PC1 is kept ‘ON’. In this case, all the pulses that enter the regen get switched back out after one pass through the cavity. The Nd:YAG pump laser consists of horizontally polarized pulses of duration $< 10ns$ at a rate of 15 Hz with a pulse energy of 40 mJ. When the pump pulse is present in the cavity, the seed pulses can get amplified on each pass through the crystal. Although the pump pulse is only 10 ns in duration, the population inversion in the Ti:sapphire crystal has a lifetime of $3.8\mu s$ [22] so that amplification can occur over a longer duration even after the pump pulse is no longer present. This is because population inversion in the crystal provides a gain for the pulse in the cavity as long as it can overcome any other losses from the cavity. The pulse to be

amplified is chosen as a seed pulse arriving at the regen just after the arrival of the pump pulse. At this time, PC is switched ‘ON’ to prevent any stray amplified light from the regen to be sent back to the modelocker which can make it unstable and to block any other pulses from arriving at the regen. PC1 is switched ‘OFF’ when the pulse enters the regen and before it has the chance to get back to PC1 for the second time and get switched out of the cavity. The pulse is allowed to stay in the cavity for about 220 ns which allows the pulse to make about 20 round-trips within the cavity and get amplified at each pass through the crystal. This delay is chosen to maximize the gain produced by the cavity. At the end of this delay, PC2 is switched ‘ON’ to send the amplified pulse out of the regen. The amplification of the pulse is monitored on a photodiode looking at the light leaking from the cavity through M1. The delays for triggering the Pockels cells are provided by a model DG535 SRS (Stanford Research Systems) digital delay generator.

The output of the regen is a 200 ps pulse with an energy of ~ 5 mJ. This corresponds to an amplification by a factor of $\sim 4 \times 10^6$ in the regen. Further amplification by a factor of up to 10 is produced using a multipass amplifier.

2.1.4 The Multipass Amplifier

The multipass amplifier as the name suggests is basically a Ti:sapphire crystal in which the amplified output of the regen gets amplified by multiple passes through the crystal. The 200 ps pulse is passed through the Ti:sapphire crystal three times along with a variable-power 532 nm pump pulse from the Nd:YAG laser. An energy

in the pump pulse of about 100 mJ produces an amplification by a factor of 10. The amplification factor can be varied by adjusting the power of the pump pulse with a half-wave plate in series with a thin-film polarizer. The multipass amplifier provides the required “tunability” to the amplification to adjust the output power depending on the requirements of the experiment [80].

2.1.5 Pulse Compressor

The 200ps pulses with energies of ~ 30 mJ per pulse have a frequency chirp that was introduced by the pulse expander before amplification. We can use a grating to reverse the frequency chirp in a manner similar to pulse expansion but using the grating in the opposite manner to how it is used in the expander. A schematic of the pulse compressor is shown in Fig 2.4.

A short pulse with high intensities experiences high-order non-linearities in the refractive index of any medium through which it has to travel and this includes transmission through air. This results in distortion of the temporal and spatial intensity profile of the pulses as it travels in the air. To minimize these effects which distort the pulse profile, we increase the area of the pulse so that it reduces the peak intensity per unit area. The 200 ps pulses which are 2-3 mm in diameter during the amplification stages are expanded and collimated in a telescope to a diameter of just over 1 cm before being sent into the compressor. We also keep the compressor as close as possible to the final destination of the pulses in the interaction region of the experiments to minimize the distance needed to be travelled by the pulses in air.

The grating in the compressor is aligned at an angle exactly equal to the angle in the expander. The pulse is diffracted off the grating four times in a geometry designed to cancel the frequency chirp introduced by the expander. The delay stage in one arm of the compressor is used to adjust the path length of the pulse in the compressor to maximize the compression. This adjustment is performed while monitoring the pulse width of the output of the pulse compressor as measured using an autocorrelator.

2.1.6 Autocorrelator

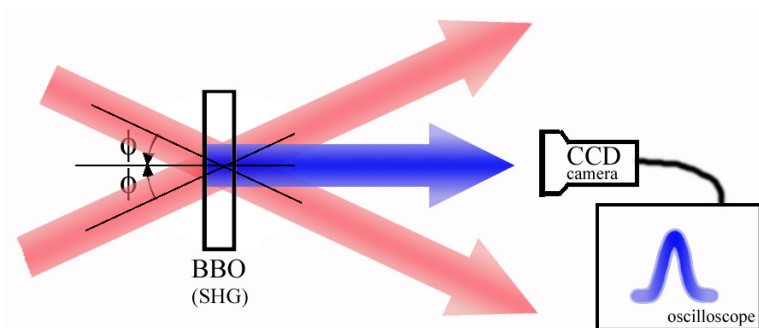


Figure 2.6: Autocorrelator for pulse width measurement

The pulse to be measured is split into two halves and each half is incident on a BBO crystal at equal but opposite angles to the normal to the crystal such that the plane of intersection of the pulses contains the normal to the crystal. The angle of the BBO crystal is adjusted to produce phase-matched Type I SHG from the overlap of the two pulses at a small angle [23]. The second harmonic is generated with greater intensity over the area of the crystal in which the two pulses overlap with the maximum amplitude. The phase-matching optimizes SHG when one component each from both beams overlap in the crystal with equal and opposite angles of incidence. This maps the temporal intensity profile of the pulse into the spatial plane in the intensity of SHG. The spatial intensity distribution of the SHG is monitored with a CCD camera on an oscilloscope.

When we say that a laser pulse has a certain duration, we need to have a way of

measuring this duration. To make a measurement of any interval of time, there has to be a smaller unit of time that can be measured or has been measured. In measuring laser pulses that are longer than a few nanoseconds, photodetectors with a fast response can be used along with fast oscilloscopes to measure their duration. Electronic detectors cannot, however, be used to measure sub-picosecond pulses at the present level of technology. In a typical lab where femtosecond pulses are generated, these pulses are most likely to be the shortest events in the lab. So the methods used to measure the duration of these short pulses involves using the pulses to probe themselves (autocorrelation) or other short pulses (cross-correlation). Since the conditions in the lab are not always identical, we would like to have a continuous monitoring of the width of the pulses available for the experiments. This is achieved by the use of a single-shot autocorrelator which uses the pulse itself as a probe of its temporal intensity profile [23].

If we can define the temporal profile of a pulse as $\mathcal{S}(t)$, then the autocorrelation of the pulse with itself is defined as

$$\mathcal{A}(t) = \int_{-\infty}^{\infty} \mathcal{S}(t+t')\mathcal{S}(t')dt' \quad (2.1)$$

The autocorrelator is used for measuring the pulse width of the pulses generated in the Ti:sapphire laser after amplification and pulse compression. A glass slide placed in the output of the compressor is used to send a small part of the compressed pulse into the autocorrelator. This pulse is split into two approximately identical pulses with a pair of half mirrors and the two pulses are overlapped inside a BBO crystal aligned such as to produce SHG from the overlap of the two pulses as shown in Fig 2.6.

SHG is an intensity dependent effect and the intensity from the overlap of the two pulses depends on the temporal overlap between the two pulses together with their instantaneous amplitudes. At different positions on the BBO crystal in the plane formed by the paths of the two intersecting pulses, the maximum overlap between the pulses in time occurs at different relative delays between the pulses. The intensity of SHG then corresponds to an autocorrelation of the temporal profile of the pulse mapped into the spatial plane as long as the beam waist of the two beams at the BBO crystal is much larger than the pulse length [23]. We use beams with a waist of close to 1 cm while the pulse length of the pulses (120 fs) is about 0.04 mm. The autocorrelation information, mapped into the spatial plane in the intensity of the SHG, is monitored by a CCD camera and viewed on an oscilloscope.

To calibrate the autocorrelator, a thin glass slide of known thickness is introduced into the two equal pulses to introduce known path length differences between the pulses. This manifests as a shift in position of the peak of the intensity distribution that is monitored on the oscilloscope. Knowing the displacement of the peak corresponding to known path delays, we can calculate the FWHM of the autocorrelation signal as $\Delta\tau_a$. Assuming a $\text{Sech}^2(t)$ form of the pulse, the FWHM of the pulse is calculated as $\Delta\tau_a/1.55$. The FWHM of the pulses are measured to be ~ 120 fs at the output of the pulse compressor.

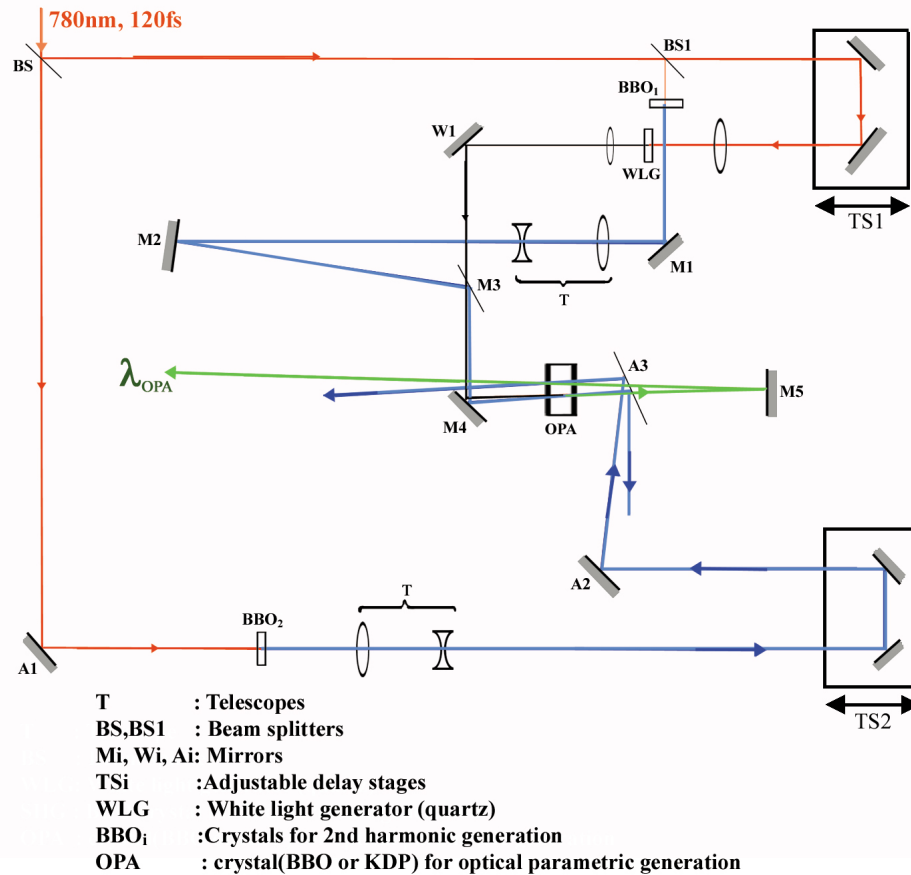


Figure 2.7: Optical Parametric Amplifier Schematic

The schematic of one of the OPAs used in the experiment. The input is a 780 nm, 120 fs pulse and the output of the OPA is tunable from ~ 450 nm to 700 nm. A 1 mm BBO (Beta Barium Borate) crystals or a 1 cm thick KDP (Potassium Dihydrogen Phosphate) crystals are used for SHG depending on the bandwidth of the output required. Thicker crystals correspond to lower bandwidth due to stricter phase-matching conditions. The OPA crystal is either a 2 mm BBO crystal or a 3 cm KDP crystal. The longer KDP crystals are used to get an output with a smaller bandwidth (longer pulse).

2.2 Optical Parametric Amplifier

An OPA (Optical Parametric Amplifier) is based on the effect of intense electric fields in a laser beam producing intensity dependent variations in the dielectric constant of non-isotropic materials [23]. This effect leads to the possibility of converting a photon of one energy (ω_1) into a set of two photons with different lower energies (ω_2, ω_3) which add up in total energy to that of the incident photon ($\omega_1 = \omega_2 + \omega_3$). Under the proper phase-matching conditions, it is possible to tune the OPA to produce photons with our choice of ω_2 and ω_3 starting from ω_1 .

We use two OPAs in the experiment with barium. The two OPAs are identical in function but are used to create pulses at two different wavelengths. Each OPA is pumped by the second harmonic of the 120 fs, 780 nm Ti:sapphire pulse. A 3 cm KDP crystal is used as a gain medium in one of the OPAs while a 2 mm BBO crystal is used in the second OPA. A schematic of one of the OPAs used in the experiments is shown in Fig 2.7.

The 780 nm pulse at the input of the OPA is split in a ratio of 3:7 by beamsplitter BS. The smaller component along BS-BS1 is used to create OPA with white light while the other component along BS-A1 is used after SHG in the BBO_2 crystal to further amplify this pulse generated by OPA. The pulse along BS-BS1 is split at BS1 into a 70% component along BS1-M1 and a 30% component along BS1-TS1. The pulse along TS1-W1 is focussed into a quartz crystal to produce white light by self-focussing and self-phase-modulation. The white light is sent via aluminum mirrors W1 and M4 to the OPA crystal. Meanwhile, the pulse sent via BS1-M1 is

sent through BBO_1 for SHG and the dichroic 390 nm, 45° mirror at M1 separates the 390 nm pulse from the 780 nm pulse. The 390 nm pulse from M1 is sent through a telescope which is adjusted to nearly focus the 390 nm light sent via M2, M3, and M4 into the OPA crystal to be overlapped with the white light(which acts as the seed light for amplification) and generate optical parametric amplification over a range of wavelengths centered at λ_{OPA} present in the white light and depending on the phase-matching condition. The translation stage at TS1 is adjusted to maximize the temporal overlap between the 390 nm pulse and the white light pulse by maximizing the amplification at λ_{OPA} in the crystal. The 780 nm pulse sent along BS-A1 is sent through a BBO crystal (BBO_2) to produce SHG which is separated by 390 nm dichroic mirrors at TS2. The 390 nm pulse sent from the BBO crystal via TS2, A2, and A3 is nearly focussed using a telescope into the OPA crystal to produce further amplification of the pulse at λ_{OPA} retroreflected from M5. The delay stage at TS2 is adjusted to make the 390 nm amplifier pulse from A3 reach the OPA crystal at the same time as the OPA pulse returns to the crystal after reflection at M5. The color of the OPA is determined by the angle of the OPA crystal to the incident pulses. All the laser beams are aligned to be parallel to the surface of the optical table.

2.3 Atom Source and the Interaction region

The lasers that we use in the laboratory have a broad range of wavelengths which can overlap with energy levels of several compounds found in the environment in the air

in the laboratory. We use a vacuum chamber to isolate the atoms being studied in the experiment as well as to remove most of the elements in the air that can interfere with the experiments.

To study the effect of the interaction between the atoms and the lasers, we need to identify the location of the interaction and the products that remain after the interaction. We do this by making the lasers interact with the atoms in a well-localized region of space inside the vacuum chamber. We also design the interaction region to be located such that the products of the interaction can be extracted in a consistent manner and measured using detectors.

2.3.1 Vacuum System

The vacuum chamber used in the experiments consists of a 45 cm diameter, 30 cm high cylindrical chamber made of aluminum with eight cylindrical flanges for any attachments or extensions. A Varian VHS-6 water cooled diffusion pump and a Welch model 1376 mechanical pump in series are used to pump the chamber down to pressures of $\sim 2 \times 10^{-7}$ torr. A schematic of the vacuum chamber is shown in Fig 2.8.

The pressure inside the vacuum chamber is monitored with a model 571 Bayard-Alpert Type Standard Range Ionization Gauge Tube and a model 843 ionization gauge controller from Varian. Pressures higher than 10^{-3} torr are measured with model 531 thermocouple gauge tubes from Varian.

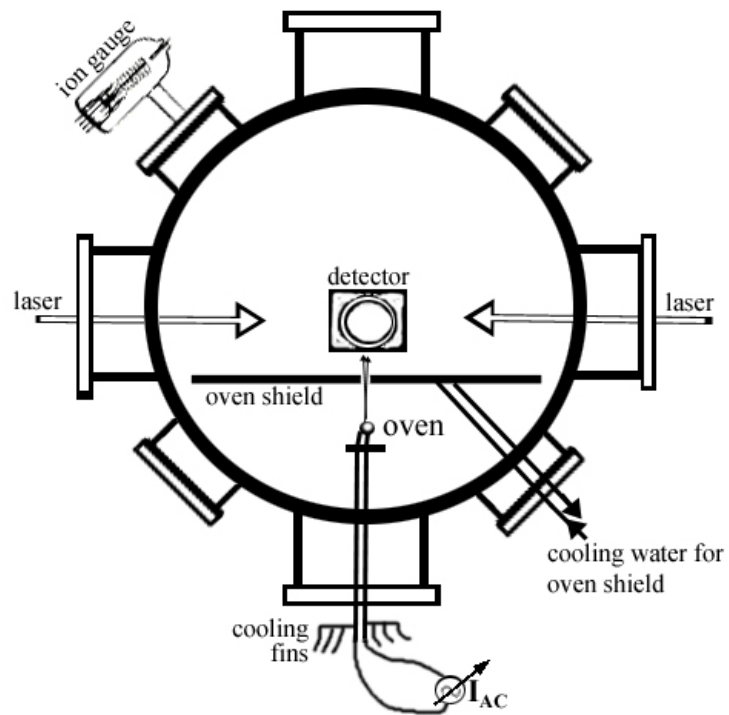


Figure 2.8: Schematic of vacuum chamber: Top view
The vacuum chamber is pumped down to pressures of less than 10^{-6} torr with a diffusion pump and a mechanical pump in series.

2.3.2 The Interaction Region

The interaction region between the lasers and the atoms is essentially a set of parallel metal plates with a small 0.5 cm diameter hole in the upper plate. The lasers are aligned so that they interact with the atoms between the plates under the hole in the top plate. The plates are connected with insulated wires to electrical feedthroughs attached to flanges on the vacuum chamber. Voltages can then be applied to these plates from outside the vacuum chamber.

The products of the interaction can be extracted through the hole in the top plate and sent to detectors that are placed here. In our experiments, the detectors are microchannel plates placed about 10 cm above the hole in the upper plate.

2.3.3 Atom oven

The alkaline earth elements, calcium and barium that we use in the experiments described here are available commercially. At room temperature, both of these elements are available as solids. The calcium that we use in our lab is in the form of small pellets while the barium is available in the form of rods immersed in mineral oil to prevent oxidation in air. To generate a vapor of calcium or barium atoms in the interaction region where they are excited using lasers, we heat the calcium or barium in steel tubes(referred to as ‘ovens’) with small holes drilled in them to direct the emerging atoms in the direction of the interaction region.

The stainless steel ovens used in the experiments described here are either $\frac{1}{4}$ " or $\frac{3}{8}$ " diameter tubes made of 316 steel and have a wall thickness of 0.006". A 0.4 mm

diameter hole is drilled into the wall of the tube close to its center. To load the oven, one end of the tube is crimped in a vice and calcium or barium is filled into the tube to a level just below the level of the hole. Then the other end of the tube is crimped and the entire tube is fixed in an oven holder such that the part of the oven with the calcium(or barium) is towards the bottom and the hole in the oven is level with and directed towards the interaction region.

The ends of the oven tube are connected with thick copper wires to an AC high power current source. This current source consists of a series of transformers which converts the 120V AC to about 6V AC and has a variable output through the use of a variac. The oven tubes have a resistance of less than 0.1Ω . To make most of the voltage drop in the circuit occur across the oven, the thick copper cables offer a very low resistance connection to the current source. We apply a current ranging up to 115Amps to heat the oven.

The atoms of calcium (or barium) are ejected as an effusive beam of neutral atoms in the direction of the interaction region. To prevent the effusive atom beams from coating the surface of all the detectors around the interaction region, we use a water-cooled plate of copper with a 4 mm high and just under 1 cm wide hole to block the atoms that are not aimed directly toward the interaction region. The water cooling of the copper plate is done to improve the efficiency of collecting the thermally excited calcium atoms striking the surface of the copper plate.

The high currents in the oven can create magnetic fields ($\sim 1.5 \times 10^{-4}\text{T}$ at the interaction region) that can affect the characteristics of the atom. To avoid the effects

of magnetic fields, the lasers in the lab are all synchronized to fire near the zero of the electric field in the AC current line [61].

2.4 Detection Apparatus

The detection apparatus consists of the detectors placed inside the vacuum chamber which include the metal plates above and below the interaction region and the microchannel plate detectors as well as the oscilloscopes and data storage devices (computers) used to collect and analyze the signals from these detectors. The interconnect between the detectors inside the vacuum chamber and the voltage sources or signal lines outside the vacuum chamber are provided by electrical feedthroughs connected on flanges on the sides of the chamber. BNC and MHV connectors and cables are used for transmission of all the signals and voltages outside the chamber.

2.4.1 Microchannel Plate Assembly

One of the methods used for detecting electrons or ions is to monitor any change in potential of a charged capacitive conductor when an electron or ion strikes the surface of the conductor. If we consider a conductor with capacitance C , with a voltage V applied to it, the total charge on the surface of the conductor is $Q = CV$. When an electron (or ion) strikes the conductor, the total charge instantaneously changes by $\mp e$, the charge on the electron(or ion). This leads to an instantaneous change in the potential on the conductor by e/C . In an experiment, we would like to be able to

distinguish the signal from the electrons or ions from the background noise. We would therefore like to maximize the change in potential on the surface of the conductor from the impact of an electron (or ion). This can be done either by significantly reducing the capacitance C or by increasing the flux of electrons/ions striking the surface.

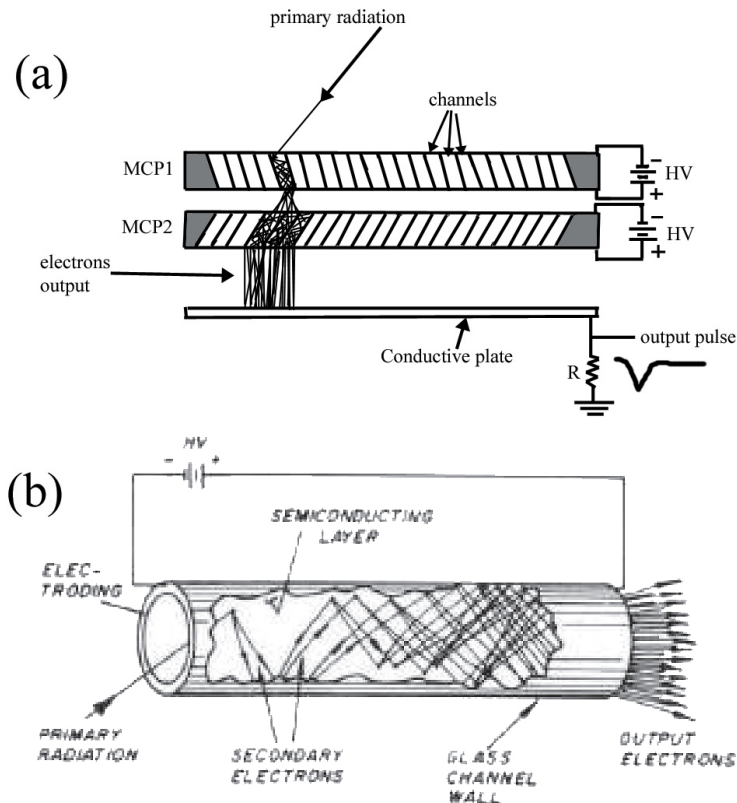


Figure 2.9: Microchannel plate Assembly

The upper figure (a) shows the setup of the microchannel plate pair to detect charged particles. The lower figure (b) shows a cutout of one of the channels in the microchannel plates. The primary radiation in these figures refers to electrons or ions hitting the microchannel plates [82].

In our experiments, we choose to enhance the signal by increasing the number of electrons striking the surface of the conductor where we monitor the changes in

potential. This is achieved by the use of microchannel plates which emit thousands of electrons for each electron striking their surface. The microchannel plates work by creating an avalanche of electrons whenever an ion or an electron hits the surface of the plates. The surge of electrons can be detected as a change in voltage on a metal plate where the electrons are impacted after emission from the microchannel plates. The signal corresponding to the electron surge is proportional to the number of electrons or ions hitting the microchannel plates under normal operating conditions. We use a pair of matched microchannel plates in series to enhance the magnification of the signal. The microchannel plates are kept at a potential difference of 2 kV for electron or ion detection. Fig 2.9 shows the operation and setup of a microchannel plate assembly.

The microchannel plate pair can produce amplification of signals by a factor of $\sim 10^6$ and combined with a time resolution better than 2ns, they are ideal for detection of electrons of varying energy by time of flight separation.

2.4.2 Data collection software

The change in potential on the microchannel plates as well as the laser pulses detected with photodiodes are observed on oscilloscopes. The oscilloscopes used in the experiments described here include a 500 MHz LeCroy 9350A, a 500 MHz Tektronix 2440, a 200 MHz Tektronix 2430, a 350 MHz Tektronix 2467 and, a 500 MHz Tektronix TDS 3052. The 500 MHz oscilloscopes with a resolution of 2 ns are used to detect the signal from the microchannel plates while the other oscilloscopes are used to look

at signals which do not need to be measured with such accuracy. Some of these oscilloscopes also have GPIB cards to allow for remote control of the oscilloscope with a computer.

A PC running DOS on an Intel 486-DX processor is used as the controller for the oscilloscopes for collecting the data. The control programs for the oscilloscopes were written by Thomas Bensky. These programs are used to set time windows over the signals seen on the oscilloscope to collect signals corresponding to specific time delays from the trigger which is synchronized with the laser repetition rate. The signals can be averaged over several shots of the laser to improve the signal to noise ratio. The programs can also control stepper motors through the parallel port(LPT1). We use stepper motors connected to translation stages to simultaneously control any delays between lasers that need to be introduced by the translation stages and the collection of data from the oscilloscopes. In some cases, two PCs have been used simultaneously to collect data from different oscilloscopes.

2.5 State Selective Field Ionization

State selective field ionization is a method for detecting and identifying rydberg states and wavepackets. The basic principle behind this method is that the potential experienced by an electron in an atom changes in the presence of an external applied electric field. This change in potential can be sufficient to allow an electron in a bound rydberg state to escape and thereby ionize the atom. This effect of the atom being

ionized in a field is termed as field ionization. When we use a ramped electric field to ionize the atoms, the atoms in different rydberg states ionizing at different times produce signals at the microchannel plates that can be resolved in time to identify the individual rydberg states present in the system [25].

Chapter 3

Autoionizing Wavepackets in Calcium

3.1 Introduction

The aim of our experiments as stated in the first chapter is to create a controlled system of two excited electrons such that we know their behavior at least at the instant of creation. We would then like to study the behavior of the atom as it evolves in time.

There is a significant amount of work on experimental [25, 83, 84, 85, 86, 87, 88, 89] and theoretical [90, 26, 91, 92] studies of rydberg wavepackets in atoms that enables us to generate radial rydberg wavepackets with the desired characteristics of electron motion. There has also been a lot of work in isolated-core excitation (ICE) techniques [33, 25, 93, 35, 36] that allows us to use short laser pulses to excite the electrons in a

two-electron atom independently using multistep laser excitation. The autoionizing states and their linewidths have been measured in several experiments in alkaline-earth atoms [94, 95, 96, 97, 98, 99, 34, 100, 101]. A number of theoretical [102, 103, 104] and experimental [105, 77] studies have also been performed to look at the dynamic behavior of wavepackets in autoionizing atoms. In a multistep excitation of a DRW, we need to understand the behavior of the electrons at each step of the excitation. We are familiar with the behavior of rydberg wavepacket from past experiments so that we can create $4sNd$ rydberg wavepackets with a good knowledge of their dynamic behavior. We use ICE to excite the inner $4s$ electron to $4p_{3/2}$ at different times during the evolution of the rydberg wavepacket and study the influence of the delay between exciting the wavepacket and the ICE on the decay characteristics of the autoionizing $4p_{3/2}Nd$ wavepacket. This is similar to an experiment performed by J.E.Thoma with autoionizing states instead of autoionizing wavepackets [106].

3.2 Experimental Procedure

Fig 3.1 shows the detector setup used in the experiment. Calcium atoms in the ground state are introduced into the interaction region by heating a $\frac{1}{4}$ " diameter steel tube filled with crushed pieces of calcium. The heated calcium atoms exit the tube through a 0.4 mm diameter hole drilled on the side of the tube toward the interaction region. The interaction region is located between two parallel plates made of aluminum with a small 5 mm diameter hole in the upper plate to extract the ions or electrons to be

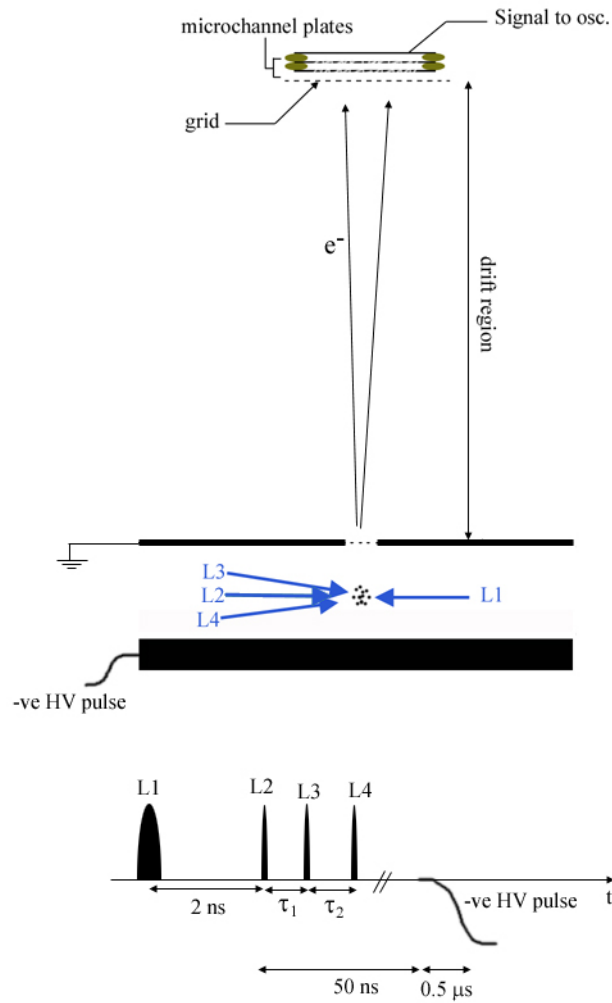


Figure 3.1: Detector Schematic

A schematic of the detector used in the experiment along with the timing diagram for the various laser pulses and the electric field pulse used to ionize the rydberg wavepacket states.

detected. The lasers, which are all polarized in the vertical direction, interact with the calcium atoms at right angles to the direction of motion of the atoms so that we can make sure that the delay between exciting the atoms with the different lasers is the same for all the atoms in the interaction region. The excitation scheme is shown in Fig 3.2.

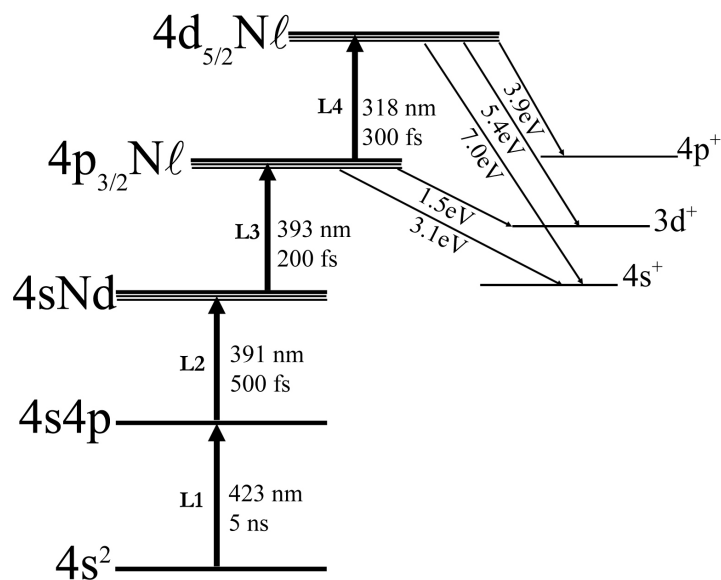


Figure 3.2: Excitation scheme in Calcium

A schematic of the excitation scheme used in the experiment to study the decay of $4p_{3/2}N\ell$ autoionizing radial wavepackets in calcium.

The excitation scheme can be viewed as consisting of three main steps. In the first main step, a radial rydberg wavepacket is excited in a two-step process. Atoms in

the $4s^2\ ^1S_0$ ground state are excited into a $4s4p\ ^1P_1$ intermediate state by a 423 nm, 5ns pulse (L1). A second 500 fs pulse (L2) at 392 nm further excites the atoms into a coherent superposition of $4snd\ ^1D_2$ states centered around an average principal quantum number N with its corresponding Kepler period $\tau_K = 2\pi N^3$ which forms a radial wavepacket. For convenience, we will refer to this wavepacket as a $4sNd$ wavepacket. The 423 nm laser pulse is generated by a dye laser with Stilbene 420 dye pumped by the third harmonic of a Nd:YAG laser. The 392 nm ultrashort laser pulse is generated by doubling a bandwidth-limited (see next section for details) 780 nm Ti:sapphire pulse in a 1 cm KDP crystal.

The second step in the excitation scheme is to excite the inner 4s electron into the $4p_{3/2}$ state of the ion by ICE [33]. This is achieved by using a 200 fs laser pulse at 393 nm. This 393 nm ICE pulse (L3) is generated by SHG in a 2 mm BBO crystal from the transform-limited 780 nm fundamental output of the Ti:sapphire laser. This excitation puts the atom which was initially in the $4sNd$ wavepacket into a coherent superposition of $4p_{3/2}N\ell$ states. These $4p_{3/2}N\ell$ states have energies above the $4s^+$ and $3d^+$ ionization limits in calcium and can therefore decay by autoionization. We will refer to this coherent superposition of $4p_{3/2}N\ell$ states as an autoionizing wavepacket. The relative phases of the different eigenstates in this wavepacket is chosen by adjusting the delay, τ_1 , between exciting the radial wavepacket and the ICE. The doubly excited atoms in the $4p_{3/2}N\ell$ states decay by autoionization into the $3d\epsilon\ell$ or $4s\epsilon\ell$ continua, releasing electrons of energies 1.5 eV or 3.1 eV respectively. These electrons are detected at the microchannel plates if they are emitted in the direction

of the hole in the upper plate of the interaction region. The work of van Leeuwen et. al suggests that we should not expect to see any wavepacket-phase-dependence in the total autoionization signal at any particular angle even though the portion of the signal contributed by the 1.5 eV or 3.1 eV electrons can change as a function of the phase [77]. Additionally, we monitor the decay of an autoionizing wavepacket by keeping the phase of the initial wavepacket constant so that any possible variation in the total autoionization signal as a function of initial wavepacket phase [79,107] is corrected by normalization of the maximum autoionization signal level to the same value at all delays, τ_1 . We will also make the assumption that all the atoms in the $4p_{3/2}N\ell$ states autoionize within 1 ns which is much shorter than the time scale on which the electrons are detected at the microchannel plates (> 150 ns). This assumption is justified by the broad resonance structures and hence short lifetimes corresponding to the $4pN\ell$ autoionizing resonances in calcium as measured by Jones [93]. The electrons travelling straight through the drift region (length of ~ 10 cm) toward the detector arrive at the detector at least 95 ns after the autoionization occurs (95 ns for 3.1 eV electrons, 137 ns for 1.5 eV electrons). Typically there is a spread in the times at which the electron is detected at the microchannel plate detector due to stray charges in the detector or due to the spread in directions of the electrons hitting the detector as well as due to the finite extent of the interaction region.

The third step is to probe the time-dependent decay of the autoionizing wavepacket. This is done by using a short pulse at 318 nm (L4) to excite the “inner” $4p_{3/2}$ electron to a $4d_{5/2}$ state by ICE [106]. L4 is delayed by a time, τ_2 with respect to the first ICE

by L3. The $4d_{5/2}N\ell$ states decay by autoionization to the $4p\epsilon\ell$, $3d\epsilon\ell$ and $4s\epsilon\ell$ continua by ejecting electrons with energies of 3.9 eV, 5.4 eV and 7.0 eV respectively. These electrons can also be detected at the microchannel plates through the hole in the top plate. The number of these high energy electrons detected is also assumed to be directly proportional to the population of $4d_{5/2}N\ell$ states. However, this assumption is strictly valid only if there is no variation in the angular distribution of electrons from the decay of the $4d_{5/2}N\ell$ states as a function of time [77]. Since the original $4sNd$ radial rydberg wavepacket is not an angular wavepacket, we are justified in making this assumption for the superposition of $4d_{5/2}N\ell$ states. These electrons travelling through the drift region can arrive at the microchannel plates within about 65 ns after autoionization (64 ns for 7.0 eV, 72 ns for 5.4 eV and 85 ns for 3.9 eV). In the rest of this chapter, we will refer to these high energy electrons as *fast* electrons which arrive at the detector at earlier times to distinguish them from the *slow* electrons emitted by autoionization of the $4p_{3/2}N\ell$ states which arrive later. The significant delay between the fast and slow electrons arriving at the detector can be used to distinguish the fast electrons alone and thereby get a relative measure of the number of atoms that are excited to the $4d_{5/2}N\ell$ states.

The number of atoms that are excited into the $4d_{5/2}N\ell$ states by L4 is assumed to be directly proportional to the population of $4p_{3/2}N\ell$ states at the instant of interaction with L4 if we neglect any effect of the position of the rydberg electron on the excitation probability of the $4d_{5/2}$ states from the $4p_{3/2}$ state by ICE. This has also been verified by monitoring the ‘fast electron’ signal while keeping the relative

delay between L3 and L4 fixed and changing the delay between L2 and L3. We do not see any time-dependent variation of the signal as a function of delay between L2 and L3.

At each value of delay, τ_1 , we monitor the ‘fast electron’ signal level at the microchannel plates due to the decay of the $4d_{5/2}N\ell$ states as a function of the delay τ_2 . This signal is interpreted as the relative survival probability of the autoionizing $4p_{3/2}N\ell$ wavepacket for a time τ_2 . This is repeated for various initial phases of the $4p_{3/2}N\ell$ wavepacket by varying τ_1 .

The rydberg states excited in the wavepacket are identified by state-selective field ionization(SSFI) by applying a high voltage negative pulse to the lower plate of the interaction region and monitoring the times at which the electrons released from the various rydberg states are incident at the detector. This calibration of the ionization times of the rydberg states is done by using a dye laser in place of L2 to excite individual $4snd$ rydberg states and detecting them with the same ionization field pulses as those used to detect the wavepacket. Fig 3.3 shows the SSFI spectrum corresponding to the ionization of $4sNd$ wavepackets centered at $N = 35$ and $N = 40$. Lasers L3 and L4 are blocked while measuring the SSFI spectra to avoid the effect of rydberg state redistribution by ICE.

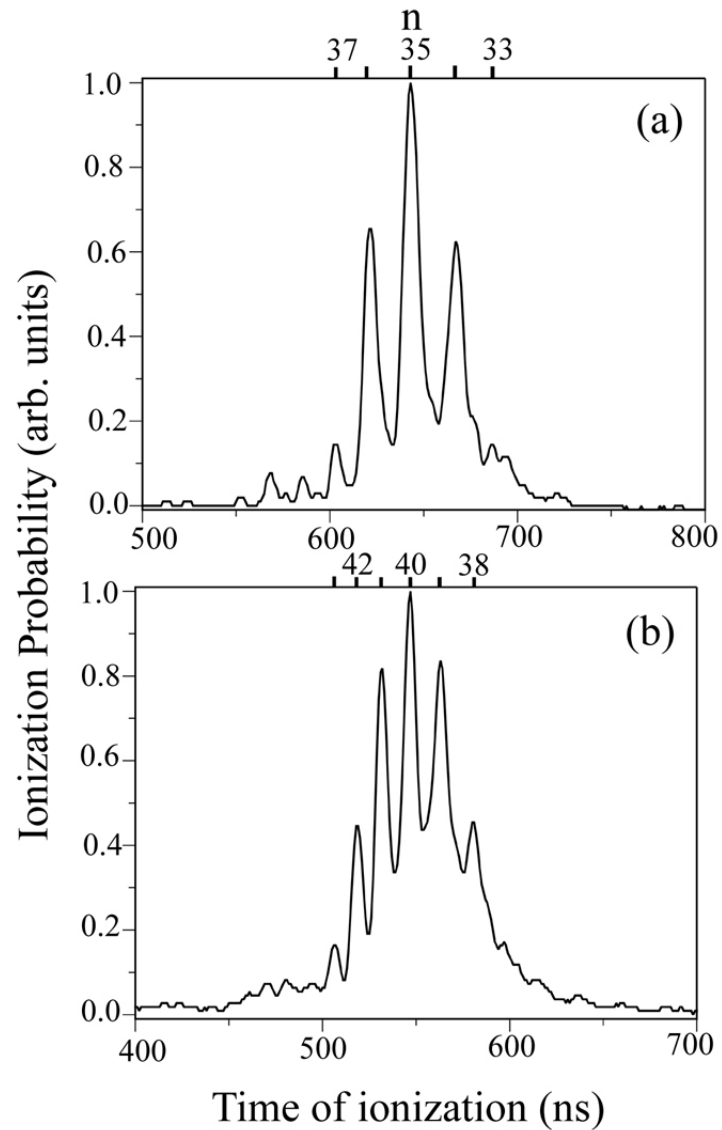


Figure 3.3: State-selective field ionization (SSFI) spectra
The graphs correspond to the SSFI electron spectra for $4sNd$ wavepackets centered
at (a) $N = 35$ and (b) $N = 40$.

3.3 Controlling bandwidths of lasers

In the semi-classical model, one can assign specific times for the electron to be near the core or away from the core. In the case of an electronic wavepacket excited in an atom using lasers, the ability to localize the electron probability at some position around the atomic core depends on the number of states that are excited coherently as well as the phase and energy distribution of the excited states.

If we excite too many states with a short pulse (i.e. greater bandwidth), then the dispersion of the wavepacket reduces the localization of the wavepacket in a very short time. On the other hand, we do not want to increase the pulse width (reduce the bandwidth) to excite too few states (one or two) because then the electron probability distribution would resemble a stationary state (exciting one state) or an oscillating set of states (exciting two states). Fig 3.4 shows the calculated change in radial probability density distribution as a function of time for various choices of laser bandwidth used to excite a wavepacket.

The $4sNd$ wavepacket is excited using the second harmonic of the fundamental 120 fs, 780 nm Ti:sapphire pulse. The SHG is created using a 3 cm KDP crystal whose angle with respect to the Ti:sapphire laser beam can be adjusted to tune the phase matching conditions and hence the central wavelength of the second harmonic. The bandwidth of a laser with a 120 fs pulse is at least 125 cm^{-1} . We see from Fig 3.4 that we need the laser bandwidth to be less than 10 cm^{-1} to be able to use a semi-classical picture to describe the wavepacket motion for more than one Kepler period. It is therefore necessary to reduce the bandwidth of the Ti:sapphire laser

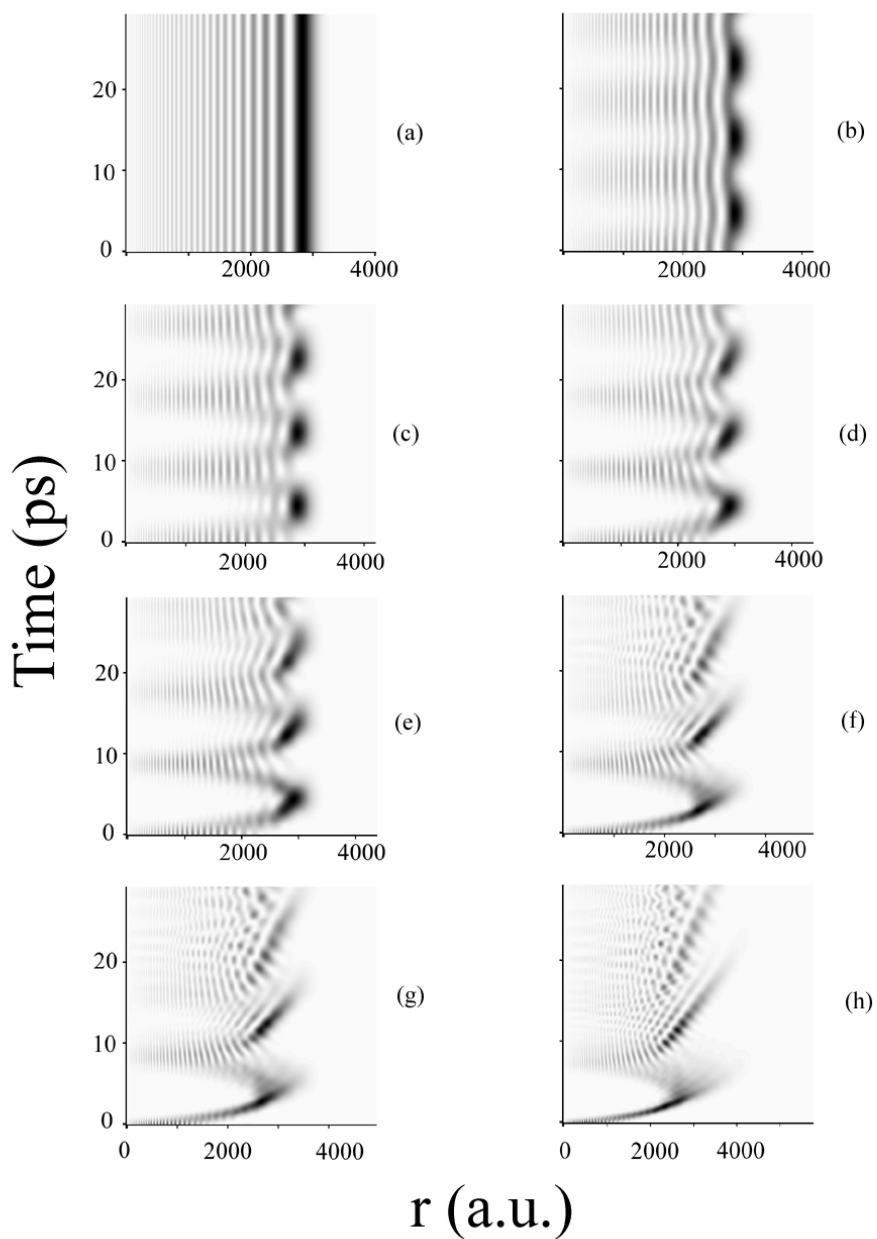


Figure 3.4: Time-dependent radial probability distribution of a $4sNd$ wavepacket in calcium

The above graphs show the calculated radial probability distribution of a $4sNd$ ($N \approx 40$) wavepacket in calcium for cases where the excitation laser bandwidth is (a) 1 cm^{-1} (b) 2 cm^{-1} (c) 3 cm^{-1} (d) 4 cm^{-1} (e) 5 cm^{-1} (f) 9 cm^{-1} (g) 10 cm^{-1} (h) 15 cm^{-1}

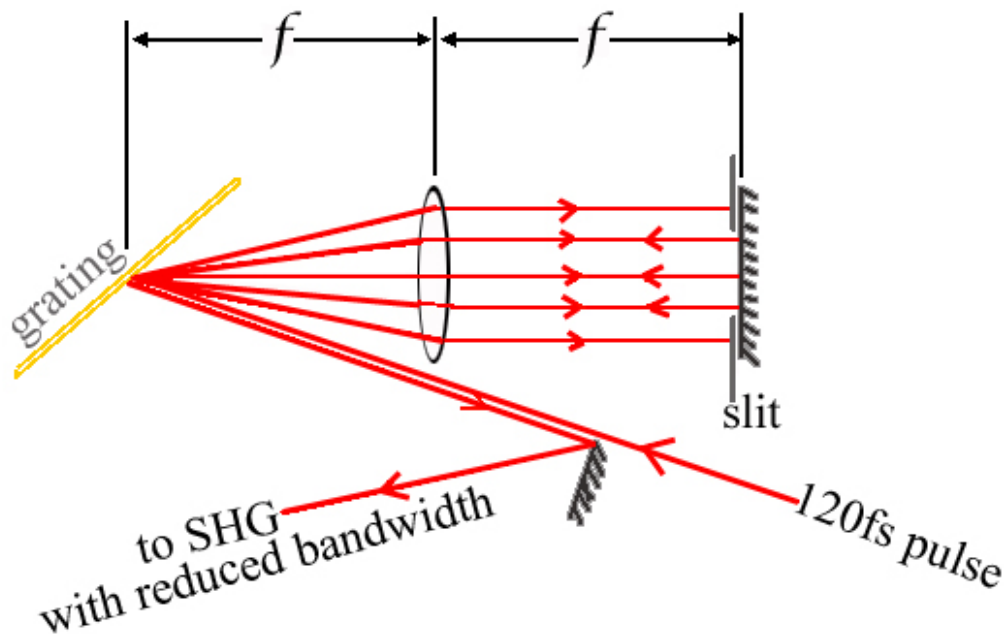


Figure 3.5: Setup for reducing the bandwidth of the Ti:sapphire laser.

used to create the second harmonic for exciting the $4sNd$ wavepacket.

In order to reduce the bandwidth of the Ti:sapphire laser pulse, we use a grating to separate the various frequency components of the pulse [23]. We then use a cylindrical lens to map the frequency spectrum into the spatial plane at its focus. A retroreflecting mirror at the focus of the cylindrical lens sends the beam back with a slight vertical displacement and is picked off after all the frequency components are recombined at the grating. An adjustable slit in front of the retroreflecting mirror is used to block parts of the frequency spectrum and thereby reduce the bandwidth of the Ti:sapphire pulse used to create the second harmonic with the KDP crystal.

This is a simpler version of more complicated pulse-shaping techniques using spectral filtering [23, 108]. Phase matching conditions in the crystal further limit the effective bandwidth of the second harmonic. The effective laser bandwidth used in the experiment is about 9 cm^{-1} . The setup used to reduce the bandwidth of the laser in the experiment is shown in Fig 3.5.

3.4 Experimental results

The decay of the $4p_{3/2}Nd$ autoionizing wavepackets are measured for the two cases with $N \sim 35$ and $N \sim 40$. For the $4snd$ states at $n = 35$ and $n = 40$, the quantum defect is ~ 1.2 so that the Kepler periods of the orbits of the two wavepackets ($\tau_K = 2\pi(n - \delta)^3 \text{ a.u.}$) are 5.9 ps and 8.9 ps respectively. The survival probability of the $4p_{3/2}N\ell$ wavepackets with $N \sim 40$ as a function of time for different initial phases of the constituent states is shown in Fig 3.6. The different curves correspond to different initial phases chosen in the autoionizing $4p_{3/2}N\ell$ wavepacket by varying the delay τ_1 in approximately equal steps of 1.33 ps.

There are a few remarkable features that stand out in the data. The main feature that we notice is a stair-step form in the decay of the wavepacket. The discrete steps in the survival probability indicate significantly higher decay rate at certain times as opposed to other times when the decay rate is negligible and hardly produces a change in the population in the autoionizing wavepacket. In a magnified view of some of these curves as shown in Fig 3.12, we can also see that there are two distinct

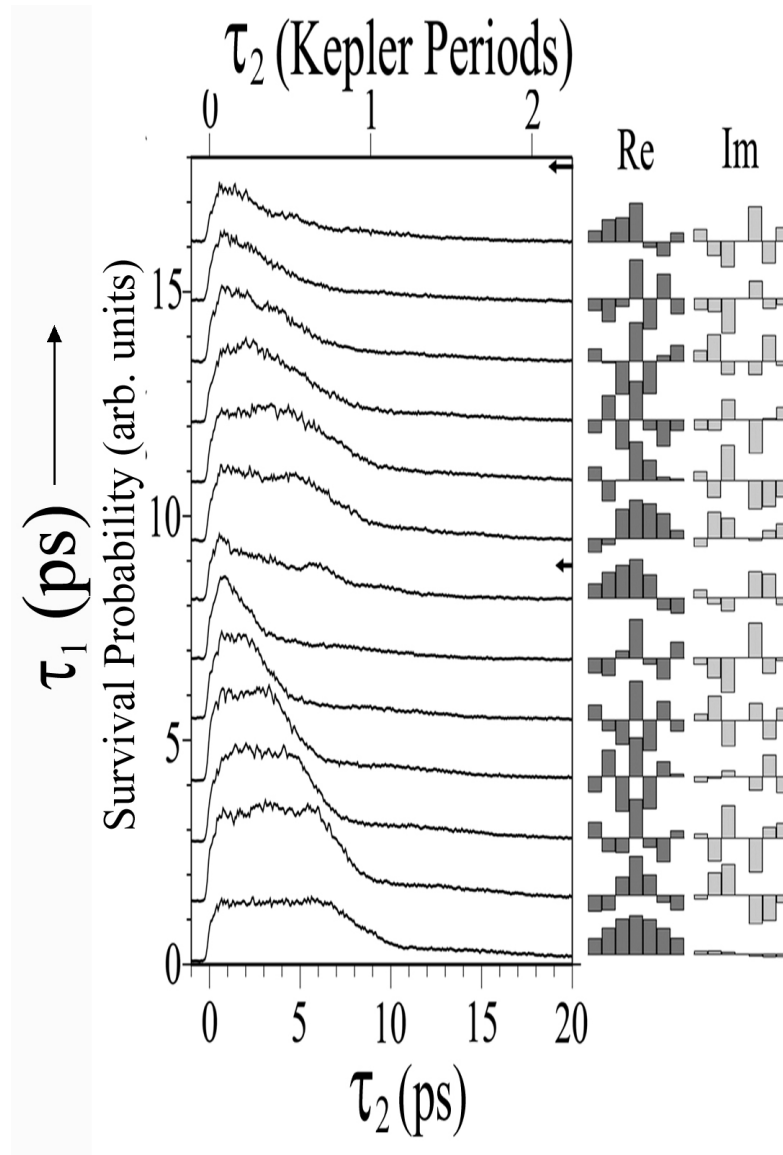


Figure 3.6: Survival probability of $4p_{3/2}Nl$, $N \sim 40$ wavepackets

The set of traces here show the survival probability of the $4p_{3/2}Nl$, $N \sim 40$ autoionizing wavepackets with different phases as a function of the delay τ_2 between the creation of the autoionizing wavepacket (L3) and the ICE probe (L4). The vertical displacement of the various traces correspond to the delay τ_1 between creating the radial $4sNd$ wavepacket (L2) and the excitation of the autoionizing wavepacket (L3). The upper scale shows the delay τ_2 in terms of the Kepler period of the radial wavepacket. From top to bottom on the right hand side, the two arrows correspond to delays of $\tau_1 = 2\tau_K$ and $\tau_1 = \tau_K$, respectively. The bar graphs on the right of the traces show the calculated real and imaginary amplitudes of the constituent $4snd$ states in the wavepacket corresponding to each trace.

steps in the decay of the wavepackets. The first step drops the population in the autoionizing wavepacket to $\sim 15\%$ of the initial population. The position of the first step following the initial flat region occurs at different times depending on the delay τ_1 . After the first step, there is another almost flat region where the population of the $4pNd$ wavepacket stays nearly constant and this is followed by another step after which the wavepacket is almost fully autoionized. The second step is more apparent in the plots of the same traces in Fig 3.12. The time interval between the two step-downs in population is spaced apart by ~ 9 ps in all the $N \sim 40$ decay curves. This interval also corresponds to the Kepler period of the $4sNd$, $N \sim 40$ wavepacket that is used to create the autoionizing wavepacket.

As we vary the delay τ_1 between exciting the radial wavepacket with L2 and the ICE by L3 used to create the autoionizing wavepacket, we notice some interesting patterns in the delays corresponding to the first step in the decay curves. As we increase τ_1 from 0 to τ_K , the delay corresponding to the first step varies from almost τ_K at $\tau_1 = 0$ to less than 1 ps when $\tau_1 \sim \tau_K$. When τ_1 increases to more than τ_K , we notice a sudden jump in the location of the first step from near 1 ps to almost τ_K . Further increase in τ_1 causes the timing of the first step to occur progressively earlier till it becomes small again near $\tau_1 = 2\tau_K$.

Fig 3.7 shows the measured autoionizing radial wavepacket survival probability for the case where $N \sim 35$. All the features seen in the case of the $N \sim 40$ wavepacket are also seen in these traces with the difference corresponding to the kepler period of the $N \sim 35$ wavepacket. For the rest of this chapter, we will only consider the case of

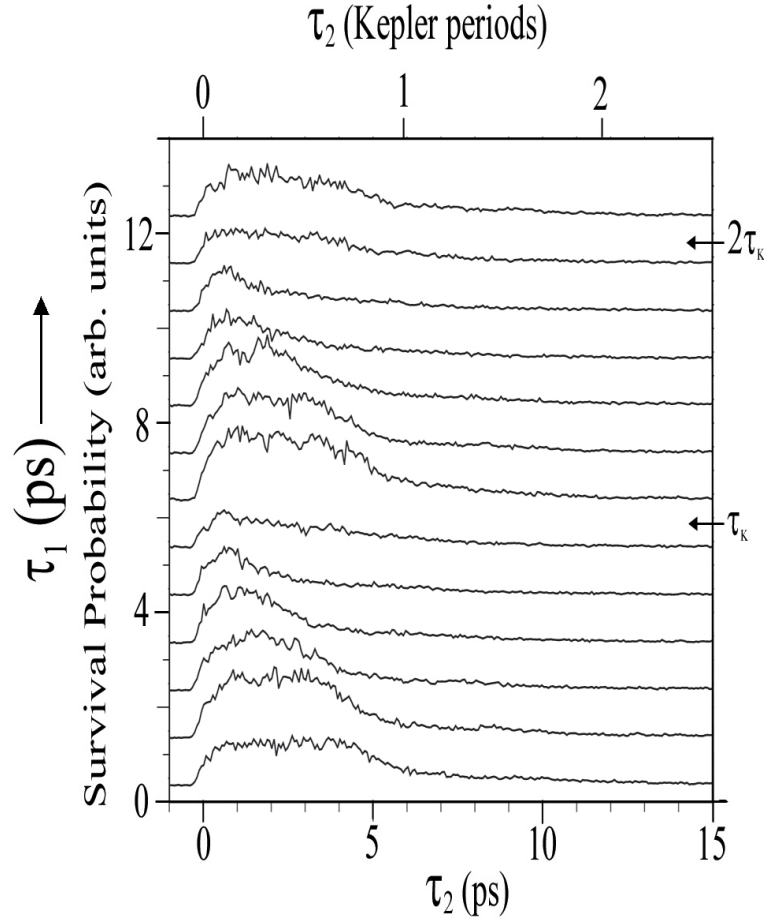


Figure 3.7: Survival probability of $4p_{3/2}N\ell$, $N \sim 35$ wavepackets

The set of traces here show the survival probability of the $4p_{3/2}N\ell$, $N \sim 35$ autoionizing wavepackets with different phases as a function of the delay τ_2 between the creation of the autoionizing wavepacket (L3) and the ICE probe (L4). The vertical displacement of the various traces correspond to the delay τ_1 between creating the radial $4sNd$ wavepacket (L2) and the excitation of the autoionizing wavepacket (L3). The upper scale shows the delay τ_2 in terms of the Kepler period of the radial wavepacket. From top to bottom on the right hand side, the two arrows correspond to delays of $\tau_1 = 2\tau_K$ and $\tau_1 = \tau_K$, respectively.

the $N \sim 40$ wavepacket but the results are equally valid for the $N \sim 35$ wavepacket.

3.5 Phase-controlled wavepackets

Consider a $4sNd$ wavepacket excited at time $t = 0$. We can write the wavefunction of the wavepacket as the sum of the wavefunctions of the individual eigenstates that make up the wavepacket.

$$|4sNd\rangle = \sum_n C_n |4snd\rangle \quad (3.1)$$

where C_n^2 corresponds to the real, time-independent probabilities of the electron being in a $|4snd\rangle$ state as measured by SSFI. As a function of time the phases of the individual eigenstates evolve at different rates.

$$|4snd\rangle_t = |4snd\rangle_0 e^{-iE_n t} \quad (3.2)$$

where $E_n = -\frac{1}{2n^{*2}}$, $n^* = (n - \delta_n)$ and δ_n is the quantum defect of the $4snd$ state. We can then write the initial wavefunction for the autoionizing wavepacket at its instant of creation as

$$|4pNd\rangle_{\tau_1} = \sum_n C_n |4pnd\rangle e^{-iE_n \tau_1} \quad (3.3)$$

In Fig 3.6, the bar graphs on the right represent the real and imaginary amplitudes of the constituent eigenstates forming the $N \sim 40$ wavepacket. The constituent eigenstates in the autoionizing wavepacket have the same relative amplitudes at all delays τ_1 when the wavepacket is initially excited. The difference lies in the phases ($\phi_n = -E_n \tau_1$) of the different constituents of the wavepacket depending on τ_1 .

In addition to the delays considered in this experiment, we have the ability to choose the relative phases of the constituent eigenstates arbitrarily by choosing a time delay τ_1 at which to excite the autoionizing wavepacket. As we see in this experiment, it is possible to change the autoionization rate of a wavepacket by a factor of five or more just by changing the phase of the states making up the wavepacket.

It is also possible to create wavepackets with specific choices of phase and amplitude components of different states by adjusting the spectrum and the phase profile of the laser pulse used to create the wavepacket [88,89]. However, this involves significantly greater experimental effort and costs compared to our method of allowing the natural evolution of the wavepacket to create the required phase relationship in the wavepacket. We can, therefore, use the method of creating autoionizing wavepackets described here as a phase-control mechanism for creating “designer” wavepackets with the required properties. The range of states to be included in the wavepacket can be adjusted by choosing the central wavelength and the bandwidth of the laser exciting the radial wavepackets.

3.6 Data Analysis

We have seen that there can be significant changes in autoionizing wavepacket decay rates by small variations of phase of the wavepacket. However, a look at the phases of the constituent states of the wavepacket does not reveal any intuitive explanation for the behavior that we observe in the wavepackets. However, since we excite radial

rydberg wavepackets in the atom, it might be more useful to consider the dynamics of the atom by using a semi-classical picture for wavepacket evolution.

3.6.1 Semi-classical Picture

Consider the calcium atom as a closed shell core with a charge of +2 surrounded by the two outermost valence electrons. Let us assume that one of the electrons is excited into a rydberg wavepacket at time $t = 0$. This corresponds to the $4sNd$ radial rydberg wavepacket. When this electron is far from the core, it sees an effective charge of +1 due to the screening by the second electron. At a time τ_1 , the inner electron is excited into a $4p_{3/2}$ state of the ion. Using a short ICE pulse, the bandwidth of the pulse is enough to account for any change in the resonance due to the presence of the outer electron far from the core [67, 79, 93]. For purposes of analysis, we will consider the excitation as an instantaneous event.

The doubly excited system can decay by autoionization when the two electrons exchange energy and angular momentum by collision through the repulsive Coulomb force between them. When the rydberg electron is far from the core, the presence of the doubly charged core next to the inner electron screens the Coulomb repulsion between the excited electrons and there is no energy exchange at this time. We can also write this as the potential experienced by the rydberg (outer) electron as

$$V_{outer} = -\frac{2}{|\vec{r}_o|} + \frac{1}{|\vec{r}_o - \vec{r}_i|} \quad (3.4)$$

where \vec{r}_o and \vec{r}_i are the position vectors of the outer and inner electrons in relation

to the core. For $|\vec{r}_o| \geq |\vec{r}_i|$,

$$\frac{1}{|\vec{r}_o - \vec{r}_i|} = \sum_{k=0}^{\infty} \frac{r_i^k}{r_o^{k+1}} \overleftrightarrow{C}_i^{(k)} \cdot \overleftrightarrow{C}_o^{(k)} \quad (3.5)$$

where C_q^k are spherical tensor operators (see Appendix B). Expanding the sum to the first two terms, we have

$$\frac{1}{|\vec{r}_o - \vec{r}_i|} = \frac{1}{r_o} + \frac{r_i}{r_o^2} \overleftrightarrow{C}_i^{(1)} \cdot \overleftrightarrow{C}_o^{(1)} + \dots \quad (3.6)$$

If we only include the first term in the expansion, we have $V_{outer} \simeq -\frac{1}{r_o}$ for $r_o \gg r_i$, i.e. the screening by the inner electron makes the outer electron ‘see’ a charge of +1 at the core. However, this case does not include any interaction between the two electrons.

If we include the first two terms in the expansion in Eqn 3.6, the interaction between the electrons that is represented by the second term becomes relevant to the potential experienced by the outer electron only when r_i and r_o become comparable. Since the inner electron is limited to a region close to the atomic core, this means that the outer electron also has to be near the core to exchange energy with the inner electron and produce autoionization.

We have already seen the effect of the bandwidth of the laser on the evolution of the radial wavepacket in Fig 3.4. Fig 3.8 shows the radial probability distribution of the radial $4sNd$ ($N \sim 40$) wavepacket in calcium that is excited in the experiment. The radial wavefunctions are calculated using the Numerov algorithm and added in the ratio of the amplitudes which are calculated as the square root of the measured (using SSFI) probability of exciting each state in the wavepacket. We notice that the

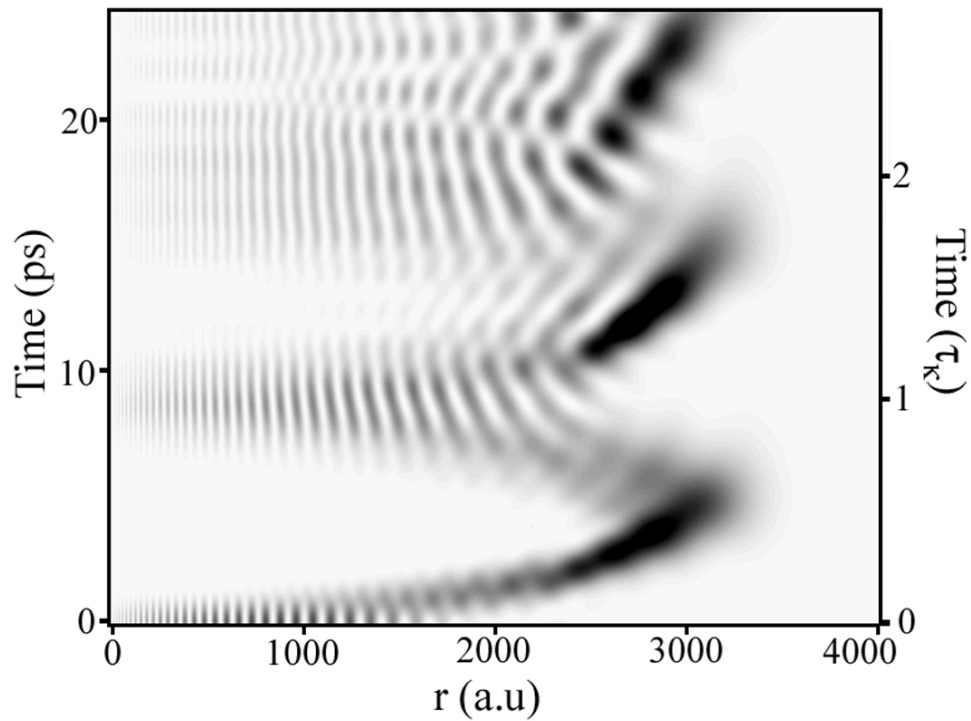


Figure 3.8: Radial probability distribution of the $4sNd$, $N \sim 40$ wavepacket in calcium

Radial probability distribution of the $4sNd$ ($N \approx 40$) wavepacket in calcium. The scale on the vertical scale on the right shows the time in steps of the classical Kepler period of the wavepacket centered at $n = 40$.

radial probability distribution evolves as a particle moving away from the core at $t = 0$ and returns to the core at $t = \tau_K$ and then again moves away from the core to return at $t \sim 2\tau_K$. This justifies the use of a classical picture to understand the dynamics of the rydberg electron in the system under consideration. We can use this picture of the electron motion to understand the features observed in the experimental data.

Consider the case where the second electron is excited by ICE just after the excitation of the radial rydberg wavepacket. At the time of excitation, τ_1 , the first electron is moving away from the core and does not get autoionized. So there is no decay of the autoionizing wavepacket at this time. The data shows this effect as a flat region without wavepacket decay for almost a Kepler period. The first occasion for autoionization decay to occur is when the first electron returns to the core after one Kepler period. At this time, the two electrons are near the core and can exchange energy by collision to cause autoionization. This is seen in the data as a rapid fall in survival probability of the $4p_{3/2}N\ell$ wavepacket. If the ICE occurs at some time after the excitation of the radial wavepacket, the first electron takes less than a kepler period to return to the core. This is seen in the data where the initial flat region in the decay curve lasts for shorter times as we increase the delay, τ_1 , until the first kepler period, τ_K . Beyond the first kepler period, the first electron would continue outward in its next orbit and ICE at this time would be similar to ICE just after excitation except for the dispersion of the wavepacket. We see this effect in the data as the initial flat section of the curves increases in width to almost a kepler period and further changes in this period are similar to the case of τ_1 less than τ_K .

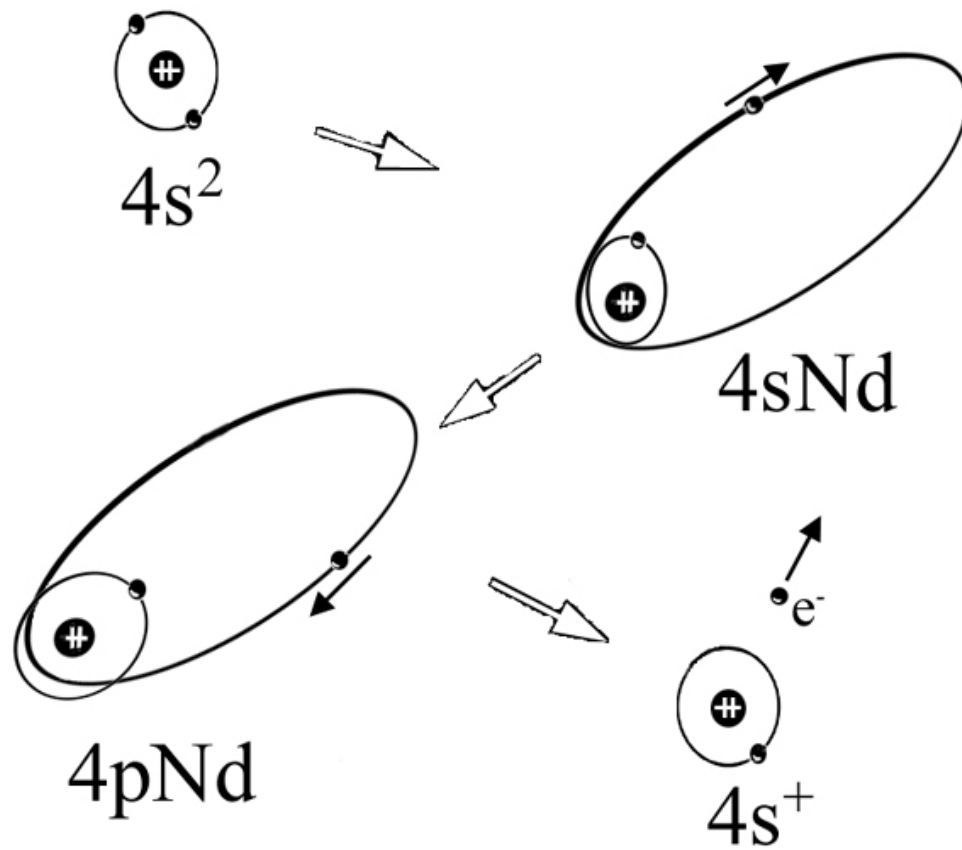


Figure 3.9: Classical Picture of Autoionization
A cartoon of the classical view of autoionization.

The part of the wavepacket that does not interact with the inner electron after its first return to the core continues in its orbit about the core and moves away from the core after $t \sim \tau_K$ and does not return to the core until after another Kepler period at $t \sim 2\tau_K$. This corresponds to the second step seen in the traces where the population in the autoionizing wavepacket remains nearly constant for τ_K and then undergoes rapid decay again when the rydberg electron returns to the core for the second time. The time between the first and second returns to the core for the rydberg electron is the same in all cases and so we see the same width for the second step for all the different delays, τ_1 , in the experiment.

We see from Fig 3.8 that the return of the radial wavepacket to the core is not an instantaneous effect but is spread over a few ps. The finite duration of the pulse ($10 \text{ cm}^{-1} \rightarrow 1.5 \text{ ps FWHM}$) also causes a spread in the time over which the autoionizing interaction occurs. These two effects contribute to the duration of the steep part of the decay curves. The wavepacket disperses rapidly after the first Kepler period and the return of the wavepacket at $t = 2\tau_K$ is spread over an even greater time than at τ_K . This accounts for the greater time for decay at the end of the second step for $\tau_1 < \tau_K$ and at the end of the first step for $\tau_K < \tau_1 < 2\tau_K$. The fractional reduction in the survival probability of the autoionizing wavepacket at each step is proportional to the scaled autoionization rate ($\gamma = \Gamma n^3$) of the constituent states in the wavepacket. γ can also be viewed as the probability for autoionization at each pass of the rydberg electron at the core and Γ is the total autoionization rate of the wavepacket. Due to the high autoionization rate and the dispersion in the wavepacket, we can only detect

two steps in the decay of the wavepacket.

The classical picture of the doubly excited atom is convenient for having a qualitative understanding of the dynamic processes leading to autoionization. However, it does not provide a quantitative prediction for the observations in the experiment. We need to use quantum mechanical methods, such as the quantum defect theory (QDT) to make any quantitative calculations of autoionization rates. Luckily for us, autoionization in two-electron systems has been studied extensively in theory and the methods developed by Cooke et.al [109, 103] have been used to reproduce quantitatively the autoionization decay rates of $4p_{3/2}nd$ states by Thoma et.al [106]. This method is applied to study the decay of autoionizing $4p_{3/2}Nd$ wavepackets in the next section.

3.6.2 Two-channel QDT calculations

The basis of the two-channel QDT model of the atom used by Thoma and Cooke et. al. [106, 109, 103] is the approximation that there are only two effective channels in the autoionization process - a bound channel and a continuum channel. From the work of Thoma, we have the energy-dependent transition moment, \mathcal{T} , from the $4snd$ to the $4pnd$ states given by

$$\mathcal{T}(W_\nu) \propto A(\nu)\Theta(\nu, n) \quad (3.7)$$

where $A(\nu) = 1/\sin \pi(\nu + \delta_f + i\gamma/2)$ is the spectral density in the $4p_{3/2}$ channel, and $\Theta(\nu, n) = [\sin \pi(\nu - n^*)]/[\pi(W_\nu - W_n)(\nu n^*)^{3/2}]$ is the normalized overlap integral for the ICE transition [29]. $W_\nu = -1/2\nu^2$ is the energy of the autoionizing

wavepacket w.r.t. the $4p_{3/2}^+$ ionization limit; $W_n = -1/2n^{*2}$ is the energy of the rydberg eigenstates w.r.t. the $4s^+$ ionization limit with effective principal quantum number $n^* = n - \delta_i$; δ_i and δ_f are the quantum defects of the $4snd$ and $4p_{3/2}nd$ state configurations respectively. $\gamma = \Gamma_n n^{*3}$ is an energy-independent scaled autoionization rate with Γ_n as the autoionization rate of the $4p_{3/2}nd$ state. Fig 3.10 shows $|A(\nu)|^2$, $\Theta(\nu, n)$, and $|A(\nu) \cdot \Theta(\nu, n)|$ with $n = 40$, $\delta = -0.19$ and $\gamma = 0.29$.

In the case of exciting an autoionizing wavepacket, the transition moment from the $4sNd$ wavepacket to the $4p_{3/2}Nd$ wavepacket as a function of the delay τ_1 is given by

$$\mathcal{T}(W_\nu, \tau_1) \propto \sum_n C_n e^{-iW_n \tau_1} A(\nu) \Theta(\nu, n) \quad (3.8)$$

where C_n is the amplitude of the eigenstate with principal quantum number n in the wavepacket. The absolute value of this transition amplitude as calculated for the wavepacket that we excite is shown in Fig 3.11.

The product of this energy-dependent transition amplitude with the spectral amplitude, $\mathcal{F}(W)$ of the laser pulse used for the excitation of the autoionizing wavepacket by ICE (L3) is the excitation amplitude of the autoionizing wavepacket. We can write this excitation amplitude as

$$\mathcal{S}(W) = \mathcal{T}(W) \cdot \mathcal{F}(W) \quad (3.9)$$

$$\Rightarrow \mathcal{S}(W_\nu, \tau_1) = \mathcal{T}(W_n, \tau_1) \cdot \mathcal{F}(W_{3/2} + W_\nu - W_n) \quad (3.10)$$

where $W_{3/2}$ is the energy of the $4p_{3/2}^+$ state w.r.t. the $4s^+$ ground state of the calcium

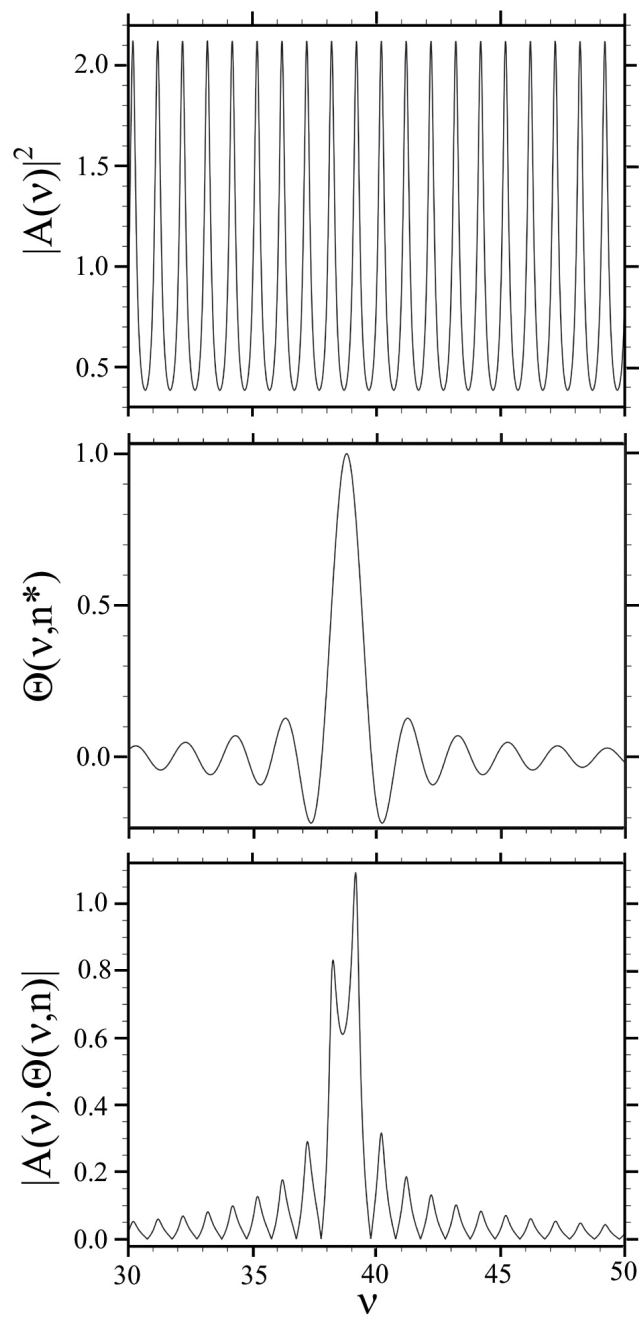


Figure 3.10: Terms in two-channel QDT calculation for autoionizing state $|A(\nu)|^2$, $\Theta(\nu, n)$, and $|A(\nu) \cdot \Theta(\nu, n)|$ with $n = 40$, $\delta = -0.19$ and $\gamma = 0.29$.

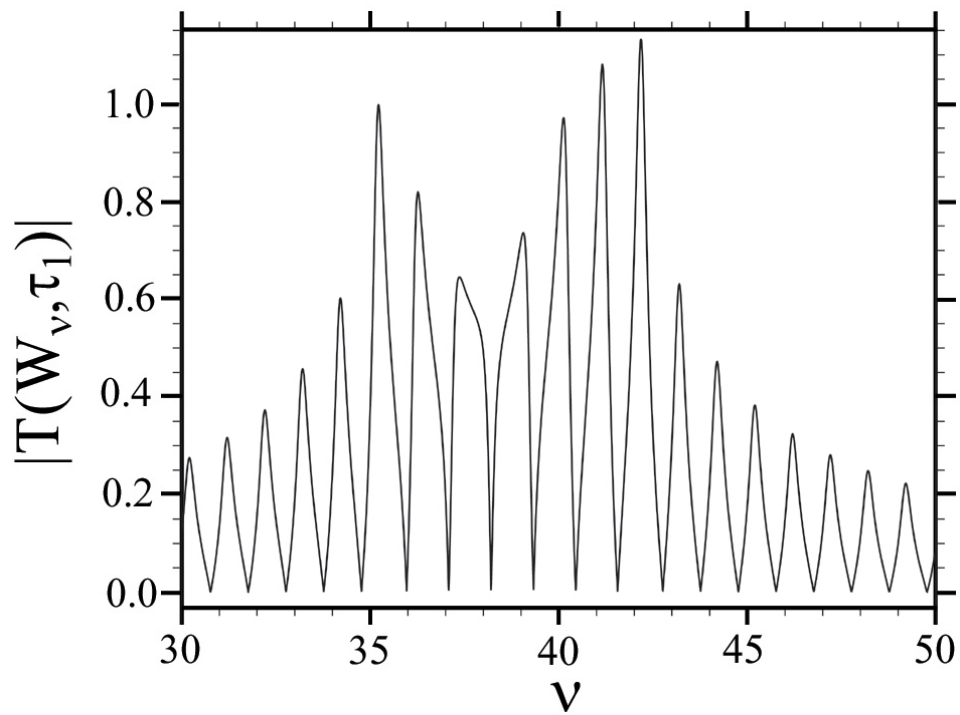


Figure 3.11: Term in two-channel QDT calculation for autoionizing wavepacket $\mathcal{T}(W_\nu, \tau_1)$ with $4sNd$ wavepacket around $N \sim 40$, $\delta = -0.19$ and $\gamma = 0.29$.

ion.

The time-dependent decay rate, \mathcal{R} , of the autoionizing wavepacket is given by the Fourier transform of its excitation spectrum as

$$\mathcal{R}(t, \tau_1) = \left| \int dW_\nu e^{-iW_\nu t} \mathcal{S}(W_\nu, \tau_1) \right|^2 \quad (3.11)$$

The time-dependent probability of autoionization, \mathcal{P}_a , is then given by

$$\mathcal{P}_a(t, \tau_1) = \frac{\int^t \mathcal{R}(t', \tau_1) dt'}{\int^\infty \mathcal{R}(t', \tau_1) dt'} \quad (3.12)$$

If we assume that all the atoms excited to the autoionizing wavepacket eventually autoionize, then by conservation of probability, the probability of atoms remaining in the $4pNd$ autoionizing wavepacket as a function of time is written as

$$\mathcal{P}(t, \tau_1) = 1 - \mathcal{P}_a(t, \tau_1) = 1 - \frac{\int^t \mathcal{R}(t', \tau_1) dt'}{\int^\infty \mathcal{R}(t', \tau_1) dt'} \quad (3.13)$$

The above calculation is performed for the specific choice of wavepackets that we excite in the experiment. The state distribution as measured by SSFI is used in the calculations along with the known quantum defects of the states in $4sNd$ and $4pNd$ wavepackets [29,110]. The only adjustable parameter in these calculations is the value of γ , the scaled autoionization rate. γ is varied to find the best fit to the experimental data. We find a value of $\gamma = 0.29$ to provide the best fit to the experiment. The comparison of the calculation with the data is shown in Fig 3.12.

The calculations made using the two-channel QDT theory are in good agreement with the experimental data for different time delays τ_1 and for the different wavepackets centered at $N \sim 35$ and $N \sim 40$.

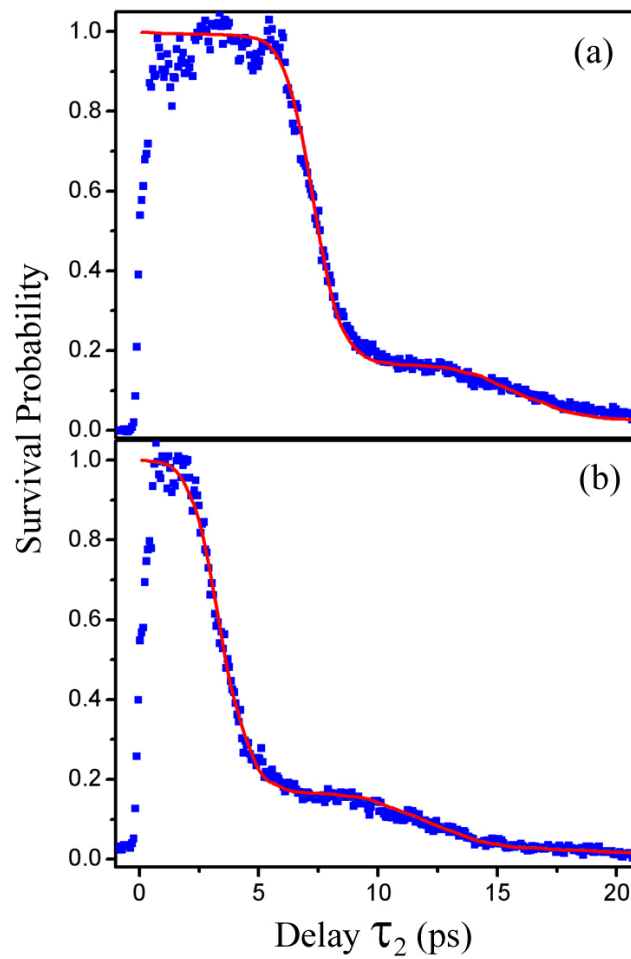


Figure 3.12: Data and two-channel calculations for $4p_{3/2}N\ell$ wavepacket decay
 Data and two-channel calculations with $\gamma=0.29$ for survival probability of a
 $4p_{3/2}Nd$, $N \sim 40$ autoionizing wavepacket for the two cases where (a) $\tau_1 = 1.4$ ps and
 (b) $\tau_1 = 5.4$ ps.

3.6.3 Autoionizing state decay in calcium

As mentioned previously, the experiment to study the time-dependent decay of autoionizing wavepackets is based on a similar experiment by Thoma [106] where the time-dependent decay of a $4p_{3/2}nd$ autoionizing eigenstate is measured. The only difference between the experiment by Thoma and this experiment with the autoionizing wavepacket is the replacement of a $5ns$ pulsed dye laser used as L2 in the former case with a short 0.5 ps pulse used as L2 in the latter. The ICE in this experiment occurs while the outer electron is in a localized wavepacket compared to a stationary state in Thoma's experiment. In terms of analyzing the data and calculating the decay rates, the same method described above is used for both experiments. However, it was found in the experiment by Thoma as well as in repetitions of that experiment by the author that the best-fit value of γ is $\gamma = 0.21$ in the case of the decay of the autoionizing state as opposed to a value of $\gamma = 0.29$ which provides the best fit to experimental data in the case of the autoionizing wavepacket.

Since γ represents an energy-independent scaled autoionization rate, this discrepancy appears to suggest that the scaled autoionization rate changes when more than one autoionizing state is simultaneously excited. All the states forming the wavepacket decay with a best-fit value of $\gamma = 0.21$ when the states are excited individually [106] but when all these states are excited coherently, the combined decay is best reproduced by a value of $\gamma = 0.29$. There is no known physical explanation to explain the phenomenon at present. We have therefore performed the calculations in a more rigorous fashion using *ab initio* K-matrices to rule out any errors introduced

by our initial approximation of the system as consisting of only two channels.

3.6.4 K-matrix MQDT calculations

Some previous experiments studying the dynamics of autoionizing wavepackets in calcium [77] have been well-reproduced theoretically by using K-matrices to perform MQDT calculations. We have used the same 28-channel K-matrices calculated for $J=1$ and $J=3$ by van der Hart and Chris Greene to calculate the channel-dependent transition spectra instead of the two-channel approximation that we used previously.

The autoionizing $4p_{3/2}nd$ states making up the wavepacket are degenerate with other bound and continuum channels in calcium. In the two-channel approximation, we neglect the presence of the other channels because all the other degenerate bound channels are energetically separated from the $4p_{3/2}nd$ states while the choice of the high rydberg states places the wavepacket well above the ionization limit of the $4p_{1/2}n\ell$ channels. In the case of the K-matrix, the effect of all the states that can have a significant influence on the $4pndJ = 1,3$ states are included. This allows us to calculate the autoionization rates directly without the need for a fitting parameter.

The calculations are based on the $J=1,3$ K-matrices calculated by van der Hart and Chris Greene shown in Table 3.1.

There are 13 $J = 1$ channels and 15 $J = 3$ channels included in the K-matrices. We neglect the slight energy dependence of the K-matrices for our calculations because it has been able to reproduce other experimental results accurately [77]. Before performing the calculations, we rotate the LS K-matrices into the jj -coupled basis.

Table 3.1: *LS* K-matrices at energy = -0.321646 a.u. [111]

1P_0	<i>4snp</i>	<i>3dnp</i>	<i>3dnf</i>	<i>4pns</i>	<i>4pnd</i>
<i>4snp</i>	-0.11385	0.12953	0.17339	-0.97642	-0.25674
<i>3dnp</i>	0.12953	-0.78481	0.33251	-1.6152	-0.098125
<i>3dnf</i>	0.17339	0.33251	-0.39437	-0.26045	0.72937
<i>4pns</i>	-0.97642	-1.6152	-0.26045	-0.97277	1.1504
<i>4pnd</i>	-0.25674	-0.098125	0.72937	1.1504	-0.53812
3P_0	<i>4snp</i>	<i>3dnp</i>	<i>3dnf</i>	<i>4pns</i>	<i>4pnd</i>
<i>4snp</i>	-0.33937	0.34323	-0.09064	-0.56855	0.29591
<i>3dnp</i>	0.34323	-0.45516	0.002109	-1.5611	-0.59313
<i>3dnf</i>	-0.090640	0.002109	-0.22377	-0.22375	0.62998
<i>4pns</i>	-0.56855	-1.5611	-0.22375	3.6092	0.44188
<i>4pnd</i>	0.29591	-0.59313	0.62998	0.44188	-0.63770
3D_0	<i>3dnp</i>	<i>3dnf</i>	<i>4pnd</i>		
<i>3dnp</i>	-0.82238	0.031903	0.46628		
<i>3dnf</i>	0.031903	-0.039409	0.40638		
<i>4pnd</i>	0.46628	0.40638	-0.32777		
1F_0	<i>4snf</i>	<i>3dnp</i>	<i>3dnf</i>	<i>4pnd</i>	<i>4png</i>
<i>4snf</i>	0.22830	0.32957	-0.14201	0.37450	-0.062271
<i>3dnp</i>	0.32957	-1.5613	-0.064441	1.1987	-0.095575
<i>3dnf</i>	-0.14201	-0.064441	-0.022135	0.53045	-0.059457
<i>4pnd</i>	0.37450	1.1987	0.53045	-1.6966	0.14259
<i>4png</i>	-0.062271	-0.095575	-0.059457	0.14259	-0.12945
3F_0	<i>4snf</i>	<i>3dnp</i>	<i>3dnf</i>	<i>4pnd</i>	<i>4png</i>
<i>4snf</i>	0.34515	-0.18247	-0.063689	0.24536	-0.041226
<i>3dnp</i>	-0.18247	-0.61997	-0.075997	-0.044269	-0.0085487
<i>3dnf</i>	-0.063689	-0.075997	0.12687	0.26260	-0.019838
<i>4pnd</i>	0.24536	-0.044269	0.26260	-0.21046	-0.040918
<i>4png</i>	-0.041226	-0.0085487	-0.019838	-0.040918	-0.10687
3G_0	<i>3dnf</i>	<i>4png</i>			
<i>3dnf</i>	0.090996	-0.0030878			
<i>4png</i>	-0.0030878	0.14447			

These K-matrices are then used to calculate the energy dependent transition moment into each of the jj -coupled continuum channels using the methods of Cooke and Cromer [109].

We define the jj K-matrices for $J = 1, 3$, as

$$\underline{K}^{jj} = \underline{V}_j^T \underline{K}^{LS} \underline{V}_j \quad (3.14)$$

with the \underline{V}_j transformation matrices for $j = 1$ and $j = 3$ given in tables 3.2 and 3.3 respectively.

Table 3.2: LS to jj transformation matrix for $J = 1$

$$\begin{array}{c}
 \left(\begin{array}{c}
 4s_{1/2}np_{1/2} \\
 4s_{1/2}np_{3/2} \\
 3d_{3/2}np_{1/2} \\
 3d_{3/2}np_{3/2} \\
 3d_{5/2}np_{3/2} \\
 3d_{3/2}nf_{5/2} \\
 3d_{5/2}nf_{5/2} \\
 3d_{5/2}nf_{7/2} \\
 4p_{1/2}ns_{1/2} \\
 4p_{3/2}ns_{1/2} \\
 4p_{1/2}nd_{3/2} \\
 4p_{3/2}nd_{3/2} \\
 4p_{3/2}nd_{5/2}
 \end{array} \right)
 =
 \left(\begin{array}{cccccccccccc}
 \frac{1}{\sqrt{3}} & \sqrt{\frac{2}{3}} & 0 & 0 & 0 & 0 & 0 & 0 & 0 & 0 & 0 & 0 & 0 \\
 0 & 0 & \frac{1}{\sqrt{3}} & \frac{-1}{\sqrt{15}} & \sqrt{\frac{3}{5}} & 0 & 0 & 0 & 0 & 0 & 0 & 0 & 0 \\
 0 & 0 & 0 & 0 & 0 & \sqrt{\frac{2}{5}} & \frac{1}{\sqrt{35}} & \frac{2}{\sqrt{7}} & 0 & 0 & 0 & 0 & 0 \\
 0 & 0 & 0 & 0 & 0 & 0 & 0 & 0 & \frac{-1}{\sqrt{3}} & \sqrt{\frac{2}{3}} & 0 & 0 & 0 \\
 0 & 0 & 0 & 0 & 0 & 0 & 0 & 0 & 0 & 0 & \frac{1}{\sqrt{3}} & \frac{1}{\sqrt{15}} & \sqrt{\frac{3}{5}} \\
 \sqrt{\frac{2}{3}} & \frac{-1}{\sqrt{3}} & 0 & 0 & 0 & 0 & 0 & 0 & 0 & 0 & 0 & 0 & 0 \\
 0 & 0 & \frac{-1}{\sqrt{6}} & \sqrt{\frac{8}{15}} & \sqrt{\frac{3}{10}} & 0 & 0 & 0 & 0 & 0 & 0 & 0 & 0 \\
 0 & 0 & 0 & 0 & 0 & \frac{1}{\sqrt{5}} & \sqrt{\frac{18}{35}} & \frac{-\sqrt{2}}{\sqrt{7}} & 0 & 0 & 0 & 0 & 0 \\
 0 & 0 & 0 & 0 & 0 & 0 & 0 & 0 & \sqrt{\frac{2}{3}} & \frac{1}{\sqrt{3}} & 0 & 0 & 0 \\
 0 & 0 & 0 & 0 & 0 & 0 & 0 & 0 & 0 & 0 & \frac{1}{\sqrt{6}} & \sqrt{\frac{8}{15}} & \frac{-\sqrt{3}}{\sqrt{10}} \\
 0 & 0 & \frac{1}{\sqrt{2}} & \sqrt{\frac{2}{5}} & \frac{-1}{\sqrt{10}} & 0 & 0 & 0 & 0 & 0 & 0 & 0 & 0 \\
 0 & 0 & 0 & 0 & 0 & \sqrt{\frac{2}{5}} & \frac{-4}{\sqrt{35}} & \frac{-1}{\sqrt{7}} & 0 & 0 & 0 & 0 & 0 \\
 0 & 0 & 0 & 0 & 0 & 0 & 0 & 0 & 0 & 0 & \frac{1}{\sqrt{2}} & \frac{-\sqrt{2}}{\sqrt{5}} & \frac{-1}{\sqrt{10}}
 \end{array} \right)
 \left(\begin{array}{c}
 4snp^1P \\
 3dnp^1P \\
 3dnf^1P \\
 4pns^1P \\
 4pnd^1P \\
 4snp^3P \\
 3dnp^3P \\
 3dnf^3P \\
 4pns^3P \\
 4pnd^3P \\
 3dnp^3D \\
 3dnf^3D \\
 4pnd^3D
 \end{array} \right)
 \end{array}$$

We have used the Cooke and Cromer formalism [109, 100] to calculate the autoionization spectrum using the K-matrices. The \underline{K}^{jj} matrices can be equated to the

Table 3.3: LS to jj transformation matrix for $J = 3$

$$\begin{array}{c}
\left[\begin{array}{l}
4s_{1/2}nf_{5/2} \\
4s_{1/2}nf_{7/2} \\
3d_{5/2}np_{1/2} \\
3d_{3/2}np_{3/2} \\
3d_{5/2}np_{3/2} \\
3d_{3/2}nf_{5/2} \\
3d_{5/2}nf_{5/2} \\
3d_{3/2}nf_{7/2} \\
3d_{5/2}nf_{7/2} \\
4p_{3/2}nd_{3/2} \\
4p_{1/2}nd_{5/2} \\
4p_{3/2}nd_{5/2} \\
4p_{1/2}n_8_{7/2} \\
4p_{3/2}n_8_{7/2} \\
4p_{3/2}n_8_{9/2}
\end{array} \right]
=
\begin{array}{c}
\left[\begin{array}{ccccccccccccccc}
0 & 0 & \frac{-\sqrt{2}}{3} & \frac{\sqrt{2}}{\sqrt{30}} & \frac{4\sqrt{2}}{9\sqrt{5}} & 0 & 0 & 0 & 0 & 0 & 0 & 0 & 0 & 0 \\
0 & 0 & 0 & 0 & 0 & \frac{-4}{7\sqrt{10}} & \frac{-3\sqrt{5}}{7\sqrt{5}} & \frac{3\sqrt{2}}{7} & \frac{2\sqrt{6}}{7} & 0 & 0 & 0 & 0 & 0 \\
0 & 0 & 0 & 0 & 0 & 0 & 0 & 0 & 0 & \frac{-\sqrt{2}}{\sqrt{30}} & \frac{\sqrt{2}}{3} & \frac{4\sqrt{2}}{9\sqrt{5}} & 0 & 0 & 0 \\
\frac{\sqrt{3}}{\sqrt{7}} & \frac{2}{\sqrt{7}} & 0 & 0 & 0 & 0 & 0 & 0 & 0 & 0 & 0 & 0 & 0 & 0 & 0 \\
0 & 0 & \frac{1}{\sqrt{3}} & \frac{-\sqrt{2}}{\sqrt{5}} & \frac{2}{\sqrt{15}} & 0 & 0 & 0 & 0 & 0 & 0 & 0 & 0 & 0 & 0 \\
0 & 0 & 0 & 0 & 0 & \frac{3}{\sqrt{35}} & \frac{\sqrt{6}}{\sqrt{35}} & \frac{-1}{\sqrt{7}} & \frac{\sqrt{3}}{\sqrt{7}} & 0 & 0 & 0 & 0 & 0 & 0 \\
0 & 0 & 0 & 0 & 0 & 0 & 0 & 0 & 0 & \frac{\sqrt{2}}{\sqrt{5}} & \frac{-1}{\sqrt{3}} & \frac{2}{\sqrt{15}} & 0 & 0 & 0 \\
0 & 0 & 0 & 0 & 0 & 0 & 0 & 0 & 0 & 0 & 0 & 0 & \frac{1}{\sqrt{3}} & \frac{1}{3} & \frac{\sqrt{5}}{3} \\
\frac{2}{\sqrt{7}} & \frac{-\sqrt{3}}{\sqrt{7}} & 0 & 0 & 0 & 0 & 0 & 0 & 0 & 0 & 0 & 0 & 0 & 0 & 0 \\
0 & 0 & \frac{2}{3} & \frac{\sqrt{8}}{\sqrt{15}} & \frac{1}{3\sqrt{5}} & 0 & 0 & 0 & 0 & 0 & 0 & 0 & 0 & 0 & 0 \\
0 & 0 & 0 & 0 & 0 & \frac{\sqrt{3}}{2\sqrt{35}} & \frac{3\sqrt{2}}{\sqrt{35}} & \frac{\sqrt{3}}{\sqrt{7}} & \frac{-1}{2\sqrt{7}} & 0 & 0 & 0 & 0 & 0 & 0 \\
0 & 0 & 0 & 0 & 0 & 0 & 0 & 0 & 0 & \frac{\sqrt{8}}{\sqrt{15}} & \frac{2}{3} & \frac{-1}{3\sqrt{5}} & 0 & 0 & 0 \\
0 & 0 & 0 & 0 & 0 & 0 & 0 & 0 & 0 & 0 & 0 & 0 & \frac{1}{2} & \frac{1}{\sqrt{3}} & \frac{-\sqrt{5}}{2\sqrt{3}} \\
0 & 0 & 0 & 0 & 0 & \frac{3\sqrt{15}}{14} & \frac{-\sqrt{10}}{7} & \frac{\sqrt{3}}{7} & \frac{-3}{14} & 0 & 0 & 0 & 0 & 0 & 0 \\
0 & 0 & 0 & 0 & 0 & 0 & 0 & 0 & 0 & 0 & 0 & 0 & \frac{\sqrt{5}}{2\sqrt{3}} & \frac{-\sqrt{5}}{3} & \frac{-1}{6}
\end{array} \right]
\end{array}
\left[\begin{array}{l}
3dnp\ ^3D \\
3dnf\ ^3D \\
4pnd\ ^3D \\
4snf\ ^1F \\
3dnp\ ^1F \\
3dnf\ ^1F \\
4pnd\ ^1F \\
4png\ ^1F \\
4snf\ ^3F \\
3dnp\ ^3F \\
3dnf\ ^3F \\
4pnd\ ^3F \\
4png\ ^3F \\
3dnf\ ^3G \\
4png\ ^3G
\end{array} \right]$$

\underline{R} matrices in the standard Cooke and Cromer formalism [109, 100]. The equation relating the \underline{K} matrix to the spectral densities of the different channels is written as [100]

$$(\underline{K} + \tan(\pi\nu))\mathbf{a} = \mathbf{0} \quad (3.15)$$

where $a_i = \cos(\pi\nu_i)A_i$. The A_i are the spectral amplitudes for the different channels. For the purposes of calculating the spectra required for the autoionizing state, it is convenient to split the \underline{K} -matrix into blocks corresponding to bound and continuum channels [109, 100]. We could then rewrite Eq. 3.15 as

$$\begin{pmatrix} [\underline{K} + \tan(\pi\nu)]_{bb} & \underline{K}_{bc} \\ \underline{K}_{cb} & [\underline{K} + \tan(\pi\nu)]_{cc} \end{pmatrix} \begin{pmatrix} \mathbf{a}_b \\ \mathbf{a}_c \end{pmatrix} = \mathbf{0} \quad (3.16)$$

where \mathbf{a}_b and \mathbf{a}_c are column vectors with n_b and n_c components respectively. n_b and n_c are the number of bound and continuum channels, respectively, contributing to the spectrum at a given energy. In an autoionizing system with the electron allowed to decay into n_c possible continuum channels, this equation has n_c independent solutions. The problem is then reduced to one of solving n_c simultaneous equations. Eqn. 3.15 is then rewritten as [100]

$$\{\underline{K}_{cb}[\underline{K} + \tan(\pi\nu)]_{bb}^{-1}\underline{K}_{bc} - \underline{K}_{cc}\}\mathbf{a}_c = \epsilon_j\mathbf{a}_c, \quad (3.17)$$

$$\mathbf{a}_b = -[\underline{K} + \tan(\pi\nu)]_{bb}^{-1}\underline{K}_{bc}\mathbf{a}_c \quad (3.18)$$

The continuum eigenvectors \mathbf{a}_c are normalized to 1 by

$$[(\epsilon_j)^2 + 1] \sum_{i=1}^{n_c} a_{ci}^2 = 1 \quad (3.19)$$

since the electron eventually ionizes into any or all of the possible $j = 1, \dots, n_c$ continuum channels.

The spectral amplitudes in the bound channels are calculated as $\mathbf{A}_b = \mathbf{a}_b \sec(\pi\nu)$ for each of the n_c solutions. \mathbf{A}_b correspond to the spectral amplitude of each bound channel in the coupled dissociation eigenvector basis (the basis corresponding to the n_c continua). To convert this to the independent particle jj-coupled basis, which is more physically intuitive, we transform \mathbf{A}_b to \mathbf{A}'_b as

$$\underline{\mathbf{A}}'_b = \underline{\mathbf{A}}_b \underline{\mathbf{a}}_c^T \quad (3.20)$$

where $\underline{\mathbf{A}}'_b$ and $\underline{\mathbf{A}}_b$ are the $n_b \times n_c$ matrices composed of the n_c column vectors \mathbf{A}'_b and \mathbf{A}_b , respectively. $\underline{\mathbf{a}}_c$ is an $n_c \times n_c$ matrix with the columns corresponding to the n_c eigenvectors \mathbf{a}_c . Physically, $\underline{\mathbf{a}}_c$ is the matrix that rotates the n_c jj-coupled continua into the n_c ‘eigencontinua’ at each energy ν .

Each of the n_c column vectors \mathbf{A}'_b represents the amplitude of the transition moment from the n_b bound channels into the respective n_c continuum channels. We then calculate the autoionization amplitude into each jj-coupled continuum channel from the initial Rydberg state $4snd$ as a function of energy for $i = 1, \dots, n_c$ as

$$\chi_i(\nu) = \boldsymbol{\kappa}_b A'_{bi}(\nu) \quad (3.21)$$

where $\boldsymbol{\kappa}_b$ are the n_b -element row vectors whose components are the transition moments from the initial $4snd$ states into the n_b bound channels. The bound states in the energy range under consideration are limited to the $4p_{1/2}n\ell$ and $4p_{3/2}n\ell$ channels.

We will assume that there is no difference in the radial transition moments from $4snd$ to the $4p_{1/2}n\ell$ and the $4p_{3/2}n\ell$ states. This reduces the calculation of the elements of κ_b to the calculation of the angular part of the transition moment into each bound channel.

The result of the calculations of κ_b for $J = 1$ and $J = 3$ are

$$\begin{aligned} \kappa_b(J=1) &= \begin{pmatrix} 0 & 0 & -\sqrt{\frac{2}{45}} & \frac{-\sqrt{2}}{15} & \frac{-\sqrt{2}}{5} \end{pmatrix} \iff \begin{pmatrix} 4p_{\frac{1}{2}}ns_{\frac{1}{2}} & 4p_{\frac{3}{2}}ns_{\frac{1}{2}} & 4p_{\frac{1}{2}}nd_{\frac{3}{2}} & 4p_{\frac{3}{2}}nd_{\frac{3}{2}} & 4p_{\frac{3}{2}}nd_{\frac{5}{2}} \end{pmatrix} \\ \kappa_b(J=3) &= \begin{pmatrix} \frac{\sqrt{2}}{5} & \frac{-1}{\sqrt{15}} & \frac{2}{5\sqrt{3}} & 0 & 0 & 0 \end{pmatrix} \iff \begin{pmatrix} 4p_{\frac{3}{2}}nd_{\frac{3}{2}} & 4p_{\frac{1}{2}}nd_{\frac{5}{2}} & 4p_{\frac{3}{2}}nd_{\frac{5}{2}} & 4p_{\frac{1}{2}}ng_{\frac{7}{2}} & 4p_{\frac{3}{2}}ng_{\frac{7}{2}} & 4p_{\frac{3}{2}}ng_{\frac{9}{2}} \end{pmatrix} \end{aligned}$$

We use the $\chi_i(\nu)$ values to replace $A(\nu)$ in Eqn. 3.8 and follow the same procedure as in the two-channel case to calculate the time-dependent decay rate into each of the n_c continuum channels. The sum of the decay rates for all channels with $J = 1$ and $J = 3$ is used to determine the total decay rate. This decay rate is equivalent to the $R(t, \tau_1)$ in Eqn. 3.11. This is applied in Eqn. 3.13 to calculate the time-dependent bound-state survival probability of the autoionizing wavepacket. This calculation is shown together with the data for two cases in Fig 3.13. There is very good agreement between the data and the calculations.

Since the reason for using the entire MQDT analysis was to test the correctness of our choice of scaled autoionization rate(γ) due to discrepancies in the best-fit value of γ for the case of the decay of a rydberg state versus the decay of the rydberg wavepacket, we have performed an MQDT analysis using the K-matrices to calculate the expected decay rate for an autoionizing state. The comparison of the data with various calculations are shown in Fig 3.14. It is found that the calculations using the K-matrices do not give the same result as the experimental decay rate in the case of the autoionizing state. The decay of the autoionizing state obtained from calculations

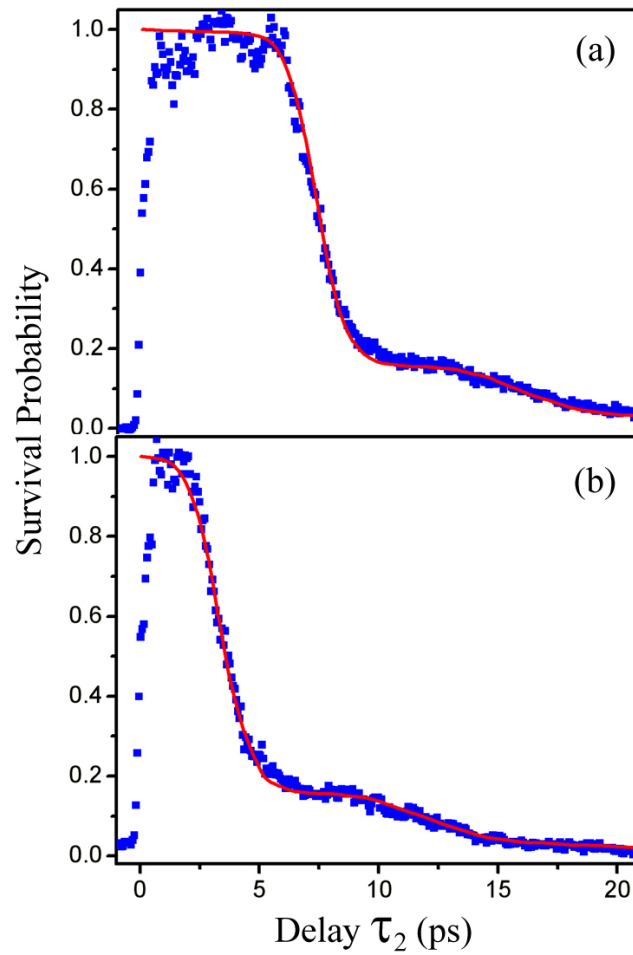


Figure 3.13: Data and K-matrix calculations for $4p_{3/2}N\ell$ wavepacket decay
 Data and K-matrix calculations for survival probability of a $4p_{3/2}Nd$, $N \sim 40$
 autoionizing wavepacket for the two cases where (a) $\tau_1 = 1.4$ ps and (b) $\tau_1 = 5.4$ ps.

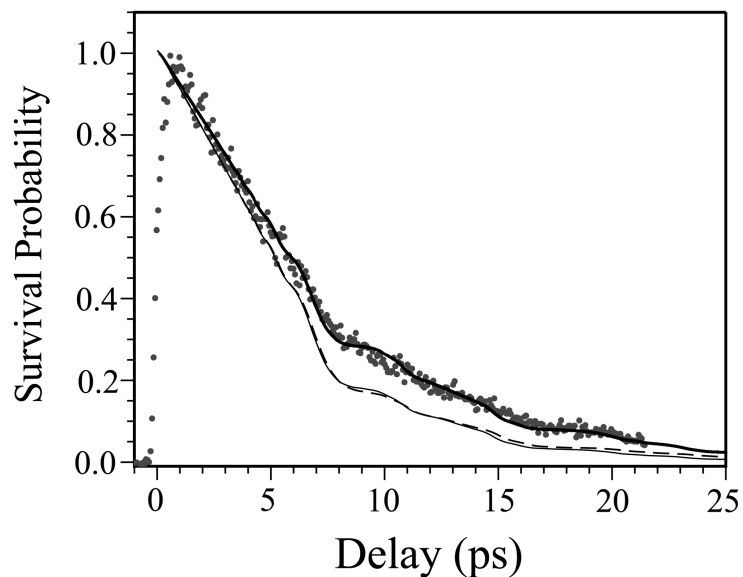


Figure 3.14: Data and calculations for $4p_{3/2}40d$ state decay
Data along with two-channel and K-matrix calculations for survival probability of a $4p_{3/2}40d$ state as a function of time after excitation. The dots correspond to the data values from the experiment. The thick dark curve with the best fit to the data is a two-channel calculation of the autoionizing state survival probability with $\gamma = 0.21$. The thin line corresponds to the two-channel calculation with $\gamma = 0.29$ while the dashed curve alongside it is the result of the MQDT analysis using the K-matrices.

using the K-matrices are close to the decay rate that would be expected if the scaled autoionization rate were $\gamma \sim 0.29$ rather than $\gamma \sim 0.21$ that is found from comparison to the experimental data.

On the basis of our calculations with the two-channel approximation as well as with the MQDT analysis using ab initio K-matrices, we can be confident about the methods used in the experiment to detect the survival probability of the autoionizing wavepacket. However, it still does not explain the discrepancy between the values of the scaled autoionization rate in the case of exciting a rydberg eigenstate as opposed to a rydberg wavepacket.

One possibility that we considered was to check for angular variation in the ejection of fast electrons [77]. This was checked by rotating all the lasers into vertical and horizontal polarizations and comparing the signal levels from the fast electrons. We find that there is no difference in the variation of signal level with delay in the case of using lasers with the two different polarizations. Calculation of autoionization rates were also performed for $4pNs$ wavepackets and states and their decay rate was found to be about half the decay rate of the $4pNd$ wavepackets/states. The inclusion of $4sNs$ states with the same amplitudes as the $4sNd$ states makes the calculations disagree with the experimental measurements significantly in the case of the autoionizing wavepacket but actually matches better with experimental data in the case of the autoionizing states. We are convinced, however, that there is no significant excitation of $4sNs$ states along with the $4sNd$ states in the experiment due to the fact that we do not see any signal from field ionization of $4sNs$ rydberg

states separate from the $4sNd$ rydberg states when a dye laser used as L2 is scanned over the energy range corresponding to rydberg $N\ell$ states. We are therefore unable to completely explain the lower decay rate for the autoionizing state than what is expected from the MQDT analysis.

3.7 Conclusions

The main result of this experiment has been the detection of the stair-step form of decay of an autoionizing wavepacket and the ability to control decay rates in autoionizing wavepackets by controlling the initial phase of the constituent eigenstates. Since the aim of our experiments is to eventually create and study controlled double rydberg wavepackets, this ability to control wavepacket decay rates allows for the creation of specific wavepackets with the desired properties in an experiment.

We find that the autoionization rate of the autoionizing wavepackets that we measure is in good agreement with the calculations performed using MQDT analysis with the K-matrices. The results of our experiment suggest that a study of the decay rates of autoionizing rydberg wavepackets can provide a more accurate measure of autoionization rates than the measurement of the decay of autoionizing states.

Chapter 4

Experiments in wavepacket dynamics

This chapter describes a few experiments that were attempted following the study of the decay of autoionizing wavepackets described in the chapter3. For various reasons, these experiments were not successful in terms of observing what we had set out to observe. In the following sections, I will be describing three such experiments which had to be abandoned for different reasons. It is possible that the failure of these experiments could have been due to reasons other than any error in the actual physics that we set out to study.

4.1 Double rydberg wavepackets in calcium

The first experiment that was attempted after our success in observing the stair-step decay of autoionizing wavepackets was to see if we could further excite the inner electron into a rydberg wavepacket and thereby create a double rydberg wavepacket. In the previous experiment, we had been able to excite one electron into a rydberg wavepacket and then excite the second electron into a $4d$ state. To excite this $4d$ state into a rydberg state of the ion, we need to provide it with just under 4.8eV through one or more laser pulses. We are also limited by the condition that we would like to perform the excitation process in as few steps as possible to minimize the number of laser sources that need to be simultaneously adjusted to get the experiment to work properly. A set of possible excitation schemes is shown in Fig.4.1.

A possible single laser excitation scheme that could work to create double rydberg wavepackets in calcium could be to excite the $4d$ state of the inner electron directly into a rydberg nf state around $n \sim 60$ with a pulse tuned to $\sim 258\text{nm}$. However, this wavelength is too close to the third harmonic of the fundamental Ti:sapphire pulse but not close enough to be tuned to with a THG(third harmonic generation) crystal. At the third harmonic of the 786nm Ti:sapphire laser pulse, we can excite states around $n \sim 25$ from the $4d$ state of the ion. However, this excitation scheme does not have the range of tunability that we would like to have in creating double rydberg wavepackets. We therefore decided to look at a two-step excitation of a rydberg wavepacket from the $4d$ state.

From the $4d$ state, the inner electron can be excited into a $4f$ state with a pulse

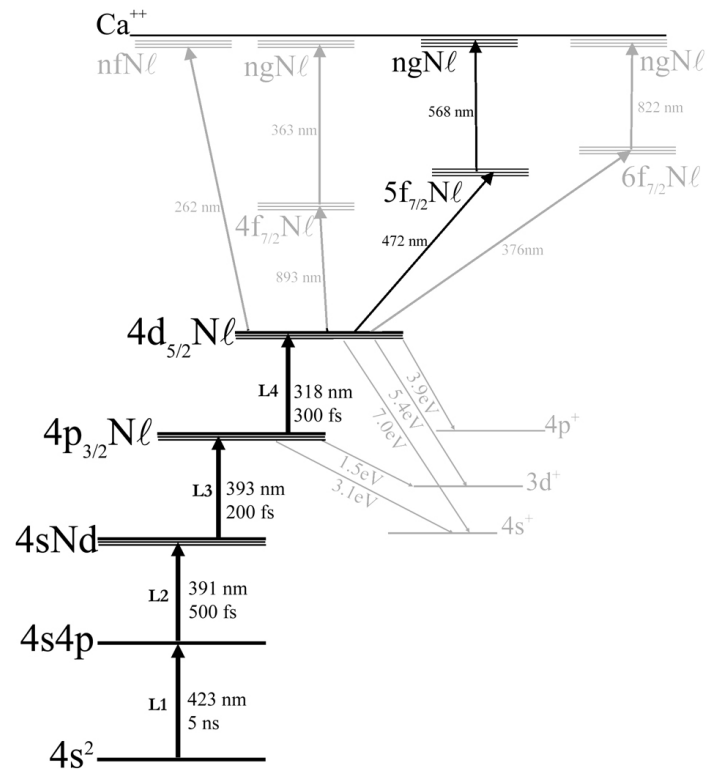


Figure 4.1: Possible double wavepacket excitation schemes in Calcium
 A schematic of the possible excitation schemes that can be used to create double rydberg wavepackets in calcium. The paths that have been shown in light grey are the paths that were not chosen due to technical difficulties that would arise in creating laser pulses of the required wavelengths. The path shown in black is the path that was attempted. An explanation for lack of success in this experiment is described in the text.

tuned to $893nm$ or to a $5f$ state with a pulse tuned to $472nm$ or to a $6f$ state with a $376nm$ pulse. Since these wavelengths are not at any integral fraction of the fundamental Ti:sapphire laser wavelength of $\sim 786nm$, we would need to use OPAs to generate the laser pulse of the required color. However, OPAs are inefficient at producing colors close to but not exactly at the color of the light they are converting from or to integral multiples of their frequencies and this makes it difficult to generate sufficient light with OPAs tuned to $893nm$ or $376nm$ which are not sufficiently far from the fundamental and second harmonic of the Ti:sapphire laser. So we chose to excite the $4d$ state into the $5f$ state of the calcium ion. An OPA was built to generate light at $1180nm$ to be mixed with $786nm$ light to generate the $472nm$ pulse. The $5fN\ell$ states are expected to decay by autoionization by emitting electrons of even higher energy than that from the decay of the $4dN\ell$ states. The idea was to try and observe the electrons from the decay of $5fN\ell$ states to measure the survival probability of $4dN\ell$ states in a manner similar to the measurement of the survival probability of the $4pNd$ wavepackets described in the previous chapter. An attempt to observe signals from the decay of the $5fNd$ states was unsuccessful and so we did some calculations to check if we should have expected to see any signal at all under ideal conditions.

Table4.1 lists transition probabilities for transitions between states in the singly positively charged calcium ion along with the laser wavelengths required to excite the transitions. The transition probability in Ca^+ from the $4d$ state to an nf state is maximum for $n = 4$ by a factor of 100 or more compared to $n > 4$ [112]. In

Table 4.1: Transition probabilities in Ca II [112]

from	to	Transition probability	Wavelength (nm)
$4s$	$4p$	1.439	393.5
$4p$	$4d$	3.396	318.0
$4d$	$4f$	6.6×10^{-1}	893.0
$4d$	$5f$	4.143×10^{-3}	472.2
$4d$	$6f$	3.753×10^{-3}	375.9
$4d$	$12f$	4.273×10^{-3}	279.1
$4f$	$5g$	6.943×10^{-1}	989.3
$4f$	$12g$	1.491×10^{-2}	405.8
$5f$	$6g$	1.772×10^{-1}	1816.3
$5f$	$12g$	1.251×10^{-2}	681.8
$6f$	$7g$	5.935×10^{-2}	3009.3
$6f$	$12g$	8.672×10^{-3}	1081.9

comparison, the $4p-4d$ transition is a factor of 2.4 greater than the $4s-4p$ transition and a factor of 5 more than the $4d-4f$ transition. This has to be considered with the fact that the signal available to us from the decay of the $4d_{5/2}Nd$ wavepacket was of the order of 100mV at the maximum signal level. We need a signal level significantly greater than the noise level of around 2mV to be able to distinguish the signal from the noise.

The factor of 800 difference between the transition probability of the $4p - 4d$ and the $4d - 5f$ transitions meant that we would have to increase the observable signal level from the decay of the $4dNd$ states by a factor of at least 20 to be able to see any signal from the decay of the $5fNd$ states. However, this would still be insufficient because we would eventually like to excite the inner electron into a much higher rydberg wavepacket. To choose an excitation scheme going along a path of transitions with the highest probability would mean increasing the number of lasers needed to excite the double wavepacket as well as increasing the intensity in all the lasers. In the face of these concerns, we decided to abandon this scheme of excitation to create a double rydberg wavepacket in calcium.

At the time of this experiment, the Ti:sapphire laser was required to be tuned to a central wavelength between 785 and 795 nm due to other experiments which made use of the same laser beamline. Moreover, two of the initial steps in our excitation scheme make use of the second harmonic of the Ti:sapphire laser around 393 nm. In the absence of such a consideration, the $4d - 4f$ transition or the $4d - 6f$ transition might be made more accessible by choosing a suitable central wavelength of the Ti:sapphire laser. One of the reasons for abandoning this excitation scheme was the requirement of a greater number of lasers than we were prepared to use. If this is not an issue, it might be possible to create double rydberg wavepackets in calcium in this manner.

However, in all of the possible excitation schemes that we have looked at in calcium to create double rydberg wavepackets, the overall transition strength from the $4d$ to

an ng rydberg state in the calcium ion through any path is almost a factor of 1000 weaker than the $4p-4d$ transition which essentially puts the condition that one would need a significantly greater measurable signal from the decay of the $4dNd$ states to be able to detect the electron decay signal from $ngNd$ double rydberg wavepackets.

4.2 Autoionization suppression through wavepacket interference

Another of the experiments leading directly out of the observation of stair-step decay in autoionizing wavepackets was to see if we could observe interference effects between wavepackets producing suppression or enhancement of autoionization. The idea is that if we can excite one electron into a coherent superposition of two radial rydberg wavepackets with some time delay between them such that the wavepackets return to the core at the same time, it might be possible to choose the phase of the wavepackets in a manner such as to suppress autoionization even when the inner electron is in an excited state.

The excitation scheme that we used was to excite two different radial $4sNd$ wavepackets in calcium with some time delay between them corresponding to the difference in the Kepler period of their orbits so that both wavepackets return to the core simultaneously. The coherence between the laser pulses is expected to be transferred into the two wavepackets to produce interference between the wavepackets when they come together at the core. The second electron is excited into the $4p$ state

at some delay after the excitation of the two wavepackets. The survival probability of the coherent superposition of the two autoionizing wavepackets that results is measured by monitoring the probability of excitation from the $4p$ to the $4d$ state for the inner electron in an identical manner to what has been described in chapter 3.

In the absence of the second radial $4sNd$ wavepacket, the decay of the single autoionizing $4pNd$ wavepacket would follow the stair-step decay pattern observed in the previous chapter. However, in the presence of the second wavepacket, interference effects can result in a change in the survival probability of the autoionizing wavepackets depending on the delay between exciting the radial wavepackets over a very small range of delays when the two wavepackets return to the core almost simultaneously and in a coherent manner. Our experiment is to try and observe this variation in the time-dependent survival probability of the autoionizing wavepackets in the form of enhancement or reduction of the autoionization rate at the time when the two coherent wavepackets return to the core.

Different methods were used to create the two coherent wavepackets and two of these methods are shown in Fig.4.2. The experiment required adjusting the path difference between the two pulses creating rydberg wavepackets in steps that were a fraction of the pulse wavelengths of around $391nm$. It also requires the wavepackets to return to the core simultaneously so the delay between the two pulses had to be adjusted precisely after measuring the kepler periods of the two wavepackets that we produced. However, the major problem plaguing this experiment in both schemes of creating the two wavepackets was that once the $786nm$ pulse was split into the

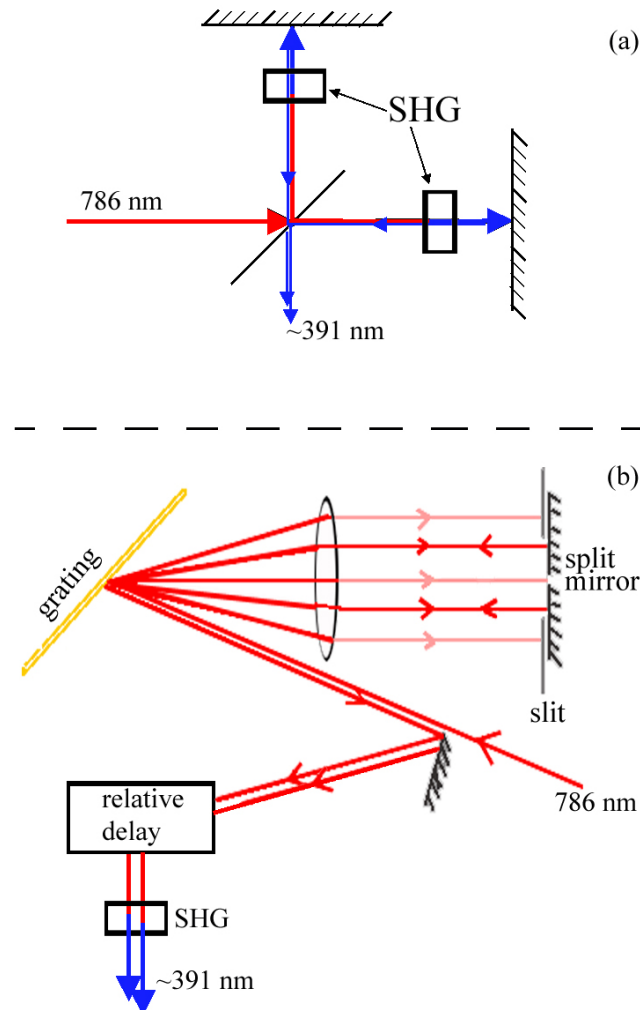


Figure 4.2: Two methods of creating coherent pulses tuned to different wavelengths. The two figures show schematics of the methods used to create two coherent pulses tuned to slightly different central wavelengths to create coherent wavepackets. In method (a), a Michelson interferometer configuration is used with two KDP crystals used to produce SHG at slightly different wavelengths in the two arms of the interferometer. In method (b), a grating in combination with a cylindrical lens is used to split the short pulse into its different wavelength components and a pair of parallel mirrors introduce slight deviations in the retroreflected beams that are then separated with adjustable delay between the components and then sent through the same KDP crystal to produce SHG centered at different wavelengths.

two parts tuned to different wavelengths, the strength of signal from the decay of the individual wavepackets had decreased significantly so that we were unable to observe clear stair-step decays in the two individual autoionizing wavepackets created through the two arms of the interferometer.

Another method to generate two coherent wavepackets was to replace the split mirror method in Fig4.2 with a single mirror but using a glass slide covering a part of the spectrum to produce the delay between two wavepackets centered at different wavelengths. Here, the problem was that first of all the two wavepackets had to be centered at wavelengths such that they could each produce wavepackets with well-defined stair-step decay (i.e states centered at states between principal quantum numbers 30 and 50). The thickness of the glass slide (after allowing for increased effective thickness by tilting the slide), limited the delay between the wavepackets to between 6 and 10 ps. The spatial width of the expanded spectrum on the mirror corresponding to the wavelengths required to produce wavepackets with the required characteristics was not wide enough to be cleanly separated by the use of the glass slide. It is possible that with the use of a wider mirror and greater spatial separation of the wavelengths, this method could produce interfering wavepackets.

In addition to having a strong signal, the requirement that the two wavepackets be coherent with each other requires the two beams producing the wavepackets to be coherent over the entire interaction region since we are trying to transfer the coherence between the light pulses to the wavepackets. The beam profile of the Ti:sapphire pulses at the time of this experiment was not very uniform at the place

where it was being used to create SHG with the result that the wavefront of the pulses was curved resulting in circular interference patterns between the pulses (instead of uniform bright or dark depending on the delay). To maintain the coherence between the pulses, only the part of the beams producing a single fringe pattern are allowed into the interaction region through the use of an aperture (so that the maximum path difference between different parts of the pulse does not exceed the central wavelength of the pulse). This is also one of the reasons for the decrease in signal size from the decay of the autoionizing wavepackets.

The experiment to observe interference between two autoionizing wavepackets was abandoned for all the reasons described above that led to an insufficient signal to noise ratio for the effects we needed to observe. It might be possible to get better results with this experiment if the intensity of the laser pulses can be improved significantly as well as by using a precise translation stage to introduce small delays between the beams producing the radial wavepackets.

4.3 Wavepacket creation by off-resonant ICE

A third experiment that arose out of the study of the decay of autoionizing wavepackets was to try and create autoionizing wavepackets starting from a rydberg state by using strong off-resonant ICE [79,93,114]. A $4snd$ rydberg state is excited in calcium using long pulsed lasers. The rydberg electrons in the excited state do not have a well-defined position in space around the core as a function of time. At some time

after the excitation of the rydberg state, a short laser pulse tuned below the $4s - 4p$ resonance of the calcium ion is applied to the excited rydberg state atoms. At the $4s - 4p$ resonance, we would expect the creation of $4pnd$ states while the rydberg electron is far from the core. However, when the rydberg electron is close to the core, there is a shift of the resonance for the excitation of the inner electron due to core polarization by the nearby rydberg electron [79,93]. We would like to make use of this shift in resonance to excite only the fraction of the total two-electron wavefunction corresponding to the outer electron being near the core and affecting the transition.

Electrons in the rydberg state spend most of the time far from the core. We can therefore expect only a small fraction of the atoms in the ensemble of excited atoms to have the rydberg electron close to the core over the duration of a short-pulse ICE (significantly shorter than the Kepler period of the electron orbit in the rydberg state). If the ICE pulse is on resonance, the autoionizing state that we create would decay in a manner identical to that measured by Thoma [106]. However, if we excite only a small fraction of the atoms with the rydberg electron close to the core off-resonance, the excitation spectral amplitudes are the off-resonant part of the spectral amplitudes shown in Fig3.10 . If this occurs in a coherent manner with all the atoms, we expect the creation of a wavepacket starting from the core with the energy of the rydberg electron shifted from the energy of the rydberg state that was initially excited by an amount equal to the shift in energy of the off-resonant ICE from resonance. In this case, the decay of the autoionizing wavepacket would show stair-steps in a manner similar to what has been observed in the previous experiment.

The motivation for this experiment was the possibility that if we could create wavepackets in this manner, we would need one less short pulse to create the autoionizing wavepacket. This could give us more options in choosing an excitation scheme to create double rydberg wavepackets compared to the case in the previous chapter.

Like the other experiments described in this chapter, this too suffered from a low signal level. As can be seen from Fig3.10, the excitation amplitude falls off rapidly as we excite the inner electron off-resonance. To avoid direct resonant ICE that can produce autoionizing states, the laser producing off-resonant ICE (L3 in Fig3.2), needs to be tuned far from ICE transition. The further we tune this laser off-resonance, the weaker is the excitation amplitude. To create a well-defined wavepacket, the bandwidth of this laser (L3) has to be reduced and this produces further reduction in the energy of the pulse available for off-resonant ICE. The reduction in bandwidth of the pulse producing off-resonant ICE was done in practice by blocking the part of the spectrum producing to resonant ICE in the setup used for controlling laser bandwidths(Fig3.5). All these factors contribute to reducing our effective signal levels.

One way of overcoming the problem of the low signal level is to increase the power in the laser used for off-resonant ICE. Another method would be to operate the Ti:sapphire laser at a wavelength such that the peak of the SHG is off-resonant from the resonant 4s-4p ICE transition in calcium. At the time of this experiment, this could not be done as the Ti:sapphire beam was being used for another experiment in calcium that required the resonant ICE transition.

Chapter 5

Double Rydberg Wavepackets in Barium

5.1 Introduction

In this experiment, we study the dynamic behavior of the two electrons in a DRW as the highly excited atom autoionizes. We can vary the delay between exciting the two wavepackets and we can also control their initial energies. The decay products of the autoionization are analyzed as a function of the initial state distributions of the wavepackets as well as the delay between the creation of the two wavepackets. The technical difficulties faced in the creation of DRWs in calcium forced us to look for other elements that could be used for this purpose. The choice is among the alkaline-earth elements where we tried to find suitable excitation schemes to create double rydberg wavepackets.

Barium (atomic number: 56, ground state electronic configuration: $[Xe]6s^2$) is an alkaline earth element with two valence electrons. The first ionization limit of barium lies 5.2 eV above the ground level ($6s^2$) energy while the double ionization limit lies 15.2 eV above the ground level. The energy levels in barium have been well documented [115, 116, 117, 118, 119] and there are several pathways available for exciting rydberg states and wavepackets with visible lasers both in Ba and Ba^+ . For all these reasons, we have chosen to work with barium to create double rydberg wavepackets.

We have attempted two different methods of creating DRWs in barium. The first effort described in this section had to be abandoned for reasons that are explained below. The second method of exciting the double rydberg wavepacket has been successful and the rest of the chapter from the next section onwards describes that experiment along with the results of our study.

In light of the fact that the problems with creating double rydberg wavepackets in calcium arose out of an inability to create ionic Rydberg wavepackets, initial experiments with barium were aimed at creating ionic Rydberg wavepackets. In experiments to study multi-photon double ionization of barium over a decade earlier [113], some multiphoton resonances had been observed in the Ba^{++} spectrum which had been identified as corresponding to ionization occurring through ionic Ba^{+*} Rydberg states.

The first attempt at creating ionic wavepackets in barium (Fig 5.1) was made by focussing short 300 fs pulses from an OPA tuned to 532 nm. The beam from the

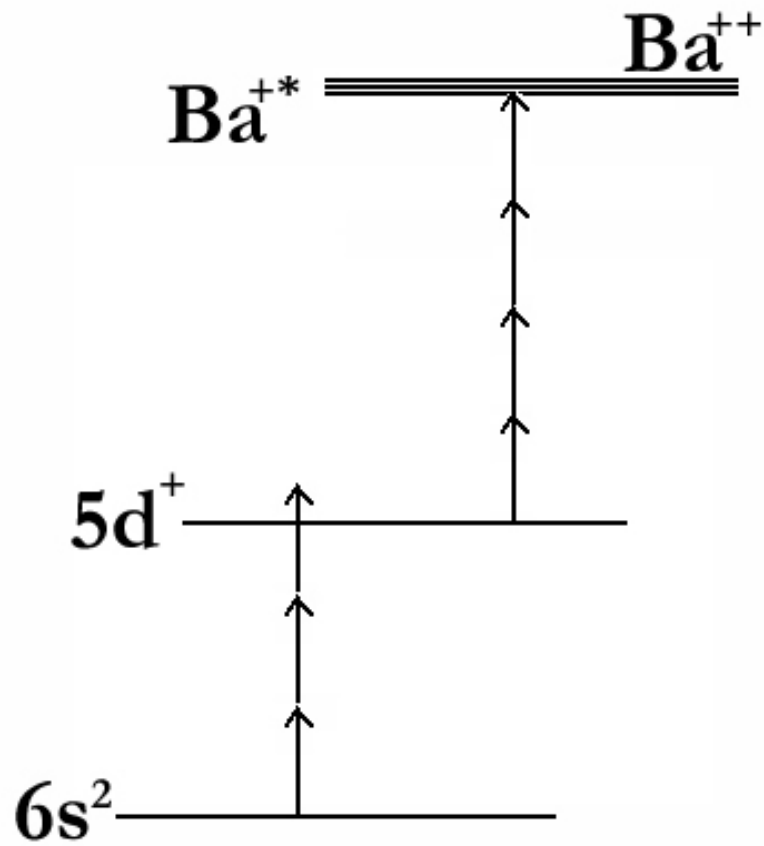


Figure 5.1: Excitation scheme to create ionic rydberg wavepackets in Barium by multiphoton excitation

OPA was focussed with a 5 cm converging lens to utilize multiphoton ionization of barium to create ionic rydberg wavepackets. This method of creating ionic rydberg wavepackets had the disadvantage that it was very hard to calibrate the wavepackets. Among the methods that were tried to calibrate the wavepackets were to look for Ramsey interference between the wavepackets and time-dependent half-cycle pulse ionization of the wavepackets.

The idea behind using wavepacket Ramsey interference to identify wavepackets is that when two identical pulses separated by some time delay are incident on an atom, both pulses can excite wavepackets in the atom and produce an interference between the wavepackets [105, 120, 121]. Since the wavepackets can only be excited when the electron is near the atomic core, the interference pattern is also modulated by the Kepler period of the wavepacket. The rms value of the interference waveform is also equivalent to the autocorrelation of the wavepacket with itself. A Fourier transform of this autocorrelation signal gives the excitation spectrum for the wavepacket [121]. This method of identifying the wavepackets did not succeed because of an inability to precisely control the path difference between the two arms of the interferometer and also limit the bandwidth of the laser pulses to excite a good wavepacket. The 7-photon process (a 3-photon step to ground state of ion plus a 4-photon process to create ionic rydberg wavepacket) at 530 nm requires the delay lengths to be controlled to within a fraction of the effective wavelength ($(530/4) \sim 132$ nm). This requirement in combination with the fact that the ionic rydberg state signal had a bad signal/noise ratio, led us to abandon wavepacket interference as a method of identifying the ionic

rydberg states.

Another method that was attempted as a means of identifying the ionic rydberg wavepackets was to use time-dependent half-cycle pulse ionization of the wavepackets [122]. The principle utilized here is to use the impulsive momentum retrieval method [123] to measure the instantaneous momentum of the wavepacket as a function of time and use the expected periodicity in wavepacket motion to identify the wavepacket. There was no significant difference observed in the voltage levels to produce HCP-ionization for different wavepackets excited by the multi-photon process. It is likely that the bandwidth of the pulse was too high or the AC stark shifts [124] during the pulse were too large to create a good localized wavepacket and so this method of exciting ionic rydberg wavepackets was discarded.

The excitation scheme and the experiment that has been successful in creating double rydberg wavepackets is described in the following sections.

5.2 Excitation Scheme

A study of the energy levels in barium revealed a possible excitation scheme for creating double rydberg wavepackets that could be accomplished by using just two OPAs together with the fundamental and second harmonic of the Ti:sapphire laser as well as a dye laser. The double rydberg wavepackets are excited in two main stages. In the first stage, we use a two-step excitation to create a rydberg wavepacket in one electron. The next stage is a two-step ICE (isolated core excitation) to excite the

second electron into an ionic rydberg wavepacket while the first electron is far from the core.

The position and velocity of the first electron at any time is known from the knowledge of its excitation spectrum or from the time-dependent decay of the wavepacket if it is an autoionizing wavepacket. An electron excited into a radial rydberg wavepacket leaves the core radially and returns periodically with a characteristic period determined by its central energy. In our excitation scheme, we excite an autoionizing wavepacket that can be probed by ICE of the inner electron to identify the rydberg wavepacket by the periodic change in autoionization rate when the rydberg electron returns to the core [103, 106, 125]. We can choose the energy of excitation of the second electron to control its initial velocity at the time of excitation. The delay of the ICE pulses that excite the second electron is adjusted to choose the position of the first electron when the second electron is excited. Thus, we can have very good control over the initial compositions and velocities of both the electrons in the double rydberg wavepacket.

The first rydberg wavepacket is excited in a two-step process. The ground state $6s^2$ is pumped into the $5d(^2D)6p$ state by a 350.2 nm, 5 ns pulse. This pulse is generated by mixing the 522 nm output of a dye laser (Coumarin 485 dye in 350mg/l solution in methanol pumped by third harmonic of a Nd:YAG laser) with the Nd:YAG fundamental at 1064 nm in a 3 cm KDP crystal. A 0.6-1 ps pulse from an OPA tuned to ~ 525 nm is used to excite $5d_{5/2}N_1d$ wavepackets with $N_1 \sim 33$. The OPA (henceforth referred to as OPA1) is pumped by 200 fs pulses from a Ti:sapphire laser

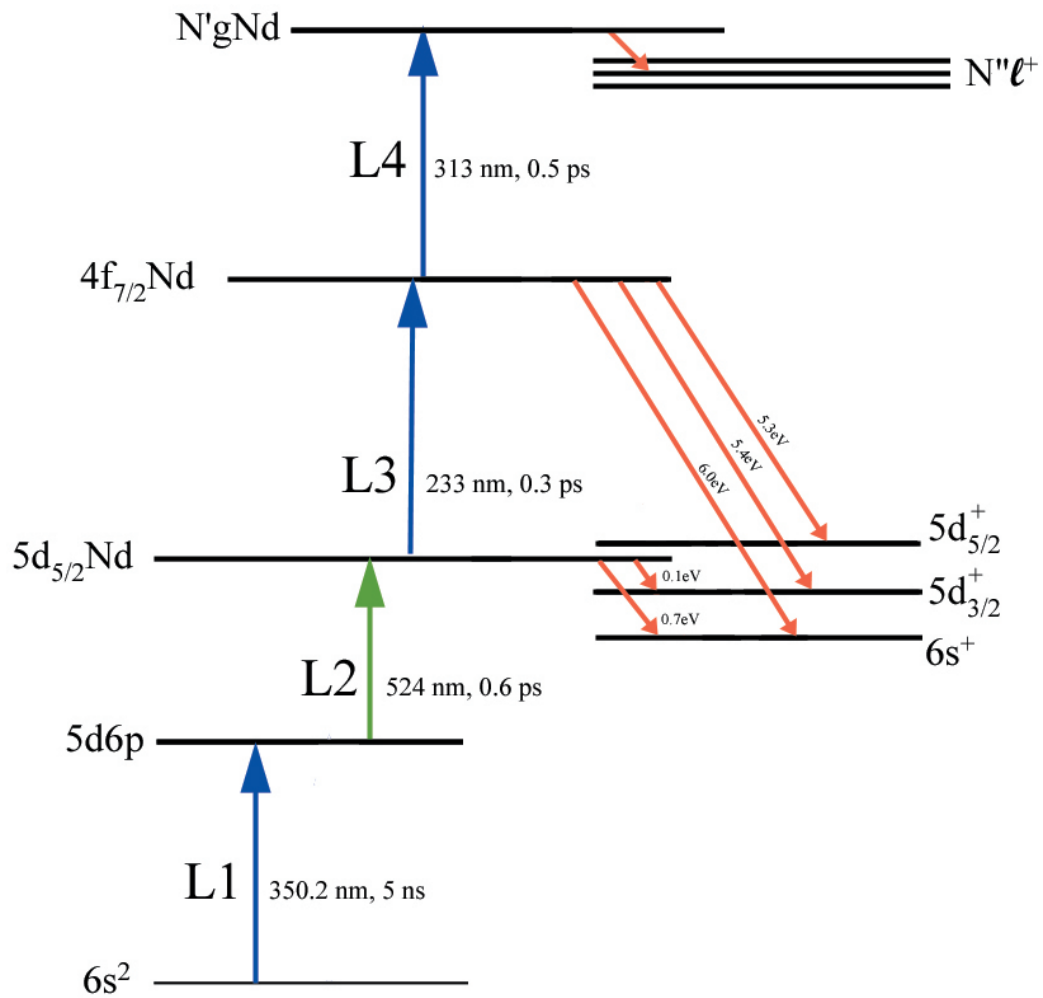


Figure 5.2: Excitation scheme to create double rydberg wavepackets

tuned to 770 nm.

The $5d_{5/2}N_1d$ wavepackets with energies above the $6s^+$ and $5d_{3/2}^+$ ionization limits in barium autoionize rapidly after excitation with each return of the rydberg electron to the core. For a wavepacket centered around $N_1 \sim 33$, this corresponds to ~ 5 ps. We have a short time window of about 10-15 ps after the excitation of the first wavepacket during which we can excite the second electron into an ionic rydberg wavepacket while the first electron remains bound and localized. A 300 fs pulse at 233 nm is used to pump the $5d_{5/2}$ “inner” electron into the $4f_{7/2}$ state. The 233 nm pulse is generated by mixing the 590 nm output of a second OPA (OPA2) with the 385 nm second harmonic of the Ti:sapphire laser. The 233 nm pulse is immediately followed by a ~ 500 fs pulse tuned to ~ 312 nm to excite the $4f$ electron to an ionic rydberg N_2g wavepacket with principal quantum number $N_2 \gtrsim 50$. This 312 nm pulse is generated by mixing the amplified output of OPA1 with the 770 nm fundamental of the Ti:sapphire laser. The excitation scheme is shown in Fig 5.2.

The doubly excited N_2gN_1d double rydberg wavepackets decay by autoionization into a range of possible $N\ell^+$ rydberg states of the Ba^+ ion which are then identified by field ionization. The delay between L3 and L4 is kept constant in the experiment while the delay between L2 and L3 is varied with a delay stage to control the delay between exciting the two wavepackets. The distribution of $N\ell^+$ rydberg states is monitored as a function of the delay between L2 and L3 to study the effect of varying the initial positions and velocities of the two wavepackets on the autoionization pathway.

5.3 Experimental Apparatus

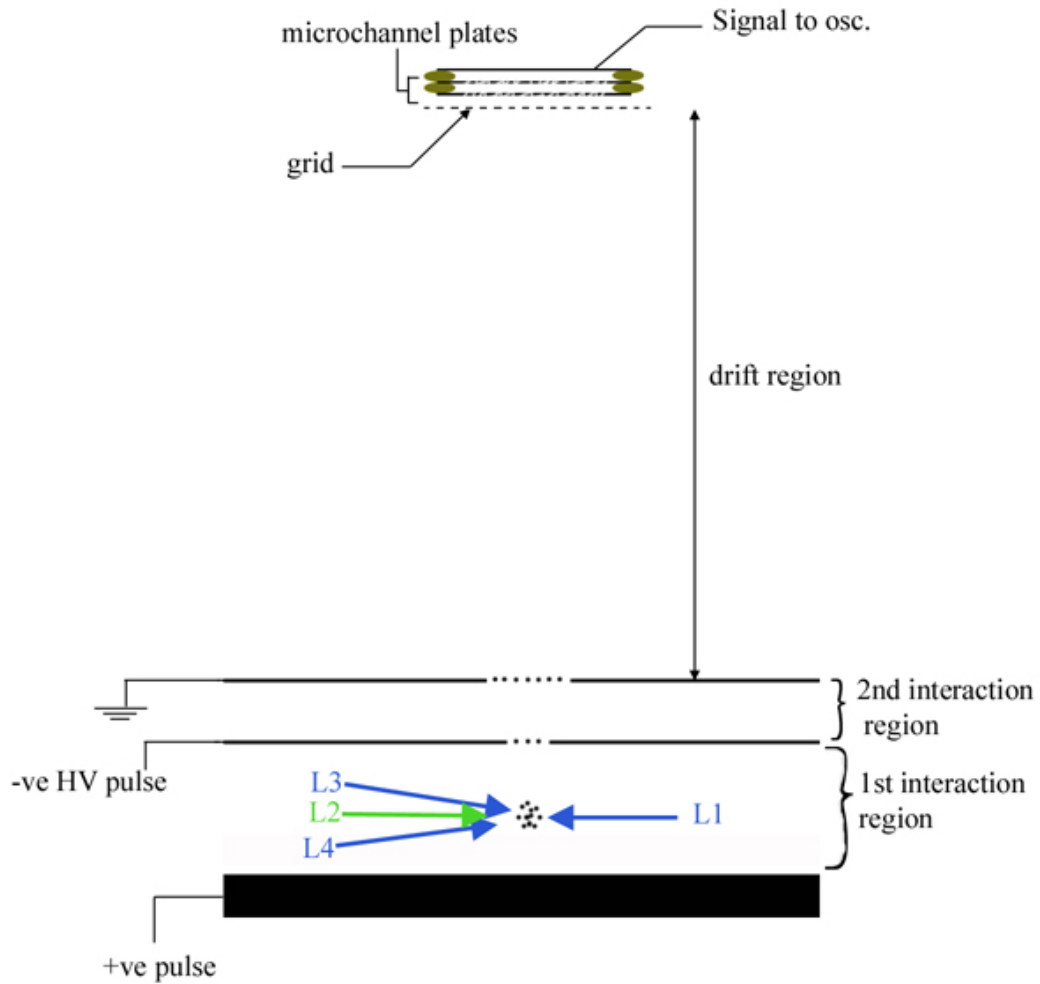


Figure 5.3: Detector schematic for double Rydberg wavepackets in barium

The experimental apparatus used in this experiment is essentially identical to the apparatus described in chapter 2. The main modification in this experiment is the addition of a second interaction region in the detector as shown in Fig 5.3.

The lasers interact with the barium atoms in the first interaction region. After the autoionization of the double rydberg wavepackets, the remaining barium ions are pushed into the 2nd interaction region by a 15V pulse applied on the bottom field plate. A negative 7.5kV/cm field pulse with a rise time of 500 ns is applied through the lower plate in the 2nd interaction region to field-ionize the rydberg states of the barium ion. The electrons released by ionization of the ionic rydberg states are detected by the microchannel plate detector. The grid in front of the microchannel plates is maintained at a $\sim 60V$ potential to provide additional acceleration to the electrons to be detected by the microchannel plates. The upper microchannel plate is maintained at a positive 2kV potential while the lower microchannel plate is biased at $\sim 60V$ through a resistor.

5.4 5dnd autoionizing wavepackets

We begin the study of the double Rydberg wavepacket by looking at the dynamics of the first Rydberg wavepacket. The energy of the $5d_{5/2}N_1d$ wavepacket is higher than the $6s^+$ and $5d_{3/2}^+$ ionization limits of neutral barium. The two electrons can therefore exchange energy by collisional processes to redistribute the energy in favor of a free electron and an ion.

The $5d_{5/2}N_1d$ autoionizing Rydberg wavepacket can decay into the $5d_{3/2}^+$ and $6s^+$ states by emitting electrons with energies of 0.1 eV and 0.7 eV respectively. A short pulse laser at 233 nm is used as a probe to measure the survival probability of the

$5d_{5/2}N_1d$ wavepacket. The 233 nm pulse excites the $5d_{5/2}N_1d$ configuration into the $4f_{7/2}N_1d$ configuration by ICE. The $4f_{7/2}N_1d$ states decay by autoionization into $5d^+$ and $6s^+$ states among others by emitting electrons with energies of 5.3 eV and 6.0 eV respectively. These higher energy electrons are distinguished by time of flight separation from the lower energy electrons released by the autoionization of $5d_{5/2}N_1d$ states. Since the high energy electrons at 5.3 eV and 6 eV can only be emitted by the decay of $4fN_1d$ states, a measurement of the signal strength due to these high energy electrons is equivalent to measuring the probability of excitation of the $4f_{7/2}$ configuration from the $5d_{5/2}$ configuration. If we now vary the delay of the ICE pulse with respect to the time of excitation of the $5d_{5/2}N_1d$ wavepacket and monitor the signal from the high energy electrons, the form of the signal as a function of delay corresponds to the survival probability of the $5d_{5/2}$ state as a function of time [106, 125].

5.4.1 Experimental results and Analysis

Fig 5.4 shows the result of the measurement of signal from the high energy electrons as a function of delaying L3 with respect to L2. We notice that the signal shows a series of steps with widths of approximately 5 ps. In this measurement, all the lasers in the experiment were polarized in the vertical direction. An unexpected result seen by using horizontal polarization is described in a later section.

The features in the decay of the $5d_{5/2}N_1d$ wavepacket can be understood by looking at the problem in a semiclassical manner similar to the case for the decay of $4p_{3/2}N_1d$

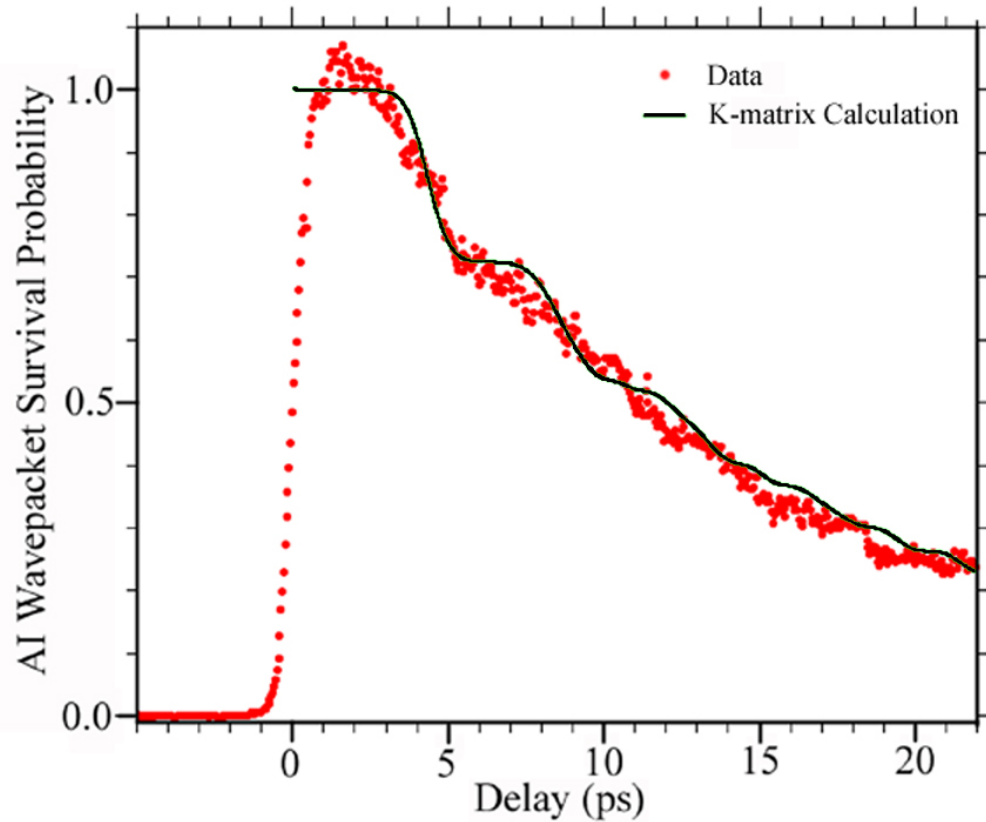


Figure 5.4: Survival probability of $5d_{5/2}33d$ autoionizing wavepackets in barium. The dotted curve represents the normalized, measured signal from higher energy electrons as a function of delay between exciting the $5d_{5/2}33d$ wavepacket and the ICE of the $5d_{5/2}$ to the $4f_{7/2}$ state. The smooth curve represents the K-matrix calculation with the $J=0$ K-matrix for barium near the $5d_{5/2}^+$ limit.

wavepackets in calcium seen in the previous chapter [125].

Autoionization occurs only at times when the two excited electrons are near the atomic core. The Rydberg electron in the $5d_{5/2}N_1d$ wavepacket moves radially outward from the core to its outer turning point and returns to the core in a time corresponding to the Kepler period of an electron with energy $\frac{-1}{2N_1^2}$ in a classical orbit around the positively charged core. This motion of the Rydberg electron results in the autoionization rate varying in the form of a series of spikes separated in time by the Kepler period of the Rydberg electron. The survival probability of the autoionizing wavepacket then displays a series of steps spaced apart by the Kepler period of the Rydberg electron [103, 106, 125]. A measurement of this survival probability as a function of time can then be used to calibrate the average energy level of the wavepacket.

The excitation of the $5d_{5/2}N_1d$ wavepackets from the $5d6p\ ^1P_1$ intermediate states can occur into either the $J = 0$ or $J = 2$ channels based on allowed excitation with a linearly polarized laser pulse. However, van Leeuwen et.al [105] observed an absence of direct excitation into the $J = 2$ channels while using the same excitation scheme. We have therefore limited our analysis to include only the $J = 0$ channels in this discussion. The calculations described in the analysis of the experiments were also performed by including $J = 2$ channels but these calculations did not agree as well with the experimental results as the case where we include $J = 0$ alone and are therefore not presented in this work. This could be due to significantly smaller transition matrix elements between the intermediate $5d6p$ state and the final $5dN_1d$

channels of $J=2$ in comparison to $J=0$ [105].

The autoionizing $5d_{5/2}N_1d$ states are degenerate with the $5d_{3/2}\epsilon\ell$ and $6s\epsilon'\ell$ continuum states. The total wavefunction of the electron over the range of energies in the $5d_{5/2}N_1d$, $J = 0$ wavepacket is then a linear combination of the bound $\phi_1(E) = (5d_{5/2}\nu(E)d_{5/2})_{J=0}$ and the continuum $\phi_2(E) = (5d_{3/2}\epsilon(E)d_{3/2})_{J=0}$ and $\phi_3(E) = (6s\epsilon'(E)s)_{J=0}$ states. [98, 77]

$$\psi(E) = A_1(E)\phi_1(E) + A_2(E)\phi_2(E) + A_3(E)\phi_3(E) \quad (5.1)$$

where $A_i(E)$ are the energy-dependent spectral amplitudes in the different channels and E is the total energy of the doubly excited states. When the electron is in a continuum channel, it means that the atom is ionized.

We will consider only the population of atoms that are directly excited into the bound $5d_{5/2}N_1d$ channel. The atoms excited directly into the continuum are not further excited into the autoionizing $4fNd$ states whose decay releases the fast electrons measured in the experiment. The use of time-domain spectroscopy in this manner allows us to measure autoionization rates into different channels without the distortions introduced by direct continuum excitation in the form of asymmetric Fano line profiles in the frequency spectra of autoionizing states [127]. After excitation into the $5d_{5/2}N_1d$ wavepacket, the two electrons redistribute the total energy between them over time and are no longer confined to the bound channel. As a function of time, the population decay rate of atoms from the bound channel into the two continuum channels can then be written as the Fourier transform of the excitation spectrum

Table 5.1: R-matrix for barium $J=0$ near the $5d_{5/2}^+$ limit [98]

$J = 0$	$5d_{5/2}nd_{5/2}$	$5d_{3/2}nd_{3/2}$	$6sns$
$5d_{5/2}nd_{5/2}$	0.0	-0.23	-0.17
$5d_{3/2}nd_{3/2}$	-0.23	0.0	-0.139
$6sns$	-0.17	-0.139	0.0

amplitude in the form:

$$R(t) = \left| \int dE e^{-iEt} A_1(E) \cdot F(E) \right|^2 \quad (5.2)$$

where $F(E)$ is the spectral amplitude of the laser pulse which is taken to have a gaussian energy profile. The excitation spectrum amplitudes into the various channels are calculated using an R-matrix formalism.

The survival probability of atoms in the $5d_{5/2}N_1d$ states as a function of time delay after excitation of the wavepacket is then given by

$$P(t) = 1 - \int_0^t R(t') dt' \quad (5.3)$$

in the same manner as the survival probability of autoionizing wavepackets in calcium is determined in the experiment with calcium [125].

5.4.2 R-matrix Calculations

The excitation spectrum amplitude in the various channels are calculated using MQDT R-matrix parameters obtained from experimental autoionization linewidth

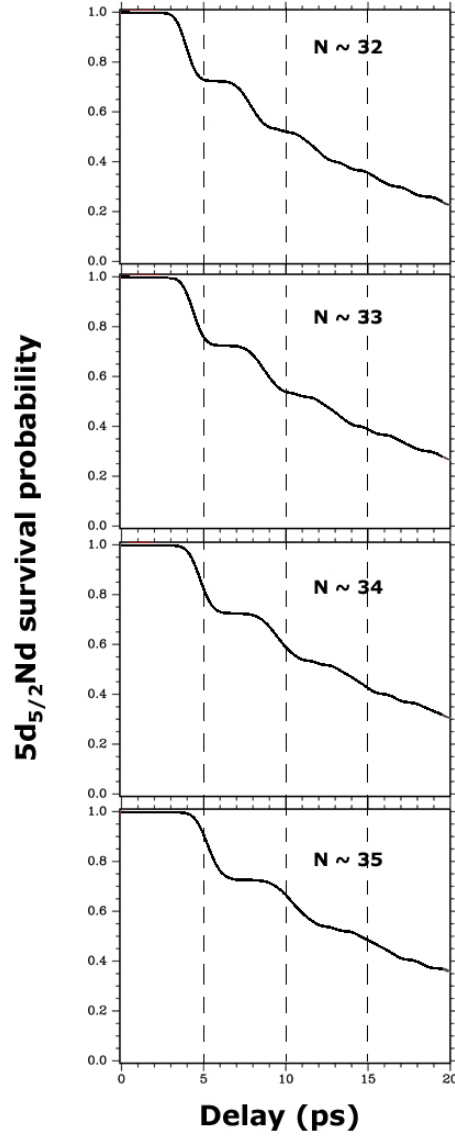


Figure 5.5: Decay of $5d_{5/2}Nd$ wavepackets for different N

The graphs in this figure show the calculated dependence of the decay rates of $5d_{5/2}Nd$ wavepackets with bandwidths of 9 cm^{-1} on the central energy level. The central energy level in the graphs varies from wavepackets centered at $N \sim 32$ to $N \sim 35$. The width of the flat sections of the decay curves is proportional to the kepler period of electrons excited with energy $-\frac{1}{2N^2}$. The dashed lines at 5 ps, 10 ps and 15 ps are to shown to bring out the differences in the decay rates of the different wavepackets.

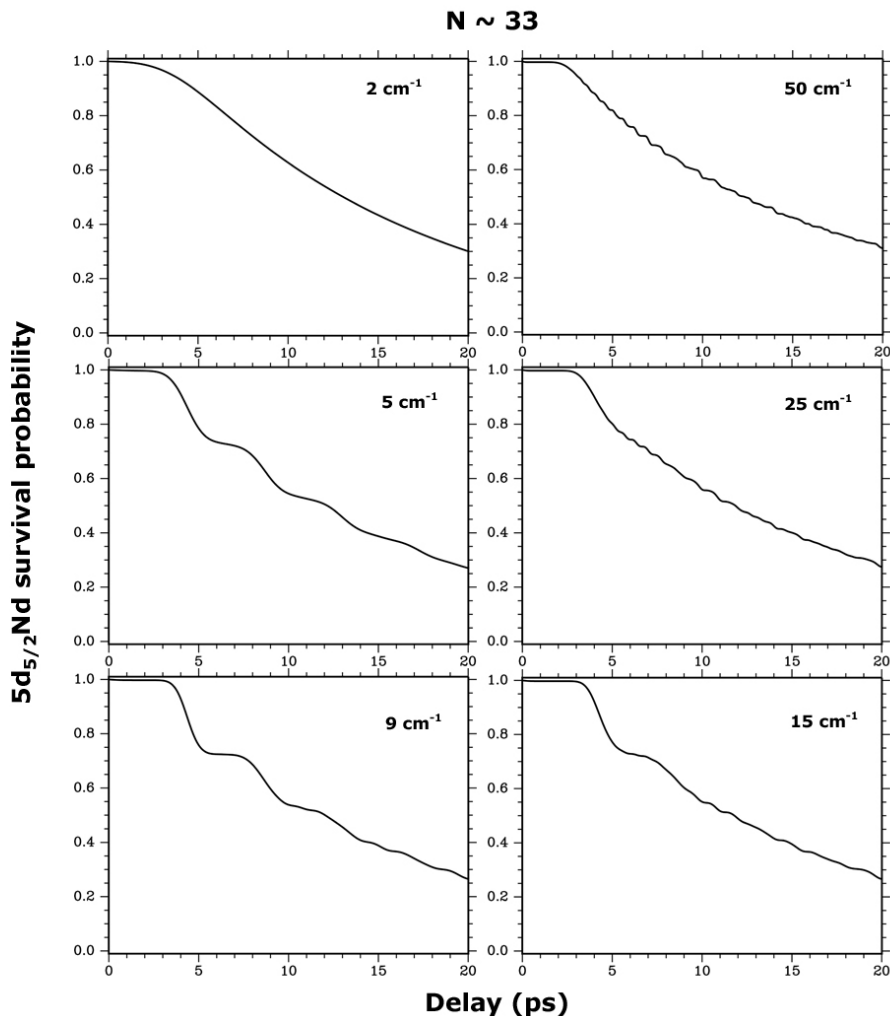


Figure 5.6: Decay of $5d_{5/2}Nd$ wavepackets with different bandwidths
 The graphs here are the calculations that show the effect of changing the bandwidth of the lasers exciting the $N \sim 33$ wavepackets on the decay rates of the wavepackets.

We notice the absence of strong time-dependent features when wavepackets are excited either with very small small bandwidths (small number of states, long pulses, time-dependent features get smeared out) or with very large bandwidths (too many states, fast dispersion of wavepacket). We want the wavepackets to be excited with bandwidths around 10 cm^{-1} to observe strong time-dependent features in the decay of the wavepackets.

measurements by Neukammer et.al [98]. The R-matrix used is given in Table 5.1. The survival probability of the $5d_{5/2}N_1d$ wavepackets is calculated using the R-matrix for different choices of energy and laser bandwidth to determine the best fit to the experimental observations. This calculation is used to calibrate the autoionizing $5d_{5/2}N_1d$ Rydberg wavepacket excited in the experiment. The method of calculation of the wavepacket survival probability using R-matrices is presented in Appendix C as well as in chapter 3. The calculated decay curves for a range of wavepackets excited with different central energies and bandwidths are shown in Figs 5.5 and 5.6.

5.5 Ionic Rydberg states in Ba^+

In the experiment to create double Rydberg wavepackets and then detect the distribution of energy levels of the ions remaining after autoionization, we need to have a reliable method of calibrating the ionic rydberg states. This is achieved by first creating the barium ion in the $5d_{5/2}^+$ state followed by excitation into the $4f_{7/2}^+$ state and then using a tunable, narrow bandwidth, 5 ns pulsed dye laser in place of L4 to excite rydberg states of the barium ion.

The barium ion is created by allowing sufficient intensity of light from the first dye laser(L1) tuned to 350.2 nm to be able to directly ionize the barium atoms in a multiphoton process. The laser L3 tuned to 233 nm then selectively excites $5d_{5/2}^+$ states of the ion to $4f_{7/2}^+$. A dye laser (Rhodamine 640 and DCM in a 1:1 mixture in methanol) pumped with the 2nd harmonic of a Nd:YAG laser is doubled in a 3 cm

KDP crystal and tuned over the range of wavelengths(316.5 nm to 310.5 nm) to excite ionic Ng^+ Rydberg states ($N \sim 27$ to ∞) from the $4f_{7/2}^+$ state.

The ionic Rydberg states are detected using a field ionization pulse in the second interaction region in the detector (see Fig 5.3). The ionic Rydberg states are ionized at different times during the pulse depending on their binding energy. This difference in ionization times during the pulse results in a measurable difference in the time of detection of electrons released by ionization of the different ionic rydberg states. The time of detection of the electrons is calibrated by measuring the signal at different time windows relative to the field pulse as a function of the ionic rydberg state. In practice, this is done by placing several time windows, called ‘gates’, on the signal detected by the oscilloscope and noting the signal level in each of these gates while tuning the dye laser over the range of rydberg states that can be field ionized and detected from the second interaction region. A simultaneous measurement of the transmission of the dye laser through an etalon is used to calibrate the relative energy separations. The number of peaks in the etalon signal between successive energy levels is used to calibrate the absolute energies of the ionic rydberg states by making use of our knowledge of the form of the energy separation between successive rydberg states [128].

Unlike the case of identifying rydberg states in calcium by state-selective field ionization as described in the third chapter, the unique identification of ionic rydberg states based solely on their time of detection is quite difficult. The reason for this is that the charged ions are not stationary in the presence of the rising electric field

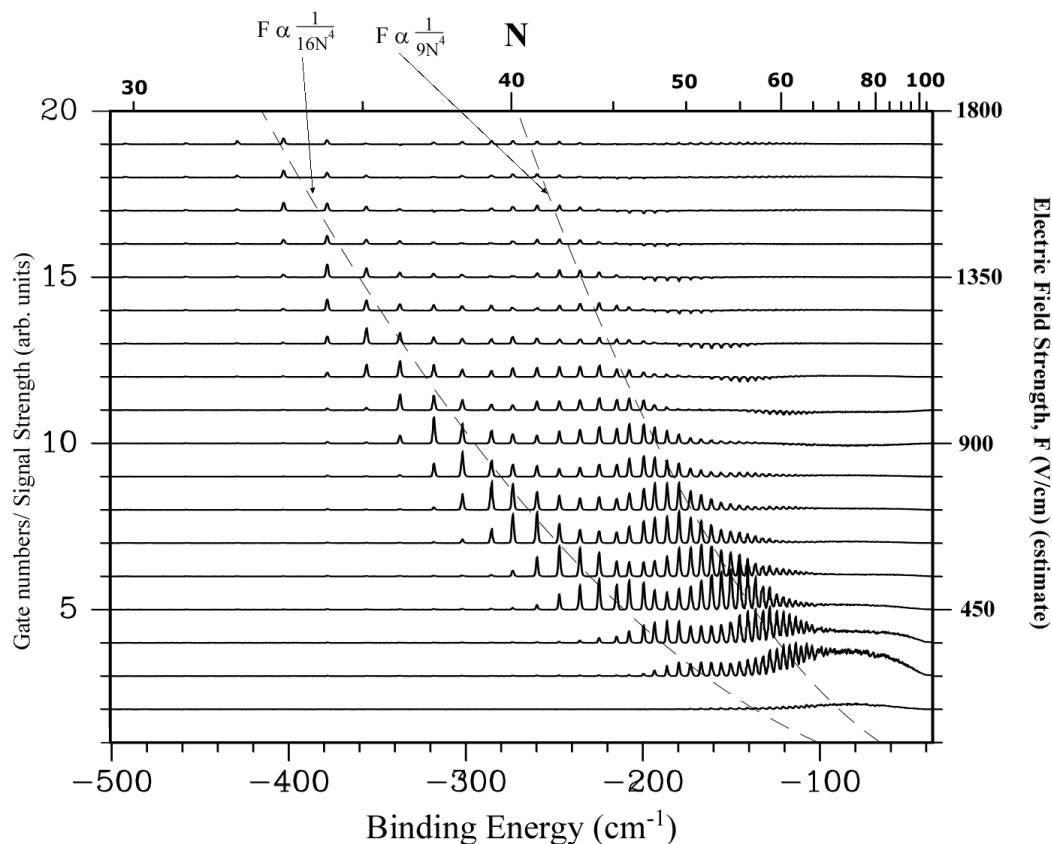


Figure 5.7: Gate calibration for ionic rydberg states

The signals in various gates as a dye laser in place of L4 is tuned over the $N\ell^+$ resonances that can be excited from the $4f^+$ level in Ba^+ . The dashed curves are an attempt to guess the absolute field assuming the two sets of peaks along the curves correspond to diabatic and adiabatic field ionization.

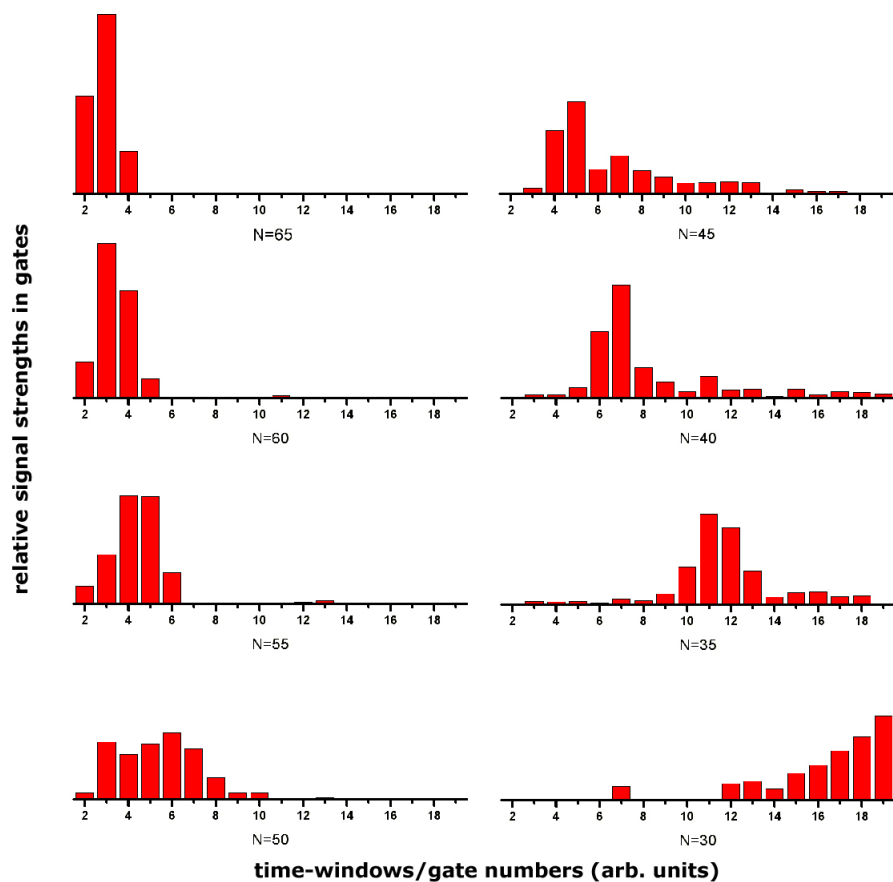


Figure 5.8: Relative signal strengths in the different gates for different ionic rydberg states

The above graphs show the relative strength of signal in the various time-windows/gates used to detect the field ionized ionic rydberg states. Lower numbered gates correspond to signals at earlier times. We see that the relative signal strength in the gates at earlier times are higher for high N and the peak relative signal strength moves towards later times as we decrease N .

ramp. This means that the ionization of the ions in various rydberg states occurs at different times as well as at different positions in the second interaction region. Combined with the spatial extent of the initial double rydberg wavepacket and the spread of the ions as they are moved from the first to the second interaction region, this additional spread in positions of the ions leads to a wide temporal spread in the signal from electrons released by field ionization of the ionic rydberg states. When we apply a negative high voltage on the bottom plate in the second interaction region, the ions that were initially moving upwards are accelerated back down at a varying acceleration rate by the ramped electric field. As ions in different rydberg states get doubly ionized by the electric field ramp, it is possible that electrons released when the ions are on their way upwards arrive at the detectors later than some electrons released when the ions are closer to the upper end of the interaction region and from lower ionic rydberg states. This is a problem since we use the SSFI with the expectation that states from higher rydberg states that get ionized at lower electric fields get to the detector at earlier times. To minimize this effect of electrons released at later times overtaking the electrons released earlier, we use trial and error to adjust the timing of the electric field ramp such that the electrons released by ionization of the highest ionic rydberg states that we can detect arrive at the detector at the earliest time and signals from ionization of the lower energy rydberg states arrive at the detector at later times. We also use a fast electric field ramp rising to the peak value within $1 \mu\text{s}$ so that we can ionize the lower energy rydberg states before they are accelerated out of the interaction region by the electric field ramp.

The spread in the time when a signal is detected at the detector from field ionization of different ionic rydberg states prevents us from using the time of arrival of the electron as a unique identifier of the rydberg state of the ion. Instead, we use the relative distribution of signal levels in the various gates to identify ionic rydberg states. In this method of identifying rydberg states, it is not possible to uniquely identify the component rydberg states and their contributions in an ionic rydberg wavepacket by analyzing the relative signal distribution in the gates but it is possible to get a good estimate of the range of states that are present in the wavepacket.

The relative strength of signal in the gates is calculated by adding together the signals in all the gates and dividing the signal in each gate by this sum. Fig 5.8 shows the relative signal strength in the gates for ionization of different ionic rydberg states.

Fig 5.7 shows the signal levels in each gate as a function of the total energy of excitation of the ionic rydberg states. There are two sets of peaks corresponding to different ranges of N states that have a maximum signal in the same time-windows/gates. Comparison of the principal quantum numbers of the states that have a maxima in different gates (each gate corresponds to a specific time-window and consequently the same electric field), gives us a factor of ~ 1.25 between the higher and lower N states that have a peaked signal at about the same field. This factor is close to the factor of 1.15 corresponding to the ratio of N states ionizing by diabatic or adiabatic field ionization at fields of $\frac{Z^3}{9N^4}$ and $\frac{Z^3}{16N^4}$ respectively [25, 126]. We assume a linear field variation over the time scale ($0.5 \mu s$) of observing the signal on the oscilloscope. The dashed curves in Fig 5.7 represent the best guesses at the field using the two maxima

of the signals in the gates as corresponding to diabatic and adiabatic field ionization. The $5d_{5/2}^+$ ions produced by the first laser have $|m| \leq 2$. The presence of both kinds of field ionization among Ng^+ states could be due to the presence of $|m| = 2$ states which behave more like hydrogen and ionize at fields proportional to $\frac{Z^3}{9N^4}$ while the $m = 0$ states ionize at fields of $\frac{Z^3}{16N^4}$ [25].

5.6 Double Rydberg wavepackets

We have so far excited and identified $5d_{5/2}N_1d$ autoionizing rydberg wavepackets in barium. We have also developed a method for exciting ionic rydberg states from the $5d_{5/2}^+$ state and can identify the ionic rydberg states by noting the distribution in time of the electrons extracted from the ionic rydberg states by time-dependent field ionization. To create double rydberg wavepackets instead of ionic rydberg states, we reduce the intensity of the first dye laser by placing a neutral density filter in the L1 laser beam to reduce the probability of multiphoton ionization of barium by the first laser. The $5d_{5/2}N_1d$ states can now be excited with the output of OPA1. The 233 nm laser pulse is used to excite the $5d_{5/2}N_1d$ states into the $4f_{7/2}N_1d$ states by ICE. Instead of a dye laser used to excite the ionic rydberg states, we use a short 300 fs laser pulse at 313 nm to excite the ionic Rydberg wavepackets by ICE immediately following the excitation of the $4f_{7/2}N_1d$ states. The double rydberg wavepackets created in this manner autoionize rapidly leaving behind the barium ion in an excited state.

After calibrating the ionic rydberg wavepackets, we use the same detection parameters for identifying the range of ionic rydberg states resulting from the autoionization of the double rydberg wavepackets.

The first electron is excited into a $5d_{5/2}N_1d$ rydberg wavepacket with an energy centered at $N_1 \sim 33$. We vary the delay between exciting the first rydberg wavepacket and the ICE pulses that excite the second electron into a wavepacket centered at $N_2 \sim 70$. The relative strength of signal in the different gates from the ionization of the ionic rydberg states is monitored as a function of delay(τ) between the excitation of the two wavepackets. The experiment is repeated with the first electron excited into the same wavepacket but changing the wavepacket excited with the second electron to one centered at $N_2 \sim 50$. These graphs are shown in Fig 5.9. We note that the relative signal strength in the lower gates (corresponding to earlier times and hence higher principal quantum numbers) for the $N \sim 70$ wavepacket shows small dips at $\tau = 0$ and at $\tau \sim 5$ ps corresponding to the instant of excitation of the first wavepacket and the Kepler period of the wavepacket at $N_1 \sim 33$. The higher gates show small humps in the relative signal at these times. There is a second hump in relative signal strength in the higher gates at ~ 9 ps corresponding to just under twice the Kepler period but it is much less pronounced than the one at ~ 5 ps. These effects are clearer in case (a) where the second wavepacket is excited into a higher energy range. We also notice an absence of strong time-dependent features in the relative signal strengths in the gates for the case (b) where the second electron is excited into an $N_2 \sim 50$ wavepacket. The use of relative signal strength in the gates instead of the

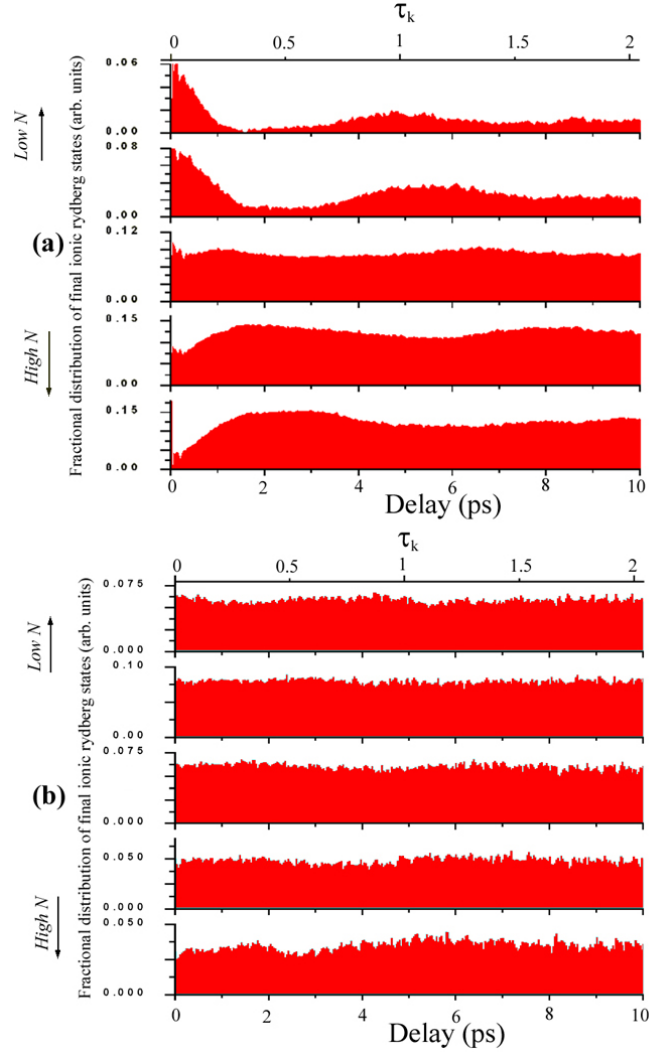


Figure 5.9: Relative signal strengths per gate in experimental data

The relative signal strengths per gate are shown as a function of delay between exciting the two wavepackets in N_2gN_1d double rydberg wavepacket. In both the cases, the first wavepacket is excited into a wavepacket at $N_1 \sim 33$. The second wavepacket is excited to (a) $N_2 \sim 70$ and (b) $N_2 \sim 50$. The different graphs are scaled according to the scales shown on the left.

total signal level allows us to study the effect of different initial conditions of the two wavepackets on the final states without worrying about the effect of the decay of the $5d_{5/2}N_1d$ wavepacket over time.

The decay of the $5d_{5/2}N_1d$ wavepacket changes the total number of doubly excited atoms in the initial double rydberg state as a function of the delay between L2 and L3. The use of relative signal strength in the gates instead of the total signal level allows us to study the effect of the different initial conditions of the two wavepackets on the final state distribution without worrying about the effect of the decay of the $5d_{5/2}N_1d$ wavepacket over time. The experiments have been repeated for different initial wavepackets by changing N_1 and noting that the features scale with the Kepler period of a rydberg wavepacket centered at N_1 . Some examples of data and other experimental details are presented in Appendix A.

The data in Fig 5.9(a) points to a preferential production of final ionic rydberg states with low principal quantum numbers when the two wavepackets are excited simultaneously or at time delays corresponding to the Kepler period of the first wavepacket. It also suggests a preferential production of ionic rydberg states with high principal quantum number when the electrons in the double rydberg wavepacket are excited at times when the first electron is expected to be far from the core.

5.7 Semi-classical Analysis

We can understand the features observed in the experimental data from a semi-classical perspective in the following manner. When the first radial rydberg wavepacket is excited, it has a high probability near the core and evolves in half a kepler period to a high probability distribution of the electron far from the core before returning to a distribution centered near the core at the kepler period. If we excite the second electron into a rydberg wavepacket of the ion at different times, we would expect the two radially localized wavepackets to interact most strongly when they overlap in space. The radial position at which this interaction occurs for the first time depends on the delay between exciting the wavepackets. If the second electron is excited when the first wavepacket is close to the core, the interaction occurs close to the core. On the other hand, if the first electron is near its outer turning point when the second electron is excited, the first interaction between the electrons occurs far from the core. The two wavepackets have different orbital periods and considerable wavepacket dispersion can occur with each overlap of the wavepackets. We can therefore expect any significant dependence of the final state distributions on the delay between the wavepacket excitations to be determined mainly by the first interaction between the wavepackets.

Assuming that autoionization occurs at their first interaction, one of the electrons escapes, leaving the other electron in a bound state with a spatial extent defined by the radial position of the first interaction. In this case, at times close to zero and integral kepler periods of the first electron, excitation of the second electron would

lead to ionic rydberg states with small radial extents corresponding to rydberg states with low principal quantum numbers and therefore from energy conservation, emission of electrons with relatively high energy. In the case where the interaction occurs far from the core, i.e. near half-integer multiples of the Kepler period, we expect to see ionic rydberg states produced with high principal quantum numbers as seen in the experimental data.

The agreement of the experimental data in the case of the $N_2 \sim 70, N_1 \sim 33$ double wavepacket with this seemingly simple physical picture suggests that at least in this case, the most important interaction between the two electrons that determines the eventual ionic rydberg state distribution is the first interaction between the electrons. However, this does not explain why we do not see any time-dependent features in the case where $N_2 \sim 50$ as opposed to the case where $N_2 \sim 70$. In the case where $N_2 \sim 50$, the second wavepacket has a radial extent ~ 1.15 times the extent of the first wavepacket. In the case of the $N_2 \sim 70$ wavepacket, the second wavepacket has a radial extent ~ 2.25 times the radial extent of the first wavepacket. In both these cases, the inner electron is launched into a wavepacket that passes through the first wavepacket on its way out from the core. To understand how the difference in radial extents in the two cases makes such a difference in the time-dependent ionic rydberg state distribution, we can consider a simple semi-classical picture that might be able to explain the features that we have observed.

5.7.1 Sudden Redistribution

The problem of autoionization processes when two wavepackets interact outside the core have been studied by several groups. The dominant process ascribed as the cause of autoionization is the impulsive/sudden redistribution of the rydberg states of the outer electron in a $Z=1$ field to rydberg states in the $Z=2$ field of the ion when the electronic wavepackets pass through each other [129, 132, 130, 131]. The model of sudden redistribution is applied to explain the effect of inner electron ionization (IEI) on the final distribution of ionic rydberg states in the remaining ion [129, 131] and even as a probe of rydberg wavepackets [133].

Our observations can be qualitatively understood by using an impulsive screening model similar to one used by Huang [132]. Initially, the first electron in a rydberg wavepacket has an energy $\frac{-1}{2n_1^2}$. The second electron has an energy just after excitation of $\frac{-2}{n_2^2}$. As a function of radial distance, the potential energies of the two electrons are $\frac{-1}{r}$ and $\frac{-2}{r}$ respectively. The first electron excited into a radial rydberg wavepacket performs radial oscillations about the core in the absence of a second excited electron. When the second electron is excited into a rydberg wavepacket with an orbital radius greater than that of the first electron as we have done in our experiments, it moves away from the core and beyond the radial extent of the first wavepacket. As long as the second electron wavepacket is smaller in radial extent than the first wavepacket, it ‘sees’ a charge of +2 at the core whereas the first electron sees a charge of +1 on the screened core. When the wavepackets cross, the second electron now becomes the outer electron and the first electron becomes the inner electron. Now the first electron

sees a charge of +2 while the second electron sees a charge of +1 on the screened core. If the two electron orbits cross at a distance R from the core, the sudden redistribution approximation suggests that the electrons interchange the effective potential energy for each electron resulting in an exchange of energy equivalent to

$$\Delta E = \left| \frac{-2}{R} - \frac{-1}{R} \right| = \frac{1}{R} \quad (5.4)$$

at the point of crossing.

If this gain in energy by the 2nd electron is sufficient to make it a free electron (i.e. $\frac{1}{R} > \frac{2}{n_2^2}$; $R \leq R_c$; $R_c = \frac{n_2^2}{2}$), the first electron stays bound in an ionic rydberg state of the ion with a radial extent close to the point of crossing. For a given value of n_2 , there is a maximum value of R where it can directly ionize by crossing through the orbit of the first electron. With a sudden increase of the binding energy of the first electron at the point of crossing, the first electron remains bound in a state with a radial extent close to the point of crossing of the electrons. This explains the ionic rydberg state distribution near low N at times near integer multiples of the Kepler period when we expect the first electron to be close to the core. Sudden redistribution causes autoionization only if the radial distance of crossing is smaller than the critical value of R at which the second electron gains sufficient energy to escape from the $Z=1$ binding potential.

On the other hand, if the energy gained by the 2nd electron does not enable it to escape the atom, the two electrons continue to be bound until they can exchange energy again at a later time. However, the evolution of the wavepackets after they cross once without autoionizing is not a regular motion and so there is no fixed

time delay at which the electrons in orbits of all orientations exchange energy. The resultant ionic rydberg state distribution in such a case essentially exhibits no time-dependent character.

In the case of $n_2 = 50(Z = 2)$, the critical radius $R_c = 1250a.u.$ is smaller than the radial extent of the first $n_1 = 33(Z = 1)$ wavepacket, $r_{1_{max}} = 2178a.u.$. In fact, the first electron is present within R_c only for a short time for $t \lesssim 0.6$ ps and near integral multiples of the kepler period, $\tau_K = 2\pi n_1^3$. We cannot resolve the effects over this short interval since the lasers used to excite the wavepackets have a duration of ≥ 1 ps. This explains the lack of any strong time-dependent character in the case of exciting double rydberg wavepackets with $N_1 \sim 33$, and $N_2 \sim 50$.

In the case of $n_2 = 70(Z = 2)$, the critical radius $R_c = 2450a.u.$ is greater than the radial extent of the first $n_1 = 33(Z = 1)$ wavepacket, $r_{1_{max}} = 2178a.u.$. This means that irrespective of the delay between exciting the two wavepackets, the atom autoionizes at the first crossing of the wavepackets and the ionic rydberg state distribution maps the redistribution of the $N_1 \sim 33(Z = 1)$ wavepacket into the $N(Z = 2)$ states at the point of crossing of the wavepackets. In this case, we can see a significant difference in the distribution of final ionic rydberg states as a function of the delay between exciting the wavepackets.

To check the validity of sudden redistribution as the mechanism behind our experimental observations, we have performed a quantum impulse calculation of the expected ionic rydberg state distribution if at different instants during the evolution of the first rydberg wavepacket, the core changes instantaneously from $Z = 1$ to the

$Z = 2$. The result of this calculation is shown in Fig 5.10 together with the result of a classical simulation of the experiment that is discussed in the next section. Since the interaction of the two electrons can produce angular momentum mixing through collisions, the final ionic rydberg state distribution can have a range of possible angular momentum states. The sudden redistribution calculation was performed for different cases of initial and final angular momentum of the $n_1 = 33(Z = 1)$ wavepacket and all of the calculations are qualitatively identical. The main difference between the different cases is that for higher initial angular momentum, the lowest principal quantum number of the ionic rydberg states that remain is spread over a lower range of N but peaked at a lower N than for lower ℓ . This is expected since for higher ℓ , the component of the wavepacket near the core decreases along with a decrease in the radial extent of the wavepacket. The quantum impulse calculation that has been plotted in Fig 5.10 corresponds to the case where we assume an equal contribution from redistribution of states with $0 \leq \ell \leq 30$ in the $N \sim 33$ rydberg wavepacket. The results of the classical simulation presented in the next section are also shown alongside the quantum calculation to show a remarkable similarity in the results obtained by two different approaches to the problem.

If the first wavepacket has a principal quantum number centered at n_1 with $Z=1$, it has a maximum radial extent close to $2n_1^2$ (for $n_1 \gg \ell$). Autoionization by sudden redistribution can happen in this case at all delays of the second wavepacket if R_c for the second electron is always greater than this radial extent. This condition is

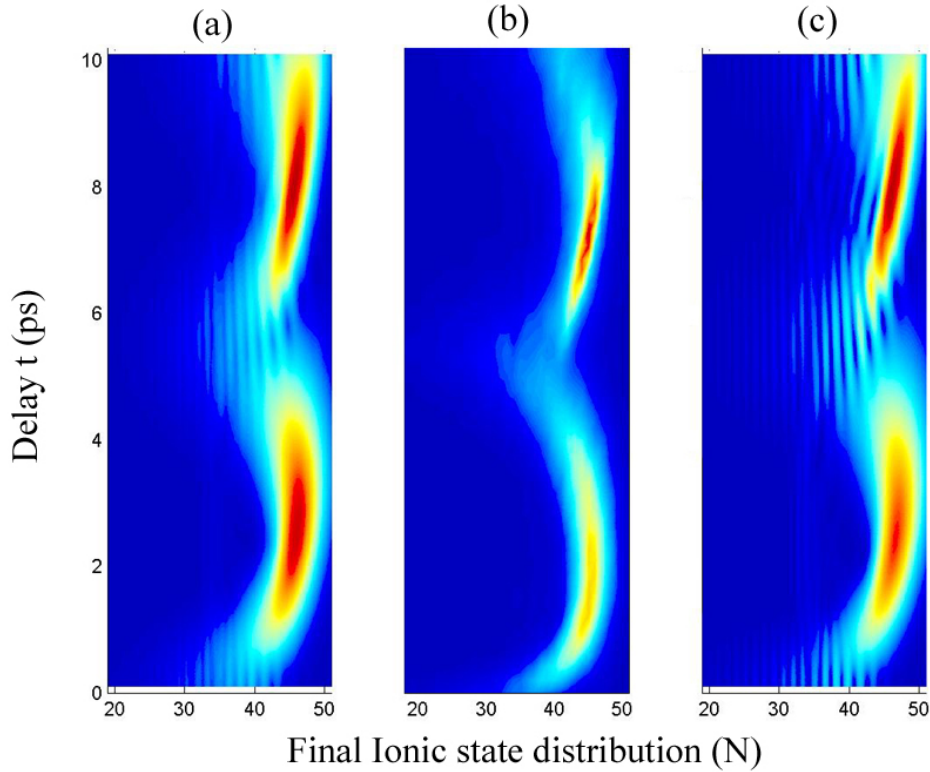


Figure 5.10: Sudden redistribution of an $N \sim 33$ ($Z=1$) wavepacket into $Z=2$. In (a) and (c), the overlap of the ionic rydberg state wavefunctions ($Z=2$) with the time-dependent wavefunction of an $N_1 \sim 33$ ($Z=1$) rydberg wavepacket is plotted as a function of time and N . This is compared to the results (b) from a classical simulation of the two-electron atom excited into a double rydberg wavepacket with $N_1 \sim 33$ ($Z=1$) and $N_2 \sim 70$ ($Z=2$). In the quantum calculation, a uniform distribution of ℓ is chosen from $0 \leq \ell \leq 30$ and added together to form the distribution shown in (a) while in (c) $\ell = 2$ is used for all states. Warmer colors (Red, yellow) indicate greater overlap than cooler colors (green, blue).

satisfied when

$$R_c \geq 2n_1^2 \Rightarrow \frac{n_2^2}{2} \geq 2n_1^2 \Rightarrow n_2 \geq 2n_1 \quad (5.5)$$

Thus, if we excite the inner electron to a rydberg wavepacket centered at a state with ionic principal quantum number more than twice the principal quantum number of the first wavepacket in the neutral atom, the autoionization occurs at the instant of the first interaction between the wavepackets at all delays between exciting the wavepackets and the final state distribution can be qualitatively reproduced using a quantum impulse model.

5.8 Classical simulations

The double rydberg wavepacket states studied in this experiment are in highly excited energy levels close to the Ba^{++} limit. MQDT is valid only in a regime where one of the electrons can be considered to be principally near the core in relation to the other electron [27, 28]. In the case of the double rydberg wavepackets that we have studied, this condition is no longer valid and we need to consider the effect of electron-electron interaction far from the ionic core. Quantum mechanical calculations become prohibitively difficult for doubly excited wavepackets as we need to include a very large number of possible energy levels for the two electrons that are bound as well as the energy levels in the continuum [134]. We have therefore decided to study the doubly excited wavepackets by modelling the system classically.

The fact that both the electrons are excited into rydberg wavepackets allows us to

view the system classically since radial rydberg wavepacket evolution can be modelled as a classical particle (electron) in a central Coulomb force potential. We have used a classical model with two spinless electrons in a central Coulomb potential that are each given initial energies and momenta and allowed to evolve in the combined potential of the central field from a doubly positively charged core and each other. The calculation of the particle trajectories is performed for different initial states and positions of the electrons as well as the delay between exciting the two electrons. The initial energies for the two electrons are chosen according to a gaussian distribution of energy with a bandwidth of 10 cm^{-1} around the central energy of the electrons in the wavepackets excited in the experiment. We have used rectangular cartesian coordinates to do all the calculations and the polarization of the lasers are taken to be along the z-axis. The calculations are performed for different average delays between the two wavepacket excitations. To simulate an experiment, in each set of trajectories (about 3000), the actual delay is chosen as a gaussian distribution with FWHM 0.5 ps around the central delay.

5.8.1 Choice of initial conditions

For the first electron, with an energy E_1 centered around principal quantum number N_1 , the effective principal quantum number for the simulation, n_1 , is calculated (in atomic units) as

$$n_1 = \sqrt{\frac{-1}{2E_1}} \quad (5.6)$$

The initial radial position of the first electron is chosen as the inner turning point of a kepler orbit of an electron with principal quantum number n_1 as

$$r_{1in} = n_1^2 \left[1 - \sqrt{1 - \frac{\ell_1(\ell_1 + 1)}{n_1^2}} \right], \quad (5.7)$$

and the initial velocity for the electron in an orbit with angular momentum $\ell_1 = 2$ as

$$v_{1in} = \frac{\sqrt{\ell_1(\ell_1 + 1)}}{r_{1in}} \quad (5.8)$$

Without loss of generality, we choose the direction of the angular momentum vector to be in the xz-plane and choose the initial orbits of the second electron in relation to this direction. The angle of the angular momentum vector of the first electron, \vec{L}_1 with respect to the z-axis is chosen such that the projection of the angular momentum on the z-axis (referred to as ‘m’) is distributed uniformly between its maximum and minimum values.

$$\vec{L}_1 \cdot \hat{z} = m \quad (5.9)$$

Once the direction of the angular momentum vector is chosen, the position of the first electron is chosen randomly on a circle of radius r_{1in} centered on the origin and in a plane perpendicular to \vec{L}_1 . The direction of the velocity vector is chosen as a tangent to this circle at that point.

The motion of the first electron in the central coulomb field of a charge +1 is calculated using adaptive Runge-Kutta techniques [135] for a time corresponding to the delay between exciting the two wavepackets. The initial energy, E_2 of the second electron is chosen at this time to be in a gaussian distribution around the energy of

an ionic rydberg wavepacket centered at principal quantum number N_2 . The effective principal quantum number of this electron is calculated as

$$n_2 = \sqrt{\frac{-2}{E_2}} \quad (5.10)$$

The initial position and velocity of the second electron with principal quantum number n_2 and angular momentum $\ell_2 = 4$ are calculated as

$$r_{2in} = \frac{n_2^2}{2} \left[1 - \sqrt{1 - \frac{\ell_2(\ell_2 + 1)}{n_2^2}} \right], \quad (5.11)$$

$$v_{2in} = \frac{\sqrt{\ell_2(\ell_2 + 1)}}{r_{2in}} \quad (5.12)$$

Since the projection of the total angular momentum along the common laser axis is zero, the direction of the angular momentum of the second electron, \vec{L}_2 , is chosen to be along a direction vector such that

$$\vec{L}_2 \cdot \hat{z} = -m \quad (5.13)$$

and the projection of \vec{L}_2 on the xy-plane makes an angle with the x-axis that is randomly and uniformly distributed between zero and 2π . The position of the second electron is chosen randomly on a circle of radius r_{2in} centered at the origin and in a plane perpendicular to \vec{L}_2 . The direction of the velocity vector is chosen as a tangent to this circle at that point.

5.8.2 Results

The motion of the two particles under the influence of the central field of the core of charge +2 and of each other is calculated by adaptive Runge-Kutta integration

techniques [135]. The calculations are performed until one of the electrons gains sufficient energy to become a free particle ($E > 0$) leaving behind the other electron in a bound state. The distribution of energies of the bound state electron is noted as a function of the various initial conditions. Using the experimental calibration of signal levels in each gate corresponding to different ionic rydberg states, the results of the classical simulation are scaled to the expected relative signal levels in the same gates that are presented in the experimental data in Fig 5.9. The results of the classical simulation are presented in Fig 5.11.

We find that the results of our classical simulations are strikingly similar to our experimental observations in Fig 5.9.

As in the experiment, for a choice of rydberg wavepackets such that the electrons are excited into states with $N_1 \sim 33$ and $N_2 \sim 70$, the distribution of ionic rydberg states is peaked at states with a low principal quantum number (lower energy) at times when the delay between exciting the electrons corresponds to the Kepler period of the first wavepacket. The state distribution also peaks at states with a higher principal quantum number (higher energy) at relative excitation times near half-integer multiples of the first wavepacket's Kepler periods.

The simulations also predict the observed difference in the form of the distribution of ionic rydberg states depending on the energy of the second electron for a fixed choice of energy for the first wavepacket. We notice the almost total absence of any time-dependent features in the ionic rydberg state distribution if the electrons are excited into $N_1 \sim 33$ and $N_2 \sim 50$.

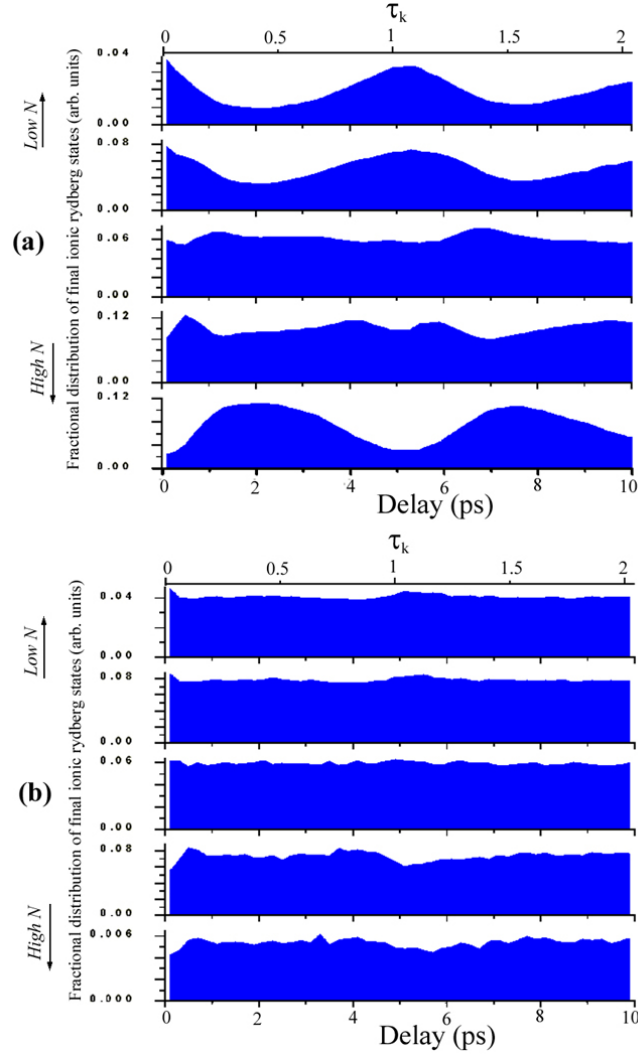


Figure 5.11: Relative signal strengths per gate from classical simulation

The relative signal strengths per gate are shown as a function of delay between exciting the two wavepackets in $N_2 g N_1 d$ double rydberg wavepacket. In both the cases, the first wavepacket is excited into a wavepacket at $N_1 \sim 33$. The second wavepacket is excited to (a) $N_2 \sim 70$ and (b) $N_2 \sim 50$. The scales of the different graphs are shown on the left.

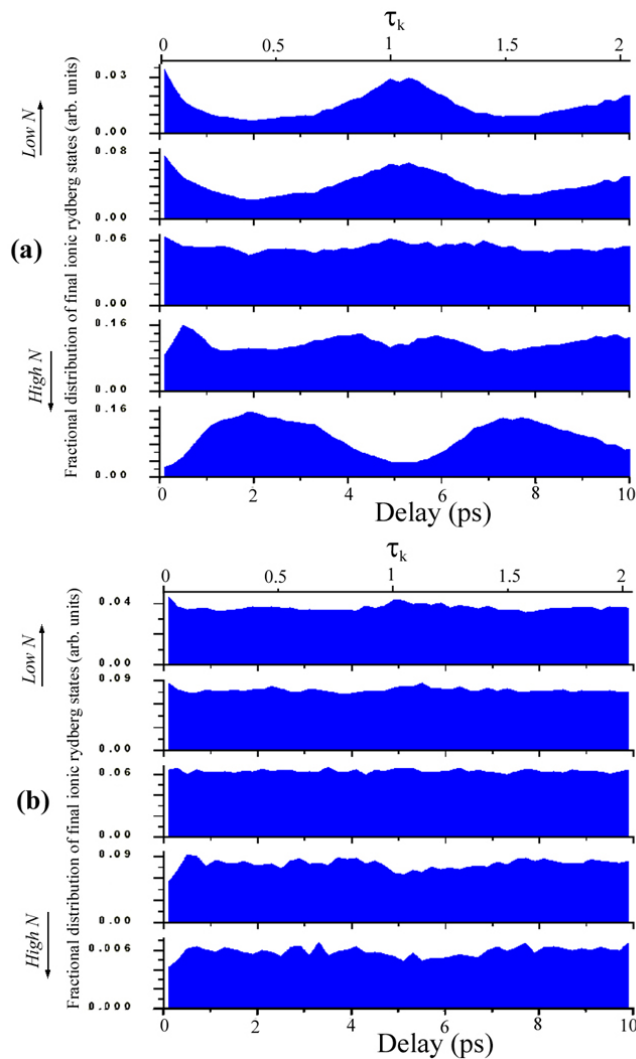


Figure 5.12: Relative signal strengths per gate from classical simulation(B)
 This is identical to Fig 5.11 with the modification that the states with $m < 2$ are assigned to gates with signal along $1/16n^4$ and states with $m > 2$ along $1/9n^4$ in Fig 5.7 to see if it agrees better with the experimental results. We do not notice any significant difference between this figure and the previous one where there is no distinction that is made between states with different m . The scales of the different graphs are shown on the left.

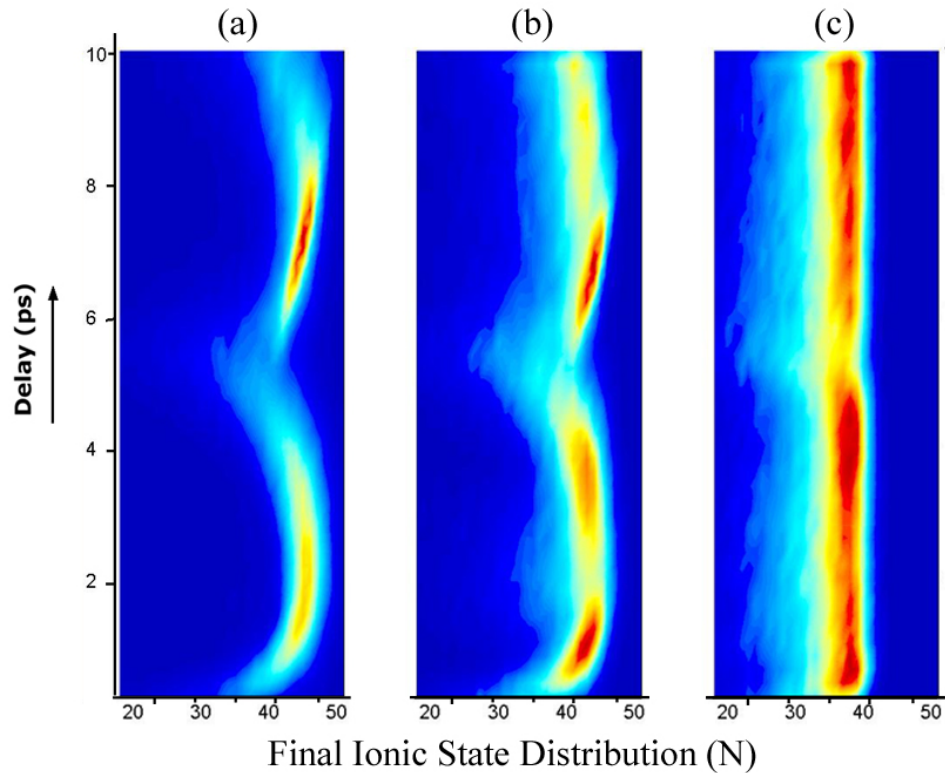


Figure 5.13: Final ionic state distribution

The distribution of final ionic states obtained from the classical simulations as a function of the delay between exciting the two wavepackets when the first electron is excited to an $N_1 = 33$ wavepacket and the second electron is excited into (a) $N_2 = 70$, (b) $N_2 = 60$, and (c) $N_2 = 50$ rydberg wavepackets with laser bandwidths of 10 cm^{-1} in all cases. Warmer colors (Red, yellow) indicate higher probability while cooler colors (blue, green) indicate lower probability.

So far, we have looked at the results of our calculations in a manner that matches with the experimental data. However, there is much more information in the calculations than what is presented in Fig 5.11. A more detailed graph of the distribution of ionic rydberg states as obtained from the calculations is shown in Fig 5.13. This figure shows significant differences in the form of the final state distribution as a function of the delay between the wavepackets for small changes in the energy of the second wavepacket. The simulation with $N_1 \sim 33, N_2 \sim 70$ shows dramatic differences in state distribution with time whereas the simulation with $N_1 \sim 33, N_2 \sim 50$ shows hardly any variation in state distribution as a function of the delay between the wavepackets. The case with $N_1 \sim 33, N_2 \sim 60$ represents an intermediate case. We also note that the maximum N-state of the final ionic rydberg state decreases as we decrease N_2 while keeping N_1 constant. This is due to energy conservation since the total energy of the doubly excited atom is different in the three cases. To just escape from the atom, the second electron needs less energy ($\frac{2}{N_2}$) at higher N_2 and therefore removes less energy from the bound electron, leaving it in a higher energy bound state.

The classical simulations also indicate a spread in the angular momentum of the the final ionic rydberg state. In the experiment, the calibration is performed with ionic rydberg states having $\ell = 4, |m| \leq 2$. According to the classical simulation the final rydberg states after the decay of the double wavepacket have $N > \ell \geq |m| \geq 0$, making the calibration less accurate for large values of ℓ, m . It is therefore not possible to uniquely identify the states present among the ions remaining after the decay of

the double wavepacket. However, according to our simulations, over 70% of the final $N\ell^+$ ionic rydberg states have $\ell < 6$ and the rydberg states we can measure have $N > 30$, which allows us to use the calibration to get a reasonable estimate of the state distributions. In our calibration of the ionic rydberg states in Ba^+ , we have noticed two sets of peaks corresponding to the ionization of the rydberg states by diabatic and adiabatic field ionization at fields of $\sim \frac{Z^3}{9n^4}$ and $\sim \frac{Z^3}{16n^4}$. We expect rydberg states with high m to ionize preferentially along the diabatic path similar to hydrogen [25]. We have therefore scaled the state distribution obtained from the simulations into the different gates depending on whether the states have $m < 2$ or $m \geq 2$. The observation of ionization along the diabatic path for direct excitation of Ba^{+*} rydberg states with $m = 0, 1, 2$ allows us to use $m \geq 2$ as a possible cut-off between diabatic and adiabatic field ionization. This m -dependent scaling does not make any appreciable difference in the relative signal strength between the different gates in Fig 5.12.

5.8.3 Two-electron dynamics from classical simulations

The classical simulations of the two-electron atom also provide a lot of information that we do not measure in the experiment but can be used to gain further insight into the dynamics of the two electrons before autoionization breaks up the atom into an ion and a free electron. In our simulations, we calculate the path of the two electrons from the moment of their excitation until one of the electrons escapes the binding potential of the screened $Z=1$ core. The distribution of radial positions of the two

electrons from the instant of excitation of the two electrons is presented in Figs 5.14 and 5.15 for the cases of exciting the first electron into $N_1 \sim 33$ and $N_2 \sim 50$, and $N_2 \sim 70$ respectively.

We note in the distribution of radial positions of the second electron that it moves far from the core just after excitation and in the case where $N_2 \sim 70$ (Fig 5.15), it continues to move away without returning to the core. This is just as we expected from the semi-classical picture that the sudden impulse redistribution gives the second electron enough energy to leave the atom as a free electron after the first interaction between the electrons. In the case of $N_2 \sim 50$ (Fig 5.14), the second electron returns to the core but it does so over a large range of times so that there is no coherence left among the different paths chosen by the second electron. This contrasts with the first electron which seems to retain its coherent motion for some time after the first interaction between the electrons. The motion of the first electron depends on the position of impact between the electrons at the first interaction. We also note that in the case of $N_2 \sim 50$, the two electrons hang around the core for long times and are released at a slow rate over a long time after the first interaction between the electrons. These long lasting bound states appear in the Fig 5.14 as light green curves that stay close to the origin (left margin for both particles) for a long time (vertical axis in the downward direction). These slowly autoionizing states are discussed in the next section.

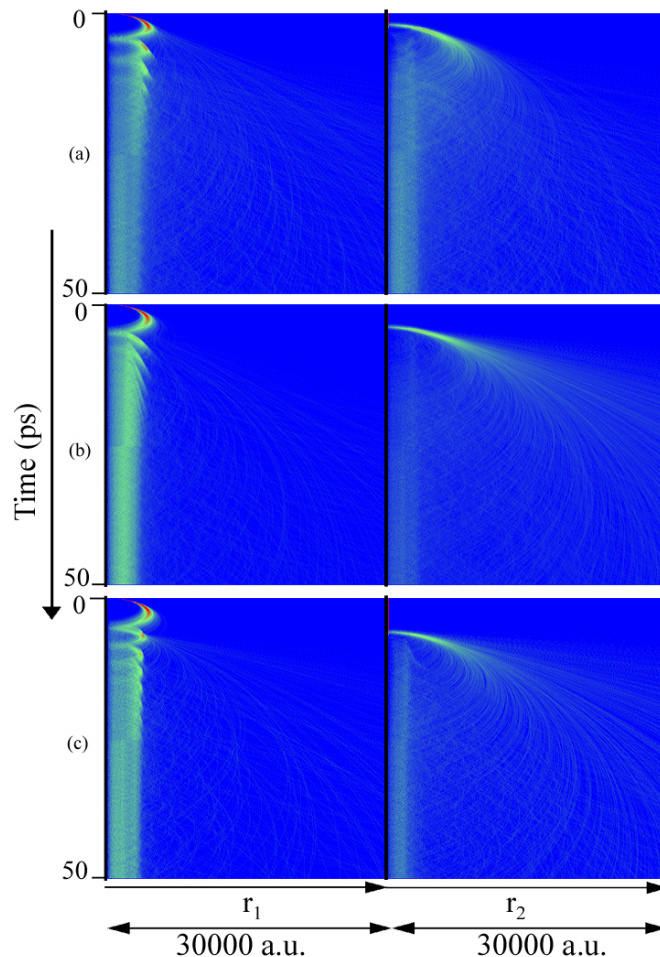


Figure 5.14: Radial positions of electrons in $N_1 \sim 33$, $N_2 \sim 50$ wavepacket. The three figures above show the distribution of positions of the two electrons as a function of time for 50 ps after the excitation of the first electron. The second electron is excited at times (a) 2 ps, (b) 4 ps and (c) 6 ps in the three cases. Warmer colors (Red \rightarrow Green) represent higher probability of finding the particle at a particular position while cooler colors (Blue \rightarrow Green) represent low probability of finding the particle at that position. The figures are split into two halves with the left half representing the distribution of the first electron and the right half representing the second electron's position.

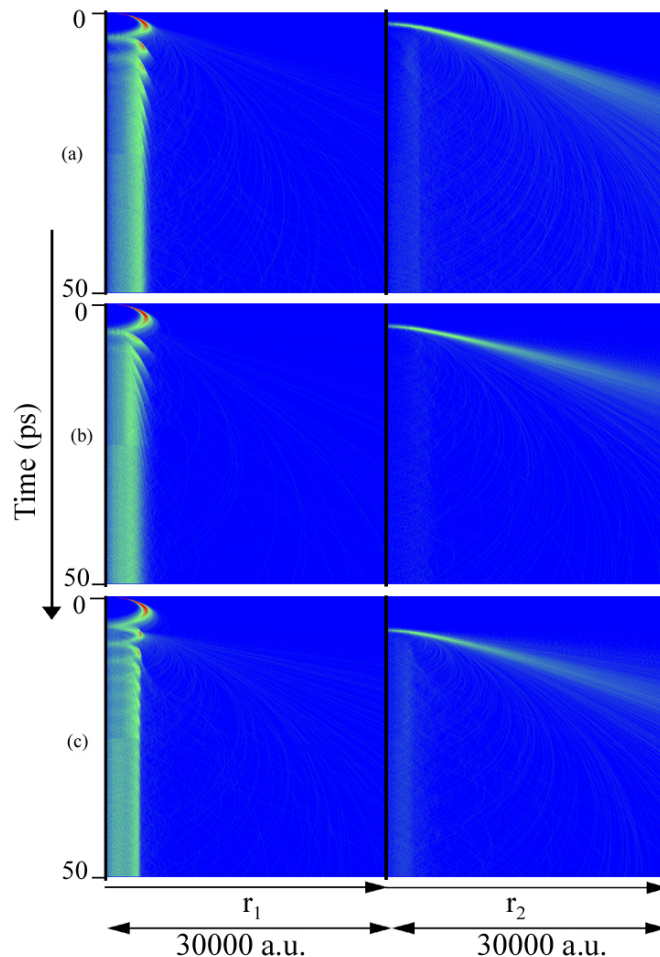


Figure 5.15: Radial positions of electrons in $N_1 \sim 33$, $N_2 \sim 70$ wavepacket. The three figures above show the distribution of positions of the two electrons as a function of time for 50 ps after the excitation of the first electron. The second electron is excited at times (a) 2 ps, (b) 4 ps and (c) 6 ps in the three cases. Warmer colors (Red \rightarrow Green) represent higher probability of finding the particle at a particular position while cooler colors (Blue \rightarrow Green) represent low probability of finding the particle at that position. The figures are split into two halves with the left half representing the distribution of the first electron and the right half representing the second electron's position.

5.9 ‘Slow’ Autoionization

In the discussions of the previous sections, we have concentrated on the process of autoionization that occurs via sudden redistribution. However, this is not always the case when we excite a double rydberg wavepacket. In the case of the $N_1 \sim 33$, $N_2 \sim 50$ wavepacket, we see the absence of time-dependent variation in the distribution of final ionic rydberg states both in experiment and in the classical simulations. From our impulse model of the sudden redistribution, we can predict that the autoionization process does not occur immediately after the first interaction but that it occurs at a later time. We can term these delayed autoionization processes as ‘slow’ autoionization to differentiate it from the case where autoionization occurs at the first interaction and will be referred to in this section as ‘fast’ autoionization.

We do not observe any strong dependence of the timing of slow autoionization on the delay of the initial wavepackets. This can be understood from the observation that when the initial interaction of the wavepackets does not cause autoionization, the two bound electrons become highly correlated and their motion can no longer be separated into the motion of individual wavepackets. In the classical simulations, this manifests in the form of a position-dependent correlated motion of the two electrons around the core. Unlike the case in fast autoionization where the two electrons in almost all the different relative orientations move in the radial direction with similar velocities and continue moving outwards after autoionization, the situation in slow autoionization becomes a lot more complicated after the first interaction. After the first interaction between the electrons far from the core, the motion of the electrons

does not have any regular periodic features that characterize the collective motion of the electrons in a wavepacket.

In spite of the absence of any time-dependent variations in the final ionic state distribution, the absence of significant variations depending on the initial configurations of the particles is in itself an interesting concept. The classical simulations predict that whenever slow autoionization occurs in the doubly excited system, irrespective of the initial energies and positions of the two electrons, the distribution of final states as a function of the principal quantum number, N , of the final states, varies as $\sim N^3$ for the most part. We can perform a semi-classical analysis of the autoionization process to see if we can reproduce the result of classical simulations in an analytical form.

In the classical simulations, the velocity of the two electron as they cross through each others' orbit is noted at the last crossing before one of the electrons is released by autoionization. We notice that in almost all the cases that we have considered, the velocity of one of the electrons is always significantly greater (order of magnitude or more) than the velocity of the other electron. This suggests that for all practical purposes, we can consider one of the electrons to be nearly stationary at some distance from the core and the other electron to have gained sufficient energy to be moving with high velocity through the orbit of the nearly stationary electron and be ionized by sudden redistribution. We can therefore think of the final ionic state probability distribution being decided by the probability of the electrons crossing at a certain distance from the core.

Let us consider a semi-classical model of the two-electron atom with the first electron ‘ e_1 ’ excited into a wavepacket around principal quantum number n_1 ($Z=1$) and the inner electron subsequently excited into an ionic rydberg wavepacket around n_2 ($Z=2$). As we have seen earlier, the motion of the wavepackets before the first interaction is well defined by a classical model and we can assign specific times to the first interaction depending on the delay between exciting the two electrons. However, after the first interaction the exact time of the next interaction is not well-defined due to e-e scattering. Without loss of generality, we can refer to the outer electron just before sudden redistribution as ‘ e_1 ’ and the inner electron that gains sufficient energy through the sudden redistribution to become free as ‘ e_2 ’.

If at the first interaction, there is no autoionization, e_2 and e_1 exchange energy $\frac{1}{R_1}$ at the first crossing point, $\frac{1}{R_2}$ at the next crossing point and so on. This continues till the exchange of energy at the k^{th} crossing occurs at a radius of R_k that is smaller than a critical radius corresponding to the effective principal quantum number $n_2(k)$ of e_2 given as $R_k < \frac{n_2^2(k)}{2}$. We will drop the subscript k for further analysis. The probability of the two electrons crossing at some R can be expressed as the probability of e_1 being at R at some time. So the partial probability of e_1 being within ΔR of R over the duration of its orbit is

$$\Delta P = \frac{\Delta t}{\tau} \tag{5.14}$$

where Δt is the time spent by e_1 within ΔR and $\tau = 2\pi n_1^3$ is the orbital period of the electron. Using $\Delta t = \frac{dt}{dR} \Delta R$, we can write

$$\frac{\Delta P}{\Delta R} = \frac{dt}{dR} \frac{1}{\tau} \tag{5.15}$$

The numerator in this term can be written as

$$\frac{dt}{dR} = \frac{1}{\frac{dR}{dt}} = \frac{1}{v_1} \quad (5.16)$$

where v_1 is the radial velocity of e_1 at R .

Since the electron is at the same R twice in each orbit, we can then write the variation in probability of e_1 being at R at the time of crossing as

$$\frac{dP}{dR} = \frac{1}{2\pi n_1^3} \frac{2}{|v_1|} = \frac{1}{\pi n_1^3} \frac{1}{\sqrt{\frac{2}{R} - \frac{1}{n_1^2}}} \quad (5.17)$$

If the bound electron in a rydberg state of the ion after autoionization has principal quantum number N from sudden redistribution, we can write

$$-\frac{2}{N^2} = -\frac{1}{2n_1^2} - \frac{1}{R} \quad (5.18)$$

$$\Rightarrow R = \left(\frac{2}{N^2} - \frac{1}{2n_1^2} \right)^{-1} \quad (5.19)$$

The dependence between the final ionic rydberg state and the point of crossing of the electrons can be expressed as

$$\begin{aligned} \frac{dR}{dN} &= - \left(\frac{2}{N^2} - \frac{1}{2n_1^2} \right)^{-2} \left(-\frac{4}{N^3} \right) \\ &= 4N \left(2 - \frac{N^2}{2n_1^2} \right)^{-2} \\ &= \frac{N}{\left(1 - \frac{N^2}{4n_1^2} \right)^2} \end{aligned} \quad (5.20)$$

The probability distribution of the final ionic rydberg states can be expressed as

$$\frac{dP}{dN} = \frac{dP}{dR} \frac{dR}{dN} \quad (5.21)$$

Using Eqn 5.17, and Eqn 5.19, we can write

$$\begin{aligned}\frac{dP}{dR} &= \frac{1}{\pi n_1^3} \frac{1}{\sqrt{2 \left(\frac{2}{N^2} - \frac{1}{2n_1^2} \right) - \frac{1}{n_1^2}}} \\ &= \frac{1}{2\pi n_1^3} \frac{N}{\sqrt{1 - \frac{N^2}{2n_1^2}}}\end{aligned}\quad (5.22)$$

Substituting Eqs 5.20 and 5.22 in Eqn 5.21, we get

$$\frac{dP}{dN} = \frac{1}{2\pi n_1^3} \frac{N^2}{\left(\sqrt{1 - \frac{N^2}{2n_1^2}} \right) \left(1 - \frac{N^2}{4n_1^2} \right)^2}\quad (5.23)$$

An electron in state n_1 in a $Z=1$ potential is more tightly bound to the core when the potential corresponds to $Z=2$ after sudden redistribution. We note that Eqn 5.23 has a denominator on the right hand side that becomes imaginary for $N \geq \sqrt{2}n_1$. So we can only have $N < \sqrt{2}n_1$. This limit corresponds to the point where the outer turning point of the ionic rydberg state equals the outer turning point of the initial rydberg state, n_1 . The radial extent of the first wavepacket, therefore, places a limit on the radial extent of possible final ionic rydberg states that are produced by sudden redistribution.

The critical radius $R_c = \frac{n_2^2}{2}$ places a further restriction on the possible values of R where ionization can occur.

$$\begin{aligned}R < R_c &\Rightarrow \frac{1}{\frac{2}{N^2} - \frac{1}{2n_1^2}} < \frac{n_2^2}{2} \\ &\Rightarrow N^2 < \frac{2}{\frac{1}{2n_1^2} + \frac{2}{n_2^2}} \\ &\Rightarrow N < \frac{2n_1}{\sqrt{1 + \frac{4n_1^2}{n_2^2}}}\end{aligned}\quad (5.24)$$

We then have a limit on the possible values of N as

$$N < \text{Min}\left(\sqrt{2}n_1, \frac{2n_1}{\sqrt{1 + \frac{4n_1^2}{n_2^2}}}\right) \quad (5.25)$$

We can make use of Eqn 5.23 and the limits on N given by 5.25 to calculate the form of the probability distribution of the final ionic rydberg states.

When e_2 crosses for the first time with e_1 without autoionizing, the energy exchange occurs such that the new energies are

$$\begin{aligned} e_1 & : -\frac{1}{2n_1^2} - \frac{1}{R_1} \\ e_2 & : -\frac{2}{n_2^2} + \frac{1}{R_1} \end{aligned}$$

At the next crossing, the energy of the two electrons are given by

$$\begin{aligned} e_1 & : -\frac{1}{2n_1^2} - \frac{1}{R_1} + \frac{1}{R_2} \\ e_2 & : -\frac{2}{n_2^2} + \frac{1}{R_1} - \frac{1}{R_2} \end{aligned}$$

and at the k^{th} crossing, the energies are given by

$$\begin{aligned} e_1 & : -\frac{1}{2n_1^2} + \sum_{i=1}^k (-1)^i \frac{1}{R_i} \\ e_2 & : -\frac{2}{n_2^2} - \sum_{i=1}^k (-1)^i \frac{1}{R_i} \end{aligned}$$

At each crossing of the electrons, we expect the maximum probability of crossing without autoionization to occur close to the outer turning point of the first wavepacket that we excite except at the last crossing where one of the electrons can autoionize within the critical radius. Assuming such a case, we expect the successive values of

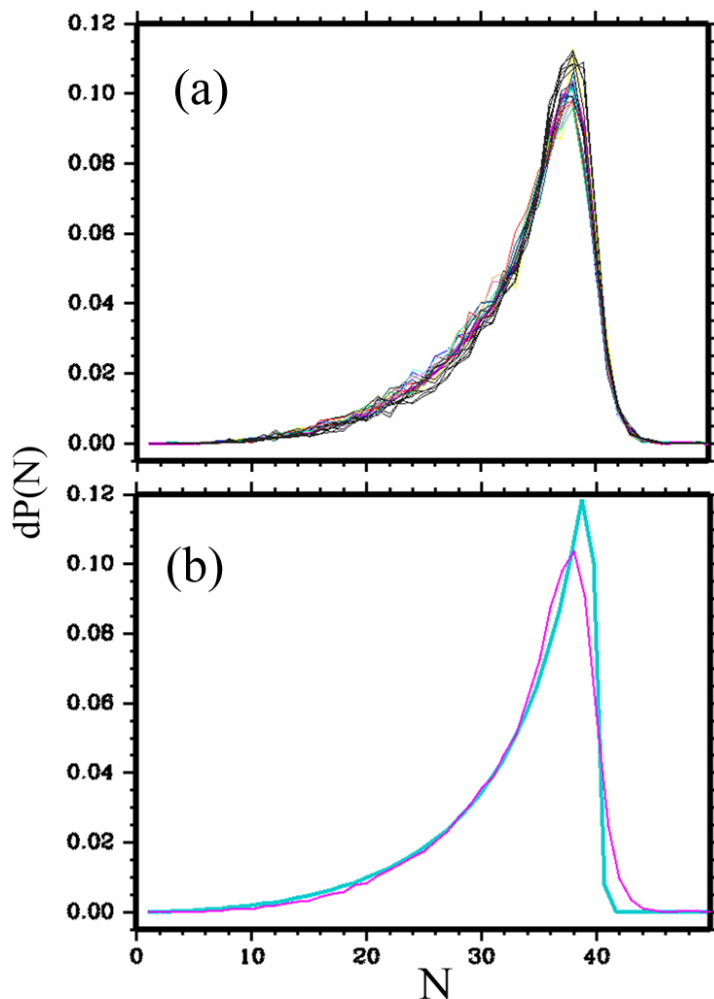


Figure 5.16: Final ionic state distribution from Slow Autoionization

The above figures show the distribution of final ionic rydberg states calculated from the classical simulation as well as from the semi-classical arguments. The upper graph, (a), shows the final state distribution starting from $N_1 \sim 33$, $N_2 \sim 50$ for a range of delays between exciting the wavepackets that goes from 0.7 ps to 4.3 ps all plotted on the same scale. This shows the almost identical distribution of final states independent of relative wavepacket delay. The lower graph, (b), compares the average form of the distribution shown in (a) as a thin curve over the thicker curve obtained from the semi-classical calculation.

R_i to be very close and almost cancel so that the distribution of states n_1 and n_2 for e_1 and e_2 just before they cross is similar to the distribution of states in the original double rydberg wavepacket. To test this assumption, we have performed a calculation of the expected form of the probability distribution as

$$dP(N) = \sum_{n_1} \sum_{n_2} g(n_1)g(n_2) \frac{dP}{dN}(n_1, N) dN \quad (5.26)$$

where $g(n_1)$ and $g(n_2)$ are the distribution of states around n_1 and n_2 respectively for e_1 and e_2 in the initial double rydberg wavepacket. This is expanded and rewritten as

$$dP(N) = \sum_{n_1} \sum_{n_2} g(n_1)g(n_2) \frac{1}{2\pi n_1^3} \frac{N^2}{\left(\sqrt{1 - \frac{N^2}{2n_1^2}}\right) \left(1 - \frac{N^2}{4n_1^2}\right)^2} \quad (5.27)$$

The distribution of final states is normalized so that the total probability is unity and this calculation has been compared with the distribution of states obtained from the classical simulation in Fig 5.16. We notice a remarkable agreement between the classical picture and the semiclassical calculation that assumes the distribution of states among the interacting electrons to be the same over time. This is not an intuitive result as one might expect the state distributions to vary significantly with each interaction between the electrons. This seems to suggest, according to the classical simulation and its comparison with the semi-classical analysis, that the energy distribution in each electron does not change significantly with successive collisions. This could be due to the fact that non-autoionizing interactions far from the core are most likely when both electrons are near their outer turning point and outside the critical radius for fast autoionization ($R_c = \frac{n_2^2}{2}$) and subsequent interactions without

autoionization also occur close to the same radial position.

5.10 Correspondence of classical and quantum approaches

We have been able to use an impulsive redistribution model of the autoionization process to explain the dependence on the delay between exciting the two electrons and their energy on the ionic rydberg state distribution remaining after autoionization. A quantum calculation of the overlap between the first wavepacket and possible final states of the ion have shown a remarkable similarity to results obtained from classical simulations of the double rydberg wavepackets. This leads us to wonder about the cause of the similarity of results given the different nature of the two approaches to the problem.

In the classical model, we perform a few thousand iterations of the three-body problem to get a distribution of final states after autoionization. This is performed for each relative delay between exciting the two electrons. In each iteration, the two electrons can be in a large possible choice of relative orientation of orbits. In each iteration, the final ionic rydberg state that results from the simulation is unique and not a distribution of states.

On the other hand, the quantum mechanical model looks at the overlap between the wavefunction of the first wavepacket and all possible ionic rydberg wavepackets at different delays after the excitation of the first wavepacket. In a single set of

calculations of the overlap integrals, this calculation predicts the distribution of final ionic rydberg states as a function of the time at which the sudden redistribution occurs.

Looking at the problem and trying to visualize it in an intuitive manner, we are tempted to look at the wavefunctions in the quantum calculation and think that it might be possible to model the wavefunctions classically as “breathing spheres” [132] instead of as thousands of iterations with point particles. However, this is not strictly the case as we cannot have any interaction between different parts of the same shell which would be the situation in a truly classical model of a charged shell. Picturing the wavepackets as shells of charge is a convenient way of visualizing the entire range of possible orbits of the electrons without worrying about their specific paths in three dimensions. We have to realize, however, that a wavefunction is the square root of the probability of finding a particle at a given location at some time and has an amplitude and a phase associated with it. To assign it a physical picture of a classical distribution of particles is not a true representation of the system.

When we perform an experiment with rydberg atoms as described in this dissertation, the classical picture tells us that we are essentially looking at several million instances of the excitation of atoms into different energy levels with each laser pulse. In each atom, we excite one particular set of energy levels and not a range of energy levels. However, in a different atom, the specific energy levels that are excited can be different. The probability of exciting a particular energy level is decided by the bandwidth of the laser used in the excitation.

The quantum mechanical picture gives us a way to visualize all the possible excitations in a collective manner that is not possible in a simple classical picture. Thus, while the quantum mechanical picture allows us to use the spatial potential energy distribution to determine the probability of finding a particle in the potential at different points in space, it does not fix the position of the particle in space. As soon as we get into the classical world and fix the position and velocity of the particle (electron), the probability distribution collapses to a single point and we no longer have a range of possible positions of the particle.

The classical simulations give us a similar result as the quantum calculation only after we perform a large number of simulations of the problem. A single instance of the classical simulation of the two-electron excitation leads to a single final ion in a well-defined energy level. The large number of possible situations that are considered in the simulations allow the overall results pictured collectively to resemble the quantum mechanical picture.

In situations where the potential energy of the system remains nearly invariant as in a one-electron atom, a quantum mechanical analysis provides a convenient way of determining the dynamics of the electron in the atom in a large number of possible orbits. However, in a doubly excited atom where the potential experienced by each of the two electrons varies considerably as a function of the position of the other electron, a complete quantum mechanical calculation becomes extremely difficult as the number of energy levels that need to be considered increases. In such a situation, classical calculations can provide an easier path towards gaining a better insight into

the dynamics of the problem.

5.11 Conclusions

In this experiment, we have been able to create controlled double rydberg wavepackets in barium. This is to our knowledge, the first experimental realization of such doubly excited coherent wavepackets where the interaction of the two electrons far from the core has been studied in a time-dependent manner. We have observed that when the two electronic wavepackets interact far outside the ionic core, the radial position of the first interaction between the wavepackets is the most important parameter that decides the final distribution of ionic rydberg states in the remaining ions after autoionization. This is to our knowledge, the first experimental time-domain study of double rydberg wavepackets where the inner $Z=2$ electron is excited into a state with a radial extent greater than $\sim 1/4$ of the radial extent of the $Z=1$ electron.

Classical simulations of the experiment that reproduce the experimental results have been understood using semi-classical analysis and provide a better insight into the dynamics of autoionization in two-electron atoms for an entire class of orbits where the inner electron is launched into an orbit that passes through the orbit of the outer electron.

Chapter 6

Controlled Post Collision Interaction

6.1 Post-Collision Interaction

In atoms excited above their first ionization limit, Auger processes (similar to autoionization) can lead to one of the electrons being ejected as a free electron while the other electron stays bound. As an example, if an electron in an inner shell of an atom is photoionized near threshold, this electron moves away from the atom with some small velocity. The remaining ion with an unfilled inner shell is not in its ground state. If any two electrons in the outer shells of the ion exchange energy with each other so that one electron fills the inner unfilled shell and the other electron is released with high energy, the electron that is released from the ion can interact with the first electron that had been released into the continuum at some distance from the core.

Such an interaction is termed as “post-collision interaction” (PCI) and the effect is seen as a broadening of transitions in x-ray studies of photoelectron excitation or in electron-ion scattering experiments. PCI in Auger processes is essentially the interaction of a slow electron released by inner-shell ionization with a fast electron released by an Auger process from the remaining ion [136]. PCI need not be between the first electron released from the inner shell and the following fast electron but could also be between the fast-moving electron and another electron in the vicinity of the atom.

In our experiments with DRWs, we have excited the inner electron into wavepackets that pass through and go beyond the first outer electronic wavepacket. We could extend such studies to the case where the outer electron is excited into a continuum wavepacket and then exciting the remaining bound electron into the continuum with a higher energy to overtake it in a manner similar to PCI in Auger processes. Thus, sequential excitation of continuum wavepackets can provide a method of studying PCI in a controlled manner by choosing the initial energy of both the electrons as well as the ability to distinguish between different final states of any recombined ions that might be created in the process. This experiment is similar to studies of inner electron ionization(IEI) from radial wavepackets [133] with the modification that the radial wavepacket is excited into the continuum.

The process of autoionization that occurs by sudden redistribution of the potential energies of the two electrons in the DRW can also be looked at in terms of the energy change of the electron that stays bound. The electron that had been excited into the first rydberg wavepacket and is the outer electron initially becomes more tightly

bound to the doubly charged positive core when the second electron moves out to a greater radial extent than the first electron. The increase in binding energy of the first electron by an amount $-\frac{1}{R}$ at the radius of interaction, R , means that it is possible for the initial energy of the first electron to be greater than zero and yet the electron can be bound after interaction with the second electron.

6.2 Experimental Realization of PCI

We test our proposition by tuning L2 (see Fig5.2) to excite the first electron into a wavepacket just above the $5d_{5/2}^+$ ionization limit. We then tune L4 such that it excites the second electron into a wavepacket above the Ba^{++} second ionization limit starting from the $4f_{7/2}^+$ state in the barium ion. If the excitation of the two electrons occur sufficiently well separated in time, we would expect the two electrons to become free and we would be left with Ba^{++} . However, if we excite the second electron soon after the excitation of the first electron such that it overtakes the wavepacket of the first electron at a distance close enough to the core to be able to recombine the first electron, we can detect ionic rydberg states.

The experiment is performed in an identical manner to the experiment looking at DRWs and the results are shown in Fig6.1(a). The graphs show the presence of recombined ionic rydberg states when the two electrons are excited with very short time delay between the excitations and an absence of ionic rydberg states at later times. We also note that the distribution of final ionic rydberg states is peaked

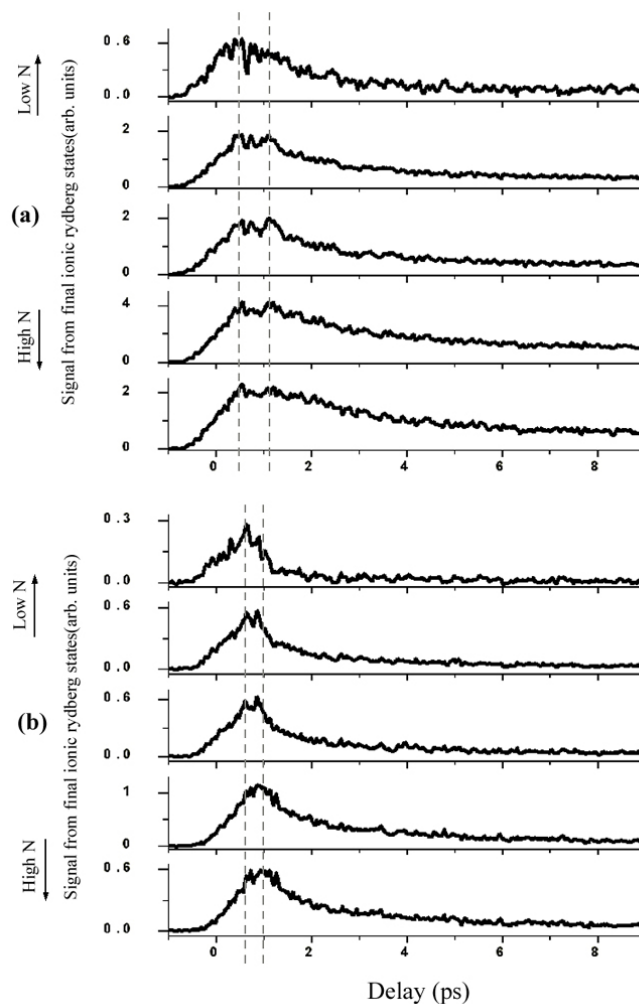


Figure 6.1: Continuum wavepacket recombination

The signals from ionization of ionic rydberg states resulting from the recombination of an electron when both electrons are excited into continuum wavepackets with a relative time delay between them. The horizontal axis represents the time delay between the excitation of the two wavepackets while the vertical axis represents the strength of signal observed in different gates. The upper graph (a), shows the case where the second electron is excited with a low energy just above the Ba^{++} limit while the lower graph, (b), shows the case where the second electron is excited by a two-photon process by L3 far above the Ba^{++} continuum. The dashed lines are shown to aid comparison of the position of the peak signal in different gates.

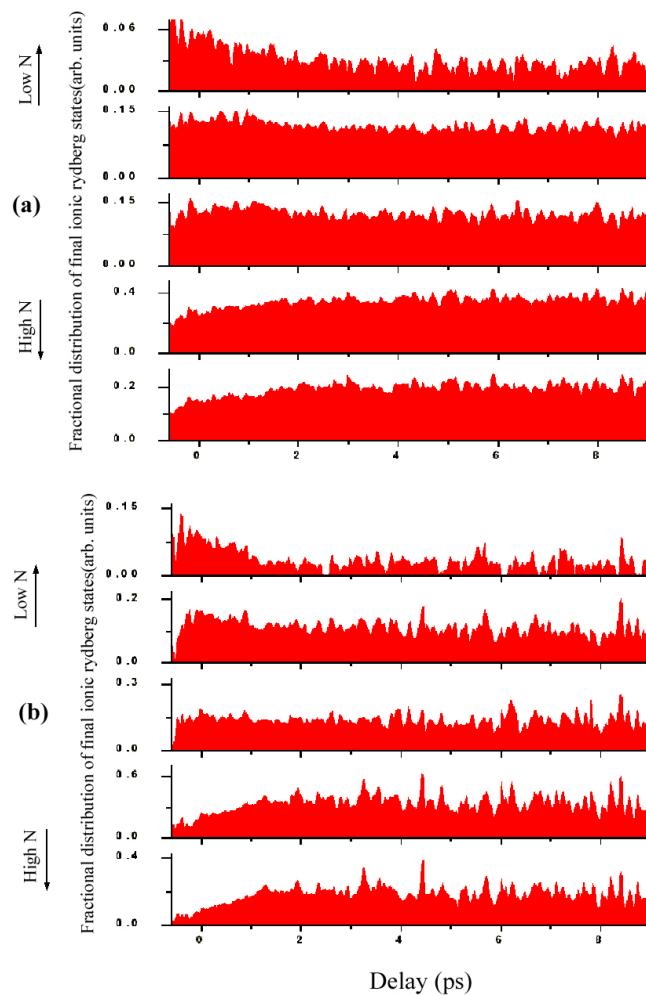


Figure 6.2: Gate distribution of signal from continuum wavepacket recombination. This shows the fractional distribution of signal from ionization of Ba^+ rydberg states resulting from the recombination of an electron when both electrons are excited into continuum wavepackets with a relative time delay between them. (a) corresponds to the case where all four lasers are used in the excitation. Case (b) corresponds to the signals in the absence of L4 where L3 is believed to produce multiphoton excitation into the continuum.

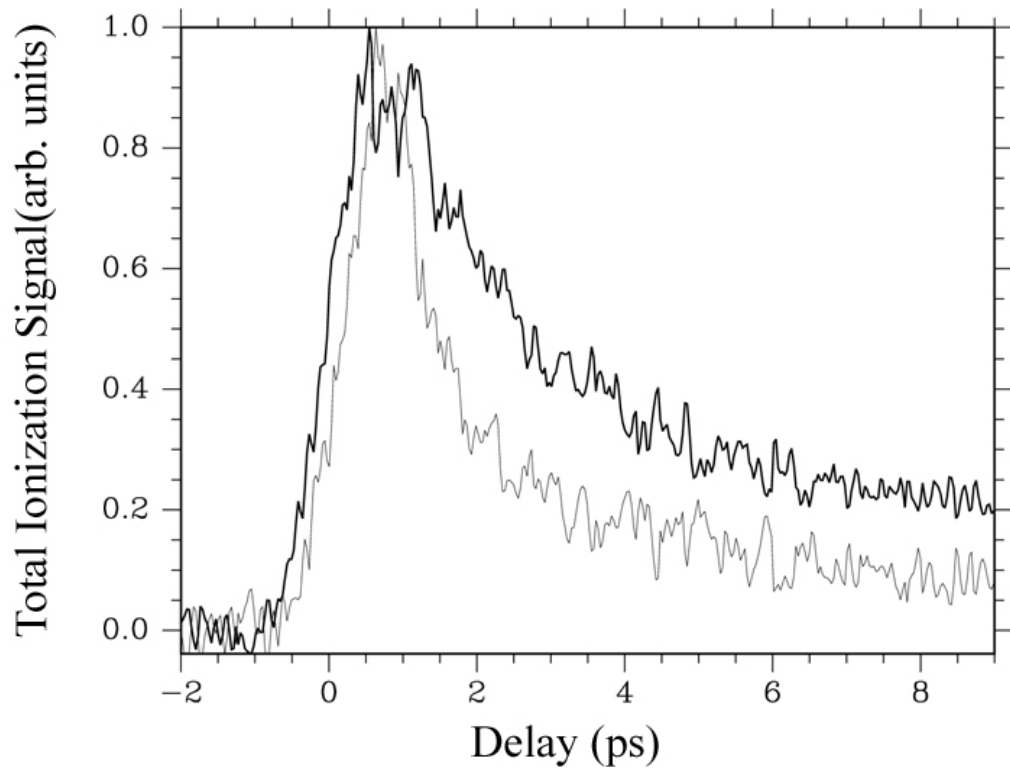


Figure 6.3: Total signal strength in continuum wavepacket recombination

The two curves in the graph show the total signal from the recombination of an electron after both electrons in Ba are sequentially excited into the continuum with a delay between excitations shown on the horizontal axis. The bold curve corresponds to the case where all four lasers are used in the excitation. The lighter curve corresponds to the signal in the absence of L4 and has been multiplied by a factor of ~ 3 to be on the same scale. Both curves are normalized to 1 at the maximum signal level.

toward states with higher binding energy (or lower principal quantum number) at times close to $t=0$ while the distribution peaks at states with lower binding energy (or higher principal quantum number) at a later time before the signals disappear completely. We had also noticed a time-dependent distribution of ionic rydberg states in the absence of L4 and the fractional distribution of this background signal is shown in Fig6.1(b). The dashed lines in the graphs in Fig6.1 from left to right are shown to point to the peaks of the distribution in the highest and lowest gates respectively. This data is also presented as the fractional distribution of the total signal in the gates in Fig6.2. The total strength of this background signal is a factor of ~ 3 smaller than the peak of the signal in the presence of L4. This background could be due to direct ionization of the electron in the Ba^+ ion by L3 through multiphoton excitation into the continuum above Ba^{++} . The total signal in all the gates from ionization of the ionic rydberg states is shown as a function of delay between lasers L2 and L3 in Fig6.3.

We can understand the signal distribution in a manner similar to the autoionization of the DRW by sudden redistribution. In this case, the first electron excited into the $5d_{5/2}\epsilon\ell$ continuum moves radially outward from the core. When the second electron is excited after some time delay into a wavepacket in the continuum above the Ba^{++} limit, this electron moving radially out from the core can catch up with and overtake the first electron at some radial distance R . In a manner identical to what has been considered previously, the effective potential seen by the two electrons is interchanged at the crossing point and the resulting exchange of energy results

in the binding energy of the first electron increasing by $-\frac{1}{R}$. When this increase in binding energy is greater than the total energy of the electron, the electron becomes bound to the core as a rydberg state of the ion. The second electron which already had enough energy to be a free electron gains an energy of $\frac{1}{R}$ and leaves the ion as a free electron. Since the recombination of the first electron can only occur at radial distances R smaller than a critical value determined by the energy, (ϵ_1) , of the first electron ($R < \frac{1}{\epsilon_1}$), we can only see this effect if the second electron is excited soon enough after the excitation of the first electron to catch up with it at distances smaller than the critical value of R . At smaller time delays between exciting the wavepackets, the two electrons cross closer to the core and leaves the first electron bound in orbits that are closer to the core and with higher binding energies.

If our analysis of the background signal in the absence of L4 is correct, then the recombination of the electron can be explained as being due to the excitation of the second electron into the Ba^{++} continuum with much higher energy than the excitation in the presence of L4. However, it does not explain why the signal from this recombination is observed for a shorter duration than the signal in the presence of L4. An intuitive picture of the recombination process suggests that if the second electron has a higher energy, it should be able to overtake and recombine the first electron at greater delays between the wavepacket excitations.

One possible explanation for the lack of such an observation could be that the multiphoton excitation by L3 occurs preferentially in the presence of L2 and L3 (hence recombination signal is strong at smaller delays) rather than in the presence

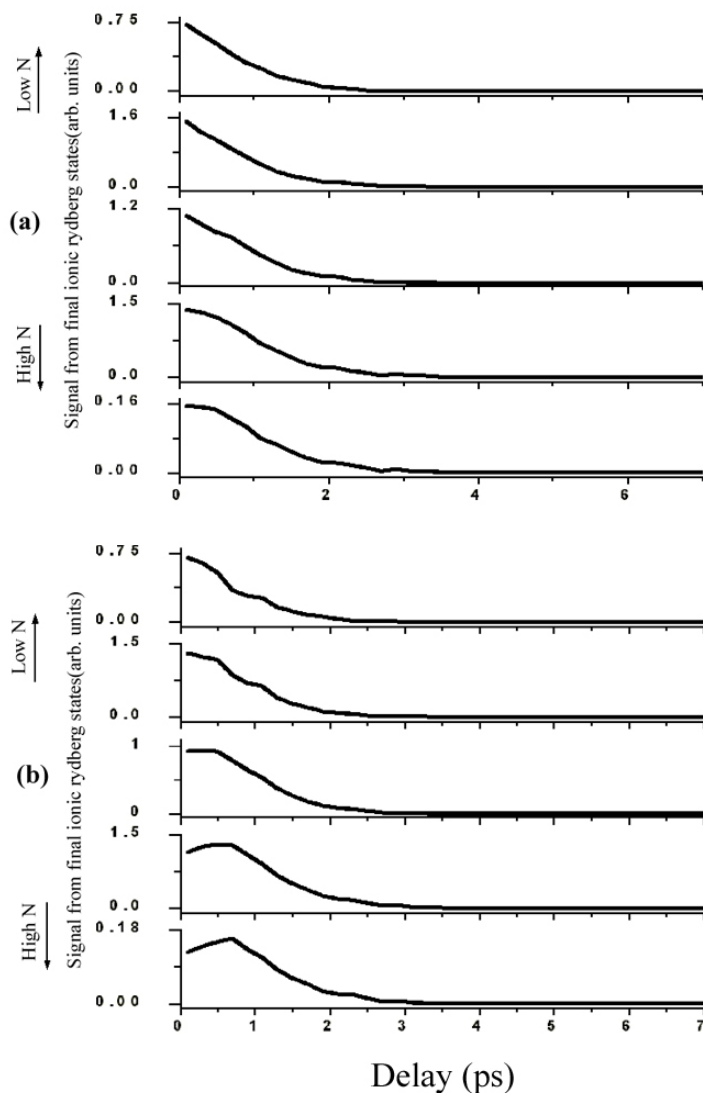


Figure 6.4: Continuum wavepacket recombination - classical simulation

The calculated form of the signals from ionization of of ionic rydberg states resulting from the recombination of an electron when both electrons are excited into continuum wavepackets with a relative time delay between them. The horizontal axis represents the time delay between the excitation of the two wavepackets while the vertical axis represents the strength of signal expected in different gates. The upper graph (a), shows the case where the second electron is excited 5 cm^{-1} above the Ba^{++} limit while the lower graph, (b), shows the case where the second electron is excited 10700 cm^{-1} above the Ba^{++} continuum.

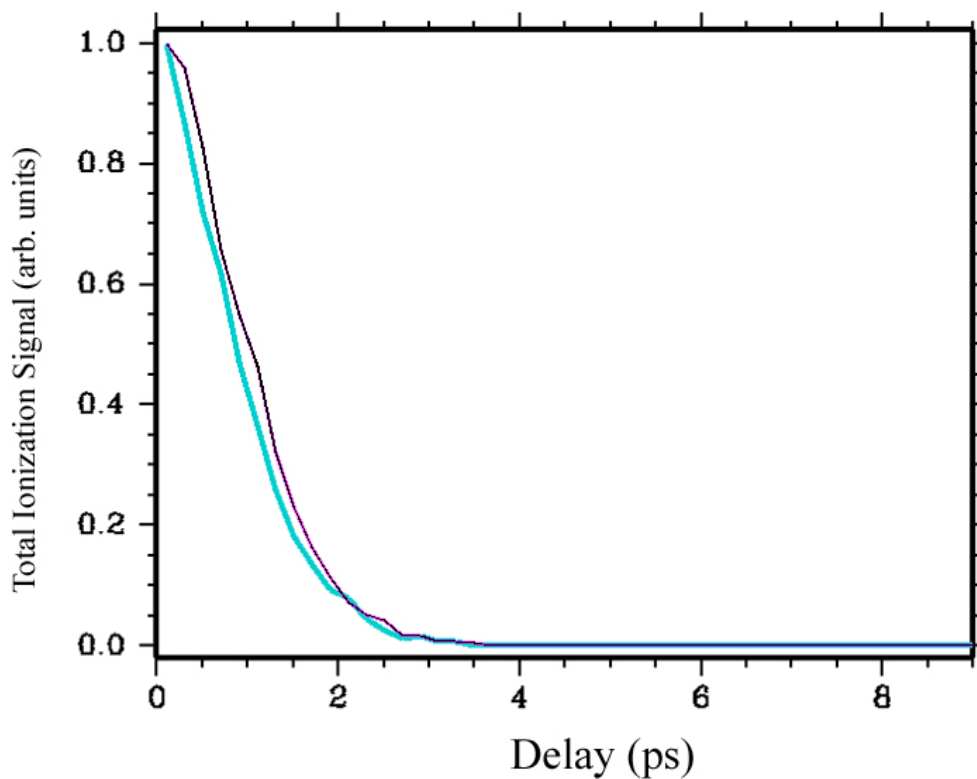


Figure 6.5: Expected signal from continuum wavepacket recombination

The two curves in the graph show the calculated form of the total signal from recombination of an electron after both electrons in Ba are sequentially excited into the continuum with a delay between excitations shown on the horizontal axis. The thick curve corresponds to the case where the second electron is excited 5 cm^{-1} above the Ba^{++} limit. The thin curve corresponds to the second electron excited 10700 cm^{-1} above the Ba^{++} limit. Both curves are normalized to 1 at the maximum expected signal level.

of L3 alone at later delays. This would explain the sharp peak in the recombined ion signal that falls off rapidly when the delay between the pulses exceeds 2 ps. Since L2 and L3 are almost 1 ps long, this would explain the 2 ps width of the signal which occurs mainly when both the laser pulses are present.

We have performed a classical simulation of the two electron excitation in a manner identical to the simulation with bound electrons in the previous chapter. The results of the classical simulation are presented as the expected form of the signal levels in different gates in Fig.6.4. The comparison of the total measured signal from recombination in the two cases where the second electron is excited just above the Ba^{++} limit and far above the limit is shown in Fig6.5. This calculation shows the result that we expected from a simple semi-classical argument. Here, the recombined signal is expected to occur for longer delays when the second electron is excited with higher energy. Although, the two cases are hardly distinguishable from the total signal, the relative signal in the gates shows a difference in the two cases.

6.3 Conclusions

The ability to excite two electrons sequentially into continuum wavepackets allows us to study PCI experimentally in a controlled manner by varying the excitation energy of the two electrons. Although the excitation scheme does not represent a true Auger process, it can still be used to study the energy dependence of electron recombination through PCI in Auger processes.

Chapter 7

Conclusion and Future Prospects

We have demonstrated the ability to create independently controlled double rydberg wavepackets by multiphoton excitation using pulsed lasers. This is an essential ingredient for further studies of the dynamics of the two-electron atom in a controlled manner. We have found that a semi-classical model of the two-electron atom can be used to understand some of the major features observed in the decay of the double rydberg wavepacket when autoionization occurs at the first collision between the wavepackets. The experiments described here are the first time-dependent measurement of any property of double rydberg wavepackets where the inner electron is excited into bound rydberg wavepackets with a greater radial extent than the first wavepacket. Previous time-dependent studies of double wavepackets have had the inner electron excited to states with radial extents that are a fraction of the radial extent of the first wavepacket [63, 78].

The classical simulations together with the experimental data allows us to explain

the process of autoionization on the basis of a sudden redistribution model for a class of double excitations where we can know that the electron-electron interaction occurs within a certain critical radius around the core. However, in our experiments, we have studied just one of the features that are predicted from the classical simulations. We can therefore perform a few other experiments that can be used to check the veracity of our classical model and check some of the other predictions made by the model.

In our classical simulations, we have observed some time-dependent behavior in the resultant rydberg ion (see Fig5.14 and Fig5.15). This opens up the possibility of using experiments to look for such dynamics in the ion in a time-dependent manner. One possible way to do this might be to use half-cycle pulses (HCP) in a manner similar to the study of rydberg wavepacket dynamics in neutral atoms [123, 137]. It might also be possible to use half-cycle pulses to recombine the electron released from the decay of the double rydberg wavepacket in a manner similar to recombination studies of electrons released into the continuum states from a neutral atom [138].

The experiments described here could be improved upon by devising a better method of detecting the ionic rydberg states. One of the possibilities that had been considered during the experiments was to use microwave pulses to ionize the ionic rydberg states. This would avoid the problem of the ions moving in the electric field ramp and limiting our resolution in identifying the rydberg states. It might be possible to use a ramped microwave field to ionize the ionic rydberg states in a time-dependent manner [139, 140].

Previous theoretical work using classical [80, 141] and quantum mechanics [142]

have predicted the possibility of creating electron wavepacket that are well-localized in three-dimensional space using half-cycle pulses and electron-ion recombination techniques. A creation of such a wavepacket in place of the first wavepacket that we have produced would allow for the study of the angular dependence of the initial positions of the two electrons on the decay channel of the double rydberg wavepackets.

Appendix A

Notes on creating DRWs

A.1 Another calibration method for N_1

In chapter 5, we have already seen that we can use the time-dependent decay of the $5d_{5/2}N_1d$ wavepackets to determine the energy and bandwidth of the first wavepacket. The decay of the $5d_{5/2}N_1d$ wavepackets changes the total population of the initial state accessible for creating double rydberg wavepackets. The total signal obtained by detection of the ionic rydberg states is therefore expected to be proportional to the population of initial states available for the excitation.

We notice a decrease in total signal from the ionization of ionic rydberg states at delays near the kepler period of the first wavepacket. Ideally, if we detect all the ionic rydberg states remaining after the decay of the double wavepacket, the total signal should be directly proportional to the survival probability of the $5d_{5/2}N_1d$ autoionizing wavepacket as a function of the delay between L2 and L3. However, the

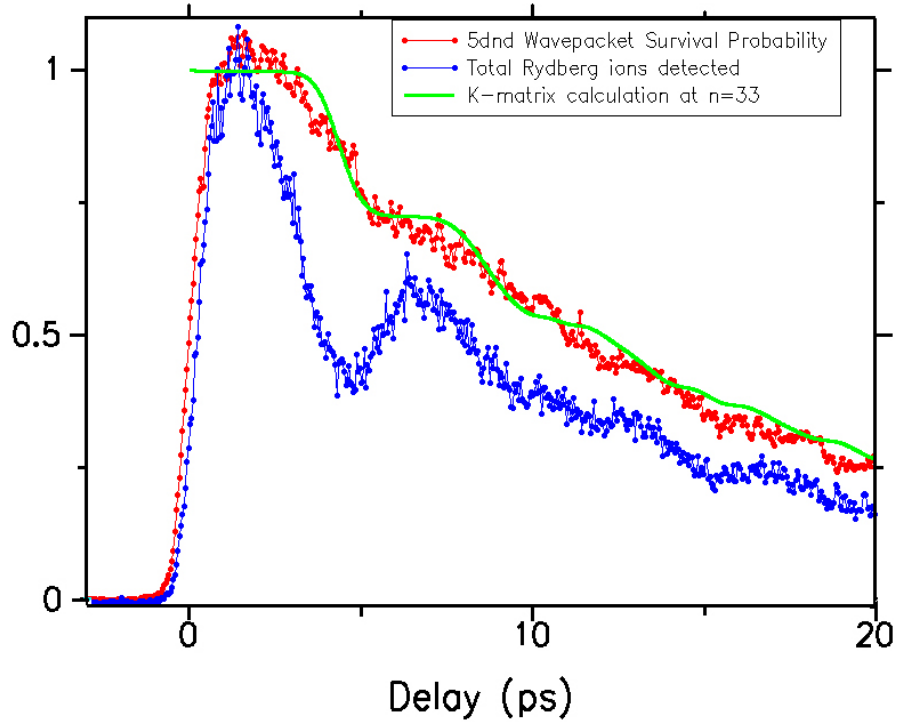


Figure A.1: Population dependence of final ionic rydberg states on wavepacket delay

The total signal from ionization of the ionic rydberg states that remain after autoionization of the N_2gN_1d double rydberg wavepacket is compared with the survival probability of the $5d_{5/2}N_1d$ autoionizing wavepacket (the first wavepacket). A K-matrix calculation of the survival probability of the first wavepacket is overlaid as a solid curve. We notice that we can use the dip in the total ionization signal to get a good estimate of the kepler period of the first wavepacket and hence its central energy without a need to separately measure the survival probability of the first wavepacket.

fraction of ionic rydberg signals that are detected by field ionization corresponds to states with principal quantum numbers, $N \gtrsim 30$. The total signal level from field ionization of the $N\ell^+$ states relative to the signal level that corresponds to $5dN_1d$ wavepacket survival probability shows dips when the final ionic rydberg states have lower principal quantum numbers than what can be measured by the field ionization.

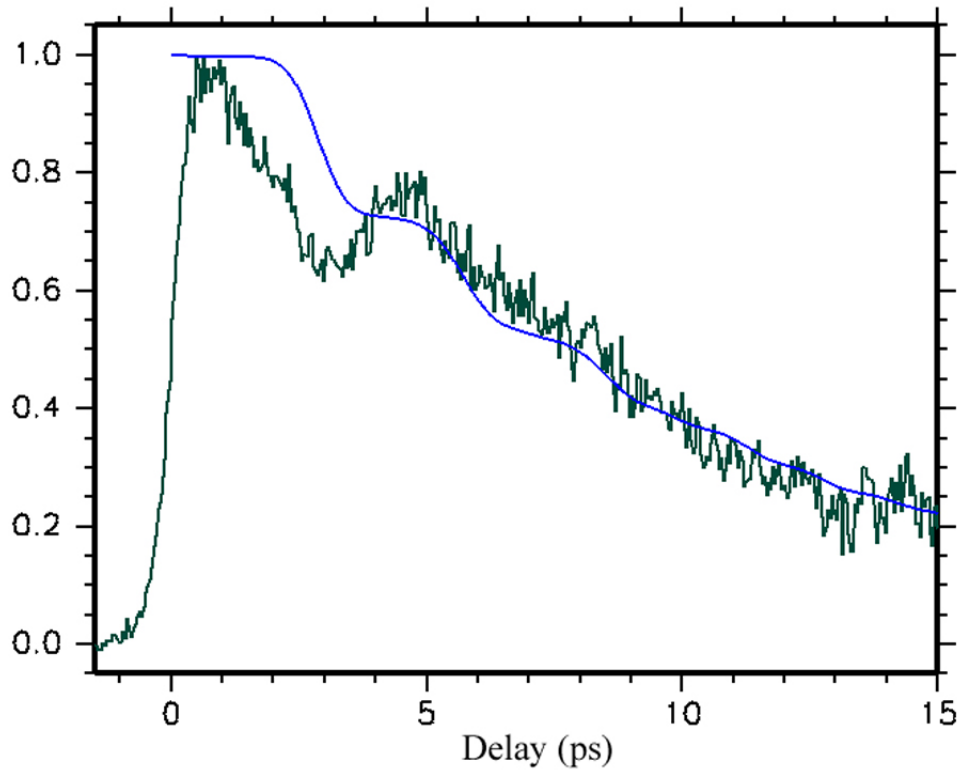


Figure A.2: Population in ionic rydberg states as a measure of N_1

The total signal from ionization of the ionic rydberg states that remain after autoionization of the N_2gN_1d double rydberg wavepacket is compared with the calculated survival probability of the $5d_{5/2}N_1d$ autoionizing wavepacket at $N_1 \sim 29$. The position of the dip in the total signal is used as a measure of the kepler period of the first wavepacket. This shows the case of exciting a different first wavepacket than that shown in the data in chapter 5.

The total signal from the ionization of ionic rydberg states that we can detect is shown along with the survival probability of the $5d_{5/2}N_1d$ wavepacket as a function of delay between exciting the two wavepackets in Fig.A.1. At times close to the Kepler period of the first electron, the fraction of final ionic rydberg states in lower N is greater than at other times and this appears as a lower signal level in the total ionization signal. The position of this dip in relation to the delay between L2 and L3 can be used as a good estimate of the kepler period of the first wavepacket. FigA.2 shows the total ionization signal when the first wavepacket is changed to $N_1 \sim 29$.

A.2 Effects of Laser Polarization

In the experiments with barium, the detector is always in the same direction in relation to the interaction region. We only detect electrons that are ejected in the vertical direction from the interaction region. However, the atoms do not distinguish between vertical and horizontal as seen by the outside observer but their orientation is fixed by their relation to the polarization direction of the laser beams interacting with them. When the lasers are polarized vertically, the signals from electrons seen at the detector arise due to emission of electrons along the direction of laser polarization. On the other hand, if the lasers are polarized horizontally, the electrons ejected perpendicular to the direction of laser polarization are the ones that are predominantly present at the detector. We can thus change the polarization direction of the laser to look for angular dependence of the emission of electrons [77].

In the experiment creating double rydberg wavepackets, all the lasers are polarized parallel to each other. We have performed this experiment with all the lasers polarized vertically as well as with all the lasers polarized horizontally to see if there is any angular dependence of the signals that we measure [77]. We found that as expected, the signals from the ionization of the final ionic rydberg states does not change when all the polarizations are rotated equally, i.e. the distribution of ionic rydberg states is the same whether all the lasers are polarized vertically or horizontally. This is because all the ions are sent into the second interaction region before field ionization irrespective of their orientation. However, it was found that the fast-electron signal showed a difference in the time-dependent signal strength depending on whether all the lasers were polarized horizontally or vertically.

We monitor the fast-electron signals arising from the decay of the $4fN_1d$ states to determine the survival probability of the $5d_{5/2}N_1d$ autoionizing wavepackets. The scaled autoionization rate (fraction of autoionizing wavepacket that decays at the end of each kepler period) of the $5d_{5/2}N_1d$ wavepackets was measured to be lower in the case where all the lasers are polarized horizontally compared to when the lasers are vertically polarized. Since we monitor the decay of the $4fN_1d$ states, the signals that we observe can be interpreted as the survival probability of the $5dN_1d$ wavepacket only if there is no angular variation in the signal level. The calculated scaled autoionization rate is found to match better with the experiment for the case where the lasers are vertically polarized rather than with the lasers polarized horizontally. van Leeuwen et. al [77] have observed experimentally and in MQDT simulations in calcium that

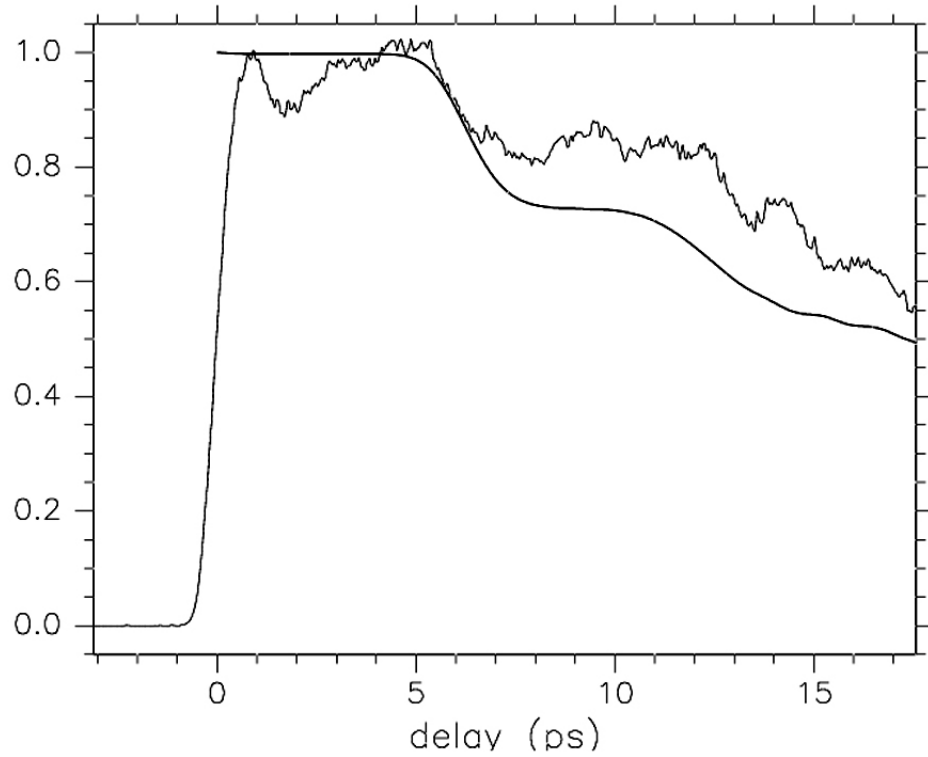


Figure A.3: Fast electron signal when lasers are polarized horizontally
 The fast electron signal in the case where all the lasers are polarized horizontally shows a stair step decay but this does not match the form of the stair-step decay predicted by the K-matrix calculations in chapter 5. The smooth curve is the calculation of the survival probability of the $5d_{5/2}N_1d$ wavepacket with $N_1 \sim 37$ and a bandwidth of 10cm^{-1} for the wavepacket excitation.

autoionization produces electrons that are ejected preferentially along the direction of laser polarization. They [77] have also calculated that ejection of electrons perpendicular to the laser polarization axis is a slow process and occurs over a longer time period than ejection along the laser polarization axis. It could have been such an effect that we see in this experiment except for the fact that we do not excite two bound channels which can interact and create an angular wavepacket. We are currently unable to account for the difference in the form of the fast electron signal ejected in the mutually perpendicular directions in the absence of a radial wavepacket. We have therefore used the data for the decay of the autoionizing $5d_{5/2}N_1d$ wavepackets from the case where all the lasers are vertically polarized since these are best reproduced by the K-matrix MQDT calculations.

The experiments with the double rydberg wavepackets were initially performed with all the lasers polarized horizontally. It was to understand the reasons for the difference in decay rates of the $5d_{5/2}N_1d$ autoionizing wavepackets from the MQDT calculation with K-matrices that we repeated the experiment with vertical polarization of the lasers without changing their central wavelengths or bandwidths. We had better signal-to-noise ratios for the signal from ionization of the ionic rydberg states when the lasers are all polarized horizontally. This could have been due to the fact that the design of the paths used to send the lasers into the interaction region had been initially optimized with horizontally polarized pulses but had to be modified without much optimization of the signals when we checked for the effect of having the lasers vertically polarized. Due to the observation that the only change between

vertical and horizontal polarization as far as the signal from ionization of ionic rydberg states is concerned is a difference in the S/N ratio, the data from ionization of the final ionic rydberg states that is presented in chapter 5 is from the cases where all the lasers are horizontally polarized.

Appendix B

One-electron Atoms

B.1 The Hydrogenic Atom

Consider an isolated hydrogenic atom (an atom with only one electron like H , He^+ , Li^{++} etc). The non-relativistic, time-independent Schrödinger equation for a spinless electron in a central Coulomb potential with the infinite nuclear mass approximation for a hydrogenic atom is (in atomic units)

$$-\left(\frac{1}{2}\nabla^2 + \frac{Z}{r}\right)\psi = E\psi \quad (\text{B.1})$$

where E is the energy of the electron and Z is the charge on the nucleus.

In spherical coordinates, the Laplacian is

$$\nabla^2 = \frac{1}{r^2} \frac{\partial}{\partial r} \left(r^2 \frac{\partial}{\partial r} \right) + \frac{1}{r^2 \sin \theta} \frac{\partial}{\partial \theta} \left(\sin \theta \frac{\partial}{\partial \theta} \right) + \frac{1}{r^2 \sin^2 \theta} \frac{\partial^2}{\partial \phi^2}$$

This allows us to rewrite the Schrödinger equation as

$$\frac{1}{r^2} \frac{\partial}{\partial r} \left(r^2 \frac{\partial \psi}{\partial r} \right) + \frac{1}{r^2 \sin \theta} \frac{\partial}{\partial \theta} \left(\sin \theta \frac{\partial \psi}{\partial \theta} \right) + \frac{1}{r^2 \sin^2 \theta} \frac{\partial^2 \psi}{\partial \phi^2} + 2 \left(E + \frac{Z}{r} \right) \psi = 0 \quad (\text{B.2})$$

We could write the wavefunction $\psi(r, \theta, \phi)$ as a product of three wavefunctions by separation of variables. Let

$$\psi(r, \theta, \phi) = R(r)\Theta(\theta)\Phi(\phi) \quad (\text{B.3})$$

Then we have

$$\frac{\partial \psi}{\partial r} = \Theta\Phi \frac{\partial R}{\partial r} ; \quad \frac{\partial \psi}{\partial \theta} = R\Phi \frac{\partial \Theta}{\partial \theta} ; \quad \frac{\partial^2 \psi}{\partial \phi^2} = R\Theta \frac{\partial^2 \Phi}{\partial \phi^2}$$

Substituting these in Eq.B.2 and multiplying by $\frac{r^2 \sin^2 \theta}{R\Theta\Phi}$ and rearranging the terms, we get

$$-\frac{\sin^2 \theta}{R} \frac{\partial}{\partial r} \left(r \frac{\partial R}{\partial r} \right) - \frac{\sin \theta}{\Theta} \frac{\partial}{\partial \theta} \left(\sin \theta \frac{\partial \Theta}{\partial \theta} \right) - 2r^2 \sin^2 \theta \left(E + \frac{Z}{r} \right) = \frac{1}{\Phi} \frac{\partial^2 \Phi}{\partial \phi^2} \quad (\text{B.4})$$

We see that the left side of the equation is a function of r and θ only while the right hand side of the equation is a function of ϕ alone. This is possible only if both sides are equal to a constant, say $-m^2$ for convenience. This reduces Eq.B.4 to a set of two equations

$$\frac{1}{\Phi} \frac{d^2 \Phi}{d\phi^2} = -m^2 \quad (\text{B.5})$$

and

$$-\frac{\sin^2 \theta}{R} \frac{\partial}{\partial r} \left(r \frac{\partial R}{\partial r} \right) - \frac{\sin \theta}{\Theta} \frac{\partial}{\partial \theta} \left(\sin \theta \frac{\partial \Theta}{\partial \theta} \right) - 2r^2 \sin^2 \theta \left(E + \frac{Z}{r} \right) = -m^2 \quad (\text{B.6})$$

We can rewrite Eq.B.6 as

$$\frac{1}{R} \frac{\partial}{\partial r} \left(r^2 \frac{\partial R}{\partial r} \right) + 2r^2 \left(E + \frac{Z}{r} \right) = \frac{m^2}{\sin^2 \theta} - \frac{1}{\Theta \sin \theta} \frac{\partial}{\partial \theta} \left(\sin \theta \frac{\partial \Theta}{\partial \theta} \right) \quad (\text{B.7})$$

In Eq.B.7, the left side is a function of r alone while the right side is a function of θ alone. So we once again equate both sides to a constant that we can choose as

$l(l+1)$. We can then write the problem of solving the Schrödinger equation for the hydrogenic atom in the form of three ordinary differential equations as

$$\frac{d^2\Phi}{d\phi^2} + m^2\Phi = 0 \quad (\text{B.8})$$

$$\frac{1}{\sin\theta} \frac{d}{d\theta} \left(\sin\theta \frac{d\Theta}{d\theta} \right) + \left[l(l+1) - \frac{m^2}{\sin^2\theta} \right] \Theta = 0 \quad (\text{B.9})$$

$$\frac{1}{r^2} \frac{d}{dr} \left(r^2 \frac{dR}{dr} \right) + 2 \left[E + \frac{Z}{r} - \frac{l(l+1)}{2r^2} \right] R = 0 \quad (\text{B.10})$$

The solution to Eq.B.8 has the form

$$\Phi_m(\phi) = Ae^{im\phi} \quad (\text{B.11})$$

where A is a normalization constant. To get a unique solution, we require that

$$\Phi_m(0) = \Phi_m(2\pi)$$

, i.e. $e^0 = e^{im2\pi}$. We can also write this as

$$1 = \cos(2m\pi) + i \sin(2m\pi)$$

This gives us the quantization condition for m , the magnetic quantum number as $m = 0, \pm 1, \pm 2, \pm 3, \dots$

The orthogonality condition

$$\int_0^{2\pi} \Phi_{m'}^* \Phi_m d\phi = \delta_{m'm}$$

together with normalizing the orthogonal set to unity gives the normalization factor

$A = \frac{1}{\sqrt{2\pi}}$. We then have the solution to Eq.B.8 as

$$\Phi_m(\phi) = \frac{1}{\sqrt{2\pi}} e^{im\phi} \quad m = 0, \pm 1, \pm 2, \pm 3, \dots \quad (\text{B.12})$$

The solution to Eq.B.9 as a function of l, m is given by [143]

$$\Theta_{lm}(\theta) = B \sin^m \theta \cdot P_l^m(\cos \theta) \quad (\text{B.13})$$

where B is the normalization constant and $P_l^m(\cos \theta)$ are the associated Legendre polynomials which are defined as

$$P_l^m(\cos \theta) = (-1)^l \frac{\sin^{|m|} \theta}{2^l l!} \frac{d^{l+|m|}}{(d \cos \theta)^{l+|m|}} \sin^{2l} \theta$$

These polynomials vanish unless $|m| \leq l$ and l is a positive integer. l is called the orbital angular momentum quantum number. The orthogonality condition for the associated Legendre polynomials leads to the normalization constant $B = \sqrt{\frac{(2l+1) \cdot (l-m)!}{2(l+m)!}}$.

We can then write the solution to Eq.B.9 as

$$\Theta_{lm}(\theta) = \sqrt{\frac{(2l+1) \cdot (l-m)!}{2(l+m)!}} \sin^m \theta \cdot P_l^m(\cos \theta) \quad (\text{B.14})$$

$$l = 0, 1, 2, 3, \dots \quad m = 0, \pm 1, \pm 2, \dots, \pm l$$

The products of the two solutions $\Theta_{lm}(\theta)$ and $\Phi_m(\phi)$ are termed as spherical harmonics and represented as

$$Y_l^m(\theta, \phi) = \sqrt{\frac{(2l+1) \cdot (l-m)!}{4\pi(l+m)!}} \sin^m \theta e^{im\phi} P_l^m(\cos \theta) \quad (\text{B.15})$$

To solve the radial part of the wave equation in Eq.B.10, it is convenient to use new variables defined as $\chi = rR$. The resulting wave equation after making the substitutions in Eq.B.10 is [13]

$$\frac{1}{\chi} \frac{d^2 \chi}{dr^2} + 2 \left(E + \frac{Z}{r} - \frac{l(l+1)}{2r^2} \right) = 0 \quad (\text{B.16})$$

The radial wavefunction for bound states should be valid and vanishing for $r \rightarrow \infty$ and $r \rightarrow 0$. As $r \rightarrow 0$,

$$\frac{1}{\chi} \frac{d^2 \chi}{dr^2} - \frac{l(l+1)}{r^2} = 0 \implies \chi = Ar^{l+1} + Br^{-l} \quad (\text{B.17})$$

The condition that $R(r)$ has to be finite as $r \rightarrow 0$ limits the solution to $\chi \propto r^{l+1}$.

As $r \rightarrow \infty$, Eq. B.16 reduces to

$$\frac{1}{\chi} \frac{d^2 \chi}{dr^2} + 2E = 0 \implies \chi \propto e^{\pm i\sqrt{2E}r} \quad (\text{B.18})$$

The case of $E > 0$ corresponds to the states in the continuum. In this case, there are no boundary conditions at $r \rightarrow \infty$ and so the radial wavefunctions are the same as that of a free particle with energy E and the boundary condition at $r \rightarrow 0$ determining the phase of the wavefunction.

$$\implies \chi_{(E>0)} = \alpha \sin(\sqrt{2E}r) + \beta \cos(\sqrt{2E}r) \quad (\text{B.19})$$

For the case of $E < 0$, the boundary conditions lead to the final solution for radial wavefunctions and is given by [13]

$$R_{nl} = N_{nl} \left(\frac{2Zr}{n} \right)^l e^{-i\sqrt{2E}r} \cdot L_{n+l}^{2l+1} \left(\frac{2Zr}{n} \right) \quad (\text{B.20})$$

where N_{nl} is the normalization constant and $L_{n+l}^{2l+1} \left(\frac{2Zr}{n} \right)$ are associated Laguerre polynomials [143]. These polynomials vanish unless $n = 1, 2, 3, \dots, \infty$. n is called the principal quantum number. For a given n , $l = 0, 1, 2, \dots, (n-1)$.

After normalization and resubstitution of variables, the solution to the radial wave equation is given by

$$R_{nl} = \sqrt{\frac{4(n-l-1)!Z^3}{[(n+l)!]^3 n^4}} \left(\frac{2Zr}{n} \right)^l \cdot e^{-Zr/n} \cdot L_{n+l}^{2l+1} \left(\frac{2Zr}{n} \right) \quad (\text{B.21})$$

$$n = 1, 2, 3, \dots, \infty \quad l = 0, 1, 2, \dots, (n-1)$$

We can now write the total wavefunction solutions for a hydrogenic atom as

$$\psi_{nlm} = R_{nl} \Theta_{lm} \Phi_m \quad (\text{B.22})$$

where the individual wavefunction solutions are given by Eq.B.12, Eq.B.14 and Eq.B.21. n , l and m are the principal, orbital and magnetic quantum numbers respectively for the eigenstates.

The probability for finding the electron at any position relative to the nucleus (which is taken to be the origin) is then given by

$$\psi_{nlm}^* \psi_{nlm} = R_{nl}^* R_{nl} \cdot \Theta_{lm}^* \Theta_{lm} \cdot \Phi_m^* \Phi_m \quad (\text{B.23})$$

which is also called the probability density.

The energies of the eigenstates are given by

$$E_n = -\frac{Z^2}{2n^2} \quad (\text{B.24})$$

$$n = 1, 2, 3, \dots$$

B.2 Non-hydrogenic Atoms

In any atom other than hydrogen, the presence of more than one electron modifies the Coulomb potential experienced by a rydberg electron. The effective potential seen by the rydberg electron is a Coulomb potential far from the core outside a critical core radius r_c but is modified close to the core for $r < r_c$. The presence of the additional electrons does not introduce any additional orientation dependence on the rydberg electrons so that the angular wavefunctions are the same for a non-hydrogenic atom as for a hydrogenic atom. We will therefore only consider the changes to the radial wavefunction in the case of a non-hydrogenic atom for $r > r_c$.

The radial part of the Schrödinger equation for the hydrogen atom as we have seen is

$$\frac{1}{\chi} \frac{d^2 \chi}{dr^2} + 2 \left(E + \frac{1}{r} - \frac{l(l+1)}{2r^2} \right) = 0 \quad (\text{B.25})$$

which has two linearly independent normalized solutions $f(\nu, l, r)$ and $g(\nu, l, r)$ [27, 25, 126] with $E = -1/2\nu^2$ for all energies. The asymptotic forms of the f and g functions are such that

$$f(\nu, l, r) \xrightarrow[r \rightarrow 0]{} r^{l+1} \quad ; \quad g(\nu, l, r) \xrightarrow[r \rightarrow 0]{} r^{-l} \quad (\text{B.26})$$

For $r \rightarrow \infty$, the asymptotic forms depend on the sign of E. For $E \geq 0$,

$$\begin{aligned} f(\nu, l, r) &\equiv f(i\gamma, l, r) \xrightarrow[r \rightarrow \infty]{} \sqrt{\frac{2\gamma}{\pi}} \cdot \sin \left[r/\gamma - \frac{1}{2}\pi l + \gamma \ln(2r/\gamma) + \sigma_{(l,\gamma)} \right] \\ g(\nu, l, r) &\equiv g(i\gamma, l, r) \xrightarrow[r \rightarrow \infty]{} -\sqrt{\frac{2\gamma}{\pi}} \cdot \cos \left[r/\gamma - \frac{1}{2}\pi l + \gamma \ln(2r/\gamma) + \sigma_{(l,\gamma)} \right] \end{aligned}$$

where $\sigma_{(l,\gamma)} \equiv \arg \Gamma(l+1-i\gamma)$ (B.27)

and for $E < 0$,

$$\begin{aligned} f(\nu, l, r) &\xrightarrow{r \rightarrow \infty} u(\nu, r) \sin \pi\nu - v(\nu, r) e^{i\pi\nu} \\ g(\nu, l, r) &\xrightarrow{r \rightarrow \infty} -u(\nu, r) \cos \pi\nu + v(\nu, r) e^{i\pi(\nu + \frac{1}{2})} \end{aligned} \quad (\text{B.28})$$

where

$$\begin{aligned} u(\nu, r) &\equiv (-1)^l \sqrt{\nu} \left(\frac{1}{\pi}\right) \left(\frac{\nu}{2r}\right)^\nu e^{r/\nu} \sqrt{\Gamma(\nu - l)\Gamma(\nu + l + 1)} \\ v(\nu, r) &\equiv (-1)^l \sqrt{\nu} \left(\frac{2r}{\nu}\right)^\nu e^{-r/\nu} \left(\sqrt{\Gamma(\nu - l)\Gamma(\nu + l + 1)}\right)^{-1} \end{aligned} \quad (\text{B.29})$$

The most general form of a solution for Eq. B.25 is

$$\chi(\nu, l, r) = f(\nu, l, r) \cos \pi\delta_l - g(\nu, l, r) \sin \pi\delta_l \quad (\text{B.30})$$

where δ_l is determined by the boundary conditions at $r = r_c$ so that the wavefunction is smooth at $r = r_c$. g is not allowed as $r \rightarrow 0$ which necessitates δ_l to be an integer for hydrogenic atoms. The solution $\chi(\nu, l, r) = f(\nu, l, r)$ for hydrogenic atoms is the same result obtained in the previous section. For bound states, the condition that the wavefunction must vanish as $r \rightarrow \infty$ requires the coefficient of u to vanish.

$$\sin(\pi\nu) = 0 \implies \nu = n \equiv \text{integer as in previous section} \quad (\text{B.31})$$

For non-hydrogenic atoms, the condition at $r \rightarrow 0$ does not exist so that Eq. B.30 represents the wavefunction. However, the condition at $r \rightarrow \infty$ still holds, requiring the coefficient of u to be zero.

$$\begin{aligned} \therefore \sin \pi\nu \cos \pi\delta_l + \cos \pi\nu \sin \pi\delta_l &= 0 \\ \implies \sin \pi(\nu + \delta_l) = 0 &\implies \nu + \delta_l = n \equiv \text{integer} \end{aligned} \quad (\text{B.32})$$

The energies of the non-hydrogenic atoms are defined as

$$E = \frac{-1}{2\nu^2} = \frac{-1}{2(n - \delta_l)^2} \quad (\text{B.33})$$

where $n = 1, 2, 3, \dots$

and δ_l is now defined as the “quantum defect”. Experimentally observed spectra are used to find the energy levels of the different elements and the best fit to an analytical expression is used to determine the quantum defect for different states.

We can also write

$$\begin{aligned} \cos(\pi\delta_l) &= \cos(\pi(n - \nu)) = \pm \cos(\pi\nu) \\ \sin(\pi\delta_l) &= \sin(\pi(n - \nu)) = \mp \sin(\pi\nu) \end{aligned} \quad (\text{B.34})$$

The radial wavefunction for the non-hydrogenic atoms can then be rewritten as

$$R_{\nu l} \propto \frac{1}{r} [f(\nu, l, r) \cos(\pi\nu) + g(\nu, l, r) \sin(\pi\nu)] \quad (\text{B.35})$$

Appendix C

Two-Electron Atoms

C.1 Independent particle model

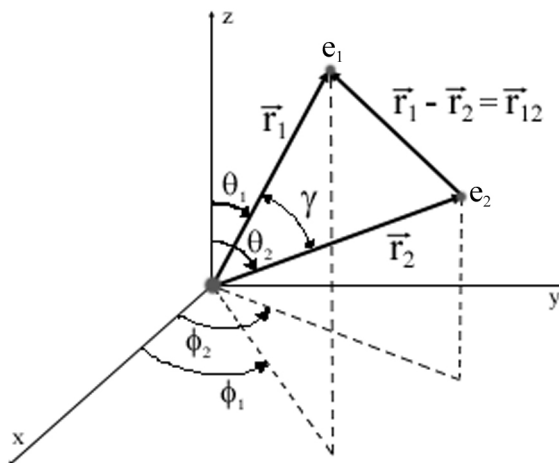


Figure C.1: Two-electron system
The coordinates of the two electrons are relative to the core as the origin.

Consider a two-electron atomic system. The spinless Hamiltonian is

$$H = \left[\frac{1}{2} p_1^2 - \frac{2}{r_1} \right] + \left[\frac{1}{2} p_2^2 - \frac{2}{r_2} \right] + \frac{1}{|\vec{r}_1 - \vec{r}_2|} \quad (\text{C.1})$$

The partial wave expansion of the scalar interaction potential can be written as [144]

$$\frac{1}{|\vec{r}_1 - \vec{r}_2|} = \frac{1}{|\vec{r}_{12}|} = \sum_{k=0}^{\infty} \frac{r_{<}^k}{r_{>}^{k+1}} P_k(\cos \gamma) \quad (\text{C.2})$$

where γ is the angle between the position vectors of the two electrons as shown in FigC.1.

This can be rewritten using the addition theorem for spherical harmonics as [144]

$$\frac{1}{|\vec{r}_{12}|} = 4\pi \sum_{l=0}^{\infty} \sum_{m=-l}^l \frac{1}{2l+1} \frac{r_{<}^l}{r_{>}^{l+1}} Y_{lm}^*(\theta_1, \phi_1) Y_{lm}(\theta_2, \phi_2) \quad (\text{C.3})$$

Using spherical tensor operators C_q^k which are defined as [143]

$$\overleftrightarrow{C}_q^k = \sqrt{\frac{4\pi}{2k+1}} Y_q^k(\theta, \phi), \quad (\text{C.4})$$

we can write the scalar interaction potential as

$$\frac{1}{|\vec{r}_{12}|} = \sum_{k=0}^{\infty} \frac{r_{<}^k}{r_{>}^{k+1}} \overleftrightarrow{C}_1^{(k)} \cdot \overleftrightarrow{C}_2^{(k)} \quad (\text{C.5})$$

We will only consider the case where one electron (say “1”) is in a rydberg state while the other electron (“2”) is in a low excited state so that $r_{>} = r_2$ and $r_{<} = r_1$ for all but a negligible fraction of their respective wavefunctions. We can then expand EqC.5 as

$$\frac{1}{r_{12}} = \underbrace{\frac{1}{r_2}}_{\text{monopole}} + \underbrace{\frac{r_1}{r_2^2} \overleftrightarrow{C}_1^{(1)} \cdot \overleftrightarrow{C}_2^{(1)}}_{\text{dipole}} + \underbrace{\frac{r_1^2}{r_2^3} \overleftrightarrow{C}_1^{(2)} \cdot \overleftrightarrow{C}_2^{(2)}}_{\text{quadrupole}} + \dots \quad (\text{C.6})$$

If we retain only the monopole term, the Hamiltonian reduces to

$$H = \left[\frac{1}{2} p_1^2 - \frac{2}{r_1} \right] + \left[\frac{1}{2} p_2^2 - \frac{1}{r_2} \right] \quad (\text{C.7})$$

This represents an independent particle system where particle 1 sees a charge of +2 while particle 2 sees a charge of +1. The total wavefunction is the product of the two wavefunctions and the energy is the sum of the energies of the two particles.

We can now include the effect of higher order terms in the electron-electron interaction as a perturbation to the independent particle model. If we denote the state of the doubly excited system as $|\psi_{ij}\rangle = |\phi_i\rangle \cdot |\xi_j\rangle$ where $|\phi\rangle$ and $|\xi\rangle$ are complete basis sets of the independent particle wavefunctions for particles 1 and 2 respectively, then the wavefunctions and energies of the system with the inclusion of the electron-electron correlation as a perturbation can be represented as

$$|\psi\rangle = |\psi_{ij}\rangle + \sum_{k \neq i, l \neq j} \frac{\langle \phi_k \cdot \xi_l | V_{dipole} + V_{quadrupole} + \dots | \phi_i \cdot \xi_j \rangle}{E_{\phi_i \xi_j} - E_{\phi_k \xi_l}} \quad (\text{C.8})$$

and

$$E_\psi = E_{\phi_i} + E_{\xi_j} + \sum_{k \neq i, l \neq j} \frac{|\langle \phi_k \cdot \xi_l | V_{dipole} + V_{quadrupole} + \dots | \phi_i \cdot \xi_j \rangle|^2}{E_{\phi_i \xi_j} - E_{\phi_k \xi_l}} \quad (\text{C.9})$$

These expressions represent a lot of terms to be added to get the energy of any state. To overcome this problem, we make use of the assumption that the energy states of the ion as experienced by the inner electron are separated to a much greater extent than the energy states of the rydberg electron. This is a valid assumption for this problem since energy separation between successive states varies with the principal quantum number as Z^2/n^3 . This allows us to calculate the interaction

for an entire configuration corresponding to a set of quantum numbers for the two electrons over a range of energies of the outer electron. These configurations are also termed as “channels”.

C.2 Multichannel Quantum Defect Theory (MQDT)

We define channels as a series of states corresponding to a certain configuration of quantum numbers for two electrons over a range of energies of the outer electron. The presence of the inner electron in an excited state is assumed to have an effect of introducing a phase shift to the wavefunction of the rydberg electron and the phase shift is termed as a quantum defect in the same way as in the case of one-electron non-hydrogenic atoms discussed in Appendix A.

The wavefunction of the rydberg electron in any channel i can be written as

$$\phi_i \propto \frac{1}{r} [f(E_i, l_i, r) \cos(\pi\nu_i) + g(E_i, l_i, r) \sin(\pi\nu_i)] \zeta_i \quad (\text{C.10})$$

where ζ_i contains all the angular and spin parts of the wavefunction along with the radial wavefunction for the inner electron. E_i is the energy with respect to the ionization limit in the i^{th} channel and ν_i is determined by the boundary conditions.

The non-hydrogenic atoms have no boundary conditions at $r \rightarrow 0$ and for $E_i \geq 0$, there are no boundary conditions at $r \rightarrow \infty$. So ν_i is undetermined for energies in the continuum. For bound states, the boundary condition at $r \rightarrow \infty$ requires $E_i = -\frac{1}{\nu_i^2}$.

At distances close to the core and $r < r_c$, the phase of the wavefunction is independent of E_i [25]. At distances close to the core, the independent particle model

eigenstates are no longer a valid basis set. We can therefore write the wavefunctions near the core as

$$\psi_\alpha \propto \frac{1}{r} \sum_i \zeta_i U_{i\alpha} [f(\nu_i, l_i, r) \cos(\pi\mu_\alpha) - g(\nu_i, l_i, r) \sin(\pi\mu_\alpha)] \quad (\text{C.11})$$

where ψ_α is assumed to be energy normalized,

$U_{i\alpha}$ is an energy independent unitary rotation matrix,

and μ_α is an energy independent phase shift.

ψ_{alpha} and ϕ_i form the two complete basis sets of the wavefunction, which can be expressed as a linear combination in either basis set. Let the total wavefunction be represented by

$$\Psi = \sum_i A_i \phi_i = \sum_\alpha B_\alpha \psi_\alpha \quad (\text{C.12})$$

Since $\zeta_i f_i$ and $\zeta_i g_i$ are linearly independent, we can equate Eq. C.10 and Eq. C.11 at any value of r so that

$$\sum_i A_i [f_i \zeta_i \cos(\pi\nu_i) + g_i \zeta_i \sin(\pi\nu_i)] = \sum_\alpha \sum_i B_\alpha U_{i\alpha} [f_i \zeta_i \cos(\pi\mu_\alpha) - g_i \zeta_i \sin(\pi\mu_\alpha)] \quad (\text{C.13})$$

$$\implies A_i \cos(\pi\nu_i) = \sum_\alpha B_\alpha U_{i\alpha} \cos(\pi\mu_\alpha) \quad (\text{C.14a})$$

$$A_i \sin(\pi\nu_i) = - \sum_\alpha B_\alpha U_{i\alpha} \sin(\pi\mu_\alpha) \quad (\text{C.14b})$$

We can multiply Eqs.C.14a and C.14b by $\sin \pi \nu_i$ and $\cos \pi \nu_i$ respectively and adding and subtracting them with each other leads to

$$A_i = \sum_{\alpha} U_{i\alpha} B_{\alpha} \cos \pi(\nu_i + \mu_{\alpha}) \quad (\text{C.15a})$$

$$0 = \sum_{\alpha} U_{i\alpha} B_{\alpha} \sin \pi(\nu_i + \mu_{\alpha}) \quad (\text{C.15b})$$

We can also use the fact that $U_{i\alpha}$ is unitary, i.e. $\underline{U}^T = \underline{U}^{-1}$ to multiply both sides of Eqs.C.14a and C.14b by $U_{i\alpha}$ and sum over i to get

$$\sum_i U_{i\alpha} A_i \cos(\pi \nu_i) = B_{\alpha} \cos(\pi \mu_{\alpha}) \quad (\text{C.16a})$$

$$\sum_i U_{i\alpha} A_i \sin(\pi \nu_i) = -B_{\alpha} \sin(\pi \mu_{\alpha}) \quad (\text{C.16b})$$

We can multiply Eqs.C.16a and C.16b by $\cos \pi \mu_{\alpha}$ and $-\sin \pi \mu_{\alpha}$ respectively and adding and subtracting them with each other leads to

$$B_{\alpha} = \sum_i U_{i\alpha} A_i \cos \pi(\nu_i + \mu_{\alpha}) \quad (\text{C.17a})$$

$$0 = \sum_i U_{i\alpha} A_i \sin \pi(\nu_i + \mu_{\alpha}) \quad (\text{C.17b})$$

Eqs.C.15a and C.17a have a non-trivial solution iff

$$\det |U_{i\alpha} \sin \pi(\nu_i + \mu_{\alpha})| = 0 \quad (\text{C.18})$$

For a system with N channels, Eqn. C.18 defines the $(N-1)$ -dimensional quantum defect surface. Plots of the quantum defect surface are termed Lu-Fano plots [126,25].

C.3 R-matrix formulation

Eq.C.18 represents a set of N simultaneous equations. There are N^2 elements in $U_{i\alpha}$ and N elements of μ_α . However, the unitary matrix \underline{U} has $N(N-1)/2$ independent elements so that the solution to Eq. C.18 is not unique. For a system with one electron in a rydberg state, the rydberg electron spends most of its time far from the core so that most of the properties of the system can be understood by knowing the values A_i to determine the wavefunction of the rydberg electron far from the core.

We can rewrite Eq. C.17b as

$$\begin{aligned}
0 &= \sum_i U_{i\alpha} A_i \sin \pi(\nu_i + \mu_\alpha) \\
&= \sum_i U_{i\alpha} A_i [\sin \pi\nu_i \cos \pi\mu_\alpha + \cos \pi\nu_i \sin \pi\mu_\alpha] \\
&= \cos \pi\mu_\alpha \left\{ \sum_i U_{i\alpha} A_i [\sin \pi\nu_i + \cos \pi\nu_i \tan \pi\mu_\alpha] \right\} \\
\implies 0 &= \sum_i U_{i\alpha} [\tan \pi\nu_i + \tan \pi\mu_\alpha] \underbrace{\cos \pi\nu_i A_i}_{a_i} \\
\implies \underline{0} &= [\underline{U}^T \underline{\tan \pi\nu} + \underline{\tan \pi\mu} \underline{U}^T] \underline{a} \tag{C.19}
\end{aligned}$$

Multiplying both sides by \underline{U} , we get

$$\underline{0} = [\underline{\tan \pi\nu} + \underbrace{\underline{U} \underline{\tan \pi\mu} \underline{U}^T}_R] \underline{a} \tag{C.20}$$

$$\implies \underline{0} = [\underline{\tan \pi\nu} + \underline{R}] \underline{a} \tag{C.21}$$

Since $\underline{\tan \pi\nu}$ is diagonal and \underline{R} is symmetric, the problem is reduced to finding $N(N+1)/2$ elements. This is a factor of 2 reduction in the number of elements to

be determined compared to Eq. C.18. This can be further transformed to separate the diagonal and off-diagonal matrix elements by defining \underline{R}' which has no diagonal elements, $\nu'_i = \nu_i + \delta_i$ and $a'_i = A_i \cos \pi \nu'_i$ so that

$$[\underline{\tan \pi \nu'} + \underline{R}'] \underline{a}' = \underline{0} \quad (\text{C.22})$$

where

$$\underline{R}' = [\underline{\cos \pi \delta} + \underline{R} \underline{\sin \pi \delta}]^{-1} \cdot [\underline{R} \underline{\cos \pi \delta} - \underline{\sin \pi \delta}] \quad (\text{C.23})$$

Since \underline{R}' is off-diagonal, all solutions occur for $\tan \pi \nu_i = 0$, i.e. for integer values of ν' . The solutions represent a set of non-interacting rydberg series with a constant quantum defect δ_i for each series. Eqs.C.21 and C.22 are equivalent to Eq.C.18. The quantum defect surface can be evaluated as

$$\det |\underline{\tan \pi \nu} + \underline{R}| = 0 \quad (\text{C.24})$$

or

$$\det |\underline{\tan \pi \nu'} + \underline{R}'| = 0 \quad (\text{C.25})$$

If we have n_b bound and n_c continuum channels then we can rewrite Eq. C.22 in blocks as

$$\begin{bmatrix} [\underline{R}' + \underline{\tan \pi \nu'}]_{bb} & \underline{R}'_{bc} \\ \underline{R}'_{cb} & [\underline{R}' + \underline{\tan \pi \nu'}]_{cc} \end{bmatrix} \begin{bmatrix} \underline{a}'_b \\ \underline{a}'_c \end{bmatrix} = \underline{0} \quad (\text{C.26})$$

where b and c correspond to the bound and continuum channels. Expanding Eq.C.26, we get

$$[\underline{R}' + \underline{\tan \pi \nu'}]_{bb} \underline{a}'_b + \underline{R}'_{bc} \underline{a}'_c = 0 \quad (\text{C.27})$$

$$\text{and } \underline{R}'_{cb} \underline{a}'_b + [\underline{R}' + \underline{\tan \pi \nu'}]_{cc} \underline{a}'_c = 0 \quad (\text{C.28})$$

which can be solved to get

$$\underline{a}'_b = - [\underline{R}' + \underline{\tan \pi \nu'}]_{bb}^{-1} \underline{R}'_{bc} \underline{a}'_c \quad (\text{C.29})$$

$$\implies \left\{ \underline{R}'_{cb} [\underline{R}' + \underline{\tan \pi \nu'}]_{bb}^{-1} \underline{R}'_{bc} - \underline{R}'_{cc} \right\} \underline{a}'_c = \underline{\tan \pi \nu'}_{cc} \underline{a}'_c \quad (\text{C.30})$$

Since $\underline{\tan \pi \nu_{cc}}$ has no relation to the energy of the system, we can choose ν_{cc} to be any value to solve the equation. The matrix elements of $\underline{\tan \pi \nu_{cc}}$ act as the n_c eigenvalues of this problem [126, 109]. We use $\sum_i^{n_c} \left| \frac{a'_i}{\cos \pi \nu'_i} \right|^2 = 1$ to normalize \underline{a}'_c and use \underline{a}'_c to calculate \underline{a}'_b and eventually A_i for all the channels.

We can thus use these MQDT R' -matrices (or R -matrices) to calculate the spectral amplitude from any channel in a two-electron system to compute the wavefunction of the system.

Appendix D

Imaging Stark Spectra

This appendix contains the publication of the experiment to study the stark spectrum of sodium and use it to calculate scaled energy spectra in which the recurrences are interpreted as corresponding to different kinds of orbits of electrons in an atom in the presence of an electric field.

PHYSICAL REVIEW A, VOLUME 61, 063405

Imaging atomic Stark spectra

S. N. Pisharody, J. G. Zeibel, and R. R. Jones
 Department of Physics, University of Virginia, Charlottesville, Virginia 22901
 (Received 28 October 1999; published 8 May 2000)

Photoabsorption spectra have been measured as a continuous function of energy and applied electric field for the $m=0, 1,$ and 2 Rydberg series in sodium. The spectra are Fourier transformed in scaled coordinates, generating scaled recurrence maps. The continuous nature of the scaled maps allows us to investigate patterns in the recurrence strength with good resolution.

PACS number(s): 32.60.+i, 32.80.Rm, 39.30.+w

I. INTRODUCTION

Electron dynamics in the presence of strong static electric fields continues to be a topic of considerable interest in atomic physics. The large spatial extent of Rydberg atoms makes them extremely sensitive to applied fields and, therefore, particularly interesting in this context. The dynamics of nonhydrogenic Rydberg electrons in the presence of the static field depend greatly on the relative strengths of the average Coulomb binding field and the applied electric field as well as the size of the non-Coulombic parts of the binding potential. In the frequency domain, these quantities determine the relative sizes of the energy splittings between (i) states of different principal quantum number $n, \Delta E_n \approx 1/n^3$; (ii) states of different parabolic quantum numbers $k, \Delta E_k \approx 3Fn$; and (iii) states with different Stark shifts undergoing avoided level crossings, ΔE_x . We use atomic units throughout and assume $n \gg 1$. In the time domain, the important time scales are the inverse of the energy splittings noted above: $\tau_{\text{Kepler}} = 2\pi n^3$ is the time required for a classical Rydberg atom to move from the nucleus to the outer turning point of the radial potential and back; $\tau_{\text{Stark}} = 2\pi/3Fn$ is the time required for the angular momentum of a classical electron to precess in the field from its initial value through all possible values and back; and $2\pi/\Delta E_x$ is the time required for an electron in a classical orbit aligned with the field to scatter into an orbit aligned opposite to the field due to precession of the Runge-Lenz vector in the non-Coulombic potential [1].

While experimental [2,3] and theoretical [4] time and frequency domain studies on this subject abound, relatively few provide a comprehensive quantitative view of the electron dynamics within a specific atom due to the large parameter space that must be investigated [5]. We have applied an imaging detection system to collect frequency domain photoabsorption spectra as a continuous function of excitation energy and static electric field. We have used Fourier transform analysis of the two-dimensional spectra to identify features in the global dynamics.

In the experiment, an entire Stark map is measured. Each map is a landscape of photoabsorption strength as a function of excitation energy and applied electric field [6]. The map can also be presented using "scaled variables," namely, scaled energy and scaled action [7]. Scaled energy is defined as the quantity $\epsilon = EF^{-1/2}$ where E is the energy relative to the zero field ionization limit and F is the applied electric field in atomic units. Scaled action is the Fourier transform variable conjugate to $\omega = F^{-1/4}$. This scaling is based on

transformation properties of the classical Hamiltonian of a hydrogen atom in an electric field, which can be written in cylindrical coordinates as

$$H = \frac{1}{2} (p_z^2 + p_\rho^2) - \frac{1}{\sqrt{\rho^2 + z^2}} + Fz. \quad (1)$$

After multiplication by $F^{-1/2}$ and the following change of variables,

$$\hat{\rho} = \rho F^{1/2}, \quad \hat{z} = z F^{1/2}, \quad (2)$$

$$\hat{p}_\rho = p_\rho F^{-1/4}, \quad \hat{p}_z = p_z F^{-1/4}, \quad (3)$$

$$\hat{t} = t F^{1/4}, \quad (4)$$

the Hamiltonian becomes

$$\hat{H} = H F^{-1/2} = \frac{1}{2} (\hat{p}_z^2 + \hat{p}_\rho^2) - \frac{1}{\sqrt{\hat{\rho}^2 + \hat{z}^2}} + \hat{z}. \quad (5)$$

This scaled Hamiltonian depends only on the scaled energy ϵ , and not on the applied field or excitation energy independently. For any given value of the scaled energy, the classical dynamics of the system do not depend independently on the binding energy and static field. The electron dynamics are revealed by Fourier transforming the photoabsorption strength I with respect to the scaled variable ω , at constant scaled energy ϵ . Resonance peaks in this "recurrence" spectrum are associated with electrons moving around the nucleus in classical periodic orbits that are closed at the atomic core [7,8].

Previous experiments in which electron dynamics were studied using recurrence spectroscopy have relied on simultaneous variation of the electric field and laser frequency to measure $I(\omega)$ at constant scaled energy [7,9–12]. Using this technique, identification of global trends in the spectra as a function of scaled energy is difficult, since typically only a small number of discrete scaled energy spectra can be measured in any reasonable amount of time. For example, Eichmann et al. looked at sodium spectra, but only for $\epsilon = -2.5$ [7]. Hogervorst and co-workers have studied the specific scaled energies of $\epsilon = -2.94, -2.35,$ and -1.76 in great detail with good experimental accuracy in barium [10]. While their choices of scaled energies represent points both above and below the classical ionization limit ($\epsilon = -2.0$), the work does not provide complete information on the evo-

S. N. PISHARODY, J. G. ZEIBEL, AND R. R. JONES

PHYSICAL REVIEW A 61 063405

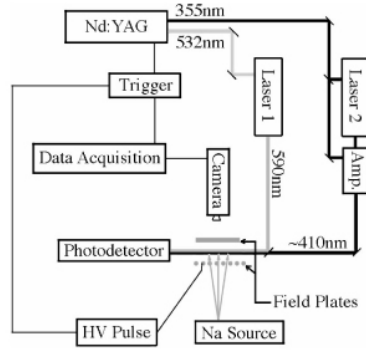


FIG. 1. A schematic representation of the experimental apparatus. Parallel wires connected through a resistor chain create a field gradient which enables spectroscopic measurements to be made over a continuous range of applied field.

lution of electron dynamics as a function of scaled energy. Courtney et al. [5,9] were the first to look for global patterns in experimental recurrence spectra. They measured photoabsorption spectra over a quasicontinuous range of scaled energies from $\epsilon = -2.6$ to $\epsilon = -4.0$ in steps of $\Delta\epsilon = 0.1$ [5]. They discovered recurrence maxima in their Li data that had no analog in computed hydrogen spectra. These features were attributed to combination orbits, apparently caused by scattering from the nonhydrogenic core. The work of Keeler and Morgan [12] in helium has come the closest to observing a recurrence spectrum that was continuous in scaled energy, with individual scaled energy scans separated by $\Delta\epsilon = 0.02$ from $\epsilon = -2.0$ to $\epsilon = -3.4$. From their recurrence maps, Keeler and Morgan identified combination orbits as well as a periodic modulation of the scaled-energy-integrated recurrence strengths within various sequences of resonance peaks corresponding to different periodic orbits [12].

While quantum simulations can reproduce the experimental data, much of the real insight into electron dynamics in external fields has come from classical and semiclassical analyses [1–4,7,8,13–15]. In particular, closed orbit theory has provided an elegant semiclassical explanation for the majority of the experimental results observed in recurrence spectroscopy [7,8]. The theory relates the observed maxima in the recurrence spectrum to the probability for launching an electron into a particular closed orbit. Despite its successes, the original theory, which assumed hydrogenic atoms, did not account for all of the observed features in the nonhydrogenic spectra [5,7,8]. In a modification of the theory, electrons incident on the nonhydrogenic core have a finite probability of being scattered into all possible orbits, leading to the observed ‘‘combination’’ peaks in the recurrence spectra [5,10,11]. However, current semiclassical theory has not yet reproduced all the details in measured nonhydrogenic recurrence spectra [5,10,11]. Shaw and Robicheaux have compared quantum scaled energy calculations with semiclassical closed orbit theory for H, K, and Cs [13]. They found slight deviations between the quantum and closed orbit calculations

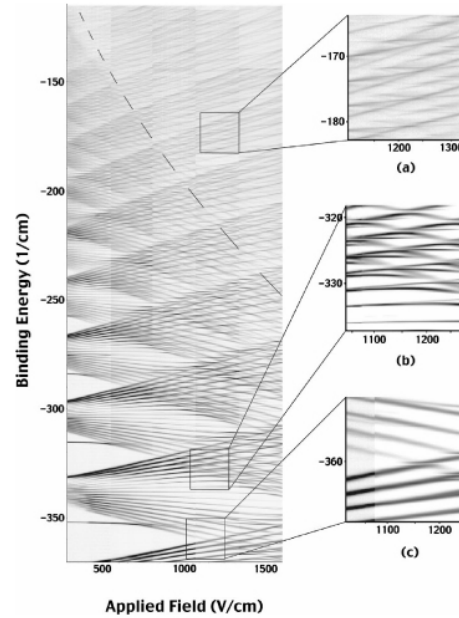


FIG. 2. Density plot of the measured Stark map of sodium for parallel field and laser polarization, $m=0,1$. Dark regions represent high excitation probability. Expanded views of selected locations in the spectrum can be found in insets (a), (b), and (c). In particular, (c) shows the avoided crossing of the $n=18$ downhill state with the $n=17$ uphill state. Such crossings between the n and $n+1$ manifolds for $17 \leq n \leq 21$ are used as an absolute field calibration. The dashed line is the classical field ionization limit, $F = 1/16n^4$.

near the locations of recurrence maxima, which they were able to account for with a correction term. They also investigated patterns observed within a given recurrence maximum as a function of scaled energy, but did not identify any overall trends.

The goal of the work described here is to investigate variations in the recurrence strength as a continuous function of scaled energy and scaled action, thereby providing a better understanding of electron dynamics in a combined Stark-Coulomb system (in this case, the sodium atom). Recurrence spectra are collected over a range of scaled energies $-4.5 \leq \epsilon \leq -1.5$ and scaled actions $0 \leq S \leq 30$. In the following sections, we describe our experimental procedure and numerical analysis of the data. We introduce a set of modified scaled parameters that guides our interpretation of the data. We then compare our results with quantum simulations for Na and H. We conclude with a brief summary of our findings.

II. EXPERIMENTAL SETUP

Figure 1 shows a schematic of the experiment. Thermally excited Na atoms from a resistively heated oven interact with

IMAGING ATOMIC STARK SPECTRA

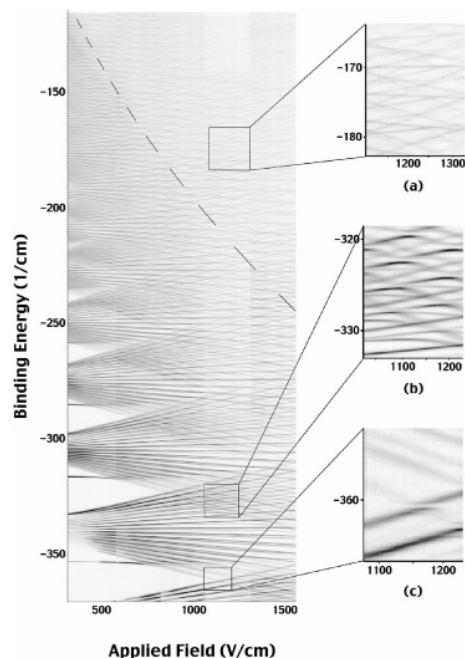


FIG. 3. Density plot of the measured Stark map for sodium for perpendicular field and second laser polarization, $m=0,1,2$. Dark regions represent high excitation probability. The $m=2$ features dominate the spectrum. Note that unlike the $m=0$ case, the $m=2$ oscillator strength is predominantly located in the center of each manifold. Therefore, the center manifold states are more visible in this figure than in the corresponding $m=0$ data in Fig. 2. Expanded views of selected locations in the spectrum can be found in insets (a), (b), and (c). The dashed line is the classical field ionization limit, $F = 1/16n^4$.

two copropagating nanosecond dye lasers in a spatially inhomogeneous electric field. The two lasers are pumped at a 15 Hz repetition rate by the second and third harmonics of a Nd:YAG (where YAG is yttrium aluminum garnet) laser, respectively. The first laser excites the 3S ground state Na atoms to an intermediate $3P_{1/2}$, $|m_j| = \frac{1}{2}$ state. The second laser pulse is delayed relative to the first by ~ 5 ns and is linearly polarized either perpendicular or parallel to the applied electric field. The parallel and perpendicular polarizations allow for excitation of pure $|m_j| = \frac{1}{2}$ or $|m_j| = \frac{1}{2}, \frac{3}{2}$ states, respectively. The frequency of the second dye laser is tunable, permitting the excitation of the $3P_{1/2}$ atoms to Rydberg states with principal quantum number $17 \leq n \leq 30$. The second dye laser is in a double-grating Littman configuration [16] and it has a linewidth of 0.14 cm^{-1} . The spatially varying electric field is prepared using a parallel plate geometry with a voltage gradient along the lower field "plate." The field gradient is produced by a set of 13 parallel wires in a

PHYSICAL REVIEW A 61 063405

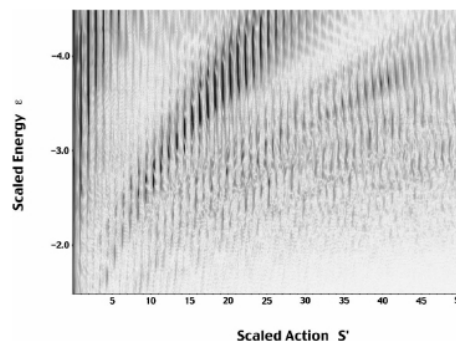


FIG. 4. Density plot of the measured scaled energy recurrence map of $m=0,1$ in sodium. The action axis used here differs by a factor of $\sqrt{2\epsilon}$ from those in previous studies. This action coordinate S' identifies the number of primary Kepler orbits. In contrast to previous work, the recurrence map represents the Fourier transform of the scaled data, not the square of the Fourier transform. This choice makes it easier to see small features in the recurrence strength.

resistor chain with a fixed voltage difference applied to the two ends of the chain. By keeping the distance between adjacent wires much smaller than the distance from the wires to the interaction region, the horizontal component of the electric field is minimized. The top field plate is 7.5 cm on a side. The lower plate wires are fixed 12 mm below the top plate and are each separated by 2 mm. The atomic beam enters the interaction region ~ 5 mm below the top plate.

Fifty nanoseconds following the Rydberg state excitation, a strong voltage pulse (~ 10 kV) is applied to all the wires in the resistor chain. Any Rydberg atoms produced by the laser are ionized either by the static field or by the voltage pulse. The resulting ions are accelerated toward a microchannel plate assembly through a $1.6 \text{ mm} \times 25 \text{ mm}$ slit in the top field plate. The microchannel plates generate electrons in di-

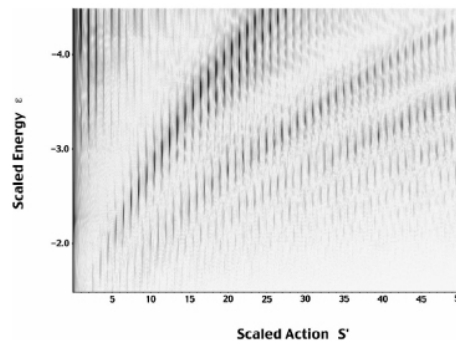


FIG. 5. Density plot of the measured scaled energy recurrence map of $m=2$ in sodium analogous to Fig. 4.

S. N. PISHARODY, J. G. ZEIBEL, AND R. R. JONES

PHYSICAL REVIEW A 61 063405

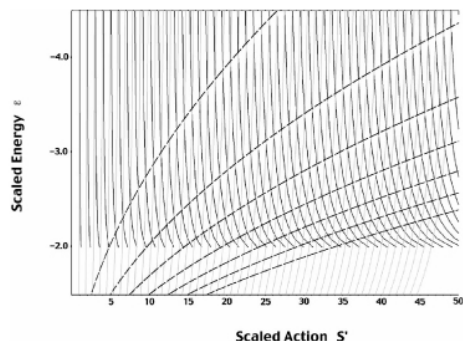


FIG. 6. Scaled actions of the primary hydrogenic uphill and downhill orbits and their repetitions as a function of scaled energy. The dark lines represent the uphill orbits, while the lighter lines represent the downhill orbits. To a good approximation, for $\epsilon < -2.5$, the i th repetition of the uphill orbit crosses the $(i+j)$ th repetition of the downhill orbit at $S' = i + j/2$. The dashed curves are the expression $\epsilon = \sqrt{3(S' + j/2)/4j}$, which identifies the crossing of the i th downhill orbit with the $(i+j)$ th uphill orbit. The approximate expression is valid for $\epsilon \leq -2.5$.

rect proportion to the number of incident ions, and these electrons are accelerated toward a phosphor screen that lies directly behind the microchannel plates. The electron-induced fluorescence from the phosphor is observed with a charge-coupled device (CCD) camera. The ionization yield as a function of position along the slit in the upper field plate is directly proportional to the excitation probability versus electric field. The range of electric fields present in the interaction region is determined by the difference in the voltages applied to the two ends of the lower "plate" resistor chain. To avoid severe nonlinearity in the field gradient, only signal originating beneath the central 50% of the extraction slit is used to generate the Stark map. The frequency of the second laser is scanned to generate a portion of a Stark map that is continuous in both energy and applied field.

In this experiment, each dye laser scan covers electron binding energies from -114.5 cm^{-1} to -371.2 cm^{-1} and a field range of approximately 300 V/cm. Five laser scans covering different field ranges are combined to produce a single Stark map over a field range from 300 V/cm to 1600 V/cm. Relative frequency calibration is achieved by monitoring the second laser transmission through a 2 mm solid étalon. The envelope of the maxima in the étalon fringe pattern is used as a normalization to correct for variations in laser intensity over the scans. Absolute frequency calibration is obtained from the known zero field s state energies. The electric field is calibrated using the theoretically calculated fields at the center of the avoided crossings of the reddest state of the $(n+1)$ th manifold with the bluest state of the n th manifold for $17 \leq n \leq 21$. Figures 2(c) and 3(c) show the avoided crossing of the reddest state of the $n=18$ manifold with the bluest state of the $n=17$ manifold for parallel and perpendicular laser polarization, respectively. Relative field calibra-

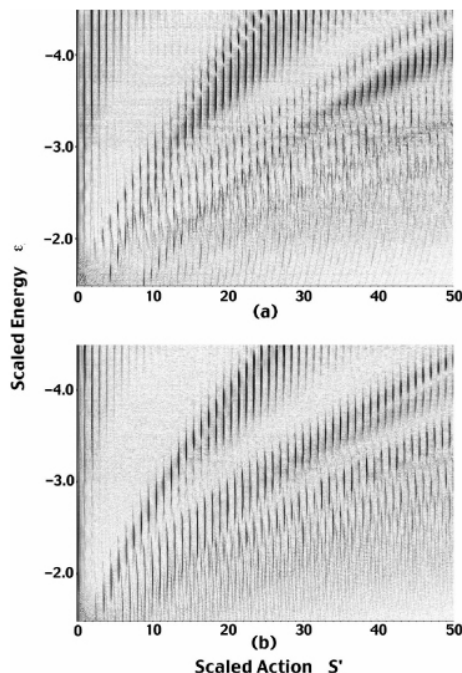


FIG. 7. Density plot of quantum calculations of the recurrence spectra of sodium. (a) shows the recurrence map with $m=0,1$ character weighted to match the experimental conditions for parallel laser polarization, while (b) shows the recurrence map with the $m=0,1,2$ characters weighted to match the perpendicular polarization case (primarily $m=2$).

tion is performed by tracking the position of a particular feature in the Stark map as the voltage offset applied to the resistor chain is varied.

Figures 2 and 3 show two Stark maps for parallel and perpendicular second laser polarization, respectively. While $m=0,1,2$ states contribute to the image in Fig. 3, the $m=2$ structure dominates. Henceforth we refer to Fig. 3 as the $m=2$ spectrum. In Fig. 2, the $m=0$ and 1 resonances have relative weights of 1:2. These Stark maps may be used to generate recurrence maps by rescaling the energy and field axes as described above, and Fourier transforming with respect to $\omega = F^{-1/4}$. However, we use a different method for displaying scaled spectroscopic data. Instead of Fourier transforming with respect to ω , we divide ω by the factor $\sqrt{2|\epsilon|}$, yielding $\omega' = 1/\sqrt{2|E|} = n^*$. Conversion to ω' before Fourier transforming serves two purposes. First, the dependence on field is removed from the new action coordinate S' , eliminating uncertainties due to the field calibration or inhomogeneity. Second, in these units the strongest recurrences are localized at integer or half-integer values of the independent variable S' .

IMAGING ATOMIC STARK SPECTRA

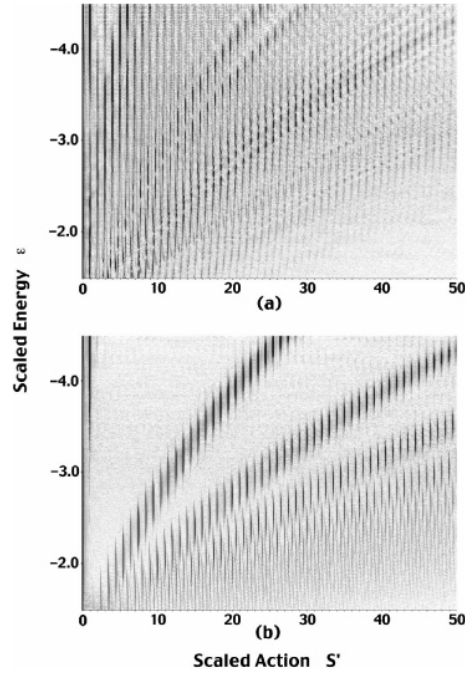


FIG. 8. Density plot of quantum theoretical calculations of the recurrence spectra in hydrogen. (a) shows the $m=0$ spectrum and (b) shows the $m=2$ spectrum.

The experimental results for $m=0,1$ (Fig. 4) and $m=2$ (Fig. 5) show clear sequences of recurrence maxima. The $m=2$ sequences are more separated and distinct than the corresponding sequences for $m=0,1$. The cross section for excitation of $m=2$ Stark spectra is larger near the center of the manifolds, while for $m=0$ the oscillator strength is peaked near the highest and lowest energy states in each Stark manifold. The Fourier transform of the $m=2$ data displays better resolved sequences in the recurrence map as the periodicity of the center of the Stark manifolds is quite evident. Successive manifolds are relatively unaffected by neighboring ones due to the small quantum defect of the higher m states. However, in the $m=0, 1$ spectra, neighboring Stark manifolds interact quite strongly due to the larger quantum defect. The strong intermanifold periodicity that was evident in the $m=2$ spectrum is not as pronounced.

In the $m=2$ recurrence map, peaks in recurrence strength occur at either integer or half-integer values of the action coordinate S' . Up to nine separate sequences of maxima are observed, each occurring for $S'=j$ or $S'=j+\frac{1}{2}$, for $j=1,2,3,\dots$. To a good approximation, for $\epsilon < -2.5$, the $m=0,1$ spectra also show maxima located primarily at either integer or half-integer values of S' . Over this range of scaled

PHYSICAL REVIEW A 61 063405

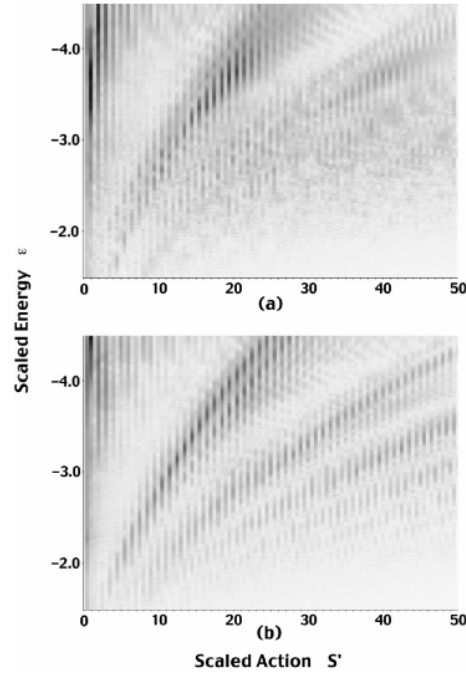


FIG. 9. Density plot of the experimental recurrence spectra of sodium with the area around each integer and half-integer value of scaled action integrated. (a) shows the recurrence map with $m=0,1$ character, while (b) shows the integrated recurrence map with mainly $m=2$ character.

energies, the actions of the "uphill" and "downhill" repetition orbits of hydrogen cross each other at integer or half-integer values of S' as well (see Fig. 6). Roughly, for $m=0,1$, the maxima in recurrence strengths occur when an uphill and downhill orbit share the same value of S' . Sequence l maxima occur at the intersection of the i th uphill and $(i+1)$ th downhill repetition orbits. For $\epsilon < -2.5$ in sequence l , these crossings occur at $S'=(i+1/2)$. More generally, sequence j maxima appear at the intersection of the i th repetition of the uphill orbit with the $(i+j)$ th repetition of the downhill orbit at $S'=i+j/2$. Figure 6 shows action versus scaled energy for the primary uphill and downhill orbits in hydrogen. It should be noted that for $\epsilon > -2.5$ the crossings of the uphill and downhill orbits and the associated maxima in the recurrence strength diverge from integer and half-integer values of S' .

III. ANALYSIS AND DISCUSSION

A. Theoretical simulations

Our experimental results can be compared to full quantum simulations. Quantum-mechanical calculations of the Stark

S. N. PISHARODY, J. G. ZEIBEL, AND R. R. JONES

PHYSICAL REVIEW A 61 063405

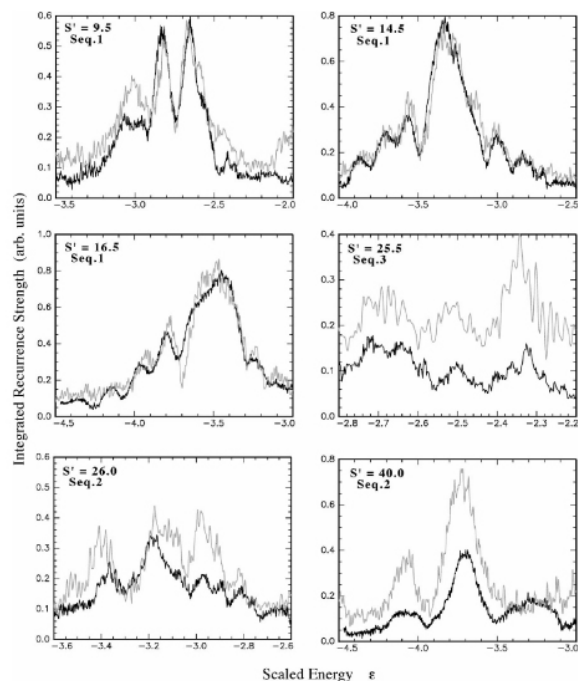


FIG. 10. Comparison between theoretical and experimental recurrence strength as a function of ϵ at constant values of S' for $m=0.1$. Quantum calculations are shown in gray and experimental data are in black. The $S' = 9.5$, 14.5 , and 16.5 curves show selected curves from the first sequence of recurrence maxima. The $S' = 26.0$ and 40.0 curves are obtained from the second sequence of recurrence maxima, while the $S' = 25.5$ graph shows a region of recurrence maxima in the third sequence.

spectrum of sodium in an applied field have been performed for $m=0,1,2$. The calculations use the known quantum defects of sodium and a Numerov integration routine to obtain the off-diagonal matrix elements of the atomic Hamiltonian in the field [6]. Only bound states with $n \leq 47$ are included in the calculation. Since no continuum levels are included, the simulation results are only strictly valid for energies below the classical saddle point, $\epsilon < -2$. The theoretical photoabsorption spectra are scaled in a manner identical to the experimental data and the corresponding recurrence spectra are displayed in Figs. 7(a) and 7(b). A weighted mixture of the different m values (32% $m=0$, 68% $m=1$ for the $m=0,1$ spectrum and 13.5% $m=0$, 29% $m=1$, 57.5% $m=2$ for the $m=2$ spectrum) is used to simulate the m state distribution in the experimental spectra. This distribution of m values is in reasonable agreement with the expected m state distributions from angular momentum coupling rules; 33% $m=0$, 66% $m=1$ for parallel polarization and 18% $m=0$, 27% $m=1$, and 55% $m=2$ for perpendicular polarization. A calculation of the Stark map of hydrogen (up to second order in the applied field) was also performed for $m=0$ and $m=2$, and scaled to obtain the hydrogenic recurrence spectra. These are presented in Fig. 8. The $m=2$ recurrence map for hydrogen closely matches both the theoretical and experimental $m=2$ spectra observed in sodium. This is to be expected due to the small quantum defect of the $\ell \geq 2$ states in sodium. While there are some similarities be-

tween the $m=0$ hydrogen recurrence map and the $m=0,1$ recurrence spectra for sodium, the agreement is not so pronounced.

B. The $m=0,1$ spectrum

The maxima in both the $m=0,1$ and the $m=2$ sodium scaled energy maps occur at or near the scaled actions corresponding to the crossing of the uphill and downhill orbits in the $m=0$ hydrogen scaled energy map. The description of the $m=0,1$ spectra is analogous to that presented by Courtney et al. in reference to their Li data [5]. In hydrogen, recurrence maxima lie along the repetitions of the primary “uphill” and “downhill” orbits (see Fig. 6). The strongest features correspond to bifurcations of these fundamental trajectories into other orbit types. However, in Na, the nonhydrogenic core allows scattering to occur directly between the fundamental uphill and downhill orbits. Maxima in the recurrence strength identify, primarily, combination orbits in which the electron precesses through a combination of uphill and downhill orbits. The static-field-induced modification of the Coulomb potential increases the period of the downhill motion while it decreases the period of the uphill motion. At the recurrence maxima, the ratios of the periods of the uphill and downhill motions are rational fractions (i.e., $i+j$ uphill orbits for every i downhill orbits). For $\epsilon < -2.5$, the changes in period of these fundamental orbits are nearly equal in

IMAGING ATOMIC STARK SPECTRA

PHYSICAL REVIEW A 61 063405

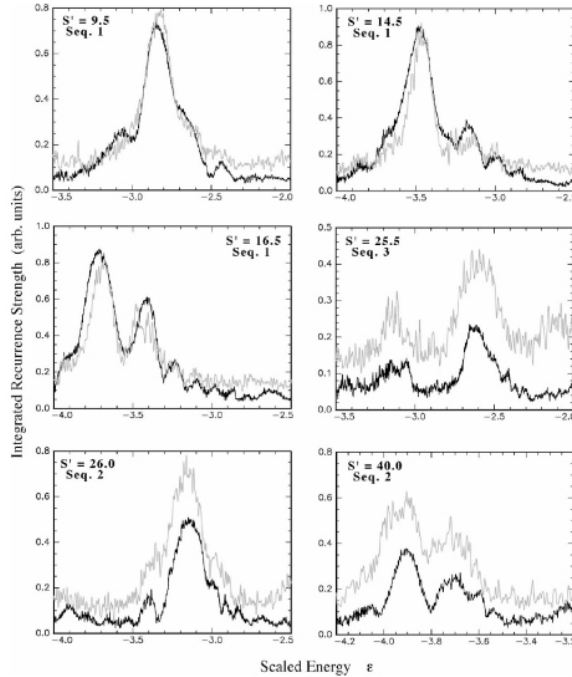


FIG. 11. Comparison between theoretical and experimental recurrence strength as a function of ϵ at constant values of S' for $m=2$. Quantum calculations are shown in gray and experimental data in black. Selected regions of scaled energies are shown for various scaled action values as described in Fig. 10.

absolute magnitude. Therefore, since the action variable S' acts as a Kepler orbit index, the action vs scaled energy curves for the $(i+j)$ th uphill orbit and the i th downhill orbit should cross at a mean value $S' = i + j/2$. Indeed, the principal features in our $m=0,1$ spectra are found at integer and half-integer values of S' for $\epsilon < -2.5$.

C. The $m=2$ spectrum

Although the recurrence maxima for the $m=2$ spectra also occur at integer and half-integer values of S' , the underlying dynamics must be different, since the uphill and downhill orbits do not exist for $m \neq 0$ [14]. Nevertheless, the strong global patterns in the experimental and theoretical scaled maps must reflect the classical dynamics in these systems. Since the $m=2$ sodium and hydrogen spectra are essentially identical, we can make a classical interpretation of the spectrum by assuming a hydrogenic atom.

In weak applied fields, the Kepler period of radial motion, $\tau_K = 2\pi n^3$, is significantly smaller than the Stark period, $\tau_S = 2\pi/3F_n$. The Stark period identifies the time scale for the pendular motion of the major axis of the Kepler ellipse about the static field axis as well as the associated precession of the electron angular momentum [1]. Electrons that are launched from the core as $\ell=2$, $m=2$ Rydberg electrons travel away from the nucleus in, or near, the xy plane. If the applied field is weak, then the net angular momentum trans-

fer per Kepler orbit due to the Stark field is small. So, after one Kepler period, there is a large probability that the electron will return to the nucleus on roughly the same trajectory with the same angular momentum. For a finite sized core, there is a range of initial launch angles which create trajectories that are not sufficiently deflected by the weak applied field to avoid being reincident upon the core after a single Kepler period. In scaled units, a weak applied field corresponds to low scaled energy, and therefore, for $\epsilon \leq -3$, there is a pronounced recurrence peak at very low scaled action corresponding to a single Kepler period (see Fig. 8). For lower ϵ there is an increasing probability that the electron will return to the nucleus before the Stark field can sufficiently affect the electron's orbit. With decreasing values of ϵ , the electron visits the core several times before its angular momentum increases to a level that prohibits its return to the nucleus. As a result, for $\epsilon < -4.0$ there are several maxima at small integer values of S' . In the limit of zero applied field, $\epsilon \rightarrow -\infty$ and $\tau_S \rightarrow \infty$, the electron returns to the nucleus after every Kepler orbit, leading to an infinite number of recurrence maxima at integer values of S' .

Note that there are fewer small action recurrence maxima in the $m=2$ data than in the corresponding $m=0$ recurrence spectra. An $\ell=2$, $m=2$ electron experiences a greater static-field-induced torque, $\tau = \vec{r} \times \vec{F}$, than the corresponding $m=0$ electron, since its orbit is essentially perpendicular to

S. N. PISHARODY, J. G. ZEIBEL, AND R. R. JONES

PHYSICAL REVIEW A 61 063405

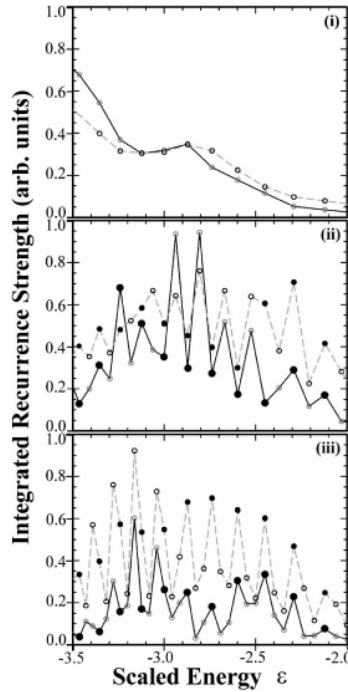


FIG. 12. Integrated recurrence strength as a function of average scaled energy for the first three sequences in $m=0,1$. Quantum calculations are indicated with dashed lines while experimental data are indicated with solid lines. Reducible orbits are indicated with filled circles while irreducible orbits are indicated with open circles. Note the periodicity of the strong features in the various sequences. The integrated recurrence strengths in each sequence are individually normalized to unity. However, a single normalization factor sets the relative amplitudes of the experiment and calculation in all three plots.

the applied field. For orbits with a greater perpendicular component, $\Delta L/\Delta t$ is greater and the electron misses the core after fewer Kepler orbits due to its increased angular momentum.

After the initial recurrences in the $m=2$ map, there is a region of scaled action values without recurrence maxima. This empty region corresponds to times when the electron's orbit is precessing around the field axis through various angular momentum values. After a number of Kepler periods, determined by the launch angle and the scaled energy, the electron returns to the nucleus as indicated by a second region of strong recurrences. These recurrence maxima (sequence I) are located at an S' value that corresponds to the Stark period. During the first Stark period, the major axis of the Kepler ellipse completes one-half of a pendular cycle about the applied field axis while the electron angular mo-

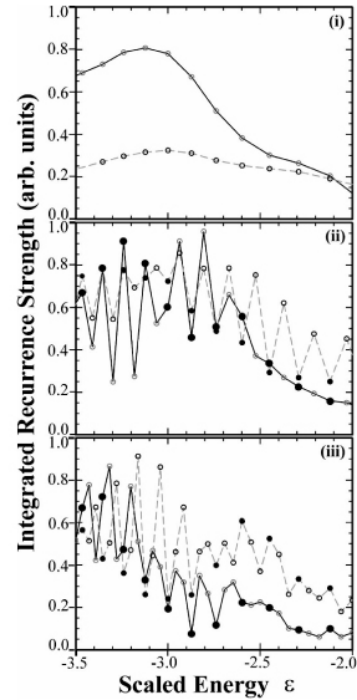


FIG. 13. Integrated recurrence strength as a function of average scaled energy for the first three sequences in $m=2$. Quantum calculations are indicated with dashed lines while experimental data are indicated with solid lines. Reducible orbits are indicated with filled circles while irreducible orbits are indicated with open circles.

mentum completes a full precessional cycle from low ℓ to high ℓ and back. When the electron returns to the core with low angular momentum at this time, the major axis of its orbit has precessed through an angle of approximately π . In essence, the pendular motion of the ellipse adds an extra half Kepler orbit to the motion. As a result, the return of the electron to the core (sequence 1 recurrence maxima) occurs at or very near a half-integer value of S' .

In a similar fashion, after another Stark period, the electron again returns to lower ℓ values and the nucleus, creating another region of recurrence maxima (sequence II) located at values of S' that are twice those of sequence I. At this time, the electron has completed two Stark periods and the major orbit of its axis has finished a full pendular cycle [1]. The returns to the nucleus occur after an integer number of primary Kepler orbits, and therefore the recurrence maxima are located at integer values of S' . Continuing in this manner, numerous sequences are observed in the recurrence spectrum, with the i th sequence corresponding to electrons that have completed i Stark periods.

For $\epsilon = -3.0$, recurrence maxima are observed for $S' = 10.5, 11.5, 12.5$, and 13.5 , corresponding to $10\frac{1}{2}, 11\frac{1}{2}, 12\frac{1}{2}$, and $13\frac{1}{2}$ Kepler orbits, respectively. If we look at the second sequence, the range of Kepler orbits that contribute recurrence strength is larger, with significant recurrence maxima observed at $S' = 22, 23, 24, 25, 26$, and 27 . In general, for a given value of ϵ , the higher the sequence number, the greater is the range of scaled actions that have significant recurrence strengths within a given sequence.

D. Global properties of the scaled energy maps

A comparison of the relative intensities of the individual recurrences within each sequence has also been performed. To facilitate the comparison, the recurrence map is binned in half-integer units of the action coordinate S' (see Fig. 9). This allows us to study several features of the scaled spectrum. First, we are able to investigate recurrence strengths at constant scaled actions S' , as a function of scaled energy. Kips et al. [11] examined recurrence strength in this manner in their theoretical calculations; however, they were unable to compare their results to any experimentally measured spectra. Figure 10 shows recurrence maxima as a function of scaled energy for various values of S' , showing both experimental data and quantum calculations for $m=0,1$ in sodium. Figure 11 shows similar graphs for $m=2$. A global shift in scaled energy of $\delta\epsilon = +0.03$ is applied to all the experimental data to obtain the best agreement between experiment and theory. Presumably, this small error is due to the uncertainty in the measurement of the applied electric field. The $S' = 26$ and $S' = 40$ graphs provide a view of a region of sequence II. The $S' = 25.5$ curve focuses on a region of sequence III. The curves in Figs. 10 and 11 are representative, and there is good overall agreement between data and theory, particularly in the first two sequences. Note that, aside from the slight shift in the experimental value of ϵ , there are no adjustable parameters in the calculation. A single normalization factor is used on the entire data set to allow comparison between experiment and theory.

Integrating the binned maps over a range of scaled energies yields the total recurrence strength for a given closed orbit as a function of sequence number. The recurrence strength value within $\pm 10\%$ of the center of each sequence is integrated to obtain the total recurrence strength per orbit per sequence. We define the center of the sequences as the crossing of the hydrogenic uphill and downhill repetition orbits (see Fig. 6). For the j th sequence and $\epsilon < -2.5$, the center is given approximately by the closed form expression for the crossing of the i th downhill repetition with the $(i+j)$ th uphill repetition,

$$\epsilon_j(S') = \sqrt{\frac{3(S' + j/2)}{4j}}. \quad (6)$$

The resulting curves (see Figs. 12 and 13) represent integrated recurrence strengths as a function of scaled energy for each sequence. In general, each curve shows a modulation with a period of j Kepler orbits for a given sequence j . The

integrated strength curves are sensitive to background noise in the recurrence map. As a result, the agreement between theory and experiment is only qualitative. Keeler and Morgan noticed similar structure within each sequence of integrated recurrence strength in their studies of helium [12]. They associated the oscillations with the types of orbit, reducible or irreducible, within each sequence. Our data, like those of Keeler and Morgan [12], exhibit strong definable modulations only over a limited range of scaled action. Figure 12 shows the integrated recurrence strength as a function of average scaled energy in the first three sequences for $m=0,1$ theory and experimental data. Figure 13 shows the corresponding sequences for $m=2$. Relative maxima and minima appear to be functions of whether the orbit in question is reducible or not; however, the functional dependence on whether reducible orbits correspond to relative maxima or to relative minima changes as a function of scaled action. In general, the scaled action values at which the crossovers occur are approximately the same as those at similar crossover features in He [12]. Also, the scaled action values at the crossovers in Na are the same in both the calculated and experimental spectra.

The observed periodicity is more evident in the $m=0,1$ experimental data than in the corresponding $m=2$ data. The lack of any such structure in the quantum calculation of the $m=2$ sodium recurrence spectrum and the small quantum defect of the $m=2$ states in sodium suggest that the presence of these features in the $m=2$ experimental data is due solely to the presence of $m=0,1$ states in the $m=2$ spectra.

IV. SUMMARY

We have measured Na Stark maps as a continuous function of energy and applied static electric field. Using a modified set of scaled variables, the data are Fourier transformed to produce recurrence maps as a continuous function of scaled energy and scaled action. We have identified several global features of the recurrence map, including a propensity for recurrence strength to cluster at integer or half-integer values of the scaled action. Because of the continuous nature of the maps, we have been able to study with high resolution the recurrence strength as a function of scaled energy and scaled action.

Complicated modulations in the differential recurrence strength (strength vs scaled energy at fixed scaled action) and integrated recurrence strength (energy-integrated strength vs scaled action) that are observed in the data are in agreement with quantum simulations. It would be extremely interesting to determine at what level semiclassical methods can reproduce these structures. Theoretical investigations along these lines are currently underway [17].

ACKNOWLEDGMENTS

We would like to thank T. J. Bensky for his invaluable help in developing the data-collection software used in this experiment. This project is supported by the Packard Foundation and the AFOSR.

S. N. PISHARODY, J. G. ZEIBEL, AND R. R. JONES

PHYSICAL REVIEW A 61 063405

- [1] T.P. Hezel, C.E. Burkhardt, M. Ciocca, L.-W. He, and J.J. Leventhal, *Am. J. Phys.* 60, 329 (1992); T.P. Hezel, C.E. Burkhardt, M. Ciocca, and J.J. Leventhal, *ibid.* 60, 324 (1992).
- [2] T.W. Ducas, M.G. Littman, R.R. Freeman, and D. Kleppner, *Phys. Rev. Lett.* 35, 366 (1975); T.F. Gallagher, L.M. Humphrey, R.M. Hill, and S.A. Edelstein, *ibid.* 37, 1465 (1976); M.G. Littman, M.L. Zimmerman, T.W. Ducas, R.R. Freeman, and D. Kleppner, *ibid.* 36, 788 (1976); M.G. Littman, M.M. Kash, and D. Kleppner, *ibid.* 41, 103 (1978); M.L. Zimmerman, T.W. Ducas, M.G. Littman, and D. Kleppner, *J. Phys. B* 11, L11 (1978); W.E. Cooke and T.F. Gallagher, *Phys. Rev. A* 17, 1226 (1978); T.H. Jeys, G.W. Foltz, K.A. Smith, E.J. Beiting, F.G. Kellert, F.B. Dunning, and R.F. Stebbings, *Phys. Rev. Lett.* 44, 390 (1980).
- [3] L.D. Noordam, A. ten Wolde, A. Legendijk, and H.B. van Linden van den Heuvell, *Phys. Rev. A* 40, 6999 (1989); B. Broers, J.F. Christian, J.H. Hoogenraad, W.J. van der Zande, H.B. van Linden van den Heuvell, and L.D. Noordam, *Phys. Rev. Lett.* 71, 344 (1993); B. Broers, J.F. Christian, and H.B. van Linden van den Heuvell, *Phys. Rev. A* 49, 2498 (1994); G.M. Lankhuijzen and L.D. Noordam, *ibid.* 52, 2016 (1995); *Phys. Rev. Lett.* 76, 1784 (1996); J. Wals and H.B. van Linden van den Heuvell, *J. Phys. B* 30, 941 (1997); M.T. Frey, F.B. Dunning, C.O. Reinhold, and J. Burgdorfer, *Phys. Rev. A* 55, R865 (1997); C. Raman, T.C. Weinacht, and P.H. Bucksbaum, *ibid.* 55, R3995 (1997); M.L. Naudeau, C.I. Sukenik, and P.H. Bucksbaum, *ibid.* 56, 636 (1997); G.M. Lankhuijzen, F. Robicheaux, and L.D. Noordam, *Phys. Rev. Lett.* 79, 2427 (1997); T.J. Binsky, M.B. Campbell, and R.R. Jones, *ibid.* 81, 3112 (1998); M.B. Campbell, T.J. Binsky, and R.R. Jones, *Phys. Rev. A* 59, R4117 (1999).
- [4] H.A. Bethe and E.E. Salpeter, *Quantum Mechanics of One- and Two-Electron Atoms* (Plenum, New York, 1977); D.A. Harmin, *Phys. Rev. A* 24, 2491 (1981); J.R. Rubbmark, M.M. Kash, M.G. Littman, and D. Kleppner, *ibid.* 23, 3107 (1981); D.A. Harmin, *Phys. Rev. Lett.* 49, 128 (1982); *Phys. Rev. A* 26, 2656 (1982); F. Robicheaux and J. Shaw, *Phys. Rev. Lett.* 77, 4154 (1996).
- [5] M. Courtney, N. Spellmeyer, H. Jiao, and D. Kleppner, *Phys. Rev. A* 51, 3604 (1995).
- [6] M.L. Zimmerman, M.G. Littman, M.M. Kash, and D. Kleppner, *Phys. Rev. A* 20, 2251 (1979).
- [7] U. Eichmann, K. Richter, D. Wintgen, and W. Sandner, *Phys. Rev. Lett.* 61, 2438 (1988).
- [8] J. Gao and J.B. Delos, *Phys. Rev. A* 49, 869 (1994).
- [9] M. Courtney, H. Jiao, N. Spellmeyer, and D. Kleppner, *Phys. Rev. Lett.* 73, 1340 (1994); M. Courtney, H. Jiao, N. Spellmeyer, D. Kleppner, J. Gao, and J.B. Delos, *ibid.* 74, 1538 (1995).
- [10] G.J. Kuik, A. Kips, W. Vassen, and W. Hogervorst, *J. Phys. B* 29, 2159 (1996); A. Kips, W. Vassen, W. Hogervorst, and P.A. Dando, *Phys. Rev. A* 58, 3043 (1998).
- [11] A. Kips, W. Vassen, and W. Hogervorst, *Phys. Rev. A* 59, 2948 (1999).
- [12] M.L. Keeler and T.J. Morgan, *Phys. Rev. Lett.* 80, 5726 (1998); *Phys. Rev. A* 59, 4559 (1999).
- [13] J.A. Shaw and F. Robicheaux, *Phys. Rev. A* 58, 1910 (1998).
- [14] F. Robicheaux and J. Shaw, *Phys. Rev. A* 58, 1043 (1998).
- [15] A.D. Peters, C. Jaffe, and J.B. Delos, *Phys. Rev. Lett.* 73, 2825 (1994); P.A. Dando, T.S. Monteiro, and S.M. Owen, *ibid.* 80, 2797 (1998).
- [16] M.G. Littman, *Opt. Lett.* 3, 128 (1978); M.G. Littman and H.J. Metcalf, *Appl. Opt.* 7, 224 (1978).
- [17] J. Shaw (private communication).

Bibliography

- [1] J. J. Thomson, *Phil. Mag.*, **44**, 293 ,(1897).
- [2] J. J. Thomson, *Proc. Cambridge Phil. Soc.*, **15**, 465 ,(1910).
- [3] J. J. Balmer, *Wied. Ann.*, **25**, 80, (1885).
- [4] H. Geiger, and E. Marsden, *Proc. Roy. Soc.*, **A82**, 495, (1909).
- [5] E. Rutherford, *Phil. Mag.*, **21**, 669, (1911).
- [6] N. Bohr, *Phil. Mag.*, **26**, 1, (1913); *Phil. Mag.*, **27**, 506, (1914).
- [7] A. Sommerfeld, *Ann. Physik.*, **51**, 1, (1916); W.Wilson, *Phil Mag.*, **29**, 795, (1915).
- [8] L. de Broglie, *Phil. Mag.*, **47**, 466, (1924); *Ann. Physik*, **3**, 22, (1925).
- [9] E. Schrödinger, *Ann. Physik*, **79**, 361, 489, 734, (1926); *Phys. Rev.*, **28**, 1049, (1926).
- [10] W. Heisenberg, *Zeit. fur Phys.*, **33**, 879, (1925).

- [11] J. Chadwick, Proc. Roy. Soc., **A136**, 692, (1932).
- [12] D. Williams (ed.), Methods of Experimental Physics, vol.13, part A, *Spectroscopy*, Academic Press, New York (1976).
- [13] L. I. Schiff, *Quantum Mechanics*, 3rd ed., New York: McGraw-Hill Book Company, 1969; A. P. Arya, *Fundamentals of Atomic Physics*, Allyn and Bacon Inc., Boston, 1971 and references therein.
- [14] A. Einstein, Physik Z., **18**, 121 (1917); S.N.Bose, Z. Physik,**26**, 178 (1924); D. ter Haar, Rev. Mod. Phys., **27**, 289 (1955).
- [15] M. H. Anderson, J. R. Ensher, M. R. Matthews, C. E. Wieman and E. A. Cornell, Science **269**, 198 (1995).
- [16] J. P. Gordon, H. J. Zeiger, and C. H. Townes, Phys. Rev. **99**, 1264 (1955).
- [17] T. H. Maiman, Nature **187**, 493 (1960).
- [18] W. Demtroder, *Laser Spectroscopy: Basic concepts and Instrumentation* , 2nd Edition (Springer-Verlag, Berlin, 1995).
- [19] T. W. Hansch, Applied Optics **11**, 895 (1972).
- [20] M. G. Littman, H. J. Metcalf, Applied Optics **17**, 2224 (1978).
- [21] L. F. Johnson, G. D. Boyd, K. Nassau, R. R. Sodden had the first continuous operation of an optically-pumped solid state laser in Nd:CaWO₄ at 1.06 μ in 1961.

- [22] W. T. Silfvast, *Laser Fundamentals*, Cambridge University Press, Cambridge, England (1996).
- [23] J. -C. Diels, W. Rudolph, *Ultrashort Laser Pulse Phenomena*, Academic Press, San Diego, California (1996).
- [24] G. G. Paulus et.al, *Nature* **414**, 182 (2001); A. E. Kaplan, P. L. Shkolnikov, *Phys. Rev. Lett.* **88**, 074801 (2002).
- [25] T. F. Gallagher, *Rydberg Atoms*, Cambridge University Press, Cambridge, England (1994) 1st edition, and references therein.
- [26] R. Bluhm, V. A. Kostelecký, *Phys. Lett. A* **200**, 308 (1995).
- [27] M. J. Seaton, *Rep. Prog. Phys.*, **46**, 167, (1983); U.Fano, *Phys. Rev. A* **2**, 353 (1970).
- [28] U. Fano, *J. Phys. B* **7**, L401 (1974).
- [29] S. A. Bhatti, C. L. Cromer, W. E. Cooke, *Phys. Rev. A* **24**, 161 (1981).
- [30] M. Poirier, *Phys. Rev. A* **38**, 3484 (1988).
- [31] W. R. Johnson, K. T. Cheng, K.-N. Huang, M. Le Dourneuf, *Phys. Rev. A* **22**, 989 (1980).
- [32] T. F. Gallagher, K. A. Safinya, W. E. Cooke, *Phys. Rev. A* **24**, 601 (1981).
- [33] W. E. Cooke, T. F. Gallagher, S. A. Edelstein, R. M. Hill, *Phys. Rev. Lett.* **40**, 178 (1978).

- [34] V. Lange, U. Eichmann, W. Sandner, J. Phys. B **22**, L245 (1989).
- [35] R. R. Jones, B. J. Lyons, M. A. Baig, Svetlana T. Djambova, T. F. Gallagher, Phys. Rev. A **62**, 033408 (2000).
- [36] F. Robicheaux, Phys. Rev. A **62**, 033406 (2000).
- [37] A. R. P. Rau, J. Opt. Soc. Am. B **4**, 784 (1987).
- [38] T. F. Gallagher, J. Opt. Soc. Am. B **4**, 794 (1987).
- [39] J. Boulmer, P. Camus, J.-M. Lecomte, P. Pillet, J. Opt. Soc. Am. B **5**, 2199 (1988).
- [40] G. Tanner, K. Richter, J.-M. Rost, Rev. Mod. Phys., **72**, 497 (2000).
- [41] A. Unsöld, Ann. Phys.(Leipzig), **82**, 355 (1927).
- [42] J. C. Slater, Proc. Natl. Acad. Sci. USA., **13**, 423 (1927).
- [43] G. W. Kellner, Z. Phys., **44**, 91 (1927).
- [44] E. A. Hylleraas, Z. Phys., **48**, 469 (1928); *ibid* **54**, 347 (1929).
- [45] Y. K. Ho, Z. Phys. D **42**, 77 (1997).
- [46] C. L. Pekeris, Phys. Rev. **112**, 1649 (1958); *ibid* **115**, 1216 (1959).
- [47] A. Bürgers, D. Wintgen, J.-M. Rost, J. Phys. B **28**, 3163 (1998).
- [48] A. Landé, Phys. Z., **20**, 228 (1919).

- [49] I. Langmuir, Phys. Rev., **17**, 339 (1921).
- [50] J. H. van Vleck, Philos. Mag. **44**, 842 (1922).
- [51] H. A. Kramers, Z.Phys., **13**, 312 (1923).
- [52] J. G. Leopold, I. C. Percival, A. S. Tworkowski, J. Phys. B **13**, 1025 (1980); *ibid* 1037 (1980).
- [53] E. A. Solov'ev, Zh. Eksp. Teor. Fiz. **89**, 1991 [Sov. Phys. JETP **62**, 1148] (1985).
- [54] G. S. Ezra, K. Richter, G. Tanner, D. Wintgen, J. Phys. B **24**, L413 (1991).
- [55] G. H. Wannier, Phys. Rev. **90**, 817 (1953).
- [56] H. Klar, J. Opt. Soc. Am. B **4**, 788 (1987).
- [57] L. Hilico et.al, Phys. Rev. A **66**, 022101 (2002).
- [58] R. P. Madden, K. Codling, Phys. Rev. Lett. **10**, 516 (1963).
- [59] S. J. Buckman, P. Hammond, F. H. Read, G. C. King, J. Phys. B **16**, 4039 (1983).
- [60] K. Schulz, G. Kaindl, J. D. Bozek, P. A. Heimann, A. S. Schlachter, Journal of Electron Spectroscopy and Related Phenomena **79**, 253 (1996).
- [61] R. R. Jones, *Double rydberg states of barium*, PhD dissertation, University of Virginia, 1990.

- [62] W. E. Cooke, R. M. Jopson, L. A. Bloomfield, R. R. Freeman, J. Bokor, AIP Conf. Proc., vol.**119**, 91 (1984).
- [63] P. Camus, T. F. Gallagher, J.-M. Lecomte, P. Pillet, L. Pruvost, J. Boulmer, Phys. Rev. Lett. **62**, 2365 (1989).
- [64] L. A. Bloomfield, R. R. Freeman, W. E. Cooke, J. Bokor, Phys. Rev. Lett. **53**, 2234 (1984).
- [65] R. R. Jones, T. F. Gallagher, Phys. Rev. A **42**, 2655 (1990).
- [66] R. van Leeuwen, W. Ubachs, P. Camus, W. Hogervorst, Phys. Rev. A **54**, R17 (1996).
- [67] U. Eichmann, V. Lange, W. Sandner, Phys. Rev. Lett. **64**, 274 (1990).
- [68] R. R. Jones, Panming Fu, T. F. Gallagher, Phys. Rev. A **44**, 4265 (1991).
- [69] U. Eichmann, V. Lange, W. Sandner, Phys. Rev. Lett. **68**, 21 (1992).
- [70] P. Camus, S. Cohen, L. Pruvost, A. Bolovinos, AIP Conf. Proc., vol.**290**, 105 (1993).
- [71] M. Seng, K.-D. Heber, M. Halka, W. Sandner, AIP Conf. Proc., vol.**290**, 99 (1993).
- [72] M. Cheret, L. Chen, D. Porterat, G. Spiess, AIP Conf. Proc., vol.**290**, 108 (1993).
- [73] B. J. Lyons, D. W. Schumacher, D. I. Duncan, R. R. Jones, T. F. Gallagher, Phys. Rev. A **57**, 3712 (1998).

- [74] P. Camus, P. Pillet, J. Boulmer, AIP Conf. Proc., vol.**146**, 480 (1986).
- [75] J. Boulmer, P. Camus, P. Pillet, J. Opt. Soc. Am. B **4**, 805 (1987).
- [76] D. W. Schumacher, B. J. Lyons, T. F. Gallagher, Phys. Rev. Lett. **78**, 4359 (1997).
- [77] R. van Leeuwen, K. Vijayalakshmi, R. R. Jones, Phys. Rev. A **63**, 033403 (2001).
- [78] C. Rosen, M. Dórr, U. Eichmann, W. Sandner, Phys. Rev. Lett. **83**, 4514 (1999).
- [79] H. N. Ereifej, J. G. Story, Phys. Rev. A **62**, 023404 (2000); Phys. Rev. A **62**, 033405 (2000); J.G.Story, H.N.Ereifej, Phys. Rev. Lett. **86**, 612 (2001).
- [80] T. J. Binsky, *Rydberg atoms and Half-cycle Pulses*, PhD dissertation, University of Virginia, 1998.
- [81] M. B. Campbell, *Rydberg wavepacket dynamics*, PhD dissertation, University of Virginia, 2000.
- [82] J. L. Wiza, Nucl. Instru. and Meth.,**162**, 587 (1979).
- [83] J. A. Yeazell, C. R. Stroud,Jr., Phys. Rev. Lett. **60**, 1494 (1988); Phys. Rev. A **35**, 2806 (1987).
- [84] A. ten Wolde et.al., Phys. Rev. Lett. **61**, 2099 (1988).
- [85] J. A. Ramswell, V. G. Stavros, Q. Hong, H. H. Fielding, Phil. Trans. R. Soc. Lond. A **356**, 363 (1998).

- [86] J. R. R. Verlet, V. G. Stavros, R. S. Minns, H. H. Fielding, *Phys. Rev. Lett.* **89**, 263004 (2002).
- [87] C. O. Reinhold, J. Burgdörfer, M. T. Frey, F. B. Dunning, *Nucl. Inst. and Meth. Phys. Res. B* **132**, 316 (1997).
- [88] T. C. Weinacht, J. Ahn, P. H. Bucksbaum, *Nature*, **397**, 233 (1999).
- [89] D. W. Schumacher, J. H. Hoogenraad, D. Pinkos, P. H. Bucksbaum, *Phys. Rev. A* **52**, 4719 (1995).
- [90] G. Alber, H. Ritsch, P. Zoller, *Phys. Rev. A* **34**, 1058 (1986).
- [91] Tsin-Fu Jiang, Shih-I Chu, *Chem. Phys. Lett.* **240**, 278 (1995).
- [92] M. Klews, W. Schweizer, *Phys. Rev. A* **64**, 053403 (2001).
- [93] R. R. Jones, *Phys. Rev. A* **58**, 2608 (1998)
- [94] W. E. Cooke, T. F. Gallagher, *Phys. Rev. Lett.* **41**, 1648 (1978).
- [95] R. J. de Graaf, W. Ubachs, W. Hogervorst, *Phys. Rev. A* **45**, 166 (1992).
- [96] R. M. Jopson, R. R. Freeman, W. E. Cooke, J. Bokor, *Phys. Rev. A* **29**, 3154 (1984).
- [97] R. M. Jopson, R. R. Freeman, W. E. Cooke, J. Bokor, *Phys. Rev. Lett.* **51**, 1640 (1983).

- [98] J. Neukammer, H. Rinneberg, G. Jönsson, W. E. Cooke, H. Hieronymus, A. König, K. Vietzke, H. Springer-Bolk, Phys. Rev. Lett. **55**, 1979 (1985).
- [99] N. H. Tran, P. Pillet, R. Kachru, T. F. Gallagher, Phys. Rev. A **29**, 2640 (1984).
- [100] C. J. Dai, G. W. Schinn, T. F. Gallagher, Phys. Rev. A **42**, 223 (1990); G. W. Schinn, C. J. Dai, T. F. Gallagher, Phys. Rev. A **43**, 2316 (1991).
- [101] R. R. Jones, T. F. Gallagher, Phys. Rev. A **38**, 2846 (1988).
- [102] F. Robicheaux, W. T. Hill III, Phys. Rev. A **54**, 3276 (1996).
- [103] X. Wang, W. E. Cooke, Phys. Rev. Lett. **67**, 976 (1991); Phys. Rev. A **46**, 4347 (1992).
- [104] F. Texier, F. Robicheaux, Phys. Rev. A **61**, 043401 (2000).
- [105] R. van Leeuwen, M. L. Bajema, R. R. Jones, Phys. Rev. A **61**, 022716 (2000).
- [106] J. E. Thoma, R. R. Jones, Phys. Rev. Lett. **83**, 516 (1999).
- [107] M. B. Campbell, T. J. Binsky, R. R. Jones, Phys. Rev. A **57**, 4616 (1998).
- [108] A. M. Weiner, J. P. Heritage, E. M. Kirschner, J. Opt. Soc. Am. B **5**, 1563 (1988); R. N. Thurston, J. P. Heritage, A. M. Weiner, W. J. Tomlinson, IEEE J. Quant. Elec., **QE-22**, 682 (1986).
- [109] W. E. Cooke, C. L. Cromer, Phys. Rev. A **32**, 2725 (1985).
- [110] J. A. Armstrong, P. Esherick, J. J. Wynne, Phys. Rev. A **15**, 180 (1977).

- [111] H. van der Hart, Chris Greene, *private communication*.
- [112] A. Lindgard, S. E. Nielsen, *Atomic Data and Nuclear Data Tables*, **19**, 533 (1977).
- [113] Y. Zhu, R. R. Jones, W. Sandner, T. F. Gallagher, P. Camus, P. Pillet, J. Boulmer, *J. Phys. B* **22**, 585 (1989).
- [114] W. Sandner, G. A. Ruff, V. Lange, U. Eichmann, *Phys. Rev. A* **32**, 3794 (1985).
- [115] E. A. J. M. Bente, W. Hogervorst, *Z. Phys. D - Atoms, Molecules and Clusters* **14**, 119 (1989).
- [116] C. E. Moore, *Atomic Energy Levels*, Vol III, Natl. Bur. Stand. (U.S.) Circ. No. 467 (U.S. GPO, Washington, D.C., 1958).
- [117] M. Aymar, P. Camus, *Phys. Rev. A* **28**, 850 (1983).
- [118] P. Camus, M. Dieulin, A. El Himdy, *Phys. Rev. A* **26**, 379 (1982).
- [119] P. Camus, M. Dieulin, A. El Himdy, M. Aymar, *Physica Scripta* **27**, 125 (1983).
- [120] L. D. Noordam, D. I. Duncan, T. F. Gallagher, *Phys. Rev. A* **45**, 4734 (1992).
- [121] R. R. Jones, C. S. Raman, D. W. Schumacher, P. H. Bucksbaum, *Phys. Rev. Lett.* **71**, 2575 (1993).
- [122] R. R. Jones, *Phys. Rev. Lett.* **76**, 3927 (1996).
- [123] M. B. Campbell, T. J. Bensity, and R. R. Jones, *Phys. Rev. A* **58**, 514 (1998).

- [124] W. E. Cooke, T. F. Gallagher, Phys. Rev. A **21**, 588 (1980).
- [125] S. N. Pisharody, R. R. Jones, Phys. Rev. A **65**, 033418 (2002).
- [126] R. R. Jones, class notes for PHYS 842 at the University of Virginia (1997).
- [127] U. Fano, Phys. Rev. **124**, 1866 (1961).
- [128] Method of calibrating ionic rydberg states from simultaneous measurement of dye laser light from etalon and the signals from field ionization of ionic rydberg states:
- $$(109737\text{cm}^{-1})\left(\frac{2}{n_1^2} - \frac{2}{n_2^2}\right) = \frac{\text{no. of fringes between } n_1 \text{ and } n_2}{2\eta d}$$
- where n_1 , and n_2 are the estimated effective principal quantum numbers for any two peaks in the scan, η is the refractive index of the etalon and d is the thickness of the etalon.
- [129] H. Stapelfeldt, D. G. Papaioannou, L. D. Noordam, T. F. Gallagher, Phys. Rev. Lett. **67**, 3223 (1991).
- [130] R. R. Jones, P. H. Bucksbaum, Phys. Rev. Lett. **67**, 3215 (1991).
- [131] D. A. Tate, T. F. Gallagher, Phys. Rev. A **58**, 3058 (1998).
- [132] W. Huang, U. Eichmann, W. Sandner, Phys. Rev. A **59**, 2744 (1999).
- [133] H. Maeda, W. Li, T. F. Gallagher, Phys. Rev. Lett. **85**, 5078 (2000); H. Maeda, T. F. Gallagher, Phys. Rev. A **65**, 053405 (2002).

- [134] F. Robicheaux, R. C. Forrey, *Calculations of double rydberg wavepackets on He*, unpublished, 1999.
- [135] W. H. Press, S. A. Teukolsky, W. T. Vetterling, B. P. Flannery, *Numerical Recipes in C: The Art of Scientific Computing*, 2nd ed., Cambridge University Press, New York, (1995).
- [136] V. Schmidt et.al, Phys. Rev. Lett. **38**, 63 (1977); S. Rioual et.al, Phys. Rev. Lett. **86**, 1470 (2001) and the references therein.
- [137] J. G. Zeibel, R. R. Jones, J. Phys. B **34**, 1213 (2001).
- [138] J. G. Zeibel, R. R. Jones, Phys. Rev. Lett. **89**, 093204 (2002).
- [139] M. Seng, U. Eichmann, V. Lange, T. F. Gallagher, W. Sandner, Eur. Phys. J. D **3**, 21 (1998).
- [140] P. Pillet et.al, Phys. Rev. A **30**, 280 (1984).
- [141] T. J. Binsky, M. B. Campbell, R. R. Jones, Phys. Rev. Lett. **81**, 3112 (1998).
- [142] F. Robicheaux, Phys. Rev. A **60**, 431 (1999).
- [143] M. A. Abramowitz, and I. A. Stegun (eds.), *Handbook of Mathematical Functions* (Natl. Bur. Stds. Appl. Math. Series 55), Washington, D.C.,1964.
- [144] J. D. Jackson, *Classical Electrodynamics*, 2nd ed., John-Wiley and Sons, 1975.